Merging galaxy clusters: probing magnetism and particle acceleration over cosmic time

Di Gennaro, G.

Cover Page

The handle http://hdl.handle.net/1887/3188671 holds various files of this Leiden University dissertation.

Author: Di Gennaro, G.
Title: Merging galaxy clusters: probing magnetism and particle acceleration over cosmic time
Issue date: 2021-07-08

MERGING GALAXY CLUSTERS

PROBING MAGNETISM AND PARTICLE ACCELERATION OVER COSMIC TIME

GABRIELLA
DI GENNARO

Merging Galaxy Clusters: probing magnetism and particle acceleration over cosmic time

Proefschrift

ter verkrijging van
de graad van doctor aan de Universiteit Leiden,
op gezag van rector magnificus prof.dr.ir. H. Bijl,
volgens besluit van het college voor promoties
te donderdag op 8 juli 2021
klokke 16:15 uur

door

Gabriella Di Gennaro
geboren te Mugnano di Napoli (Naples), Italië
in 1992

Promotiecommissie

Promotor: Prof. Dr. Huub J. A. Röttgering
Co-Promotor: Dr. Reinout J. van Weeren

Overige leden: Prof. Dr. Henk Hoekstra
Prof. Dr. Jelle S. Kaastra (SRON/Universiteit Leiden, the Netherlands)
Prof. Dr. Joop Schaye
Dr. Ruta Kale (NCRA-TIFR, Pune, India)
Dr. Maxim Markevitch (NASA/GSFC, Greenbelt MD, USA)
Prof. Dr. Dongsu Ryu (UNIST, Ulsan, Korea)
Dr. Tiziana Venturi (IRA-INAF, Bologna, Italy)

A mia sorella
la mia forza, la mia roccia,
il mio porto sicuro.

To my sister
my strength, my rock,
my safe harbour.

CONTENTS

CHAPTER

1

INTRODUCTION

1.1. Galaxy clusters

Galaxy clusters are the largest virialized structures in the Universe. They can contain more than a thousand galaxies within a radius of $\sim 1 - 2$ Mpc. However, galaxies only represent a small percentage of the cluster's mass, which is about 10^{14-15} $M_\odot$. The bulk of the cluster mass is in the form of *dark matter* (70–80%), although its nature is still unknown. The remaining mass of a cluster, the *baryonic* content, is dominated by a dilute and hot plasma. This intracluster medium (ICM) fills the space in between the cluster member galaxies.

According to the current Cosmology (ΛCDM[1], where Λ refers to the cosmological constant and CDM stays for Cold Dark Matter), structure formation is thought to be a consequence of a hierarchical growth of small density fluctuations under the effect of gravity (e.g. Peebles, 1980; Coles & Chiang, 2000). Such variations could be produced by cosmic inflation, and are detected as temperature anisotropies in the cosmic microwave background (CMB), which maps the surface of last scattering between matter and radiation. In this framework, galaxy clusters are the latest structures to form, at the intersections of filaments in the cosmic web.

The gravitational collapse of the small fluctuations is usually studied via hydrodynamical cosmological simulations (e.g. Illustris, Fig. 1.1, Vo-

---

[1]The values for the density contrast of the cosmological constant and of the matter are $\Omega_\Lambda = 0.7$ and $\Omega_m = 0.3$, respectively.
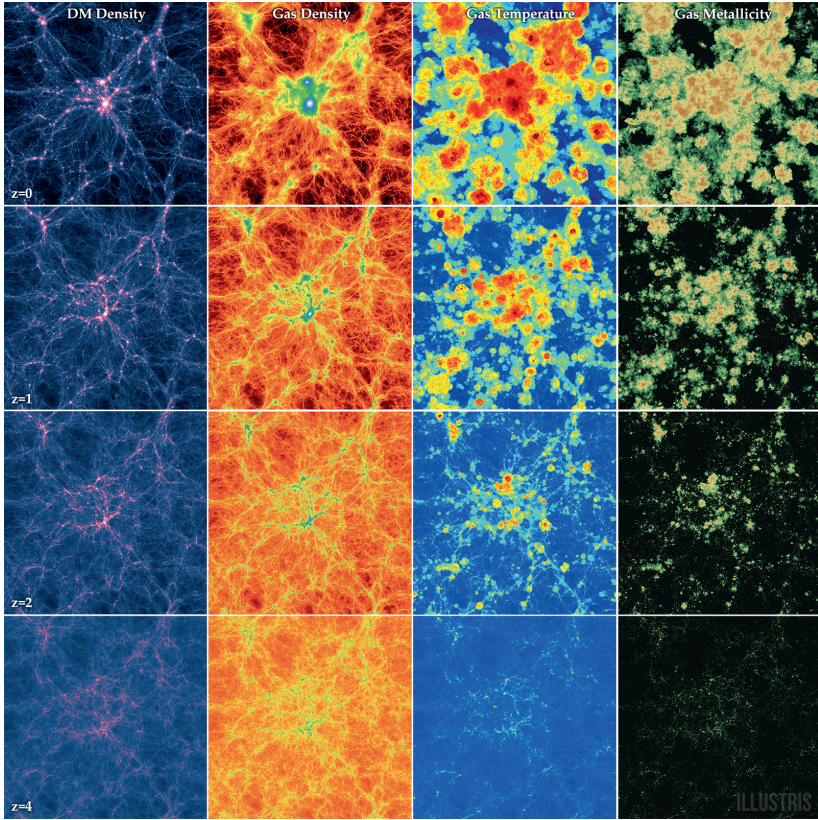
Figure 1.1: Illustris simulation of the redshift evolution of the most massive cluster at $z = 0$ from $z = 4$ (the box size is 106.5 Mpc). The four columns show four quantities from the of the simulation (from left to right, dark matter density, gas density, gas temperature and gas metallicity; Vogelsberger et al., 2014).

gelsberger et al., 2014). Their concordance with observational results is considered a key test to disentangle different cosmological models, structure formation scenarios, and the properties of the dark matter.

From the observational point of view, defining the moment when the first structures are sufficiently overdense to be defined as galaxy clusters is not trivial (for a review see Overzier, 2016). Traditionally, high redshift clusters are selected from optical/near-infrared large surveys, where galaxies are selected either by photometry or by the identification of their Balmer break (e.g. Gladders & Yee, 2005). X-ray surveys were also used to detect high redshift clusters (e.g., from the XMM-Newton Large Scale Structure survey, XMM-LSS; Pierre et al., 2004, 2011). This selection method is however limited to the most massive objects and to redshifts of $z \sim 1.5$ due
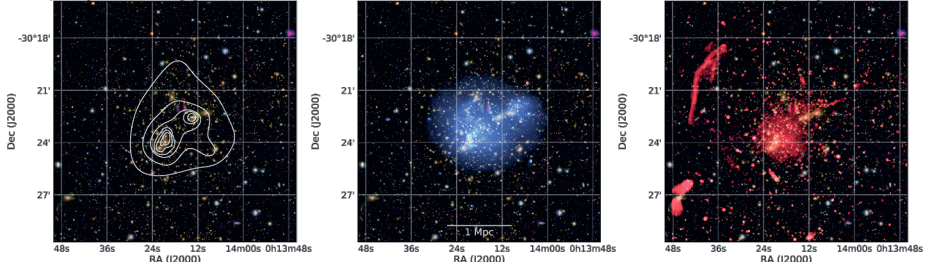
Figure 1.2: The galaxy cluster Abell 2744 in optical (left panel; Subaru *BRz* and contours of mass surface density, Medezinski et al., 2016), X-ray (central panel; Chandra 0.5–2.0 keV band in blue, Pearce et al., 2017) and radio (right panel; VLA 1–4 GHz band in red, Pearce et al., 2017). Image credit: van Weeren et al. (2019).

to surface brightness dimming. Surveys based on the Sunyaev-Zel'dovich (SZ) effect, through the spectral distortion of the Cosmic Microwave Background (CMB) photons traversing the ICM, have resulted to be very effective in detecting almost complete samples of high redshift clusters. The South Pole Telescope (SPT; Bocquet et al., 2019; Bleem et al., 2020; Huang et al., 2020), the Atacama Cosmology Telescope (ACT; Hilton et al., 2021) and the Planck satellite (PSZ2; Planck Collaboration et al., 2016) have found the largest number of clusters, reaching a redshift of $z = 2$. The epoch for the formation of the first massive structures is usually set at $z \sim 1.5 - 2.0$, i.e. 3–4 Gyr after the Big Bang. Nonetheless, virialized structures at higher redshift, with detected X-ray extended emission, have been observed (e.g., Andreon & Huertas-Company, 2011; Willis et al., 2013; Miller et al., 2018; Willis et al., 2020).

1.1.1. Merging Galaxy Clusters

The formation and growth of large-scale structures are processes that occur at any moment after the formation of the first massive structures, via accretion of matter along filaments in the cosmic web and/or via merger of (sub)clusters and galaxy groups (Press & Schechter, 1974; Springel et al., 2006). Cluster mergers are the most energetic events in the Universe since the Big Bang. These events release an energy up to 10^{64} ergs during a cluster crossing time, i.e. ~ 1 Gyr (Markevitch et al., 1999). They can have a large impact on the cluster environment, affecting the galaxy distribution and evolution (left panel in Fig. 1.2; e.g. Golovich et al., 2019a), and changing the properties of the diffuse cluster plasma by means of turbulent motions, thermal discontinuities (such as shocks and cold fronts), and gas heating (middle panel in Fig. 1.2; see Markevitch & Vikhlinin, 2007, for a review). Moreover, a small fraction (< 1%) of energy released during the merger is thought to be channelled into the acceleration of CRs

and magnetic field amplification (right panel in Fig. 1.2; see Brunetti & Jones, 2014, for a review). All these events make merging clusters unique laboratories where to address fundamental questions in astrophysics and in plasma physics. To investigate the physics of particle acceleration, the energy transport from the largest to the smallest scales, and the origin and topology of cosmic magnetic fields, a multi-frequency approach is required.

1.2. The Sunyaev-Zel'dovich effect

The Sunyaev-Zel'dovich effect (SZ; Sunyaev & Zeldovich, 1972) is a small distortion of the Cosmic Microwave Background (CMB) black body spectrum. It is caused by Inverse Compton (IC) scattering of the "cold" CMB photons that interact with the "hot" electrons in the ICM. As a result, the CMB intensity decreases (increases) at frequencies lower (higher) than 218 GHz. This change in the spectrum is proportional to the integral along the line of sight of the product of electron density and temperature, i.e. $y \propto \int_0^\infty n_e T_e dl$. This quantity is called the Compton parameter, and the SZ signal Y is obtained by integrating over the solid angle covering the cluster, i.e. $Y = \int_\Omega y d\Omega \propto 1/D_A^2 \int_0^\infty dl \int_A n_e T_e dA$ (with D_A the angular diameter distance and A the cluster area). Since this effect is a fractional change in the brightness of the CMB, it does not suffer from redshift dimming. Therefore, SZ-selected surveys are the most effective way to search for high redshift clusters, although the current surveys are limited by poor angular resolution (1 – 2 arcmin). An important property of the SZ signal is that it tightly correlates with the cluster mass (Arnaud et al., 2010):

$$Y_{500} D_A^2 \propto f_{\mathrm{gas}} M_{500}^{5/3} H(z)^{2/3} \,, \tag{1.1}$$

where the subscript 500 indicates the value within a radius that encompasses a density 500 times higher than the critical density of the Universe at the given redshift, f_{gas} is the fraction in mass of the ICM, and $H(z) = H_0 \sqrt{\Omega_\mathrm{m}(1+z)^3 + \Omega_\Lambda}$ the Hubble parameter.

1.3. Thermal emission

The ICM represents the bulk of the baryonic content of the cluster mass. It is a hot ($T = 10^7 - 10^8$ K or $kT = 1 - 10$ keV) and rarefied ($n_e \sim 10^{-4} - 10^{-3}$ cm^{-3}) plasma, emitting X-ray radiation via thermal Bremsstrahlung emission (e.g. Forman et al., 1982), with emissivity as a function of frequency ν given by[2] $\varepsilon \propto n_e^2 T_e^{-1/2} \exp{(-h\nu/kT_e)}$. X-ray satellites, such as ROSAT and ASCA in the past, and Chandra, XMM-Newton and Suzaku more recently,

---

[2]Here, n_e and T_e are the electron number density and temperature, while h and k are the Planck and Boltzman constants, respectively.

have determined the density and temperature properties of clusters. These
are done by means of spectral and surface brightness analyses and under
the assumption of spherical symmetry (e.g. Markevitch & Vikhlinin, 2007).
These observations revealed that the ICM mostly consists of fully ionised
hydrogen and helium, plus a small fraction of highly ionised heavier ele-
ments at about a third of the solar abundance ($Z = 0.3 \, Z_\odot$).

X-ray observations are important to determine the dynamical state of
galaxy clusters. Relaxed (undisturbed) clusters have usually roundish and
symmetrical shapes, with a central peak of X-ray emissivity. For the den-
sity distribution, a hydrostatic isothermal sphere is generally assumed
(Cavaliere & Fusco-Femiano, 1976). This density profile results in the
well-known β-model profile for the surface brightness (e.g. Jones & For-
man, 1984), with a slope of $0.5 - 3\beta$ (with β being $\sim 2/3$; Arnaud, 2009).
Relaxed clusters also tend to have a so-called cool core, i.e., a drop in the
ICM temperature within the $0.1 R_{500}$ radius, where R_{500} is the radius where
the cluster density is 500 above the critical density of the Universe at that
redshift. However, it is important to keep in mind that a spherical sym-
metrical morphology and a cool core do not necessarily imply the absence
of dynamical activity. This can be the case of merger events seen along
the line of sight, or sloshing events (e.g. Markevitch & Vikhlinin, 2007).
Since relaxed clusters are usually brighter than disturbed systems, X-ray
surveys host a larger fraction of cool core clusters compared to the Planck-
SZ selected samples (Rossetti et al., 2017; Andrade-Santos et al., 2017;
Lovisari et al., 2017). This is known as the cool core bias (Eckert et al.,
2011).

1.3.1. Shock fronts

In the simple scenario of a merger between two clusters with masses
M_1 and M_2, the merger velocity v at distance d is determined by (Sarazin,
2002):

$$v_{[\mathrm{km\,s^{-1}}]} \sim 3000 \left(\frac{M_1 + M_2}{10^{15}\,\mathrm{M_\odot}} \right)^{1/2} \left(\frac{d}{1\,\mathrm{Mpc}} \right)^{-1/2} \left[\frac{1 - (d/d_0)}{1 - (b/d_0)^2} \right]^{1/2}, \qquad (1.2)$$

where b is the impact parameter and d_0 is the initial cluster separation. As
consequence of the merger, shock waves are generated and propagate per-
pendicularly to the merger axis. Shocks are revealed in X-ray observations
as sharp discontinuities in the surface brightness profile. In this frame-
work, the Chandra satellite, given its high angular resolution of $1''$, is the
best instrument to date to investigate such features. Behind the shock, in
the so-called *downstream* or *post-shock region*, the gas is compressed and
heated proportionally to the Mach number of the shock ($\mathcal{M} = v_{\mathrm{shock}}/c_{\mathrm{s}}$; see
Fig. 1.3). Given the typical temperature and density ahead of the shock
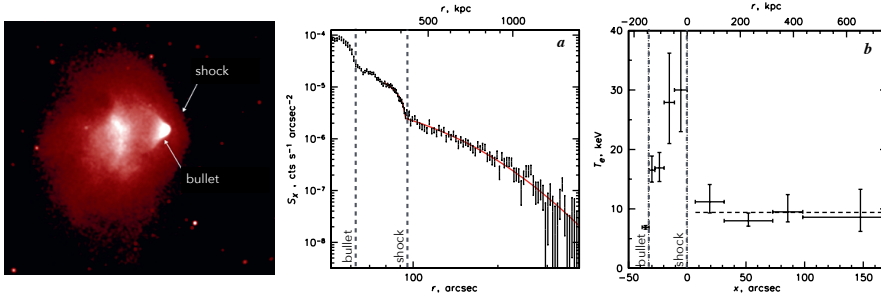
Figure 1.3: The Bullet galaxy cluster (1E 0657-56; Markevitch, 2006a). Left panel: 500 ks Chandra ACIS-I image in the 0.8–4 keV band. Middle panel: surface brightness profile covering the bullet and the shock front, highlighted by the dashed vertical lines; the red solid line represent a model for a shock front. Right panel: projected temperature profile in a narrow sector across the shock; the two vertical dashed lines show the boundaries of the cool bullet and the shock; the horizontal dashed line shows the average pre-shock temperature.

(the so-called *upstream* or *pre-shock region*), the sound speed[3] in clusters it is of the order of ~ 1000 km s^{-1}. Thus, the shocks in cluster mergers are expected to be only moderately supersonic, with Mach numbers of $\mathcal{M} \lesssim 3$. The shock Mach number ($\mathcal{M}$) is estimated using the Rankine-Hugoniot jump conditions (Landau & Lifshitz, 1959). Assuming a monatomic gas ($\gamma = 5/3$), then the temperature and density jumps detected in the cluster spectrum and surface brightness profile lead to:

$$\frac{T_{\text{post}}}{T_{\text{pre}}} = \frac{5\mathcal{M}^4 + 14\mathcal{M}^2 - 3}{16\mathcal{M}^2} \tag{1.3}$$

and

$$\frac{n_{\text{post}}}{n_{\text{pre}}} = \frac{4\mathcal{M}^2}{\mathcal{M}^2 + 3} \,. \tag{1.4}$$

From an observational point of view, detecting temperature jumps is more difficult because it requires the detection of a large number of photons. This is not always possible, especially in the pre-shock region which is usually faint (e.g. Bartalucci et al., 2014). However, determining $T_{\text{post}} > T_{\text{pre}}$ is necessary to define the nature of the discontinuity and to discriminate it from a cold front (see below).

1.3.2. Cold fronts

Cold fronts are sharp contact discontinuities which are in pressure equilibrium. They form at the boundaries of cold gas clouds moving through

---

[3]The sound speed is defined as $c_{\text{s}} = \sqrt{\gamma k T / \mu m_{\text{p}}}$

a hotter and less dense surrounding gas (ZuHone & Roediger, 2016). Simulations have shown that, during the cluster merger, the lower-entropy gas cores can be dense enough to resist the disruption by the shocks and stay attached to their host dark matter. Moreover, the gas pressure appears to be continuous across the discontinuity. Observations of these sharp discontinuities have been possible thanks to the extremely high resolution of the Chandra satellite. These observations enable the study of the physical properties of the cluster plasma, the mean free path of electrons and ions, and thermal conduction and flow instabilities. One of the textbook example of X-ray observations of a merging cold front is seen in the Bullet cluster (1E 0657-56; Markevitch, 2006a, see Fig. 1.3). Unlike shock fronts, these discontinuities can be also observed in relaxed clusters and they are the signature of recent minor merger and related gas sloshing event in the cluster core (e.g. Perseus cluster, Simionescu et al., 2012; Walker et al., 2018).

1.3.3. Turbulence

During a merger event, a non-negligible amount of turbulence is injected in the ICM. The degree of turbulence can be quantified by the Reynolds number, which is defined as the ratio between the inertial and viscous forces (i.e. $Re = v_L L / \nu$, where v_L and L are the velocity and injection scale of the turbulence, and ν the plasma viscosity). Turbulence is dissipated throughout the cluster volume, propagating from large to small scales. Given typical ICM values, and assuming that the largest scale for the injected turbulence is the size of the cluster core, theories predict an effective Reynolds number of $Re \sim 10^3$ (Brunetti & Jones, 2014). Including the kinetic and magnetic instabilities and considering the weakly collisional nature of the ICM, the Reynolds number can reach much larger values.

ICM turbulence is usually quantified via numerical simulations (e.g. Ryu et al., 2008; Miniati & Beresnyak, 2015; Vazza et al., 2017). Recently, direct evidence for ICM turbulence has been studied in the Perseus Cluster, thanks to Hitomi (Hitomi Collaboration et al., 2016; ZuHone et al., 2018), and in the Coma Cluster, thanks to Chandra Zhuravleva et al. (2019). These works point to large Reynolds numbers ($Re > 10^3$), suggesting that the ICM is highly turbulent.

1.4. Non-thermal emission

Galaxy clusters display a large variety of radio emission from non-thermal synchrotron radiation. Radio galaxies are a particular class of active galactic nuclei (AGN; Urry & Padovani, 1995), and are the most common sources of synchrotron emission. Unlike those observed in isolated environments, cluster radio galaxies display peculiar morphologies. As they move in the

cluster potential well, their jets are not symmetric but they bend in the opposite direction of the motion due to ram pressure (Miley, 1980). They are therefore called *head* (HT), *narrow-angle* (NAT) and *wide-angle* (WAT) tails, depending on the bending angle of the radio jets, and can be used to trace the cluster dynamics. The morphology of cluster radio galaxies can be strongly affected by a merger event, causing additional changes to their shapes (e.g. IC 711 in Abell 1314, see Wilber et al., 2019).

In merging galaxy clusters, diffuse radio emission[4], extending from 500 kpc up to 1-2 Mpc and not directly associated with galaxies, is also detected. These are referred to as *radio relics* and *radio halos* (Sect. 1.4.1 and 1.4.2, respectively; see Brunetti & Jones, 2014; van Weeren et al., 2019, for theoretical and observational reviews). The observations of these radio sources proves the presence of relativistic particles, i.e. cosmic rays (CRs) with Lorentz factor $\gamma_L \sim 10^4$ or GeV energies, and magnetic fields in the ICM (see also Sect. 1.5). A fundamental problem arises for the origin of the CRs[5] associated with these diffuse sources. The typical distribution of CRs follows a power law, i.e. $N(E) = N_0 E^{-\delta} dE$, with the spectral slope $\alpha = (1-\delta)/2$ reflecting the physics of the particle acceleration and the electron energy losses. The characteristic lifetime of relativistic particles is set by the combination of synchrotron and inverse Compton (IC) energy losses, according to (e.g. van Weeren et al., 2011b):

$$t_{[\text{yr}]} \approx 3.2 \times 10^{10} \frac{B^{1/2}}{B^2 + B_{\text{CMB}}^2} \left[(1+z)\nu\right]^{-1/2} , \qquad (1.5)$$

where B is the cluster magnetic field, $B_{\text{CMB}} = 3.25(1+z)^2 \, \mu$Gauss is the equivalent magnetic field strength of the CMB, ν is the observing frequency in MHz and z is the source redshift. In clusters, where the relativistic particles have energies up to ~ 1 GeV, the typical age of the relativistic particles results to be $t < 10^8$ yr. This lifetime is much shorter than the time needed to transport these particles within the cluster volume, i.e. $t \sim 10^9$ yr. This is also known as *diffusion problem*. Therefore, the ultra-relativistic particles in radio halos and radio relics cannot be simply associated with output from AGN or galactic winds, but they need to be continuously (re-)accelerated in-situ (Jaffe, 1977).

---

[4]Additional diffuse radio emission in cool-core clusters are sometimes detected, on smaller scales (i.e. $\lesssim 500$ kpc, see Giacintucci et al., 2017). These are called *mini-halos*, and will not be described in this thesis.

[5]In this thesis, we refers to relativistic electrons (i.e. CRe) as the primary component of the CR populations in galaxy clusters producing diffuse radio emission. Relativistic protons (CRp) are difficult to be observed directly, and would generate γ-ray emission due to $p + p$ decay, which has not been detected with the Fermi-LAT satellite (Ackermann et al., 2016).

1.4.1. Radio relics

Radio relics (Fig. 1.4) are large, from 500 kpc up to 2 Mpc, diffuse radio sources located in the cluster outskirts (Vazza et al., 2012b). They have elongated, usually arc-like, shapes and are generally co-spatial with the shock discontinuities detected in the X-ray band. For this reason, they are also called *radio shocks* (van Weeren et al., 2019). Radio relics are found to be strongly polarised at frequencies above ∼ 1 GHz (from 20% up to 60%, e.g. Ensslin et al., 1998; van Weeren et al., 2010), with the polarisation electric vectors orientated perpendicularly to the shock surface. Recent GHz observations at high resolution have shown that these sources have filamentary structures (e.g. Abell 2256, Owen et al., 2014; 1RXS J0603.3+4214, Rajpurohit et al., 2018a; CIZA J2242.8+5301 Di Gennaro et al., 2018). The origin of this filamentary morphology is still not fully understood. It has been proposed that it can be due to the complex shape of the shock surface (Vazza et al., 2012a; Skillman et al., 2013) or because of changes in the magnetic field (Wittor et al., 2019), or a combination of these two effects. A particular class of radio relics are the so-called *double radio relics* (e.g. Roettiger et al., 1999, right panel in Fig. 1.4). These are the result of a cluster merger that occur very close to the plane of the sky, where a pair of shock waves are generated at same time at the core passage. As they do not suffer from geometrical projection effects, double radio relics are useful tools to constrain the merger parameters and dynamics (van Weeren et al., 2011a; Molnar & Broadhurst, 2017; Golovich et al., 2019b).

Radio relics are characterised by steep integrated radio spectra, with $\alpha_{\text{int}} < -1$. The power-law shape of their spectra has been observed over a wide frequency range, from hundreds MHz up to tens GHz (Rajpurohit et al., 2020; Loi et al., 2020). At the outermost edge of the relic, where the shock is located, a flatter spectral index is observed, with $\alpha \sim -0.8$. The spectral index steepens towards the cluster centre, reaching values $\alpha \lesssim -1.5$. This steepening in the post-shock region is caused by synchrotron and inverse Compton energy losses.

All the characteristics mentioned above point to (re-)acceleration of CRs and compression and amplification of magnetic fields, due to the merger-induced shock (Brunetti & Jones, 2014; Donnert et al., 2018), to explain the origin of radio relics. Models for the radio relic population by Nuza et al. (2012) predict that the radio relic occurrence rate should increase with redshift, that the most massive clusters should have the highest probability to host relics, and that they should be distributed closer to the cluster centre than those observed at $z = 0$ (Vazza et al., 2012b).

The two main mechanisms invoked to explain the origin of radio relics are the diffusive shock acceleration (DSA; Blandford & Eichler, 1987) and the re-acceleration of fossil plasma (Markevitch et al., 2005).
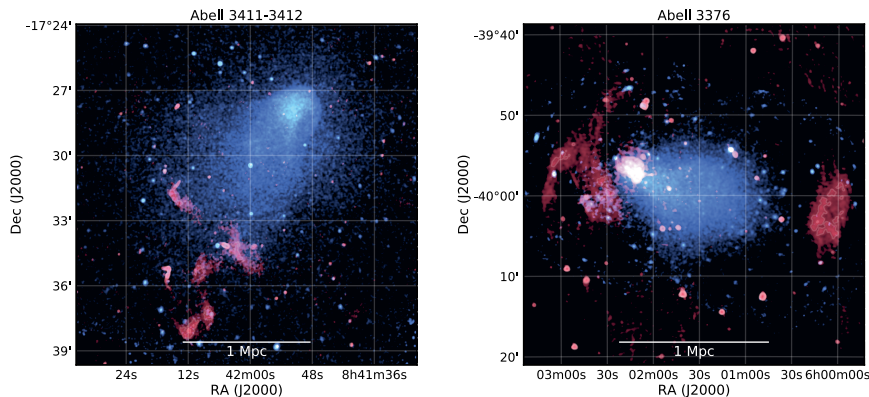
Figure 1.4: Examples of radio relics. Left panel: the single relic in Abell 3411-3412 (GMRT 325 MHz, van Weeren et al., 2017a; Andrade-Santos et al., 2019). Right panel: the double relic in Abell 3376 (GMRT 317 MHz, Kale et al., 2012; Urdampilleta et al., 2018). The radio emission is shown in red colour, while in blue there is the thermal X-ray emission (Chandra 0.2–2.0 keV and XMM-Newton 0.3–2.0 keV, respectively). Images are taken from van Weeren et al. (2019).

Diffusive shock acceleration (DSA) mechanism

Diffusive shock acceleration is a first-order Fermi acceleration mechanisms. According to this, particles from the thermal pool scatter upstream and downstream from the shock due to magnetic inhomogeneities. At each crossing, particles gain some energy until they become relativistic enough to produce synchrotron radiation. An important prediction of this mechanism is that the integrated spectrum of the accelerated CRe follows a power-law distribution, which depends only on the shock Mach number:

$$\alpha_{\mathrm{int}} = \frac{\mathcal{M}^2 + 1}{\mathcal{M}^2 - 1} \, . \tag{1.6}$$

Comparing the shock Mach number measured from X-ray and radio observations is one of the key tests for the DSA mechanisms. If the lifetime of the shock and the electron diffusion time are much longer than the electron cooling time, the integrated spectral index relates with the injection spectral index according to $\alpha_{\mathrm{inj}} = 0.5 + \alpha_{\mathrm{int}}$ (Kardashev, 1962). Nonetheless, in several cases deviations from the injected-integrated spectral indices relation (e.g. van Weeren et al., 2012, 2016; Hoang et al., 2017) and discrepancies between the X-ray and radio Mach numbers (e.g. Akamatsu et al., 2017) are observed. A suggested explanation for this latter issue is that, unlike X-ray observations, radio observations are sensitive to the "high-value tail" of the shock Mach number distribution (e.g. Wittor et al., 2017)

The stronger issue with the DSA mechanisms is that, to explain the surface brightness observed in radio relics, high acceleration efficiencies ($\eta \gtrsim 10\%$) are required. While this is not a problem for high Mach numbers (like for shocks produced in the supernova remnants, $\mathcal{M} \sim 10^3$), this appears particularly unrealistic for cluster shocks ($\eta \lesssim 1\%$, Kang & Ryu, 2013).

Re-acceleration scenario

The challenge of the low acceleration efficiency can be solved if we consider a source of pre-existing accelerated plasma, instead of the thermal pool. In this case the particles are already relativistic, therefore even a weak shock (e.g. Di Gennaro et al., 2019; Andrade-Santos et al., 2019) can re-accelerate them and produce strong radio emission. Since the physics in act is still DSA, apart from the change in the initial seed particles, the spectrum of the ultra-relativistic particles is still described by Eq. 1.6.

The sources for this pre-existing plasma are usually found in cluster radio galaxies. Connections between lobes of radio galaxies and radio relics have been observed (e.g. Shimwell et al., 2015; van Weeren et al., 2017a,b; Di Gennaro et al., 2018). Numerical models have been successful in reproducing the observed radio flux density and volume-integrated spectral index, at least for the radio relics in 1RXS J0603.3+4214 and CIZA J2242.8+5301 (Kang & Ryu, 2011; Kang et al., 2012, 2017).

1.4.2. Radio Halos

Radio halos are large-scale (1–2 Mpc) diffuse radio sources located in the cluster centre (van Weeren et al., 2019, Fig. 1.5). They have roundish shapes, which follow well the X-ray emission from the ICM. Recent deep and high-resolution observations have shown that these sources might not be completely smooth, but they can be characterised by filamentary shapes (Botteon et al., 2020). Unlike radio relics, radio halos are not polarised. This is probably due to poor angular resolution, which results in beam depolarisation. Expected polarisation values of 15–35% have been predicted for high-resolution observations using magneto-hydrodynamical simulations (Govoni et al., 2013).

Radio halos are characterised by steep spectral indices, with values ranging from $-1.3 < \alpha < -1.0$ (Giovannini et al., 2009; Feretti et al., 2012; van Weeren et al., 2019). The spectral index is usually rather constant across the halo, although a few halos display inhomogeneities on small scales (Orrú et al., 2007; Shimwell et al., 2016). For a few objects with observations at several different frequencies, curved spectra have been observed (e.g. Thierbach et al., 2003). Last but not least, the discovery of ultra-steep spectrum radio halos (USSRH; Brunetti et al., 2008; Dallacasa
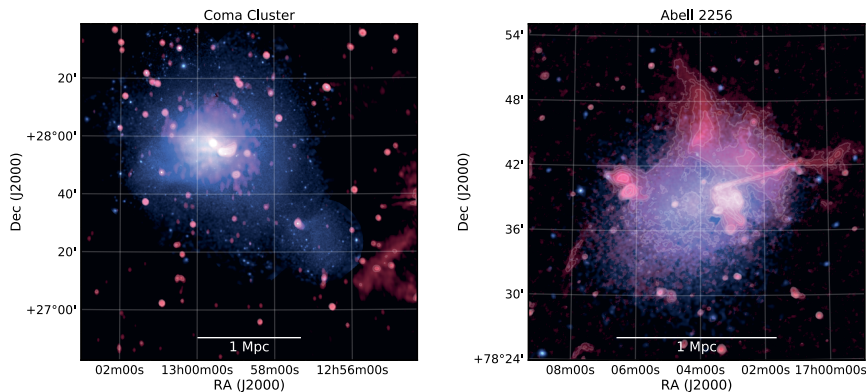
Figure 1.5: Examples of radio halos. Left panel: Coma cluster (WSRT 352 MHz, Brown & Rudnick, 2011). Right panel: Abel 2256 (LOFAR 120–170 MHz, van Weeren et al. in prep). The radio emission is shown in red colour, while in blue there is the thermal X-ray emission (XMM-Newton 0.4–1.3 keV). Images are taken from van Weeren et al. (2019).

et al., 2009; Wilber et al., 2018) has provided compelling information on the underlying acceleration mechanism.

Several studies have linked the radio emission from halos to the X-ray emission of the ICM. In particular, the most powerful radio halos have been found in the most massive and X-ray luminous clusters (e.g. Cassano et al., 2013). Moreover, a clear bi-modality between merging and relaxed cluster is observed, with the former hosting radio halos and the latter showing no radio emission.

Re-acceleration scenario

This observed bi-modality suggests that the dynamical state of the cluster should be connected with the formation mechanism of radio halos (Brunetti et al., 2001; Petrosian, 2001). The general idea is that the large scale MHD turbulence produced during a cluster merger is transferred to smaller and smaller scales (Brunetti & Jones, 2014). Turbulence on small scales can result in second-order Fermi processes, where particles scatter due to magnetic inhomogeneities. Since the particle motion is random in the ICM, a slight net gain of energy occurs after many scatterings. A challenge for this scenario is that it requires the presence of mildly–relativistic electrons in the ICM, as MHD turbulence is not efficient enough to accelerate electrons from the thermal pool. This mechanism satisfies the diffusion problem mentioned in Section 1.4, the presence of radio halos in disturbed systems and the correlation between the halo radio power and the cluster mass. It also explains the observation of USSRHs, where

the radiative energy losses are stronger than the re-acceleration processes (Cassano & Brunetti, 2005; Cassano et al., 2006). A consequence of this model is that radio halos should be transient events in the cluster life-time.

In the last decade, models based on the turbulent re-acceleration theory have been developed to investigate the occurrence rate of radio halo as a function of cluster mass and redshift (Cassano et al., 2010a, and references therein). These models predict that the detectable fraction of clusters at high z hosting halos should decrease at GHz frequencies, and that, for a given mass, these radio halos are expected to have steeper radio spectral indices than their low-z counterparts (i.e. $\alpha < -1.5$). This latter prediction is due to the IC energy losses which limit the maximum energy of the accelerated electrons (Cassano et al., 2006). Before this Thesis, only few single objects have been observed at redshift above 0.6 ("El Gordo" at $z = 0.87$, Lindner et al. 2014; PLCK G147.3-16.6 at $z = 0.65$, van Weeren et al. 2014; PSZ2 G099.86+58.45 at $z = 0.616$, Cassano et al. 2019).

Secondary models

Secondary products of inelastic hadronic collisions between CRp and thermal protons in the ICM (i.e. $p+p$ collisions) would also be able to generate the electrons and positrons responsible for the radio halo emission (e.g. Blasi & Colafrancesco, 1999). This mechanism solves the diffusion problem and the connection between the radio and the X-ray emission. The main issue of this scenario is that it would predict diffuse radio emission from both disturbed and relaxed clusters, which has not been observed (Cassano et al., 2013). Moreover, these collision would also produce γ-ray emission, whose detection is still missing (e.g. Ackermann et al., 2010b, 2014, 2016; Prokhorov & Churazov, 2014a; Brunetti et al., 2017).

1.5. Cluster magnetic fields

Magnetic fields are ubiquitous in the Universe, from stars to the largest structures (Klein & Fletcher, 2015). Although not directly observable, in clusters they are thought to play key roles not only for particle (re-)acceleration, but also to regulate AGN feedback, thermal conduction, and the ICM pressure budget (Carilli & Taylor, 2002).

There are several methods to retrieve the magnetic field strengths in clusters (Carilli & Taylor, 2002; Govoni & Feretti, 2004a). These studies lead to volume-averaged strengths of a few μGauss. A common method is to use the Faraday Rotation Measure (RM) from background/inside polarised sources. When a linearly polarised emission passes through a magnetised plasma, it experiences a phase shift $\Delta\chi$ of its left and right circularly polarised components. This results in a rotation of the polarisation plane at higher (lower) wavelengths λ (frequencies ν), $\Delta\chi = \mathrm{RM}\lambda^2$.

The Rotation Measure is defined as the integral along the line of sight L of the product of the electron density and the parallel component of the magnetic field, i.e. RM $\propto \int_0^L n_e B_\parallel dl$. Therefore, if n_e is known (i.e., from X-ray observations), $B_\parallel$ from the ICM can be estimated by measuring RM from several polarised sources located inside and/or background the cluster (Bonafede et al., 2010a). In relaxed clusters, where a β model can be assumed to describe the electron density profile, central magnetic fields of 1–15 μGauss have been estimated with decreasing values in the cluster outskirts. Several issues arise with this method (Johnson et al., 2020). First, the number of background polarised sources per cluster is usually low (Rudnick & Owen, 2014). At high redshift, this number is even lower, and therefore applying this method is more challenging. Furthermore, determining the location of embedded sources is difficult, and quantifying the effect of the interaction between the ICM and the radio galaxy plasma on the measured RM is not straightforward. Secondly, since RM is an integrated value, it collects the signal from all the material along the line of sight. It is therefore difficult to separate the contribution of foreground layers, e.g. the Galactic plane (Oppermann et al., 2015). In this case, the RM-Synthesis technique (Brentjens & de Bruyn, 2005) is more sensitive to multiple Faraday screens. Thirdly, it is hard to characterise the inhomogeneities in the magnetic field structures and the turbulent spatial scales in the ICM. Investigating all these most common issues, Johnson et al. (2020) derived an accuracy for the magnetic field strength from Rotation Measures of a factor ~ 3.

Another method to obtain the cluster magnetic field strength is by comparing the synchrotron (which is proportional to B^2) and the X-ray emission in the hard band (i.e. > 10 keV). The latter is caused by IC scattering between CMB photons and ICM electrons, and therefore proportional to B_{CMB}. The main challenge with this method is that the cluster X-ray emission at > 10 keV is difficult to detect. Only upper limits on the magnetic field strengths have been obtained so far by this method.

Finally, equipartition arguments have also been used in the past to determine cluster magnetic field strengths (Feretti et al., 2012).

1.5.1. Origin and amplification of cluster magnetic fields

One of the still open question in astrophysics is how the Universe we observe now is magnetised on the large scales. The general idea is that initial "seeds" of magnetic field get amplified as the Universe expands. It is still unclear where the magnetic field seeds come from. Two main scenarios have been proposed to address the origin of these seeds (see Subramanian, 2016, for a theoretical review). The first one assumes that magnetic field seeds have *primordial* origins. They are thought to be generated during the inflationary phase of the Universe, i.e. much before galaxy clusters form as

gravitationally bound systems. In this case, perturbations due to primordial magnetic fields will induce temperature and polarisation anisotropies, which should be detectable in the CMB. Based on measurements of the CMB, it has been found that an initial magnetic field strength of $B_0 \lesssim 1$ nGauss should permeate the entire Universe (Dolag et al., 2005; Planck Collaboration et al., 2016). Another possibility is that these seeds are generated around $z \sim 2-3$ from *astrophysical* objects, i.e. galactic winds, AGN, and/or starbursts. The impact of these objects on the cluster medium is observed, for instance, in the large-scale metallicity distribution (e.g. Baumgartner & Breitschwerdt, 2009; Biffi et al., 2018; Simionescu et al., 2019; Urdampilleta et al., 2019). It is therefore plausible that these objects are also able to inject magnetic field seeds in clusters, which can reach initial values of $B_0 \sim 0.1$ μGauss (Dolag et al., 2005).

In both scenarios, the initial magnetic field seeds are expected to be amplified during structure formation (see Donnert et al., 2018, for a recent review). Considering only the amplification due to gravitational collapse without any "external" effects, the magnetic field amplification is expected to be extremely slow, and would not reach the $\sim \mu$Gauss level we currently measure in galaxy clusters. The main mechanism for magnetic field amplification in galaxy clusters is the *small-scale dynamo* (Kraichnan & Nagarajan, 1967; Goldreich & Sridhar, 1997; Schekochihin & Cowley, 2007). The general idea is that merger-induced kinetic turbulent energy is transferred to magnetic energy, which stretches and folds the pre-existing magnetic field lines and locally amplifies the magnetic fields. This process takes several eddies turnover times, i.e. several Gyrs (Beresnyak & Miniati, 2016).

1.6.   X-ray and radio instruments

In the last decades, the synergy of radio telescopes and X-ray satellites has provided enormous advances in the understanding of the physics of galaxy clusters, spanning from the thermal to non-thermal phenomena.

Since the launch of the Chandra X-ray satellite in the late 1990s, impressive details in the ICM have been observed. The satellite, which orbits about 140,000 km above the Earth's atmosphere, is formed by four pairs of concentric mirrors which focus X-ray photons in the energy range of 0.1–10 keV to the High Resolution Camera (HRC) and the Advanced CCD Imaging Spectrometer (ACIS). The high accuracy of the mirrors results in the impressive resolution of $< 1''$ (corresponding to less than 1 kpc at $z < 0.05$), and therefore Chandra is the optimal instrument to detect sharp edges in clusters. On the other hand, the effective area of Chandra is rather small, 800 and 400 cm^2 at 0.25 and 5 keV respectively. Regarding effective area, XMM-Newton is a better instrument, with an effective area of about 1500 cm^2 at 1 keV. This instrument, however, looses in resolution

(about 15″).

The study of the large-scale non-thermal components has been historically carried at GHz frequencies. At these frequencies, the Karl-Jansky Very Large Array (VLA), located in New Mexico (US), represents one of the best instruments. This radio interferometer is composed by 27 parabolic dishes of 25 meters diameter which can move on a Y-shaped rail track. The option to move the antennae allows the interferometer to have four different configurations (A, B, C and D) which are sensitive to different angular scales. The observing frequency coverage spans from 0.74 to 50 GHz, which is divided in ten observing bands (e.g. the L- and S-bands cover the 1–2 and 2–4 GHz frequency bands, respectively). The angular resolution depends on both the array configuration and the observing frequency, spanning from subarcsec to the arcmin. The presence of steep-spectra radio emission has pushed the observations in the ∼ 100 MHz regime. The Giant Metrewave Radio Telescope (GMRT), located in India, consists in 30 parabolic wire-made dishes of 45 meters diameter which observe from 150 MHz to 1.4 GHz. The interferometer has been recently upgraded from a narrow-band to a wide-band system, significantly improving the noise levels. Given its location, the GMRT can also observe part of the southern sky (from −53° to +90°). The Low-Frequency Array (LOFAR) is the largest interferometer to-date. It is mostly located in the Netherlands, plus additional stations placed in several countries in Europe. Contrary to the VLA and GMRT, this interferometer is formed by dipoles which collect radio waves that are then combined electronically to form a station beams using the *aperture phase array technique*. This technique also allows one to simultaneously observe different part of the sky, although it requires high computing power. LOFAR consists of two sets of antennas in each station, the Low Band Antennas (LBA, 10–90 MHz) and the High Band Antennas (HBA, 110–240 MHz). At such low frequencies, the distortions of the radiation due to the ionosphere is limiting for high-resolution imaging, and needs to be corrected with "local" direction-dependent calibration. Novel algorithms attempt to solve this issue, and now the realisation of the deepest and highest resolution images at MHz frequencies is possible. Particularly, the LOFAR Two-Meter Sky Survey (LoTSS) has reached a sensitivity of less than 100 μJy beam^{-1} and a resolution of 5″. Its combination with the LOFAR Low-frequency Sky Survey (LoLSS) aims to unveil the low energetic population of electrons in the northern sky.

1.7. This Thesis

This thesis is aimed to understand the origin of the diffuse radio emission in merging galaxy clusters, and its connection with the disturbed thermal gas. To address these topics, high-resolution and high-sensitivity radio and X-ray observations are required. The thermal ICM is investigated

using observations from the Chandra and Suzaku X-ray satellites. The non-thermal radio emission is studied by means of large radio interferometers, i.e., the Very Large Array (VLA), the Giant Metrewave Radio Telescope (GMRT) and the Low-Frequency Array (LOFAR).

The main questions addressed in this thesis are:

- How are the particles accelerated to ultra-relativistic energies at radio relics (Chapter 2)?

- How is the shock strength related with the presence of diffuse radio emission (Chapter 3)?

- What is the occurrence rate of diffuse radio emission at the epoch of the formation of the largest scale structures (Chapter 4)?

- How is large-scale magnetic field compressed and amplified by shocks (Chapter 5)?

- Are re-acceleration models also valid at the time when the first large structures formed (Chapter 6)?

In this context, observations of double radio relics are crucial to investigate the properties of merger-induced shocks, as they reflect merger events close to the plane of the sky and, therefore, minimise the effect of geometrical projection. Survey at low-frequencies are required to create a sufficiently large sample of high-z clusters, to determine the radio halo occurrence rate and its evolution.

In **Chapter 2**, a deep 1–4 GHz Very Large Array (VLA) study is carried out of the merging galaxy cluster CIZA J2242.8+5301 (van Weeren et al., 2010). We investigated the particle acceleration mechanisms that generate the two relics in this system, and attempted to explain the filamentary morphology of the northern relic. The VLA data were combined with existing GMRT (van Weeren et al., 2010) and LOFAR (Hoang et al., 2017) observations. The results from the radio analysis are compared with the shock properties reported in the literature (Ogrean et al., 2014; Akamatsu et al., 2015). The spectral index analysis and modelling suggest that the three-dimensional shape of the shock cannot be neglected, and we underlined some tensions for the DSA scenario for the particle acceleration. I also detected a clear connection between the southern relic and a tailed radio galaxy. This supports the idea that the fossil plasma of the radio tail is re-accelerated by the shock wave, as we also suggest with re-acceleration modelling. High-resolution mapping of other tailed radio galaxies and patches of diffuse emission also supports a scenario where fossil plasma is revived by the merger event.

In **Chapter 3**, the thermal properties of the double shock in the merging galaxy cluster ZwCl 0008.8+5215 are studied by means of deep Chandra

and Suzaku observations. In this system, a double radio relic was previously found by van Weeren et al. (2011b). The deep Chandra observations confirmed the presence of a cold front, with a morphology resembling that in the Bullet cluster. Ahead of it, a shock discontinuity was detected. Interestingly, the radio relic located at this position traces only partly the X-ray detected shock. On the opposite side, where the larger and brighter relic is found, no clear thermal discontinuity was detected. The comparison between thermal and non-thermal properties of the system strongly suggests that the origin of the radio relics is due to re-acceleration of fossil plasma.

In **Chapter 4**, we investigate the occurrence of diffuse radio emission at the epoch of cluster formation. LOFAR observations of a Planck Sunyaev-Zel'dovich selected sample of galaxy clusters were used to search for large-scale diffuse radio emission. We found that radio halos in massive, distant clusters are common in our sample, with an occurrence fraction of about 50%. The radio luminosities from radio halos, in spite of the strong Inverse Compton losses at high redshift, are comparable to those measured in nearby clusters in the same mass range. This also indicates that these clusters have magnetic field strengths that are similar to those in nearby clusters. Therefore, we propose a fast magnetic field amplification during the first phases of cluster formation.

In **Chapter 5**, deep 1–4 GHz VLA observations were used to investigate the polarisation properties of the northern relic in CIZA J2242.8+5301. In order to do so, we used the QU-fitting approach assuming a (de)polarisation model to fit directly the Stokes I, Q and U fluxes obtained from each channel of the observing band. We detected, for the first time, the filamentary shape of the relic also in polarised light, suggesting it is tracing the magnetic structure of the radio shock. We found increasing intrinsic polarisation fraction in the relic post-shock region. This could be explained by complex geometrical projection and/or the relic's shape. Finally, strong Rotation Measure fluctuations are found within and outside the cluster. Since the cluster is very close to the Galactic place, it is unclear how much of these fluctuations are due to the ICM or the the Galaxy.

In **Chapter 6**, observations with the upgraded GMRT (uGMRT) in Band 3 and 4 (250–500 and 550-900 MHz, respectively) were conducted to investigate the spectral index properties of the distant radio halos presented in Di Gennaro et al. (2021a). This is the first time that low-frequency observations were followed-up at higher frequencies. We find extended diffuse radio emission at the uGMRT frequencies in five of the nine clusters in the sample. These are also the most massive systems in our sample, with masses $M = 6-8 \times 10^{14}$ M$_\odot$. For these, an average global spectral index between -1 and -1.4 has been estimated. For the non-detected radio halos, we obtain an upper limit on the spectral indices of $\alpha < -1.5$. This supports

the scenario where only the most energetic (i.e. massive) mergers are able to accelerate particles at $\nu > 600$ MHz.

1.8. Future prospects

Despite the progresses achieved in the last decades, there are several crucial open questions regarding the physics of particle acceleration, the origin of cosmic rays, the evolution of the merger energetics, the amplification of magnetic fields, and the growth of cluster's baryonic content. In this framework, the development of new radio (LOFAR, MWA, SKA, ASKAP, MeerKAT) and X-ray (eROSITA, Athena) facilities, as well as the upgrade of the previous generation of radio telescopes (VLA, GMRT, WRST), is crucial to improve our knowledge of the thermal/non-thermal physics in galaxy clusters. This is extremely important both at low and high redshift.

To date only incomplete samples of galaxy clusters are available at $z > 0.6$, and they are restricted to the most massive systems. For this reason, comparisons with cosmological simulations are difficult. The work presented in Chapter 4 (Di Gennaro et al., 2021a) represents the first crucial step towards the characterisation of the non-thermal emission in distant galaxy clusters. The launch of the X-ray satellite eROSITA (Merloni et al., 2012) is very timely in this context, as its main goal is to test the current Cosmology observations of distant galaxy clusters. The eROSITA all-sky survey (eRASS) is expected to detect up to several hundreds of galaxy clusters at redshifts above 0.6 (Merloni et al., 2012). The constantly increasing sky area observed by the LOFAR Two-Meter Sky Survey (LoTSS; Shimwell et al., 2017, 2019) will allow an immediate follow up of these systems, searching for diffuse radio emission. Moreover, new powerful radio telescopes in the Southern Hemisphere (e.g. ASKAP and MeerKAT) are close to be fully operational. They will observe an almost unexplored part of the sky, where large mass-selected sample of clusters are already available (e.g., from the SPT survey; Ebeling et al., 2010; Bleem et al., 2020). Combining these X-ray and radio observations will allow the investigation of the morphological and spectral properties of the diffuse radio emission, and the comparison with the cluster dynamical state. In particular, measuring spectral index in distant radio halos will be the key test for the validation of the re-acceleration turbulent scenario (Cassano et al., 2006). Observations with the upgraded GMRT (uGMRT) at $\nu \sim 600$ MHz and with LOFAR LBA at $\nu < 100$ MHz will provide the sensitivity and the resolution for such studies (Di Gennaro et al., in prep).

The recent high-resolution (arcsecond) observations at GHz frequency have challenged the acceleration mechanisms aimed to explain radio relics (Owen et al., 2014; Di Gennaro et al., 2018; Rajpurohit et al., 2018a). Tensions have been found regarding the exact location of the (re-)acceleration site. Observations at ~ 100 MHz frequency at the same high resolution

of VLA are required to investigate such issues. The International LOFAR Telescope (ILT), which contains stations from several European countries, together with the VLA will be able to study the spectral index coherence along the relic length. This is crucial to understand whether those filament are tracing the complex shape of the shock surface. Moreover, the understanding of merger-induced shocks will be boosted up by the launch (expected around 2030) of the Athena X-ray satellite (Nandra et al., 2013), whose energy resolution and collecting area will be revolutionary to directly measure turbulence in galaxy clusters.

The magnetic field properties at radio relics are also still poorly known. Only few bright relics have been studied in polarised light, and the origin of their filamentary structures is a mystery. It remains unclear whether the observed polarisation properties are peculiar cases or whether they apply to the entire population of relics. The complex Faraday structure of these sources and of the foreground layers require wide-band observations at GHz-frequency, to avoid depolarisation. VLA and MeerKAT observations can be used to investigate single objects in detail. Moreover, surveys aimed to observe a large number of polarised sources (e.g. POSSUM) are necessary to improve the statistical results on the Faraday Rotation Measurements in clusters. The SKA precursors, such as LOFAR and ASKAP, will allow the study of the cluster magnetic field topology in great detail.

Finally, theoretical models to connect the morphologies of radio tails in galaxy clusters to the merger-induced shock waves have been recently developed (Jones et al., 2017; O'Neill et al., 2019). High-resolution observations of the tail-relic interplay are essential to validate such models, and to determine the re-acceleration time scale of magnetised plasma swept up by a shock wave.

CHAPTER

2

DEEP VERY LARGE ARRAY OBSERVATIONS OF THE MERGING CLUSTER CIZA J2242.8+5301: CONTINUUM AND SPECTRAL IMAGING

G. Di Gennaro, R.J. van Weeren, M. Hoeft, H. Kang, D. Ryu et al. *Astrophysical Journal*, 865, 24 (2018)

Abstract. Despite progress in understanding radio relics, there are still open questions regarding the underlying particle acceleration mechanisms. In this paper we present deep 1–4 GHz VLA observations of CIZA J2242.8+ 5301 ($z = 0.1921$), a double radio relic cluster characterized by small projection on the plane of the sky. Our VLA observations reveal, for the first time, the complex morphology of the diffuse sources and the filamentary structure of the northern relic. We discover new faint diffuse radio emission extending north of the main northern relic. Our Mach number estimates for the northern and southern relics, based on the radio spectral index map obtained using the VLA observations and existing LO-FAR and GMRT data, are consistent with previous radio and X-ray studies ($\mathcal{M}_{RN} = 2.58 \pm 0.17$ and $\mathcal{M}_{RS} = 2.10 \pm 0.08$). However, color-color diagrams and modelings suggest a flatter injection spectral index than the one obtained from the spectral index map, indicating that projection effects might be not entirely negligible. The southern relic consists of five "arms". Embedded in it, we find a tailed radio galaxy which seems to be connected to the relic. A spectral index flattening, where the radio tail connects to the relic, is also measured. We propose that the southern relic may trace AGN fossil electrons that are re-accelerated at a shock, with an estimated strength of $\mathcal{M} = 2.4$. High-resolution mapping of other tailed radio galaxies also supports a scenario where AGN fossil electrons are revived by the merger event and could be related to the formation of some diffuse cluster radio emission.

2.1. Introduction

Cluster mergers are the most energetic phenomena in the Universe since the Big Bang, involving kinetic energies of $\sim 10^{63} - 10^{65}$ erg, released over a time scale of 1–2 Gyr (e.g. Sarazin, 2002) depending on the cluster's mass and on the relative velocity of the merging dark matter halos. In a hierarchical cold dark matter (CDM) scenario, these phenomena are the natural way to form rich cluster of galaxies. Cluster mergers produce shock waves and turbulence in the intracluster medium (ICM). It has been proposed that ICM shocks and turbulence can (re-)accelerate cosmic rays (CRs) which then produce diffuse radio synchrotron emitting sources in the presence of μGauss magnetic fields. These diffuse sources are known as *radio halos* and *radio relics* (see Brunetti & Jones, 2014; Feretti et al., 2012, for a theoretical and an observational review).

Radio halos are centrally located unpolarized sources with a smooth morphology, roughly following the X-ray emission from the ICM. The currently favored formation scenario for the formation of radio halos involves the re-acceleration of pre-existing CR electrons (energies of $\sim$ MeV, e.g. Brunetti et al., 2001; Petrosian, 2001) via magneto-hydrodynamical turbulent motions, induced by a merging event. Moreover, radio halos are characterized by a steep-spectrum ($\alpha < -1$, with $S_\nu \propto \nu^\alpha$, e.g. Brunetti et al., 2008). A correlation between the halo radio power and the cluster X-ray luminosity exists (e.g. Cassano et al., 2013), showing that the most X-ray luminous clusters host the most powerful radio halos. Moreover, Cassano et al. (2010a) showed a clear correlation between the cluster's dynamical state, measured from the X-ray surface brightness distribution, and the presence of giant radio halos, providing strong support that mergers play an important role in the formation of these sources.

As with the radio halos, radio relics are characterized by a steep spectral index ($\alpha \approx -0.8$ to -1.5). They are generally elongated sources located in the outskirts of clusters, and they are suggested to trace outwards traveling shock fronts, where the ICM and magnetic fields are compressed. (e.g. Ensslin et al., 1998; Finoguenov et al., 2010; van Weeren et al., 2010). As a consequence, the magnetic field is amplified and aligned, producing polarized radio emission. One formation scenario for relics is the *diffusive shock acceleration* (DSA) mechanism, similar to what occurs in supernova remnants (e.g. Blandford & Eichler, 1987; Drury, 1983; Ensslin et al., 1998). This model involves particles (electrons) that are accelerated from the ICM's thermal pool into CRs at shocks, while the electrons in the downstream region suffer synchrotron and inverse Compton (IC) energy losses. A prediction of the DSA model is a relation between the Mach number of the shock and the radio spectral index at the shock location (e.g. Giacintucci et al., 2008). However, recent observations suggest fundamental problems with the standard DSA model: (1) in a few cases, there are cluster merger shocks without corresponding radio relics (e.g. the main shock in

the Bullet Cluster, Shimwell et al., 2014) (2) sometimes, the spectral index derived Mach numbers are significantly higher than those obtained from the X-ray observations (e.g. van Weeren et al., 2016), and (3) some relics require an unrealistic shock acceleration efficiency (for DSA) to explain their observed radio power (e.g. Vazza & Brüggen, 2014; Botteon et al., 2016a). Another formation scenario is *shock re-acceleration* of relativistic fossil electrons (e.g. Markevitch et al., 2005; Macario et al., 2011; Kang & Ryu, 2011; Kang et al., 2012; Bonafede et al., 2014; Shimwell et al., 2015; Kang et al., 2017; van Weeren et al., 2017a). This mechanism addresses the DSA efficiency problem, and implies a direct connection between radio relics and radio galaxies, which are supposed to be the primary sources of fossil plasma.

Radio "phoenices" are another class of relics that are characterized by their steep curved spectra and often complex toroidal morphologies. They are supposed to trace AGN fossil plasma lobes which have been adiabatically compressed by merger shock waves (Enßlin & Gopal-Krishna, 2001; Enßlin & Brüggen, 2002; de Gasperin et al., 2015).

Relics have a range of sizes and morphologies. So-called *double relic* systems, with two relics located on diametrically opposite sides of the cluster center (e.g. Rottgering et al., 1997; Bagchi et al., 2006; Venturi et al., 2007; Bonafede et al., 2009; van Weeren et al., 2009; Bonafede et al., 2012; de Gasperin et al., 2014) are an important subclass. Numerical simulations (e.g. van Weeren et al., 2011b) suggest that these systems are the result of binary mergers between two-comparable mass clusters (mass ratio of 1:1 or 1:3), with the line connecting the two relics representing the projected merger axis of the system.

In this paper we present a radio continuum and spectral analysis of the merging cluster CIZA J2242.8+5301, which hosts two opposite radio relics and a faint radio halo, by means of new deep 1–4 GHz Karl G. Jansky Very Large Array (VLA) observations. The paper is organized as follows: in Sect. 2.2 we provide an overview of CIZA J2242.8+5301, presenting the results of previous studies performed in the optical, X-ray and radio bands; in Sect. 2.3 we describe the radio observations and the data analysis; the radio images, the spectral index maps are presented Sect. 2.4. We end with a discussion and conclusions in Sects. 2.5 and 2.6, respectively.

In this paper, we adopt a flat ΛCDM cosmology with $H_0 = 70$ km s^{-1} Mpc-1, $\Omega_m = 0.3$ and $\Omega_\Lambda = 0.7$, which implies a conversion factor of 3.22 kpc/$''$ and a luminosity distance of ≈ 944 Mpc, at the cluster's redshift ($z = 0.192$ Kocevski et al., 2007).

2.2.   CIZA J2242.8+5301

CIZA J2242.8+5301 (hereafter CIZA2242) is a merging galaxy cluster located at $z = 0.1921$ which was first observed in X-ray by *ROSAT* (Ko-

cevski et al., 2007). This merging cluster has been well studied across the electromagnetic spectrum, from radio, optical, to X-ray bands (van Weeren et al., 2010; Ogrean et al., 2013; Stroe et al., 2013; Ogrean et al., 2014; Stroe et al., 2014; Akamatsu et al., 2015; Dawson et al., 2015; Jee et al., 2015; Okabe et al., 2015; Donnert et al., 2016; Stroe et al., 2016; Kierdorf et al., 2017; Rumsey et al., 2017), and it has been used as a textbook example for numerical simulations aimed to model the shock physics (van Weeren et al., 2011b; Kang et al., 2012; Kang & Ryu, 2015; Donnert et al., 2017; Molnar & Broadhurst, 2017; Kang et al., 2017).

In the radio band, CIZA2242 shows the presence of a spectacular double relic, located $\sim$ 1.5 Mpc north and south from the cluster center. The northern relic is composed of an arc-like structure, $\sim$ 2 Mpc long and $\sim$ 50 kpc wide, which suggests the relic traces a shock propagating outward, and which gave the cluster the nickname of the "Sausage" cluster. The cluster also contains a low surface brightness radio halo (van Weeren et al., 2010; Stroe et al., 2013; Hoang et al., 2017). Numerical simulations performed by van Weeren et al. (2011b) suggested that the mass ratio of the colliding clusters is between 1.5:1 and 2.5:1, and that the relics are seen close to edge-on (i.e. $|i| \lesssim 10°$). Donnert et al. (2017) showed that, in the northern shock, the upstream X-ray temperatures and radio properties are consistent with each other, and consistent with weak lensing cluster masses. Dawson et al. (2015) found two comparable subcluster masses ($16.1^{+4.6}_{-3.3} \times 10^{14}$ M$_\odot$ and $13.0^{+4.0}_{-2.5} \times 10^{14}$ M$_\odot$ for the northern and southern clusters, respectively). Their data was consistent with the interpretation of a merger occurring on the plane of the sky. The time since core passage was estimated to be about 0.6 Gyr by Rumsey et al. (2017).

The cluster has an X-ray luminosity of L_{500} = 7.7 $\pm$ 0.1 $\times 10^{44}$ erg s^{-1} in the 0.1–2.4 keV energy band, within a radius of R_{500} = 1.2 Mpc (Hoang et al., 2017). Several X-ray surface brightness discontinuities were detected with *Chandra* and *XMM-Newton* by Ogrean et al. (2014). Due to the faint X-ray emissivity at the relic location, the temperature measurements across the shock fronts were obtained by means of *Suzaku* observations (Akamatsu et al., 2015). The estimated shock Mach numbers were $\mathcal{M}^X_N = 2.7^{+0.7}_{-0.4}$ and $\mathcal{M}^X_S = 1.7^{+0.4}_{-0.3}$, for the northern and the southern relics respectively. Despite the initial discrepancy from the Mach numbers found in the radio band ($\mathcal{M}^{radio}_N \sim 4.6$ and $\mathcal{M}^{radio}_S \sim 2.8$, for the northern and southern relic respectively, van Weeren et al., 2010; Stroe et al., 2013), recent observations show an agreement between the X-ray and the radio Mach number ($\mathcal{M}^{radio}_N = 2.9^{+0.10}_{-0.13}$ Stroe et al., 2014, $\mathcal{M}^{radio}_N = 2.7^{+0.6}_{-0.3}$ Hoang et al., 2017 and $\mathcal{M}^{radio}_S = 1.9^{+0.3}_{-0.2}$ Hoang et al., 2017).

The Sausage relic has also been observed at high frequencies ($\gtrsim$ 2 GHz), where there is still some debate on the integrated radio spectral shape of the relic. New radio observations (up to 30 GHz) revealed a possible steepening in the integrated radio spectrum from $\alpha \sim -1.0$ to $\alpha \sim -1.6$ at $\nu > 2.5$

GHz (Stroe et al., 2016), questioning the single power-law spectrum predicted from the DSA model (Ensslin et al., 1998). Possible explanations involve a non-negligible contribution from the Sunyaev-Zel'dovich (SZ) effect (Basu et al., 2016), the presence of a non-uniform magnetic field in the region (Donnert et al., 2016) and evolving shock and re-acceleration models (Kang & Ryu, 2015). Contrary to the interferometric observations, no steepening at high frequencies is revealed by single dish observations (Kierdorf et al., 2017) at 4.85 and 8.35 GHz, with the Effelsberg Telescope, nor by the combined single-dish Sardinia Radio Telescope interferometric measurements from Loi et al. (2017). This result led Loi et al. (2017) to suggest that the interferometric observations at very high frequency might lose diffuse flux on large angular scales due to the limitation of the minimum baseline length (although Stroe et al. 2016 did attempt to correct for this effect).

Another interesting characteristic is that the northern relic is strongly polarized at high frequencies (i.e. $\sim$ GHz), with an observed polarization fraction in some regions of about 60% (at 8.35 GHz, Kierdorf et al., 2017). Also, from the relic's width, the magnetic field strength was estimated to be between 5 and 7 μG (van Weeren et al., 2010). Diffuse central emission, classified as a radio halo, was detected at 1.4 GHz with the Westerbork Synthesis Radio Telescope (WSRT; van Weeren et al., 2010), at 325 and 153 MHz with the Giant Metrewave Radio Telescope (GMRT; Stroe et al., 2013), and at 145 MHz with LOFAR (Hoang et al., 2017). The radio halo has a spectral index of $\alpha = -1.06 \pm 0.06$, which remains approximately constant across the ~ 1 Mpc^2 halo region. Moreover, Hoang et al. found that the radio halo power is in agreement with the known correlation between the X-ray luminosity and radio power for giant radio halos, and suggested that the halo traces electrons re-accelerated by turbulence generated by the passing shock wave.

2.3. Observations and data reduction

CIZA2242 was observed by the VLA with all the four array configurations in the L- and S-bands, covering the frequency range from 1 to 4 GHz. The total recorded bandwidth was 1 GHz for the L-band, and 2 GHz for the S-bands, split into 16 spectral windows each having 64 channels (1 and 2 MHz width, for the L- and S-band respectively). Due to the large angular size of the cluster and the S-band field of view (FOV), we observed three separate pointings. These pointings were located north-west, north-east and south with respect to the cluster's center. An overview of the frequency bands and observations is given in Table 2.1.

For the primary calibrators we used 3C138 and 3C147, observed $\approx$ 5–10 minutes each at the end of the observing run. In some configurations 3C48 was also observed ($\approx$ 8 minutes) near the middle or at the end of the

Table 2.1: Log of the observations.

Band and Array	Obs. date	Freq. coverage [GHz]	Channel width [MHz]	Integration time [s]	Time on source [s]	θ_{FWHM}[a] ["]	LAS[b] ["]
L-band D-array	30 Jan 2013	1–2	1	5	3538	40	970
	31 Jan 2013	1–2	1	5	3538	40	970
	27 Jan 2013	1–2	1	5	7175	40	970
	03 Feb 2013	1–2	1	5	7160	40	970
L-band C-array	03 Jun 2013	1–2	1	5	21530	11	970
	02 Sep 2013	1–2	1	5	21535	11	970
L-band B-array	30 Oct 2013	1–2	1	3	28719	4	120
L-band A-array	11 May 2014	1–2	1	1	28720	2	36
S-band D-array	23 Feb 2013	2–4	2	5	3580	16	490
	27–28 Feb 2013	2–4	2	5	7175	16	490
	18 Feb 2013	2–4	2	5	3580	16	490
	27 Jan 2013	2–4	2	5	7170	16	490
	27 Jan 2013	2–4	2	5	3505	16	490
S-band C-array	28 Jun 2013	2–4	2	5	28775	5	490
S-band B-array	21 Oct 2013	2–4	2	3	28716	1.5	58
S-band A-array	13 Apr 2014	2–4	2	1	28718	0.6	18

Note: a synthesized beamwidth; b largest angular scale.

observing run, depending on whether this source was observed in addition to, or in substitution of, the other two primary calibrators. J2202+4216 was included as a secondary calibrator, and observed for $\approx$ 3 minutes at intervals of 30-40 minutes. All four polarization products (RR, RL, LR and LL) were recorded.

The data were reduced with CASA[1] (McMullin et al., 2007) version 4.7.0, and processed in the same way for all the different observing runs. As a first step the data were Hanning smoothed. We removed radio frequency interference (RFI) using the *tfcrop* mode from the flagdata task and applied the elevation dependent gain tables and antenna offsets positions. We determined complex gain solutions for the central 10 channels of each spectral window. In this way we removed possible time variations of the gains during the calibrator observations. We pre-applied these solutions to find the delay terms (gaintype='K') and bandpass calibration. Applying the bandpass and delay solutions, we re-determined the complex gain solutions for the primary calibrators using the full bandwidth. We determined the global cross-hand delay solutions (gaintype='KCROSS') from the polarized calibrator 3C138, taking a RL-phase difference of $-10°$ (both L- and S-band) and polarization fractions of 7.5% and 10.7% (L- and S-band respectively). We used 3C147 to calibrate the polarization leakage terms (poltype='Df'), and 3C138 to calibrate the polarization angle (poltype='Xf'). If not present, we replaced 3C147 with J2355+4950 as polarization leakage calibrator. All relevant solutions tables were applied on the fly to determine the complex gain solution for the secondary calibrator J2202+4216 and to obtain its flux density scale. The absolute flux scale from the primary calibrators was calculated assuming the Perley & Butler (2013) model. The RFI removal was repeated after applying the derived calibration solutions, using the *tfcrop* mode first and followed by the *rflag* mode.

All the solutions were transferred to the target source, and then the data were averaged by a factor of two in time and a factor of four in frequency (we excluded the first 7 and the last 10 channels). Finally, a last round of RFI flagging was performed with AOFlagger (Offringa et al., 2010), to remove the remaining interference from the dataset.

To refine the calibration for the target field, we performed two rounds of phase-only self-calibration and two of amplitude and phase self-calibration on the individual datasets. The only exceptions were the northeastern and northwestern pointing of the A-array data taken in the S-band, for which the low signal-to-noise ratio (SNR) allowed only for phase-only self-calibration, combining both polarizations (gaintype='T'). All imaging in CASA was done with w-projection (Cornwell et al., 2005, 2008), which takes the non-coplanar nature of the array into account. We also used briggs weighting (Briggs, 1995) with a robust factor of 0. The spectral index was

---

[1]https://casa.nrao.edu

Table 2.2: Image (`CASA`) information.

Band	Resolution [''×'']	weighting	robust	uv-taper ['']	σ_{rms} [μJy beam^{-1}]
	1.6×1.6	briggs	0	none	5.3
	2.5×2.5	uniform	N/A	2.5	6.5
L-band	6×6	uniform	N/A	5	5.8
	10×10	uniform	N/A	10	8.9
	25×25	uniform	N/A	25	19
	1.3×1.3	briggs	0	none	3.4
	2.5×2.5	uniform	N/A	2.5	4.1
S-band	6×6	uniform	N/A	5	4.5
	10×10	uniform	N/A	10	5.6
	25×25	uniform	N/A	25	23

Table 2.3: Image (`WSClean`) information.

Band	Resolution [''×'']	weighting	robust	uv-taper ['']	σ_{rms} [μJy beam^{-1}]
L-band	2.1×1.8	briggs	0	none	3.8
S-band	0.8×0.6	briggs	−0.5	none	2.7
	3.8×3.8	briggs	0	2.5	3.4
LS-band	6×6	briggs	0	5	4.2
	11×11	briggs	0	10	6.2
	26×26	briggs	0	25	16.7

taken into account during the deconvolution, using `nterms=3` (Rau & Cornwell, 2011). To deconvolve a few bright sources outside the main lobe of the primary beam, image sizes of up to 9720^2 pixels were needed (in A-array configuration). Clean masks were employed during the deconvolution. Initially, the clean masks were automatically made with the `PyBDSM` source detection package (Mohan & Rafferty, 2015), and then updated after each imaging cycle. We manually flagged some additional data during the self-calibration process by visually inspecting the self-calibration solutions.

The final images were obtained by combining the data from all array configurations and performing a final self-calibration with a long solution interval to align the datasets. We produced images over a wide range of resolutions and with different uv-tapers and weighting schemes to emphasize the radio emission on various spatial scales. Moreover, to ensure the recovery of flux on the same spatial scale for the complementary observations (150 MHz LOFAR, Hoang et al., 2017, and 610 MHz GMRT, van

Weeren et al., 2010), we kept data on common uv-distances, discarding all the data below 120λ. The final image resolutions are $1.6''$ and $1.3''$ (full resolution, L- and S-band respectively), and $2.5''$, $5''$, $10''$ and $25''$ (see Table 2.2). We used a multiscale `clean` (Cornwell et al., 2008), with scales of $[0, 3, 7, 25, 60]\times$ the pixel size[2] to make these images. The images were corrected for the primary beam attenuation, with the frequency dependence of the beam taken into account (`widebandpbcor` task[3]).

To create a set of "deep" images, we employed the w-Stacking Clean algorithm (`WSClean`) by Offringa et al. (2014) (Table 2.3). We also stacked images from the L- and S-band data. We only use these images for viewing purposes and determinations of source morphologies. No flux density measurements or other quantitative measurements in this paper have been extracted from them, since `WSClean` just provides an averaged flux density across the bandwidth without taking into account the spectral index during the deconvolution.

2.4.   Results

In Figs. 2.1 and .1.1 we present our deep, high-resolution VLA images of CIZA2242, in L- (1–2 GHz, $2.1'' \times 1.8''$, weighting briggs' robust 0 and uniform) and S-band (2–4 GHz, $0.8'' \times 0.6''$, weighting briggs' robust -0.5 and uniform) respectively. The rms noise is 3.8 μJy beam^{-1} at 1–2 GHz and 2.7 μJy beam^{-1} at 2–4 GHz (Table 2.3). We also show all the 1–4 GHz lower resolution images produced (Fig. 2.3). In all the images we detect the two main relics (north and south), and five other areas/regions of diffuse emission and several tailed radio sources above the $3\sigma_{\mathrm{rms}}$ level. We label the cluster sources using the same convention of Stroe et al. (2013) and Hoang et al. (2017), see Fig. 2.2.

At full resolution, the length of the northern relic (RN) remains constant between the two frequencies (i.e. $\sim$ 1.8 Mpc), while the width decreases from 80 to 40 kpc, in L- and S-band, respectively. The high resolution radio maps show, for the first time, that the relic structure is not continuous, but broken into six different "sheets" or "filaments" (Fig. 2.7) with lengths of about 200–600 kpc. This is visible at both frequencies (Figs. 2.1 and .1.1). The integrated flux densities of RN, measured within the $3\sigma_{\mathrm{rms}}$ region, are 128.1 ± 3.2 mJy and 56.1 ± 1.4 mJy at 1.5 and 3.0 GHz, respectively. We did not included the western emission (R3), for which we measured 12.1 ± 0.3 mJy and 4.5 ± 0.2 mJy, at 1.5 and 3.0 GHz respectively[4]. We also note the presence of additional faint emission at the $3\sigma_{\mathrm{rms}}$ level located northeastward of the northern relic (4.2 ± 0.2 mJy and 2.1 ± 0.1 mJy, in L- and

---

[2]We chose the pixel size so that the beam is sampled by $\approx$ 5 pixels.

[3]This task was run by means of `CASA` version 5.0, which has an update beam shape model.

[4]Hoang et al. (2017) measured one single integrated flux value for RN and R3 (1548.2 ± 4.6 mJy at 145 MHz)
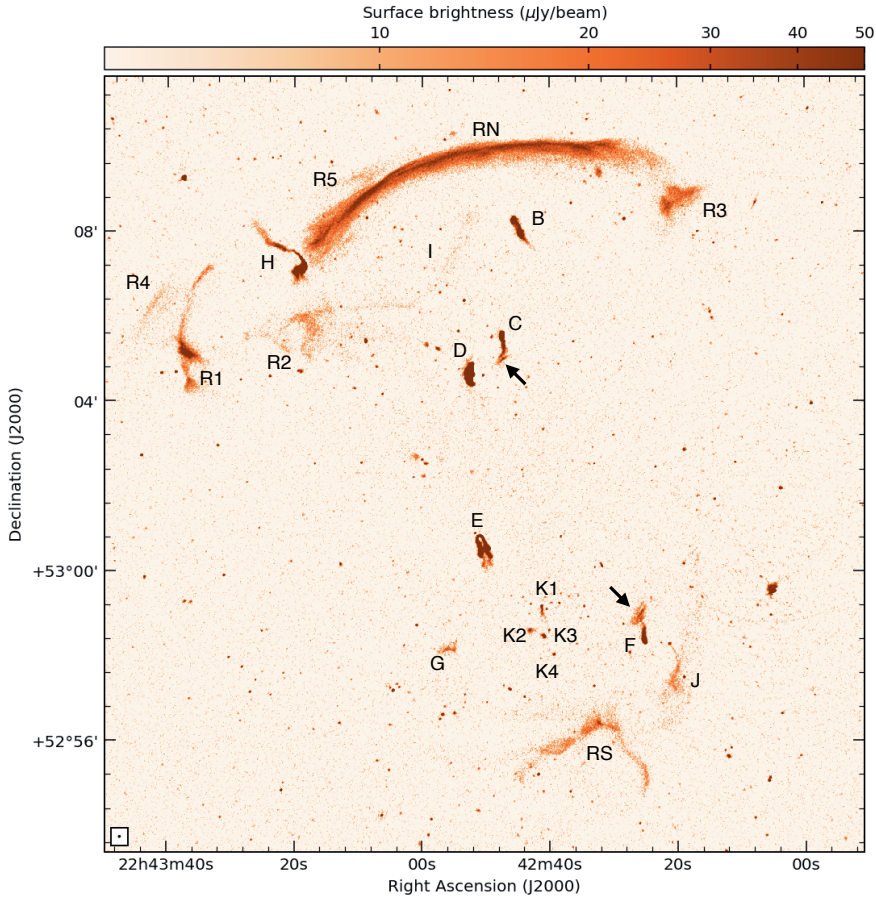
Figure 2.1: L-band (1.5 GHz) VLA high-resolution image of CIZA2242. The map has a noise of $\sigma_{\mathrm{rms}} = 3.8$ μJy beam^{-1}. The black arrows highlight the "broken" nature of the radio tails. Sources are labeled following Stroe et al. (2013) and Hoang et al. (2017) (see Fig. 2.2 for a more complete labeling).
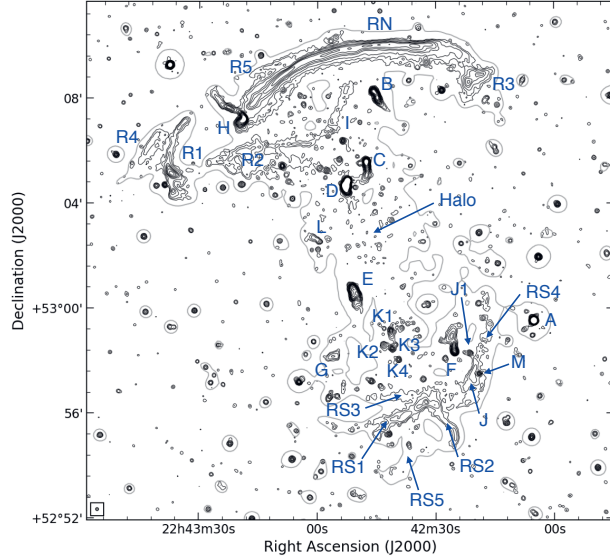
Figure 2.2: Labeled cluster sources, adapting the scheme from Stroe et al. (2013) and Hoang et al. (2017). We used the 5″ resolution (black solid line) to emphasize the diffuse emission. The grey solid line is the 3σ radio contour at 25″ resolution. The radio contours are the same of the ones in Fig. 2.3).

S-band respectively). We label this emission as R5 (see Fig. 2.2) and, as for R3, it was not included into the RN surface brightness measurement. R5 has an extent of 215 kpc in the full resolution image, but its size increases up to 660 kpc in the 10″ resolution image (Fig. 2.3). On the eastern side, at a distance of about ~ 30 kpc, a wide-angle tailed source (H in Fig. 2.2) is located, which has a much higher surface brightness than the relic at both frequencies. Comparing the optical and the radio contours of this source (right panel in Fig. 2.6(d)), we note that the northern lobe breaks ~ 50 kpc from the AGN and then proceeds quite straight, while the southern lobe bends immediately, in projection. We also note that the surface brightness of the northern lobe increases by a factor ~ 4 about 85 kpc northeast of the host galaxy. The southern lobe, on the other hand, is ~ 7 times brighter than the northern one ($F_{\text{lobe S}} = 21.5$ mJy and $F_{\text{lobe N}} = 3.2$ mJy at 1.5 GHz). The zoom on the the northern relic (Fig. 2.7) shows that the flux boost in the northern lobe coincides with the RN6 filament, while the brighter southern lobe is approximately located along the extent of the RN1 filament.

At a distance of about 600 kpc east of source H, there is another arc-like patch of diffuse emission, labeled R1. This relic extends in the north-south direction for a length of $\approx$ 610 kpc, while the width changes from about

20 kpc to 100 kpc, going from north to south. The flux density of this diffuse source is about one order of magnitude lower than RN: we measure 16.0 ± 0.5 mJy and 7.8 ± 0.3 mJy, at 1.5 and 3.0 GHz respectively. We also note that the southern part of R1 is brighter than the rest of this relic. East of R1, faint emission, labeled as R4, extends for ≈ 315 kpc in NW-SE direction. The size of R4 increases up to 640 kpc, at $10''$ resolution. This emission was also detected by Hoang et al. (2017), who labeled it as R1 east (and R1 as R1 west). South of RN/H, we detect a patch of extended emission with a toroidal morphology, labeled R2. Although the $3\sigma_{rms}$ emission is seen only within a region of 180×210 kpc, some residuals cover a broader region, which is better detected at lower resolutions (Fig. 2.3). At $5''$ resolution, the size increases to 710×250 kpc. Towards the west, we detect source I, which was also reported by Stroe et al. (2013) and Hoang et al. (2017). It is barely detected in our high-resolution images, but it is clearly visible in our low resolution images (Fig. 2.3). Our images reveal that source I is a ≈ 825 kpc long filament that connects with R2.

At full resolution, the southern relic (RS) is well detected only in the L-band image. It is located ≈ 2.5 Mpc south of RN, and formed by two "arms", labeled RS1 and RS2 in Fig. 2.2. They measure 530×70 and 25×380 kpc, respectively. We measure a total flux density for these two "arms" of 16.7 ± 0.5 mJy and 7.7 ± 0.3 mJy, at 1.5 and 3.0 GHz respectively. Moreover, at lower resolutions we also detect three additional "arms", labeled RS3, RS4 and RS5, extending eastwards and westwards (Fig. 2.2). The southern relic has a total size of ≈ 1.5 Mpc at $25''$ resolution.

A patch of faint emission is seen to the west of RS1 and RS2 (source J). Our deep VLA observations reveal for the first time a connection between source J and an AGN core located northwards, and labeled as J1 (RA = $22^h42^m21^s.35$ and DEC = $+52°58'17''.92$, J2000). Hereafter, we will refer to the whole radio source as J, and to the core as J1. We measure a flux density for its radio lobe of 6.3 ± 1.9 mJy and 1.7 ± 0.2 mJy, at 1.5 and 3.0 GHz respectively. Moreover, at low-resolution source J seems to be completely embedded into the southern relic (bottom right panel in Fig. 2.3).

Towards the north of RS, the patchy extended emission detected by Stroe et al. (2013) and Hoang et al. (2017) is now resolved into four different sources, which are now labeled in Fig. 2.2 as K1 (tailed radio source), K2, K3 and K4 (compact radio sources). All these sources have and optical counterpart (see Fig. .1.2 and the zoom in right panel in Fig. 2.6(g)). A patch of diffuse emission is detected on the east of these radio galaxies, namely source G. No clear optical counterpart has been found to be associated to this source from previous optical studies (Dawson et al., 2015, Fig. .1.2 and the zoom in right panel in Fig. 2.6(f)).

The radio halo, already detected by other authors (i.e. van Weeren et al., 2010; Stroe et al., 2013; Hoang et al., 2017) becomes visible at $10''$ resolution (bottom left panel in Fig. 2.3), at a level of $3\sigma_{rms}$ ($\sigma_{rms} = 6.2 \ \mu$Jy beam^{-1}).
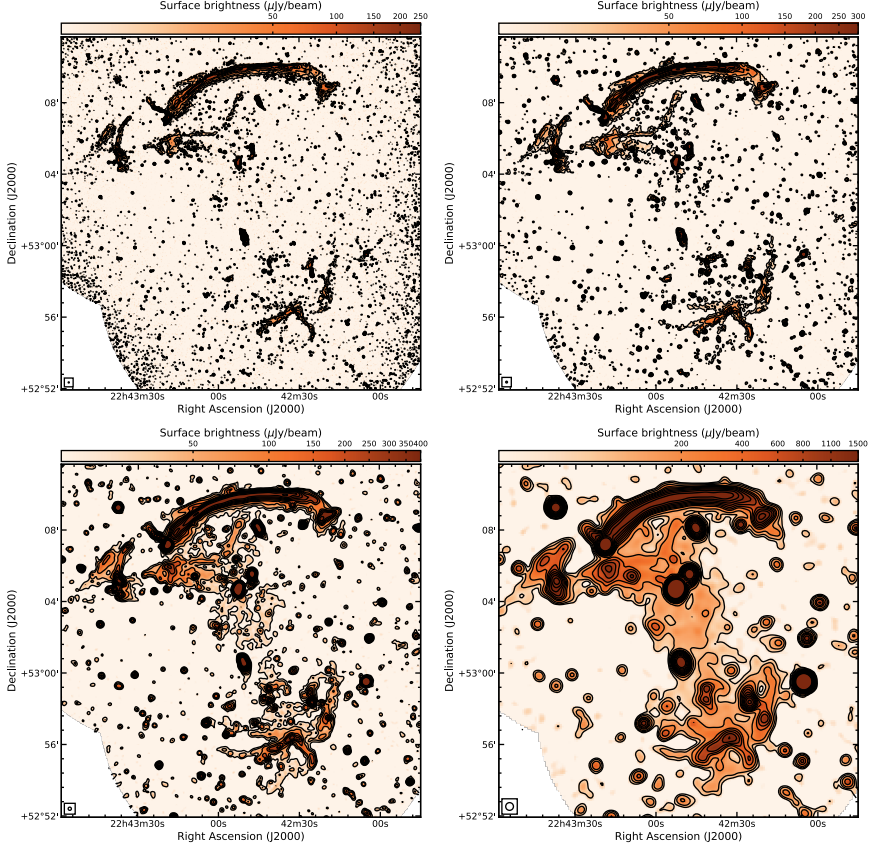
Figure 2.3: Combined L- and S-band (1–4 GHz) VLA deep images at low resolution (2.5″, top left; 5″, top right; 10″, bottom left; 25″, bottom right). The beam size is displayed in the bottom left corner of each image. The radio contours are at $3\sigma_{\rm rms} \times \sqrt{[1, 4, 16, 64, \ldots]}$, where $\sigma_{2.5″} = 3.4$ μJy beam^{-1}, $\sigma_{5″} = 4.2$ μJy beam^{-1}, $\sigma_{10″} = 6.2$ μJy beam^{-1}, $\sigma_{25″} = 16.7$ μJy beam^{-1}.

The halo is visible up to $6\sigma_{\rm rms}$ ($\sigma_{\rm rms} = 16.7$ μJy beam^{-1}) level at 25″ resolution (bottom right panel in Fig. 2.3). It extends the entire distance between RN and RS, with a size of about 2.1 Mpc×0.8 Mpc (N-S and E-W directions, respectively), at this resolution. To estimate the halo radio flux density, we need to remove the contribution of radio galaxies and other sources. This is not trivial, since some these sources are also characterized by some extended emission.

To construct a model for the emission of the extended and compact sources (e.g. radio galaxies, R2 and source I), we imaged the data with the same settings as for the 5″ resolution image (uniform weighting and a uv-

taper of 5″), since it catches properly the diffuse emission from the tails. To avoid the emission of the halo, we include an inner uv-cut of $0.86k\lambda$, which filters out the emission scales larger than 4′ ($\sim$ 770 kpc at cluster's redshift). The model of the radio galaxies was then subtracted from the uv data by means of the task `uvsub`. Finally, the new visibilities were re-imaged at low resolution (i.e. a uv-taper of 35″ and uniform weighting) and the final image was primary-beam corrected.

The measured halo radio flux density at 1.4 GHz is 25.2 ± 4.1 mJy. This flux density measurement agrees with the previous result found by Hoang et al. (2017). The flux density results in a 1.4 GHz radio power[5] of $P_{1.5\ \text{GHz}} = (2.69 \pm 0.37) \times 10^{24}$ W Hz^{-1}. The total error on the halo flux density has been estimated including the flux scale uncertainty (i.e. 2.5%), image noise (i.e. $\sigma_{35''} = 36.3\ \mu$Jy beam^{-1}) scaled to halo area, and the uncertainty due to the subtraction of the discrete radio sources in the same region (σ_{sub}, see Eq. 1 in Cassano et al., 2013). We used $\sigma_{\text{sub}} = 2.5\%$ of the total flux of the subtracted radio galaxies, given by the ratio of the post-source subtraction residuals to the pre-source subtraction flux of a nearby compact source (RA = $22^{\text{h}}41^{\text{m}}33^{\text{s}}.02$ and DEC = $+53°11′05″.63$, J2000). Additional uncertainties come from the estimation of the halo size and from the flux recovered during the imaging (Bonafede et al., 2017). Therefore, we consider this value a lower limit. Unfortunately, the LAS (largest angular scale) of the halo does not allow us to properly recover all the halo flux at 3.0 GHz, hence we do not report a flux density measurement at this frequency.

A study of the tailed radio galaxies was performed in detail by Stroe et al. (2013). Similar to this previous work, we find that the majority of the radio tails are stretched in the north-south direction, tracing the merger direction. Interestingly, our deep high-resolution images reveal that source C and F have "broken" tails (see black arrows in Fig. 2.1 and .1.1), although they are located at different places in the cluster. In contrast with the previous classification as a head-tail radio galaxy (Stroe et al., 2013), our highest resolution images reveal that source B is a double-lobe source, but where some emission from the lobes has been stripped backwards in the north-south direction, suggesting possible stripping of lobe plasma related to the merger event. We also underline the proximity between this tailed radio galaxy and source I (Figs. 2.2 and 2.3), although no direct connection is visible in our images. Classical radio tail shapes are seen in sources E and K1, with a tail extension of 160 and 48 kpc, respectively, based on our 1.5 GHz image. The integrated flux densities of the diffuse sources at 1.5 and 3.0 GHz[6] and the spectral index between these two frequencies, are reported in Table 6.4. All the spectral index values are in agreement

---

[5]$P_{1.4\ \text{GHz}} = 4\pi D_{\text{L}}^2 S_{1.4\ \text{GHz}}(1+z)^{-(\alpha+1)}$ W Hz^{-1}, where $D_{\text{L}} = 944$ Mpc is the luminosity distance and $(1+z)^{-(\alpha+1)}$ the k-correction; we use a spectral index of $\alpha = -1.03 \pm 0.09$ (Hoang et al., 2017)

[6]In the flux density estimation we used identical regions at both frequencies.

with previous works, i.e. Stroe et al. (2013) and Hoang et al. (2017). We estimated the spectral index uncertainties by taking into account the map noise (σ_{rms}) and a flux scale uncertainty of 2.5%, using:

Table 2.4: Flux densities and integrated spectral index of the diffuse cluster sources measured from the full resolution VLA images.

Source	$S_{1.5\ \mathrm{GHz}}$ [mJy]	$S_{3.0\ \mathrm{GHz}}$ [mJy]	α_{int}
RN	128.1 ± 3.2	56.1 ± 1.4	-1.19 ± 0.05
RS	16.7 ± 0.5	7.7 ± 0.3	-1.12 ± 0.07
R1	16.0 ± 0.5	7.8 ± 0.3	-1.03 ± 0.06
R2	10.3 ± 0.4	4.5 ± 0.2	-1.19 ± 0.09
R3	12.1 ± 0.3	4.3 ± 0.2	-1.43 ± 0.07
R4	4.0 ± 0.2	2.3 ± 0.1	-0.93 ± 0.11
R5	4.2 ± 0.2	2.1 ± 0.1	-0.93 ± 0.12
I	3.4 ± 0.2	1.5 ± 0.2	-1.18 ± 0.17
Halo	25.2 ± 4.1	$\ldots$	$\ldots$

$$\sigma_\alpha = \frac{1}{\ln \frac{\nu_{1.5\,\mathrm{GHz}}}{\nu_{3.0\,\mathrm{GHz}}}} \sqrt{\left(\frac{\Delta S_{1.5\,\mathrm{GHz}}}{S_{1.5\,\mathrm{GHz}}}\right)^2 + \left(\frac{\Delta S_{3.0\,\mathrm{GHz}}}{S_{3.0\,\mathrm{GHz}}}\right)^2} \tag{2.1}$$

where $\Delta S_\nu = \sqrt{\sigma_{\mathrm{rms}}^2 \left(\frac{A_{\mathrm{source}}}{A_{\mathrm{beam}}}\right) + (0.025 \times S_\nu)^2}$ is the total uncertainty on S_ν, while A_{source} and A_{beam} are the area of the source and beam respectively.

2.4.1. Spectral index maps

We combine our 1–2 and 2–4 GHz VLA images with previous observations performed at 610 (van Weeren et al., 2010) and 145 MHz (Hoang et al., 2017) to obtain spectral index maps over a wide frequency range. To take into account the differences of each dataset (e.g. interferometer uv-coverage), we produced new radio images for the previous datasets, cutting at a common uv-distance (120λ). We used uniform weighting to compensate for differences in the uv-plane sampling. The images of each dataset were then convolved to the same resolution, and re-gridded to the same pixel grid (i.e. the LOFAR image). The effective final resolutions and the noise levels are listed in Table 2.2.

We obtained the spectral index maps by fitting both first and second order polynomials through the flux measurements. Although the maximum signal to noise ratio (SNR) is given by the former case, the latter one allows us to take into account possible non-negligible deviation from a straight spectrum. We proceeded as follow:

- fit with a second order polynomial;

- determine if the spectral index shows significant curvature (i.e. above the $2\times\sigma$ threshold, with σ the uncertainty associated with the second order term);

- if the second order term is consistent with zero, we redo the fit and use a first order polynomial; otherwise we keep the second order result.

For the spectral index maps, we accepted the α values only when the associated uncertainty was above a given threshold, i.e. $\sigma_\alpha = 0.2$ and $\sigma_\alpha = 0.4$, for the first and second order polynomial fits respectively. In this way we prevent a noisy measurement at a certain frequency from rejecting a possible good fit.

For a first order polynomial fit (i.e. $y = a_0 + a_1 x$), the spectral index α is defined as the slope of the fit, i.e. $\alpha = a_1$, while the spectral curvature C is defined as:

$$C = -\alpha_{\nu_2}^{\nu_1} + \alpha_{\nu_3}^{\nu_2} \qquad (2.2)$$

where ν_1 is the lowest of the three frequencies, ν_2 the middle one and ν_3 the highest, as described by Leahy & Roger (1998). In this convention, the curvature is negative for a convex spectrum. Since this curvature definition works only when we have three frequencies, we define the curvature C in the following way (Stroe et al., 2013):

$$C = \alpha_{\text{high}} - \alpha_{\text{low}} \qquad (2.3)$$

where, in our case, the low frequency spectral index was calculated using the LOFAR and the GMRT observations, and the high low frequency spectral index was calculated using the L- and S-band VLA observations. The uncertainty associated with this measure is:

$$\sigma_C = \sqrt{(\sigma_{\alpha_{\text{low}}})^2 + (\sigma_{\alpha_{\text{high}}})^2} \qquad (2.4)$$

where the spectral index uncertainties $\sigma_{\alpha_{\text{low}}}$ and $\sigma_{\alpha_{\text{high}}}$ were obtained similarly to Eq. 6.2.

When the second order polynomial fit (i.e. $y = a_0 + a_1 x + a_2 x^2$) was used, we defined the curvature, C, and the spectral index, α, as

$$C = a_2 \qquad (2.5)$$

$$\alpha = \left. \frac{dy}{dx} \right|_{x \equiv \nu = 608 \ \text{MHz}} = a_1 + 2a_2 x, \qquad (2.6)$$

respectively. By using this convention, convex spectra are characterized by more negative values of C. The uncertainties associated with α and C were obtained via Monte Carlo simulation.
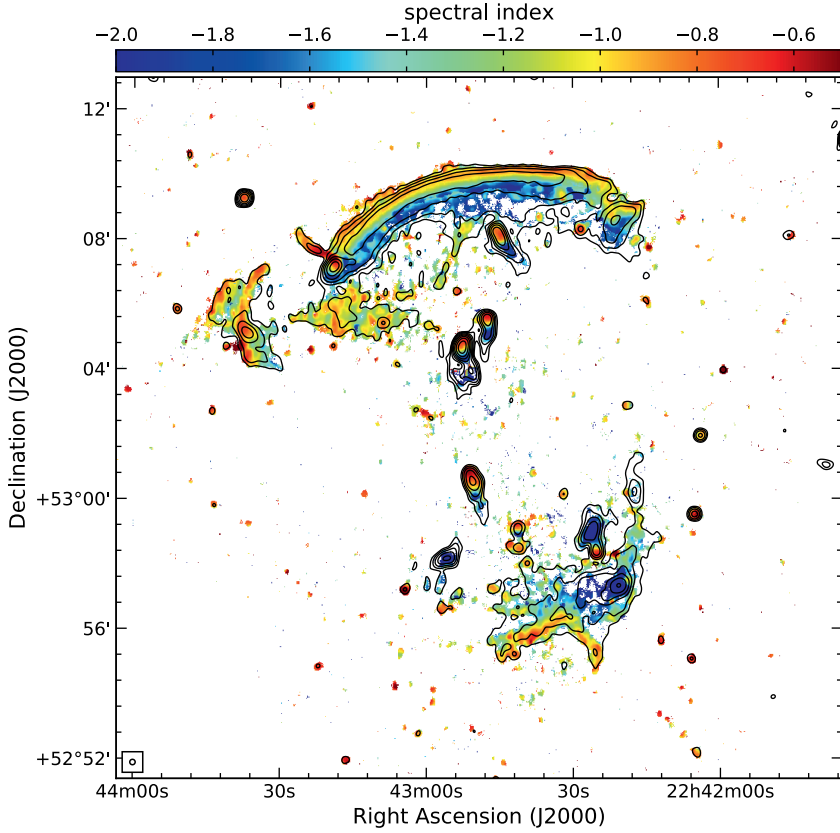
Figure 2.4: 10″ spectral index map of CIZA2242 obtained between 145 MHz, 610 MHz, 1.5 GHz, and 3.0 GHz. The radio contours are from the LOFAR image, with contours drawn at levels of $3\sigma_{\mathrm{rms}} \times \sqrt{[1, 4, 16, 64, 256, \ldots]}$, with $\sigma_{\mathrm{rms}} = 230\ \mu$Jy beam^{-1}. The most important cluster sources have been labeled as Fig. 2.2.

The spectral index maps at 10″ and 25″ of the entire cluster are shown in Figs. 2.4 and 2.5, respectively. The corresponding spectral index uncertainty map at 10″ resolution is presented in Fig. .2.2.

In the 10″ map (Fig. 2.4) a spectral index gradient across the two main relics is seen from the outskirts toward the cluster center. In the northern relic (RN) and in R3, the spectral index values range between −0.8 to −1.7, across their width. Two flatter spots, detected in the southern part of RN, are associated with two point-like sources. A weaker gradient is also seen in R1 and R3, from east to west (from −0.7 to −1.2), and in the southern relic (RS), from south to north. A spectral index of about −0.8 is measured
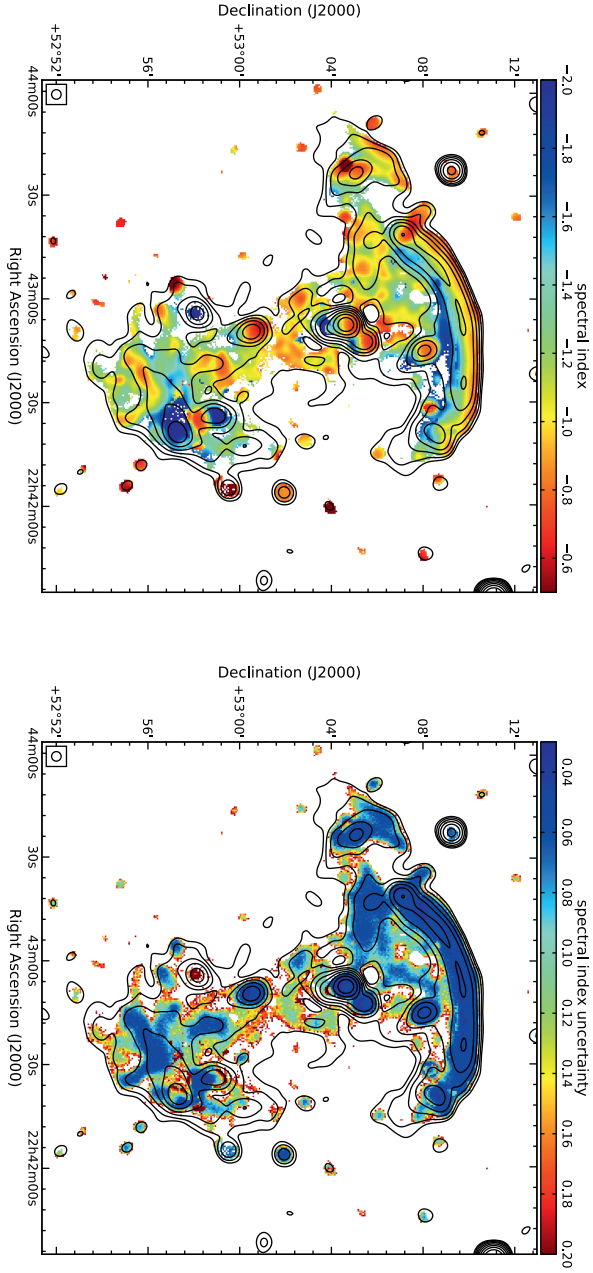
Figure 2.5: 25″ spectral index (left panel) and spectral index uncertainty (right panel) maps of CIZA2242 obtained between 145 MHz, 610 MHz, 1.5 GHz, and 3.0 GHz. The radio contours are from the LOFAR image, contours are drawn at levels of $3\sigma_{\rm rms} \times \sqrt{[1, 4, 16, 64, 256, \ldots]}$, with $\sigma_{\rm rms} = 340\ \mu{\rm Jy\ beam}^{-1}$.
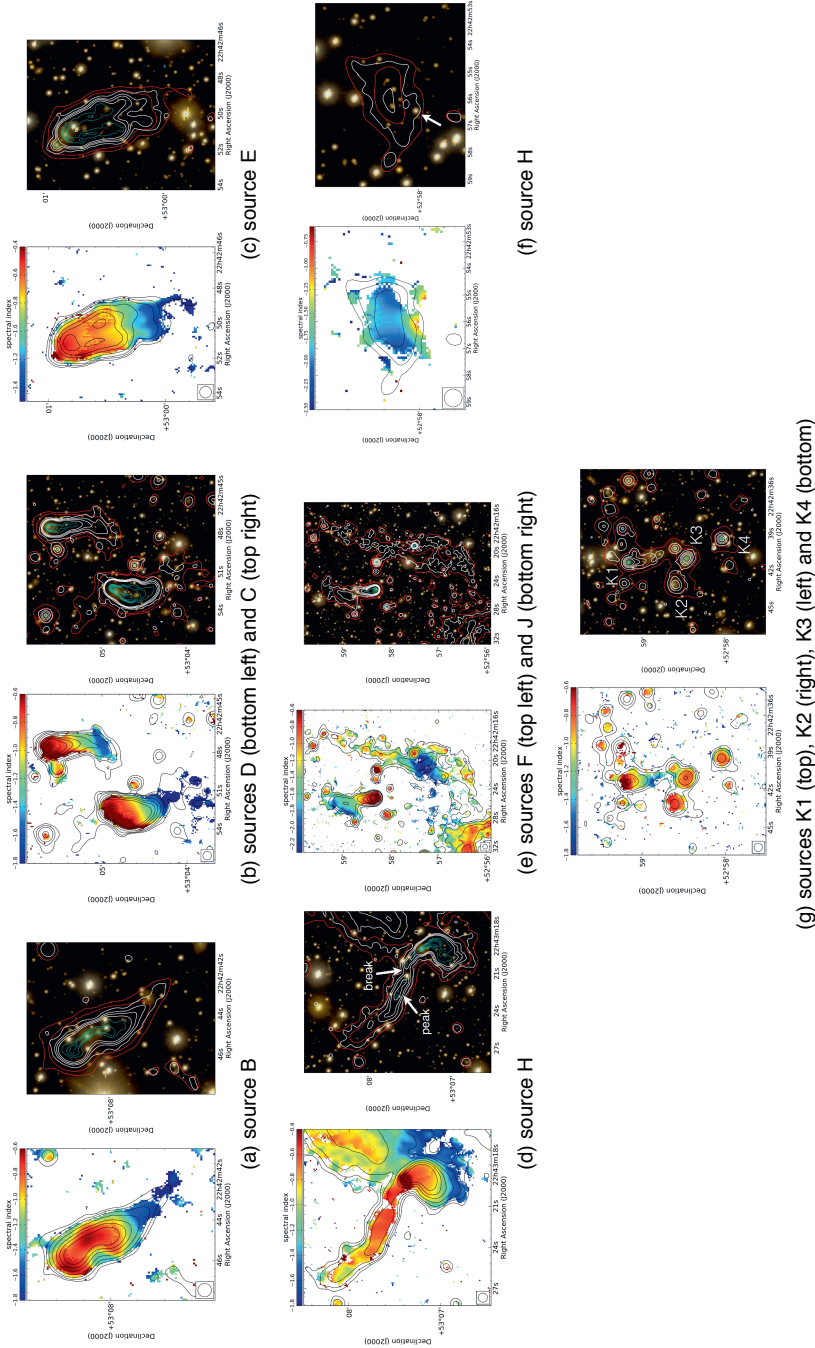
Figure 2.6: Tailed radio galaxies in CIZA2242 (for the labels see Fig. 2.3). Left panels: 5″ resolution spectral index map with the 1–4 GHz radio contours at the same resolution. Right panels: Subaru *gri* composite optical images (Dawson et al., 2015; Jee et al., 2015) with the 0.8″×0.6″ (cyan) 2–4 GHz, and 2.5″ (white) and 5″ (red) 1–4 GHz radio contours. For both panels, the radio contours are drawn at $3\sigma \times \sqrt{(1, 4, 16, \ldots)}$ levels.

both on the outskirts of RS1 and RS2, while an average spectral indices of ≈ -1.2 and ≈ -1.5 are measured for RS3 and RS4, respectively. No strong gradient is seen for R2, for which we measure steep ($\alpha \approx -1.2$) spectral index values. Relic R5 is barely detected in our spectral index map, because of its low surface brightness in the S-band. For these relics, the spectral index values are about -0.8.

All the radio galaxies show a spectral index gradient, as expected from cluster galaxies, with a steepening from $\alpha \approx -0.6$ in the nuclei to $\alpha \approx -2.0$ in the tails (sources E and K1, left panel in Figs. 2.6(c) and (g), respectively). An exception is source B, where the spectral index gradient ($\alpha \sim 2$) is seen in the south-west direction and not along the nucleus-lobe axis (left panel in Fig. 2.6(a)), supporting a scenario of plasma stripping as consequence of the cluster merger. A remarkable steep gradient is detected in sources F and J (left panel in Fig. 2.6(e)), the spectral index reaching values lower than -2.5. Moreover, for the first time we detect spectral index values across the region connecting J1 ($\alpha \approx -0.6$) and the lobe of source J, with values of about -1.6 (left panel Fig. .2.1). Particularly interesting is source H, where the spectral index has a gradient (from $\alpha \approx -0.6$ to $\alpha \approx -1.9$) only in the southern lobe, while it remains quite constant in the northern lobe (from $\alpha \approx -0.6$ to $\alpha \approx -0.9$, left panel in Fig. 2.6(d)). We also note that the spectral index of source G is rather uniform and steep, with an average value of ~ -1.7 (left panel in Fig. 2.6(f)). A suggestion of spectral index flattening is seen at the southern boundary of the source, in correspondence of a cluster galaxy which could be a candidate optical counterpart of this diffuse emission, although no spectroscopic confirmation has been found so far (Dawson et al., 2015, Fig. .1.2).

We made use of the 25″ resolution images (Fig. 2.5) to determine the spectral properties of the radio halo, which are consistent with the ones obtained by Hoang et al. (2017). No gradient is seen across the halo, and the spectral indices range between -1.2 and -1.0.

2.5. Discussion

The Sausage cluster is a well known double-relic system. Due to its size, regularity, and radio brightness, it offers a unique opportunity to study the particle (re-)acceleration mechanisms at shocks, and the particle aging in the shock downstream region, with a relatively small contribution from projection effects. Indeed, numerical simulation by van Weeren et al. (2011b) has shown that CIZA2242 is a binary cluster merger seen very close to edge-on (i.e. $|i| \lesssim 10$). Here we discuss the relics' morphologies, formation scenarios, and underlying particle (re-)acceleration mechanisms.

2.5.1.   Radio Mach number estimates

For the DSA model, there is a relation between the radio injection spectral index α_{inj} and the Mach number $\mathcal{M}$ of the shock (e.g. Drury, 1983; Blandford & Eichler, 1987):

$$\mathcal{M} = \sqrt{\frac{2\alpha_{inj} + 3}{2\alpha_{inj} - 1}} \,. \qquad (2.7)$$

One usually assumes a standard power-law energy distribution of relativistic electrons just after acceleration[7]. For "stationary conditions", with the lifetime of the shock and the electron diffusion time being much longer than the electron cooling time, the integrated spectral index α_{int} is steeper than the injection index by 0.5 (Kardashev, 1962):

$$\alpha_{inj} = 0.5 + \alpha_{int} \,. \qquad (2.8)$$

However, the assumption that the timescale on which the shock properties change is much longer than the electron cooling time does not necessarily have to hold for relics (Kang, 2015). For example, for a spherically expanding shock, Kang established that the slow decline of the injected particle flux over time could increase the low frequency radio emission downstream away from the shock. This means that α_{inj} calculated by Eq. 2.8 can lead to significant errors in the derived Mach number (i.e. 0.2 units in α).

Therefore, a more accurate way to compute the Mach number from the radio spectral index, would be to directly measure α_{inj} at the shock front and not use α_{int}. At the shock front, where the particles have recently been (re-)accelerated, the injection spectral index should be "flat", while it should steepen in the downstream region because of synchrotron and IC energy losses. However, directly measuring α_{inj}, requires (i) highly-resolved maps of the downstream cooling region, to avoid the mixing of different electron populations and (ii) minimum projection effects, which means that the merger should have to occur in, or close to, the plane of the sky. Numerical simulations (e.g. van Weeren et al., 2011b; Kang et al., 2012) have indicated that for CIZA2242 the projection effects are probably small, at least for the northern relic, with a merger axis angle $|i| \lesssim 10°$. Furthermore, the mixing of emission from regions with different spectral ages can be largely avoided thanks to our high-resolution images, as described in Sect. 2.4.1.

2.5.2.   Spectral index profiles and color-color diagrams

To investigate possible differences in the spectral index properties at the shock and the energy losses in the post-shock region, we analyzed the

---

[7]$\frac{dN(E)}{dE} \propto E^{-\delta_{inj}}$, where $\delta_{inj} = 1 - 2\alpha_{inj}$

spectral index profile across the radio relics. We extracted flux densities across the width of the relics in narrow annuli spaced by the beam size. To avoid mixing of emission from regions with different amounts of aging, we used the highest resolution images available for all frequencies, i.e. $5''$. The flux densities were fitted with a first order polynomial. Following van Weeren et al. (2012), we did not include the calibration uncertainties (15% on S_{LOFAR}, 5% on S_{GMRT} and 2.5% on S_{VLA}) in the estimation of the flux density uncertainties, as this would shift measurements in different annuli/regions in the same way.

Another way to investigate the spectral shapes is by means of so-called color-color (cc) diagrams (Katz-Stone et al., 1993; Rudnick & Katz-Stone, 1996; Rudnick, 2001). These diagrams emphasize spectral curvature, since they represent a comparison between spectral indices calculated at low- and high-frequency ranges. In our case, we plot $\alpha_{150\mathrm{MHz}}^{610\mathrm{MHz}}$ on the x-axis and $\alpha_{1.5\mathrm{GHz}}^{3.0\mathrm{GHz}}$ on the y-axis (see bottom panel in Fig. 2.9). Moreover, cc-diagrams are particularly useful to discriminate between different theoretical synchrotron spectral models, and to give constraints on the injection spectrum.

The time evolution of the CR electron energy distribution depends on two parameters:

$$\frac{dE}{dt} = -(\varepsilon_{\mathrm{sync}} + \varepsilon_{\mathrm{IC}})E^2 \,, \qquad (2.9)$$

where $\varepsilon_{\mathrm{IC}}$ is the contribution of the IC energy losses, (i.e. $\varepsilon_{\mathrm{IC}} \propto B_{\mathrm{CMB}}^2$, where $B_{\mathrm{CMB}} = 3.25(1+z)^2$ μG), while $\varepsilon_{\mathrm{sync}}$ is the contribution of the synchrotron energy losses, whose parametrization depends on the aging model assumed. Generally, a JP (Jaffe & Perola, 1973) aging model is used, which involves a single burst of particle acceleration, and a continued isotropization of the angle between the magnetic field and the electron velocity vectors (the so-called pitch angle) on a time-scale shorter than the radiative timescale[8]. Here, the synchrotron losses are described by the $\varepsilon_{\mathrm{sync}} \propto B^2$ relation. Other models include continuous particle acceleration (CI; Pacholczyk, 1970) or a modification to the JP model with a finite period of electron acceleration (KGJP; Komissarov & Gubanov, 1994).

One characteristic that makes cc-diagrams particularly useful is that the shape of the different models only depends on the injection spectral index, while it is independent of the magnetic field value, adiabatic compression/expansion and radiation losses.

---

[8]Another aging model is the KP (Kardashev, 1962; Pacholczyk, 1970) one, but it assumes a constant pitch angle in time.
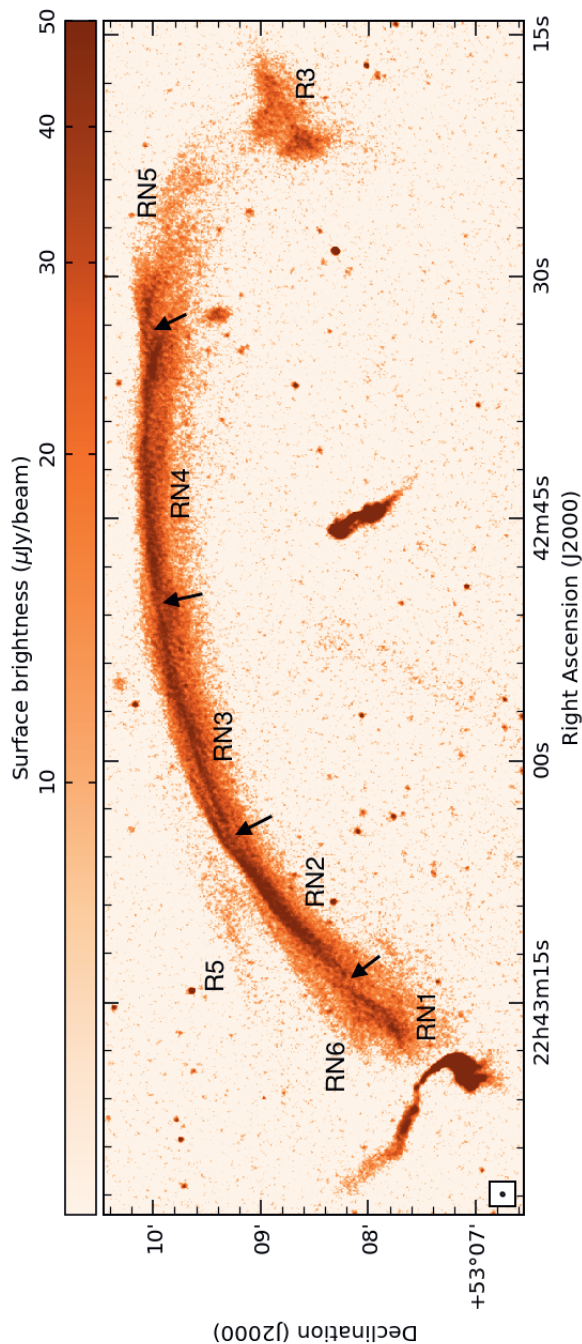
Figure 2.7: Full resolution ($2.1'' \times 1.8''$) L-band image zooming in the northern relic. The black arrows indicate the points where the relic breaks into several separate sheets.

2.5.3. Northern Relic

Our high-resolution images reveal that the northern relic contains filamentary substructures. We labeled these sheets as RN1, RN2, RN3, RN4, RN5 and RN6 in Fig. 2.7. To avoid mixing of different electron populations, we obtained the spectral index profiles in several sub-sectors (RN1–RN5). We define each sector such that it does not include regions where two sheets overlap, or contain compact sources. Despite their different locations, RN1 to RN5 display similar $\alpha_{\rm inj}$ values at the shock, and similar trends in the downstream region (see Table 2.5).

The injection spectral index for the RN was estimated by considering a narrow region (with a width identical to the beam-size, i.e. the combined red boxes in Fig. 2.8, bottom panel) following the length of the relic. From this region, we obtain $\alpha_{\rm inj} = -0.86 \pm 0.05$, corresponding to a Mach number of $\mathcal{M}_N = 2.58 \pm 0.17$ (Eq. 2.7). The injection spectral indices of the different filaments in the northern relic, and the corresponding Mach numbers, are reported in Table 2.5. We find a good agreement with the X-ray Mach number estimate ($\mathcal{M}_N = 2.7^{+0.7}_{-0.4}$ Akamatsu et al., 2015) and with the previous radio studies ($\mathcal{M}_N = 2.9^{+0.10}_{-0.13}$, Stroe et al., 2014; $\mathcal{M}_N = 2.7^{+0.6}_{-0.3}$, Hoang et al., 2017).

Table 2.5: Spectral indices and Mach numbers for the relics in CIZA2242. A comparison with literature values is shown in columns 5, 6 (radio) and 7 (X-ray).

Region	res. ['']	$\alpha_{\rm inj}$	$\mathcal{M}_{\rm radio}$[⋆]	$\mathcal{M}_{\rm radio}$[†]	$\mathcal{M}_{\rm radio}$[‡]	$\mathcal{M}_{\rm X-ray}$[◇]
RN	5	-0.86 ± 0.05	2.58 ± 0.17	$2.9^{+0.10}_{-0.13}$	$2.7^{+0.6}_{-0.3}$	$2.7^{+0.7}_{-0.4}$
RN1	5	-0.89 ± 0.05	2.47 ± 0.14			
RN2	5	-0.90 ± 0.03	2.46 ± 0.07			
RN3	5	-0.89 ± 0.04	2.47 ± 0.10			
RN4	5	-0.81 ± 0.04	2.72 ± 0.16			
RN5	5	-0.89 ± 0.10	2.48 ± 0.38			
RN6	5	-0.84 ± 0.16	2.62 ± 0.86			
RS	10	-1.09 ± 0.05	2.10 ± 0.08	$2.8^{+0.19}_{-0.19}$**	$1.9^{+0.3}_{-0.2}$**	$1.7^{+0.4}_{-0.3}$
R1	10	-0.82 ± 0.02	2.69 ± 0.06		$2.4^{+0.5}_{-0.3}$	$2.5^{+0.6‡}_{-0.2}$
R4	10	-0.86 ± 0.04	2.57 ± 0.12			
R5*	10	-1.06 ± 0.21	2.13 ± 0.55			

Note: [⋆] this work; [†] Stroe et al. (2014, 2013), for the north and south relics, respectively; [‡] Hoang et al. (2017); [◇] Akamatsu et al. (2015). * Source is only visible in our new deep VLA images, hence we calculated the spectral index (and derived the Mach numbers) only between 1.5 and 3.0 GHz flux density measurements. ** Obtained at different resolutions: 18'' Stroe et al. (2013) and 25'' (Hoang et al., 2017).

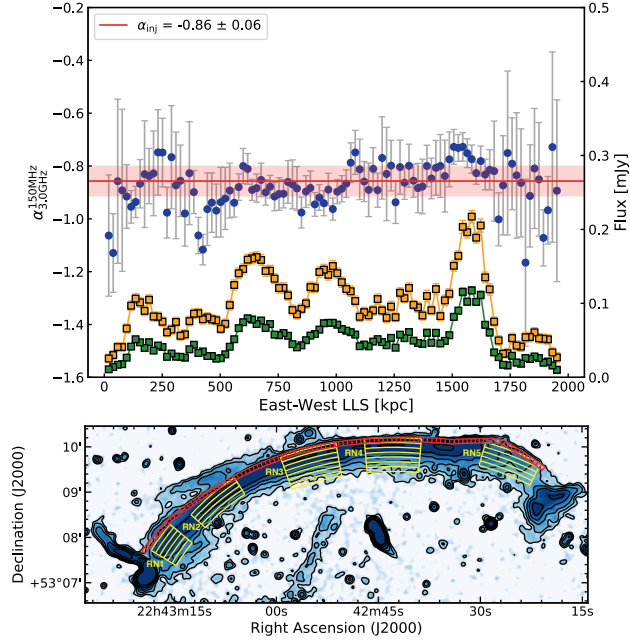To investigate possible variations across the length of RN, we calculated

Figure 2.8: Top panel: East-west spectral index profile (blue circles) obtained with a first order polynomial fit and VLA flux densities at 1.5 and 3.0 GHz (orange and green squares, respectively) at 5″-resolution of the northern relic. The filled red region represents the standard deviation associated with the injection spectral index (red solid line). Bottom panel: 1–4 GHz 5″ resolution image of the northern relic. The red boxes show the beam-sized region where the spectral indices were extracted. The yellow sectors represent the regions where we extracted the spectral index and curvature profiles and the color-color diagram.

the spectral index in individual beam-sized regions at the shock front (red boxes in Fig. 2.8 bottom panel). The results are shown in the top panel in Fig. 2.8 and suggest that the eastern part ($\lesssim$ 1 Mpc) of RN is slightly steeper than the western one. However, given the uncertainties on the spectral indices of the two relic sides, i.e. $\alpha_{\mathrm{inj},\lesssim 1\mathrm{Mpc}} = -0.89 \pm 0.05$ and $\alpha_{\mathrm{inj},\gtrsim 1\mathrm{Mpc}} = -0.81 \pm 0.08$, this difference is not significant. Significant spectral index variation are visible on smaller scales (i.e. $\sim$ 200 kpc): we measure a flattening of the spectral index around 1600 kpc, and a steepening around 400 and 1000 kpc (see Fig. 2.5.3). Mach number variations, or different aging trends with the broken-shaped shock surfaces, different amounts of mixing, and magnetic field variation are possible explanations (see Sect. 2.5.3).
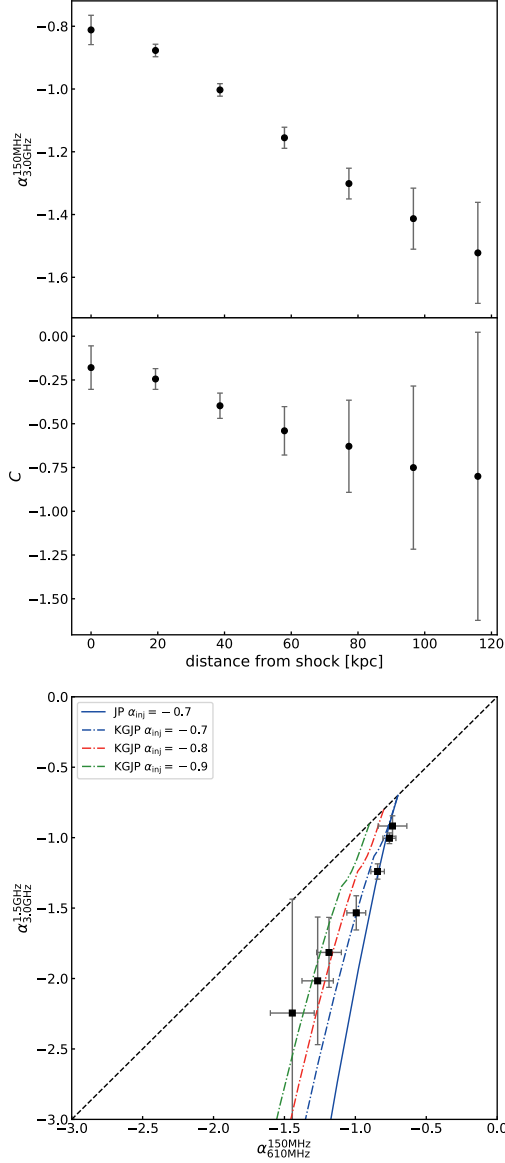
Figure 2.9: Spectral index profile (top panel), curvature profile (middle panel) and color-color diagram (bottom panel) towards the cluster center obtained via a first order polynomial fits to the flux density measurements of the RN4 filament of the northern relic at 5″ resolution. The color-color diagram shows the JP (blue solid lines) and the KGJP (dot dashed lines) aging models obtained for different injection spectral indices ($\alpha_{inj} = -0.7$ in blue, $\alpha_{inj} = -0.8$ in red, $\alpha_{inj} = -0.9$ in green).

Spectral curvature

In Fig. 2.9 we display the spectral index and the curvature profiles, and the color-color diagram for the RN4 filament (see the bottom panel of Fig. 2.8 for the sector placement), obtained with a first order polynomial fit. The steepening of the spectral index in the post-shock region (top panel in Fig. 2.9) qualitatively agrees with synchrotron and IC energy losses. The non-negligible curvature in each annulus, which was also detected by Stroe et al. (2013), is better seen in the middle panel in Fig. 2.9, where the curvature profile is shown. All the points in the plot lie below the $C = 0$ line, and the convexity of the spectrum ($C < 0$, see Eq. 2.3) increases further towards the cluster center. In the cc-diagram we also show the JP and KGJP (solid and dash-dotted lines, respectively) aging models. The $\alpha_{150\mathrm{MHz}}^{610\mathrm{MHz}} = \alpha_{1.5\mathrm{GHz}}^{3.0\mathrm{GHz}}$ line (black dashed) represents a power-law spectral shape, as there are no differences between the spectral index calculated in the low- and the high-frequency range. Our data lie between the $\alpha_{\mathrm{inj}} = -0.7$ and $\alpha_{\mathrm{inj}} = -0.9$ curves, assuming a KGJP model with a particle injection time of 0.6×10^8 yr for a magnetic field of $B = 7$ μG. The JP model with an injection spectral index of -0.7 fits well only for the first three annuli, which correspond to a linear size of about 60 kpc. A possible, at least partly, explanation can be that, as one progresses further downstream, the emission becomes progressively more affected by projection effects, or by actual mixing of different electron populations. Mixing of different electron populations would indeed generate a spectrum closer to the power-law shape, generating the discrepancy with the models (solid and dot-dashed lines in the bottom panel in Fig. 2.9). This result is not completely a surprise since the northern relic is almost 2 Mpc long and it is likely that it is also characterized by extended emission in the third dimension. This would easily led to regions with slightly different amounts of spectral aging being contained in a single annulus. Moreover, we note that this effect is stronger further downstream towards the cluster center. A similar result has also been seen for the Toothbrush cluster (van Weeren et al., 2012). We describe the effects of the projection in Sect. 2.5.3.

Interestingly, the injection spectral index directly obtained from the spectral index map is slightly different from the one obtained via the cc-diagram ($\alpha_{\mathrm{inj,2Dmap}} \approx -0.8$ while $\alpha_{\mathrm{inj,model}} = -0.7$). The first point in our color-color diagram, at the relic's outer edge, already shows a small amount of spectral curvature indicating that even at this location there is already some mixing of emission with different spectral ages, likely due to projection effects. Extrapolation in the cc-diagram to the $\alpha_{\mathrm{low}} = \alpha_{\mathrm{high}}$ line might therefore provide a more reliable estimate than simply taking the flattest spectral index from a map. This discrepancy between the two methods, shows the limitation of the direct estimation of the injection spectral index from a radio map. In this sense, we can only assert that the injection spectral index, estimated from the maps, is equal to or steeper than the

real injection spectral index.

3D model

When computing the spectral model in Section 2.5.3, it was assumed that the relic is caused by a planar shock front perfectly aligned with the line of sight. The actual shock front in a merging cluster, which causes a radio relic, has certainly a much more complex geometry. A better approximation, although still very simplistic, is the assumption that the shock front is shaped like a spherical cap with uniform Mach number.

Before we assess the spherically-shaped shock front, we model the profile of a plane shock, i.e. without including any projection effects. We compute the radio emission in the downstream region as described by Hoeft & Brüggen (2007). The model assumes a power-law spectrum for the electron energy distribution at the location of injection. A proper average over pitch angles was recently included (Hoeft et al. in prep.) to best represent the fast electron velocity isotropization according to the JP model. The resulting model profiles are convolved with the observation resolution, i.e. 5″. The top row in Figure 2.10 shows the profiles for our four observing frequencies (left panel), and the spectral index (central panel) and curvature (right panel) profiles assuming a shock aligned with the line of sight ($\psi = 0°$), a Mach number of $\mathcal{M} = 2.7$ (i.e. $\alpha_{int} = -0.82$) according to the X-ray analysis (see Akamatsu et al., 2015) and spectral index profile (see Tab. 2.5), and a homogeneous magnetic field of $B = 3$ μG. As a result, the peak of the flux density profiles is shifted towards to the downstream region of the shock, even though the injection is located at the rising flank of the profiles. Although the flux profile at 150 MHz is matched well, this model fails to describe the profiles at the other frequencies, resulting in a much steeper spectral index profile with respect to that observed (central top panel in Fig. 2.10).

A possible fix might be made by introducing projection effects, which mix the emission coming from the outermost region and what appears to be in the downstream region in the 2D plane. To create a toy model, we adopt a curvature radius of the shock of $R = 1.5$ Mpc and an opening angle of $2\psi = 36°$. This implies that, in projection, there is injection up to about 60 kpc in the downstream direction. The middle row in Figure 2.10 shows the resulting profiles. Evidently, the flux profiles (left panel) get wider and the spectral index profile (central panel) is less steep, at least up to about 70 kpc. However, the profiles are now too much smeared out, showing only a weak peak at about 20 kpc. Moreover, the spectral index profile is still generally too steep.

As argued in the previous Section, the injection spectral index estimated from the RN4 profile (see top panel in Fig. 2.9) is a limit, and the real one can be flatter. To assess the implications, we adopt a quite flat injec-
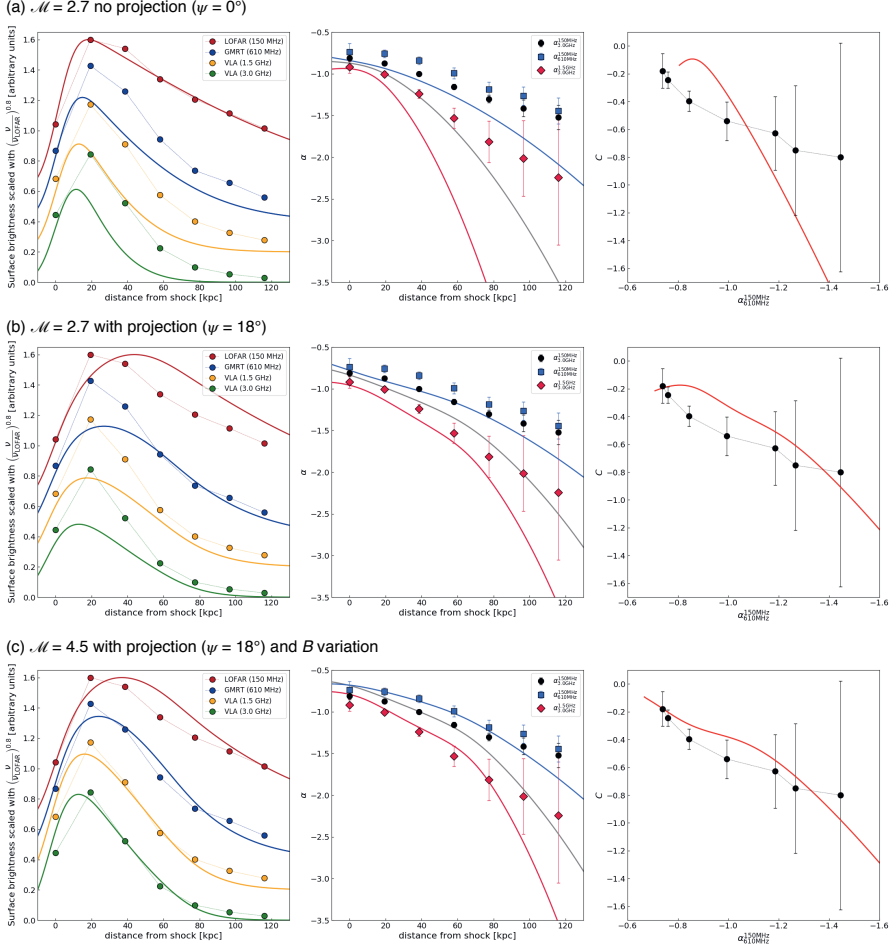
Figure 2.10: Left panels: 150 MHz LOFAR, 610 MHz GMRT, 1.5 GHz VLA and 3.0 GHz VLA flux profiles (red, blue, orange and green solid lines, respectively) convolved with the resolution of the observation, i.e. $5''$; filled circles display the flux density measurements from RN4 with the same color-code of the solid lines. Central panels: observed and modeled spectral index profiles calculated between 150 MHz and 3.0 GHz (black filled circles and solid lines), 150 and 610 MHz (blue squares and solid lines) and 1.5 GHz and 3.0 GHz (red diamonds and solid lines). Right panels: observed (black filled circles) and modeled (red solid line) curvature profile. The three rows show the different results assuming different Mach numbers ($\mathcal{M}$), spherical projection (ψ) and magnetic field variation (B_0 and $\log \sigma$). All the models assume a curvature radius $R = 1.5$ Mpc and a downstream temperature $T = 7$ keV.

tion index, namely $\alpha_{inj} = -0.6$ ($\mathcal{M} = 4.5$)[9]. Moreover, as it has been pointed out for the "Toothbrush" cluster (Rajpurohit et al., 2018b), since we expect that the magnetic field is not homogeneous for a projected Mpc-size shock front, we also included a log-normal distribution for the magnetic field B in the downstream region (see Eq. 7 in Rajpurohit et al., 2018b). The best match of our observed and modeled profiles is given by a magnetic field strength of $B_0 = 1$ μG and scatter $\log \sigma = 1.0$. The resulting profiles are shown in the bottom row in Figure 2.10. The flux densities now match reasonably well and the shapes of the profiles are similar to the observed ones. Although, there are still clear deviations for distances larger than 80 kpc. The discrepancy between the toy model and the observed profiles might be attributed to a much more complex shape of the shock front, injection spectral index and efficiency variations across the shock front, and a more complex magnetic field distribution including large scale modes. However, our study, combined with the recent results by Rajpurohit et al. (2018b) on the "Toothbrush" relic, seems to support the importance of the combination of projection effects and magnetic field variation in the downstream region to explain the cooling of the electrons.

Origin of the filaments

The existence of filaments/sheets in the northern relic is not completely unexpected, since numerical simulations show that shock surfaces are complex-shaped structures (e.g. Vazza et al., 2012a; Skillman et al., 2013) and the shock Mach numbers are not constant. In combination with a highly non-linear shock acceleration efficiency (e.g. Hoeft & Brüggen, 2007) this would lead to morphologically complex radio relics, with the radio emission primarily tracing localized regions with higher Mach numbers.

Another possibility is that the sheets trace magnetic structures. If they are produced by strands of strong magnetic fields this would imply strong magnetic fields with coherence lengths of Mpc in cluster outskirts. This would constitute a strong constraint on magnetogenesis models. A rough estimate of the amount of magnetic field (B) variation necessary to explain the radio flux density variations along the relic's length (top panel in Fig. 2.8) is given by (Eq. 4 in Katz-Stone et al., 1993):

$$\frac{S_1}{S_2} = \left(\frac{B_1}{B_2}\right)^{1-\alpha}, \qquad (2.10)$$

where α is, in our case, the injection spectral index, -0.86 (see Tab. 2.5). According to Eq. 2.10, to explain a flux variation of $\sim 55\%$ (i.e. between the flux density peak at ~ 1600 kpc and the plateau between ~ 1100–1400

---

[9]Such choice comes from Eq. 2.8, where $\alpha_{int} = -1.1$ given the 150 MHz and 3.0 GHz integrated fluxes (1550, Hoang et al., 2017, and 56 mJy, respectively).

kpc[10], i.e. $S_2 \approx 0.22$ and $S_1 \approx 0.1$ mJy at 1.4 GHz, see top panel in Fig. 2.8), we need a magnetic field variation of about 30%. The possible influence of the magnetic field on the radio emission can be addressed via polarization measurements. A Faraday Rotation Measure analysis for CIZA2242 will be presented in an upcoming paper.

Another possibility to generate non-uniform radio emission is in the re-acceleration scenario. In this case, brightness variations might reflect initial variations in the distribution of fossil radio plasma. A non-uniform distribution of fossil plasma is to be expected considering the complex morphologies of tailed radio galaxies in clusters.

Observational evidence of filaments in radio relics has been found in instances, for example in A 2256 (Owen et al., 2014) and in 1RXS J0603.3+ 4214 (i.e. the "Toothbrush" cluster, Rajpurohit et al., 2018b). However, with the current data in hand we cannot distinguish between the various scenarios above. It is also possible that the sheet-like, filamentary morphology is due to a combination of two or more effects.

2.5.4. Southern Relic

Our low-resolution images ($> 10''$) show that the southern relic has a complex morphology. Unlike RN, which is characterized by a single arc-like shape at low resolution, this relic is formed by five "arms" (see Fig. 2.2). This complex morphology does not allow us to produce a clear spectral index profile. Thus, we only calculated the radio Mach number from the injection spectral index, following the same procedure as carried out for RN, avoiding the compact sources. We did that at $10''$ resolution, a compromise between resolution and SNR. We follow the relic from RS1 to RS4, including the lobe of source J (see the red boxes in the bottom panel in Fig. 2.11). From the region given by the combination of these boxes, we obtain an injection spectral index of $\alpha_{\mathrm{inj}} = -1.09 \pm 0.05$, which corresponds to a Mach number of $\mathcal{M} = 2.10 \pm 0.08$. However, a clear variation of spectral index values from east to west is seen (top panel in Fig. 2.11). We measure flatter α values at LLS$_{\mathrm{EW}} \lesssim 350$ kpc ($\alpha_{\mathrm{inj},\lesssim 350\mathrm{kpc}} = -0.93 \pm 0.08$ and $\mathcal{M} = 2.36 \pm 0.18$), and steeper values at LLS$_{\mathrm{EW}} \gtrsim 350$ kpc ($\alpha_{\mathrm{inj},\gtrsim 350\mathrm{kpc}} = -1.36 \pm 0.08$ and $\mathcal{M} = 1.19 \pm 0.05$). We notice that the steepest spectral index values are coincident with the location of source J. Around 400 kpc, we measure the steepest spectral index values, coincident with the end of the tail of source J (see Fig. 2.5).

X-ray observations performed with *Suzaku* (Akamatsu et al., 2015) found a Mach number for RS of $1.7^{+0.4}_{-0.5}$. Although this value is comparable within the uncertainties to our radio spectral index derived Mach number, the injection spectral index is affected by the presence of the embedded source J,

---

[10]The flux density peak at ~ 1600 kpc is located in the RN4 filament, while the plateau partly covers both RN3 and RN4. We chose these regions because they represent the strongest flux variation.
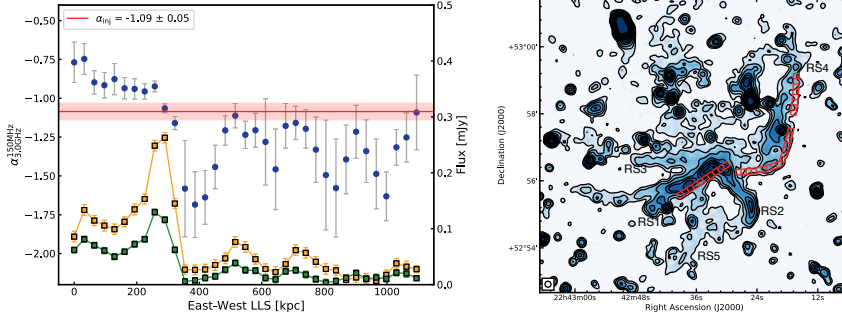
Figure 2.11: Left panel: East-west spectral index profile (blue circles) obtained with a first order polynomial fit and VLA flux densities at 1.5 and 3.0 GHz (orange and green squares, respectively) at 10″-resolution of the southern relic. The filled red region represents the standard deviation associated with the injection spectral index (red solid line). Right panel: 1–4 GHz 10″ resolution image of the southern relic. The red boxes shown the beam-sized region where the spectral indices were extracted.
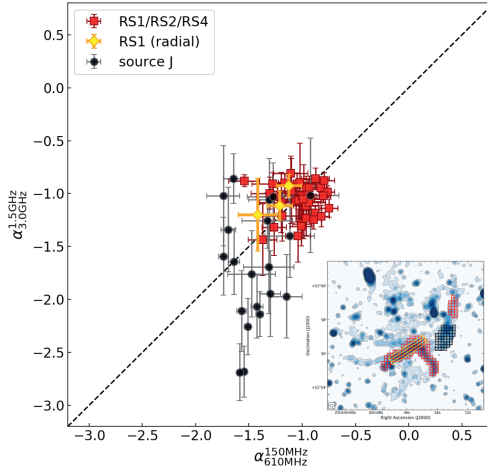
Figure 2.12: Color-color diagram of the southern region of CIZA2242, using the flux densities extracted in 10″×10″ boxes as shown in the inset in the bottom right corner (same images as the bottom panel in Fig. 2.11). Red squares are obtained from the area covered by the RS1, RS2 and RS4 "arms" of the southern relic. The black dots come from the lobe of source J. The yellow diamonds represent the values obtained from the radial binning (yellow annuli in the inset).

which is characterized by a very steep spectral index (see Fig. 2.5). The actual injection spectral index might thus be somewhat flatter.

The spectral index map shows a spectral index steepening from the relic outskirts towards the cluster center (Fig. .2.1). To investigate whether this region is characterized by curved spectra, like RN, we created a cc-diagram using the flux densities extracted in $10'' \times 10''$ boxes (i.e. the beam size) covering RS1, RS2, RS4 and the lobe of source J (see the red and black boxes, respectively, in the inset in the bottom right corner in Fig. 2.12). To keep the values with the best SNR, we selected only flux densities above a threshold of $4\sigma_{\mathrm{rms},\nu}$ (where $\sigma_{\mathrm{rms},\nu}$ the noise of each radio map, see Tab. 2.2). Moreover, we also created a cc-diagram dividing the RS1 "arm" in $10''$-wide annuli (yellow sector in the same inset). Interestingly, we found that all the values for the RS1, RS2 and RS4 regions (red squares in Fig. 2.12), as well as the radial distribution (yellow diamonds in the same Figure), fall along the $\alpha^{610\mathrm{MHz}}_{150\mathrm{MHz}} = \alpha^{3.0\mathrm{GHz}}_{1.5\mathrm{GHz}}$ line. This is somewhat surprising result as curved spectra would be expected due to aging. These results suggest that (i) at each location, there is an actual power law which represents the steady-state solution to the local shock strength, and that shock strength varies throughout the region, or (ii) there is at each location a very broad range of magnetic fields and/or electron loss histories which smear out the underlying spectra, and make them close to power-law. It remains an open question, though, why different power laws at different locations are present for this relic.

2.5.5. A case for fossil plasma re-acceleration?

There are several issues with the DSA model for radio relics. For some relics, the required fraction of energy flux through the shock surface that needs to be transfered to CR electrons to explain the observed radio power is too large (e.g. Vazza & Brüggen, 2014; van Weeren et al., 2016). The absence of relic emission at some shocks (e.g. Shimwell et al., 2014) is also puzzling. In addition, in a few cases, discrepancies have been found between the Mach numbers measured from X-ray observations and those calculated from the radio spectral index (e.g. van Weeren et al., 2016). The re-acceleration of fossil electrons would address some of these problems.

CIZA2242 represents an interesting case to study the interplay between the diffuse radio emission and the tailed radio galaxies. We propose that Source J, which is completely embedded in the southern relic RS, presents a possible case of shock re-acceleration because: (i) there is a morphological connection between the tailed radio galaxy, source J, and the relic. We find that source J consists of an active radio core (J1) and a single jet that ends up in a lobe-like structure (right panel in Fig. 2.6(e)); (ii) A *Suzaku* analysis revealed the presence of a temperature jump roughly at the location of RS (Akamatsu et al., 2015); finally, (iii) the spectral index map displays a steepening from the radio core (J1) through the radio lobe and then a flattening at the cluster shock (right panel in Fig. 2.6(e)). Also, the cc-diagram for the lobe of source J (black dots in Fig. 2.12) shows
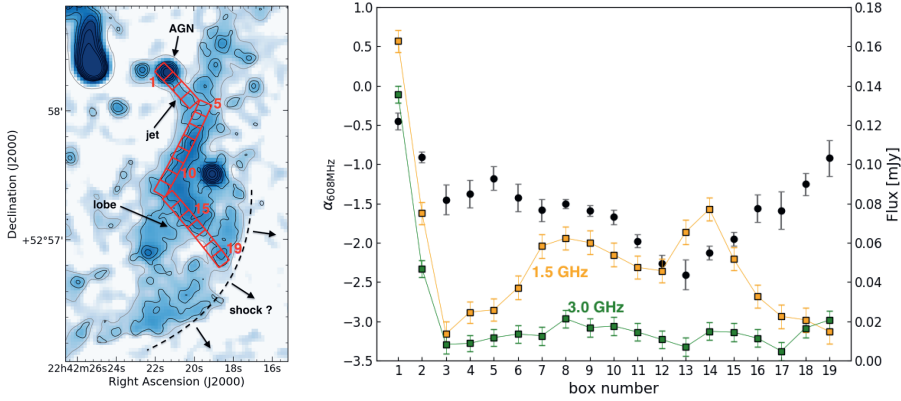
Figure 2.13: Left panel: 1–4 GHz 5″ resolution image of source J. We overlay the 5″ (gray) and 2.5″ (black) resolution radio contours, at 3σ and $3\sigma \times \sqrt{(1, 4, 16, \ldots)}$, respectively. Right panel: Spectral index profile at 608 MHz, derived by a second order polynomial fit (Eq. 2.6), across source J obtained from the red boxes in the left panel. The yellow and green squares trace the VLA L- (1.5 GHz) and S-band (3.0 GHz) flux densities across the radio tail, respectively.

values both on and below the $\alpha^{610\mathrm{MHz}}_{150\mathrm{MHz}} = \alpha^{3.0\mathrm{GHz}}_{1.5\mathrm{GHz}}$ line. Radio galaxy's lobes are indeed expected to have curved spectra, described by a JP model (or modification thereof), since electrons experience aging going further from the AGN. Then if the shock passes through the lobe it could re-accelerate or re-energize the electrons. In this case, electrons with steeper spectra than the "critical" spectral index associated with the shock will be flattened out and "moved" towards the power law line. Such flattening has been observed recently in the Abell 3411-3412 system (van Weeren et al., 2017a), MACS J0717.5+3745 (van Weeren et al., 2017b) and Abell 1033 (de Gasperin et al., 2017).

Modeling the spectral index change with re-acceleration

Following Kang et al. (2017), we attempt to model the observed spectral index change from the lobe of source J to the relic RS[11]. We assume a region of fossil plasma that is run over up by a spherically expanding shock propagating through the cluster outskirts. To obtain the spectral index distribution across the relic, we extract the flux densities at 5″ resolution, following the shape of the tail (left panel in Fig. 2.13). We consider an energy spectrum of the fossil electrons following a power-law distribution with exponential cutoff, of the type:

---

[11]See Kang & Ryu (2015) for the geometry of the cloud containing the fossil electrons.

$$f(\gamma_e) \propto \gamma_e^{-s} \exp\left[-\left(\frac{\gamma_e}{\gamma_{e,c}}\right)^2\right], \tag{2.11}$$

where $s = 1 - 2\alpha$ is the injection index from the AGN and $\gamma_{e,c}$ the cutoff Lorentz factor. We use a typical AGN injection spectral index, i.e. $\alpha = -0.75$ (e.g. Mullin et al., 2008), corresponding to $s = 2.5$. The spectral index where the tail meets the relic (box 13), i.e. $\alpha = -2.4$ at 608 MHz (right panel in Fig. 2.13), gives a cutoff Lorentz factor of $\gamma_{e,c} = 4.2 \times 10^3$. This parameter mimics the steepening of the fossil plasma along the radio tail, and is expected to change with distance from the AGN. We set the post-shock temperature to 9.0 ± 0.6 keV, based on the *Suzaku* data (Akamatsu et al., 2015), and assume an "extension angle" of $\psi = 12°$ (van Weeren et al., 2017a). We also included post-shock turbulent re-acceleration with $\tau_0 = 10^8$ yrs (for details see Kang et al., 2017), which prevent the faster steepening behind the shock (purple dotted line in the top panel of Fig. 2.14). The pre-shock magnetic field was assumed to be 2.2 μG, similar to the magnetic field in the lobes of radio galaxies, leading to a post-shock value of 4.9 μG.

The post-shock profile of the radio spectral index depends mainly on the shock Mach number and the magnetic field strength (top panel Fig. 2.14). Our best-fit model reproduces the spectral change from box 13 (i.e. just before the re-acceleration) to box 19 (i.e. immediately after re-acceleration behind the shock) by assuming a sonic Mach number of $\mathcal{M}_s = 2.4$, corresponding to a pre-shock temperature of 3.4 keV[12]. Such Mach number is chosen to match the radio spectral index $\alpha_{608\ \text{MHz}} \approx -0.9$ at the relic edge (box 19 in Fig. 2.13). This value is not consistent with the *Suzaku* analysis (i.e. $\mathcal{M} = 1.7^{+0.4}_{-0.3}$ and $T_{\text{pre}} = 5.1^{+1.5}_{-1.2}$ keV, respectively), although the Mach number in the latter case could be underestimated because of instrumental limitations. It is also true, though, that since the fossil electrons are expected to cool due to Coulomb and synchrotron/IC losses advecting away from the AGN core, assuming a constant value for $\gamma_{e,c}$ is a simplification. However, $\gamma_{e,c}$ would not change significantly over ~ 100 kpc scales, i.e. the length of the re-acceleration region, since the radiative cooling time scale for electrons with $\gamma < 4.2 \times 10^3$ is $t_{\text{cool}} > 2.2 \times 10^8$ yr, which is much longer than the shock crossing time (i.e. $\approx 6.7 \times 10^7$ yr). Additionally, it has been shown that changes in the $\gamma_{e,c}$ value do not affect significantly the energy spectrum of post-shock electrons, since the re-acceleration process "erases" most of the spectral information from the seed fossil particles (see also Supplementary Figure 10 in van Weeren et al., 2017a). Last but not least, the complex radio tail morphology with a superposition of electron populations could also be the reason of the $\mathcal{M}_{\text{radio}}/\mathcal{M}_{\text{X-ray}}$ discrepancy.

---

[12] $\frac{T_{\text{post}}}{T_{\text{pre}}} = \frac{5\mathcal{M}^4 + 14\mathcal{M}^2 - 3}{16\mathcal{M}^2}$, see (Landau & Lifshitz, 1959).
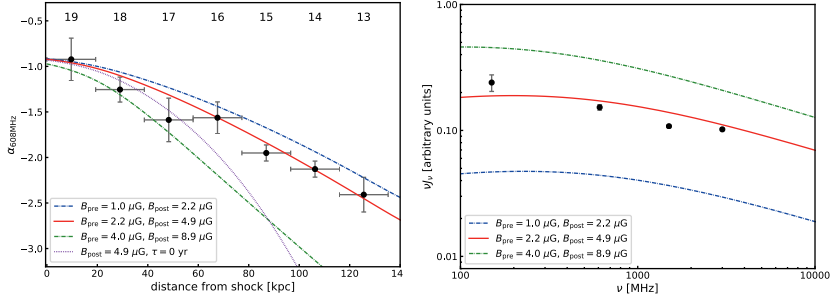
Figure 2.14: Left panel: Spectral index profile calculated at 608 MHz with a second order polynomial fit (Eq. 2.6) from the shock position to the region just before the re-acceleration (boxes from 19 to 13 in the left panel in Fig. 2.13). Right panel: Volume-integrated spectrum of the shock region, obtained by assuming a constant pre-shock electron density distribution. Lines display models for different pre- and post-shock magnetic fields as indicated in the legend of the figures.

For the re-acceleration, the radio flux density profile across the relic's width and the integrated spectrum also depend on the spatial variation of fossil electrons. Generally, the radio emission is expected to be the brightest at the approximate shock location, while it fades downstream of the shock because of energy losses. Instead, we find an opposite trend, with the highest fluxes decreasing towards the shock front (see left panel Fig. 2.13, from box 13 to 19). However, the model can reproduce reasonably well the observed volume-integrated spectrum (red solid line in the bottom panel of Fig. 2.14). Likely, the shock downstream region is "contaminated" by radio plasma from the lobe of source J, which is embedded in the relic. The failure to accurately predict the flux profiles in the shock downstream region highlights the difficulties of modeling complex AGN lobe emission and its interactions with a shock, in addition to particle re-acceleration in the same general region.

2.5.6. The relation between tailed radio galaxies and diffuse cluster sources

As discussed above, RS, or at least part of RS, seems to be related to the tailed radio source J. However, this could not be the unique case in CIZA2242, which contains a number of complex shaped relics (R1, R2, I, R3, and RS) and tailed radio sources (sources C, D, F, and H). In this section, we speculate that some of the other diffuse relics are also related to AGN fossil plasma that has been revived, either by re-acceleration or solely by adiabatic compression.

The toroidal morphology of R2, similarly to the ones found in Slee et al.

(2001), and the large attached filament I (see Fig. 2.3) could be the result of a fossil plasma lobe/tail that has been compressed by a merger shock wave. Source G could be another example of an old radio galaxy lobe which has been revived by a merger shock. Additional evidence of revived fossil plasma is provided by the several tailed radio sources whose tails suddenly brighten (e.g. source H), suggesting that some re-energizing of the lobe electron population due to adiabatic compression and/or re-acceleration (e.g. Pfrommer & Jones, 2011; Cuciti et al., 2018; de Gasperin et al., 2017) might have taken place, and implying we are witnessing the birth of other radio relics or radio "phoenices". Moreover, recent numerical simulations (Jones et al., 2017) show that in the presence of a "cross wind", resulting from a passing shock, jet plasma could be revived and displaced, producing the "bottle-neck" morphology we see for the radio tails C, D and F.

CIZA2242 thus seems to display the entire range of evolutionary stages of AGN fossil plasma and relic formation, from classical NAT/HT sources (E and K1), to currently active tailed radio sources with signs of revived lobes (C, D, F), active tailed source connected to a relic (J, RS), patch of fossil plasma (G), and large Mpc-sized complex shaped diffuse sources (RS, R2-I). Whether fossil plasma and re-acceleration are required to produce the main northern relic remains an open question though. Despite the fact the formation scenario for the northern relic remains unclear, our observations do imply that to produce realistic models of diffuse cluster radio emission, fossil plasma will need to be included in simulations.

2.6.   Conclusions

We have presented deep 1–4 GHz VLA observations of the galaxy cluster CIZA J2242.8+5301 ($z = 0.1921$). This cluster is one of the best examples of a merging system, hosting two Mpc-size relics and several other diffuse radio sources. Our images reached a resolution of $2.1'' \times 1.8''$ and $0.8'' \times 0.6''$ and a noise level of 3.8 μJy beam^{-1} and 2.7 μJy beam^{-1} at 1.5 and 3.0 GHz respectively. These observations were combined with existing GMRT 610 MHz and LOFAR 150 MHz data (van Weeren et al., 2010; Stroe et al., 2013; Hoang et al., 2017) to carry out a radio continuum and spectral study of the cluster. The main results of our study are summarized below:

- The high-resolution images reveal that the northern relic (RN) is not a continuous structure, but is broken up into several filaments with a length of $\sim 200 - 600$ kpc each. Moreover, we detect and characterize additional radio emission north of RN, labeled as R5.

- In agreement with previous studies, we find a trend of North-South spectral steepening for the northern relic, indicative of IC and syn-

chrotron energy losses in the downstream region of a shock. We measure an injection spectral index at the shock front from the radio map of -0.86 ± 0.05, corresponding to a Mach number of $\mathcal{M} = 2.58 \pm 0.17$. Although this value is consistent with the Mach number estimated from X-ray studies, a color-color diagram shows a small amount of spectral curvature at the relic's northern edge indicating mixing of emission with different spectral ages, possibly due to projection effects. This suggests that the true injection spectral index is slightly flatter ($\alpha \sim -0.7$).

- The low-resolution VLA images reveal that the southern relic (RS) has a complex morphology, characterized by the presence of five "arms". The origin of this complex morphology is unclear, but it might be partly explained by the presence of AGN fossil plasma that has been revived by the passage of a shock wave. Interestingly, the color-color diagram revealed no curvature in the downstream region of the southern relic, which can be explained either by a sum of power-law spectra with different α_{inj} at different locations or smearing of broad range of magnetic fields and/or electron loss histories.

- We identify source J, a tailed radio galaxy embedded in RS, as possible source of fossil radio plasma. Our spectral index maps suggest that old plasma from the lobe of source J is re-accelerated. We attempted to model the flattening of the spectral index from the lobe to the relic RS. We find that a $\mathcal{M} = 2.4$ is compatible with the observed spectral index change.

- The cluster contains several tailed radio galaxies, which show disturbed morphologies likely due to the interaction between the radio plasma, ICM, and the merger event. In addition, the cluster contains a number of complex diffuse radio sources that seem to be related to plasma from tailed radio sources (source G, RS, I, R2). The range in morphologies of tailed-radio sources, strong signs of interactions with the ICM, and presence of nearby complex-shaped relics suggest that fossil plasma from cluster radio galaxies plays an important role in the formation of (at least some) diffuse radio sources. To produce realistic models of diffuse cluster radio emission, this fossil plasma will need to be included in simulations.

.1. Additional radio and optical images

Here, we present additional radio and optical images of the galaxy cluster (Figures .1.1 and .1.2).

Figure .1.1: S-band (3.0 GHz) VLA high-resolution image of CIZA2242. To aid the visibility of the sources, we smoothed the image with a 3-pixel (1.5″) Gaussian. The black arrows highlights the "broken" nature of the radio tails. The map has a noise of $\sigma_{\mathrm{rms}} = 2.7$ μJy beam^{-1}.

.2. Additional spectral index and spectral index uncertainty maps

Here, we present additional spectral index and spectral index uncertainty maps (Figures .2.1 to .2.3).
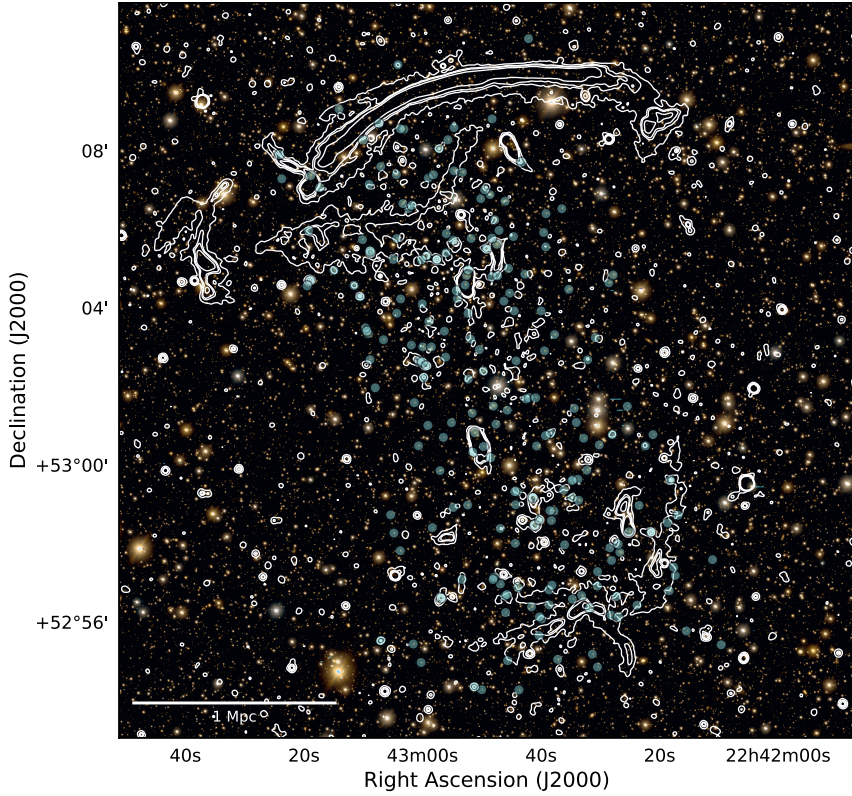
Figure .1.2: Subaru *gri* composite optical image (Dawson et al., 2015; Jee et al., 2015) with the 1–2 GHz radio contours (5″ resolution) overlaid. Light-blue dots indicate the spectroscopically confirmed cluster galaxies, with $0.17 \leq z \leq 0.2$ (Dawson et al., 2015).
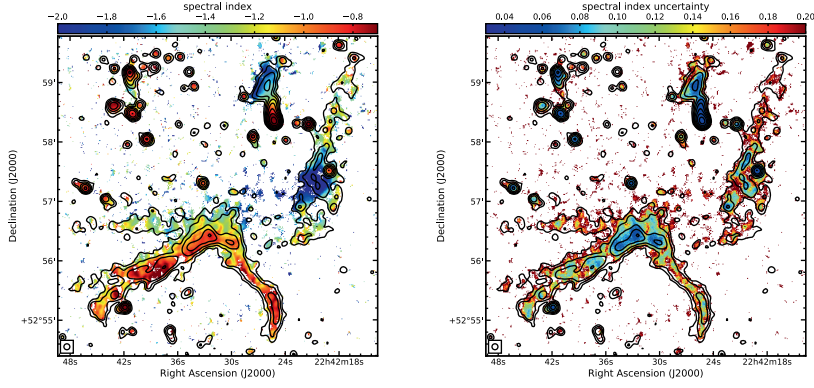
Figure .2.1: 5″ spectral index map (left panel) and the correspondent uncertainty map (right panel) of the southern relic obtained between 145 MHz, 610 MHz, 1.5 GHz and 3.0 GHz. The radio contours are from the combined L- and S-band observation, leveled in the same way as the top right panel in Fig. 2.3.
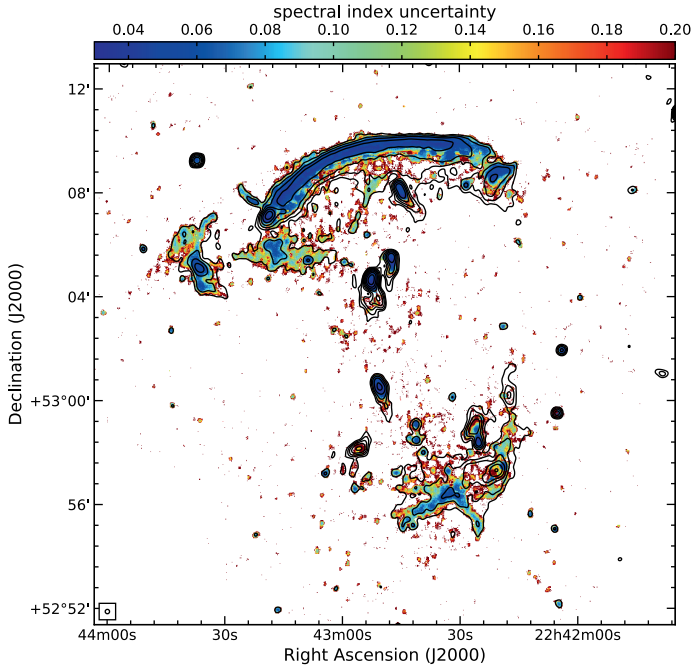
Figure .2.2: The correspondent spectral index uncertainty map of Fig. 2.4.

Figure .2.3: The correspondent spectral index uncertainty maps of the left panels in Fig. 2.6. From the top left to the bottom right: source B, C and D, E, H, F and J, G and K1-4.

CHAPTER

3

EVIDENCE FOR A MERGER INDUCED SHOCK WAVE IN ZWCL 0008.8+5215 WITH *CHANDRA* AND *SUZAKU*

G. Di Gennaro, R.J. van Weeren, F. Andrade-Santos, H. Akamatsu, S.W. Randall et al. *Astrophysical Journal*, 873, 64 (2019)

Abstract. We present the results from new deep *Chandra* ($\sim$ 410 ks) and *Suzaku* ($\sim$ 180 ks) observations of the merging galaxy cluster ZwCl 0008.8+ 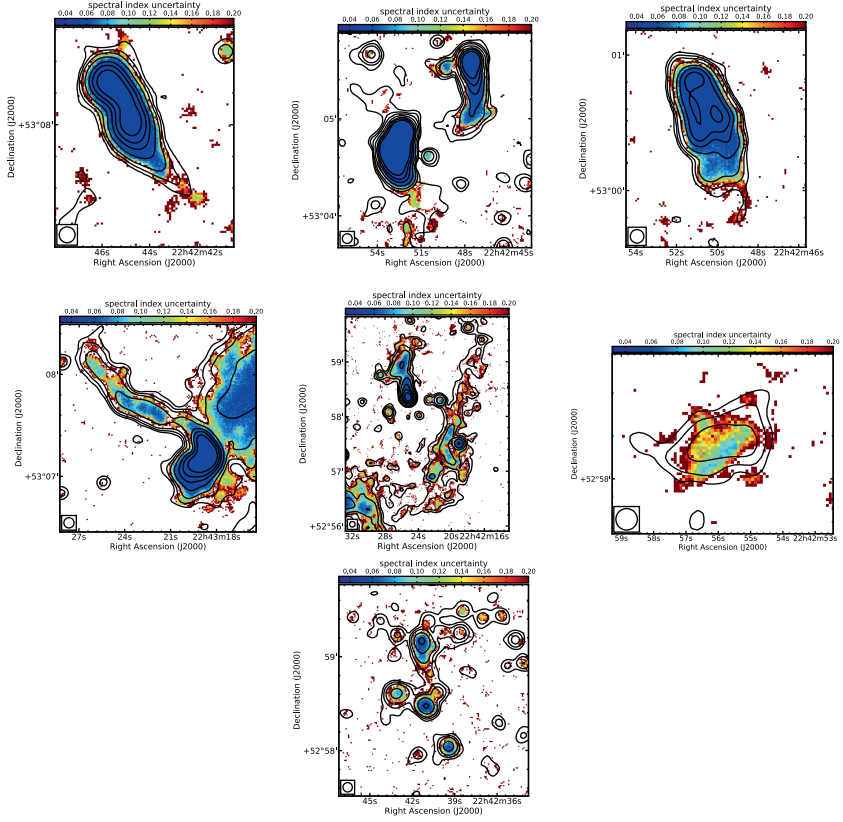5215 (z = 0.104). Previous radio observations revealed the presence of a double radio relic located diametrically west and east of the cluster center. Using our new *Chandra* data, we find evidence for the presence of a shock at the location of the western relic, RW, with a Mach number $\mathcal{M}_{S_X} = 1.48^{+0.50}_{-0.32}$ from the density jump. We also measure $\mathcal{M}_{T_X} = 2.35^{+0.74}_{-0.55}$ and $\mathcal{M}_{T_X} = 2.02^{+0.74}_{-0.47}$ from the temperature jump, with *Chandra* and *Suzaku* respectively. These values are consistent with the Mach number estimate from a previous study of the radio spectral index, under the assumption of diffusive shock acceleration ($\mathcal{M}_{RW} = 2.4^{+0.4}_{-0.2}$). Interestingly, the western radio relic does not entirely trace the X-ray shock. A possible explanation is that the relic traces fossil plasma from nearby radio galaxies which is re-accelerated at the shock. For the eastern relic we do not detect an X-ray surface brightness discontinuity, despite the fact that radio observations suggest a shock with $\mathcal{M}_{RE} = 2.2^{+0.2}_{-0.1}$. The low surface brightness and re-duced integration time for this region might have prevented the detection. *Chandra* surface brightness profile suggests $\mathcal{M} \lesssim 1.5$, while *Suzaku* tem-perature measurements found $\mathcal{M}_{T_X} = 1.54^{+0.65}_{-0.47}$. Finally, we also detect a merger induced cold front on the western side of the cluster, behind the shock that traces the western relic.

3.1.   Introduction

Galaxy clusters grow via mergers of less massive systems in a hierarchical process governed by gravity (e.g. Press & Schechter, 1974; Springel et al., 2006). Evidence of energetic ($\sim 10^{64}$ erg) merger events has been revealed, thanks to the *Chandra*'s high-angular resolution (i.e. 0.5″), in the form of sharp X-ray surface brightness edges, namely *shocks* and *cold fronts* (for a review see Markevitch & Vikhlinin, 2007). Both shocks and cold fronts are contact discontinuities, but differ because of the sign of the temperature jump and because the pressure profile is continuous across a cold front. Moreover, while large-scale shocks are detected only in merging systems (e.g. Markevitch et al., 2002, 2005; Markevitch, 2006b; Russell et al., 2010; Macario et al., 2011; Ogrean et al., 2016; van Weeren et al., 2017a), cold fronts have been commonly detected also in cool-core clusters (e.g. Mazzotta et al., 2001; Markevitch et al., 2001, 2003; Sanders et al., 2005; Ghizzardi et al., 2010). Shocks are generally located in the cluster outskirts, where the thermal intracluster medium (ICM) emission is faint. Hence they are difficult to detect. Constraints on the shock properties, i.e., the temperature jump, can be provided by the *Suzaku* satellite due to its very low background (though its angular resolution is limited, i.e. 2 arcmin; e.g. Akamatsu et al., 2015). Other complications arise when shocks and cold fronts are not seen edge-on, i.e., the merger axis is not perfectly located in the plane of the sky. In such a case, projection effects reduce the surface brightness jumps, potentially hiding the discontinuity.

Merger events can also be revealed in the radio band, via non-thermal synchrotron emission from diffuse sources not directly related to cluster galaxies. Indeed, part of the energy released by a cluster merger may be used to amplify the magnetic field and to accelerate relativistic particles. Results of such phenomena are the so-called *radio relics* and *halos*, depending on their position in the cluster and on their morphological, spectral and polarization properties (for reviews see Feretti et al., 2012; Brunetti & Jones, 2014).

ZwCl0008.8+5215 (hereafter ZwCl0008, z = 0.104, Golovich et al., 2017) is an example of galaxy cluster whose merging state was firstly observed in the radio band. Giant Meterwave Radio Telescope (GMRT) at 240 and 610 MHz and the Westerbrook Synthesis Radio Telescope (WSRT) observations in the 1.4 GHz band revealed the presence of a double radio relic, towards the east and the west of the cluster center (van Weeren et al., 2011b). The radio analysis, based on the spectral index, suggests a weak shock, with Mach numbers $\mathcal{M} \sim 2$. Interestingly, no radio halo has been detected so far in the cluster, despite its disturbed dynamical state (Bonafede et al., 2017). A recent optical analysis with the Keck and Subaru telescopes showed a very well defined bimodal galaxy distribution, confirming the hypothesis of a binary merger event (Golovich et al., 2017). This analysis, in combination with polarization studies at 3.0 GHz

(Golovich et al., 2017), 4.85 and 8.35 GHz (Kierdorf et al., 2017), and simulations (Kang et al., 2012), sets an upper limit to the merger axis of 38° with the respect to the plane of the sky. The masses of the two sub-clusters, obtained via weak lensing analysis, are $M_{200,1} = 5.73^{+2.75}_{-1.81} \times 10^{14}$ $M_{\odot}$ and $M_{200,2} = 1.21^{+1.43}_{-0.63} \times 10^{14}$ $M_{\odot}$, corresponding to a mass ratio of about 5. N-body/hydrodynamical simulations by Molnar & Broadhurst (2018) suggested that the cluster is currently in the outgoing phase, with the first-core crossing occurred less then 0.5 Gyr ago.

The detection of radio relics strongly suggests the presence of shock fronts (e.g. Giacintucci et al., 2008; van Weeren et al., 2010, 2011a; de Gasperin et al., 2015; Pearce et al., 2017). A previous shallow (42 ks) *Chandra* observation revealed the disturbed morphology of the ICM, but could not unambiguously confirm the presence of shocks (Golovich et al., 2017). In this paper, we present results from deep *Chandra* observations, totaling ~ 410 ks, of the galaxy cluster. We also complement the analysis with *Suzaku* observations, totaling ~ 183 ks.

The paper is organized as follows: in Sect. 3.2 we describe the *Chandra* and *Suzaku* observations and data reduction; a description of the X-ray morphology and temperature map of the cluster, based on the *Chandra* observations, are provided in Sect. 3.3; X-ray surface brightness profiles and temperature measurements are presented in Sect. 3.4. We end with a discussion and a summary in Sects. 3.5 and 3.6. Throughout the paper, we assume a standard ΛCDM cosmology, with $H_0 = 70$ km s^{-1} Mpc^{-1}, $\Omega_m = 0.3$ and $\Omega_{\Lambda} = 0.7$. This translates to a luminosity distance of $D_L = 483.3$ Mpc, and a scale of 1.85 kpc/″ at the cluster redshift, $z = 0.104$. All errors are given as 1σ.

3.2. Observations and data reduction

3.2.1. *Chandra* observations

We observed ZwCl 0008 with the Advanced CCD Imaging Spectrometer (ACIS) on *Chandra* between 2013 and 2016 for a total time of 413.7 ks. The observation was split into ten single exposures (see the ObsIDs list in Table 3.1). The data were reduced using the `chav` software package[1] with `CIAO v4.6` (Fruscione et al., 2006), following the processing described in Vikhlinin et al. (2005) and applying the `CALDB v4.7.6` calibration files. This processing includes the application of gain maps to calibrate photon energies, filtering out counts with ASCA grade 1, 5, or 7 and bad pixels, and a correction for the position-dependent charge transfer inefficiency (CTI). Periods with count rates with a factor of 1.2 above and 0.8 below the mean count rate in the 6–12 keV band were also removed. Standard

---

[1] http://hea-www.harvard.edu/~alexey/CHAV/
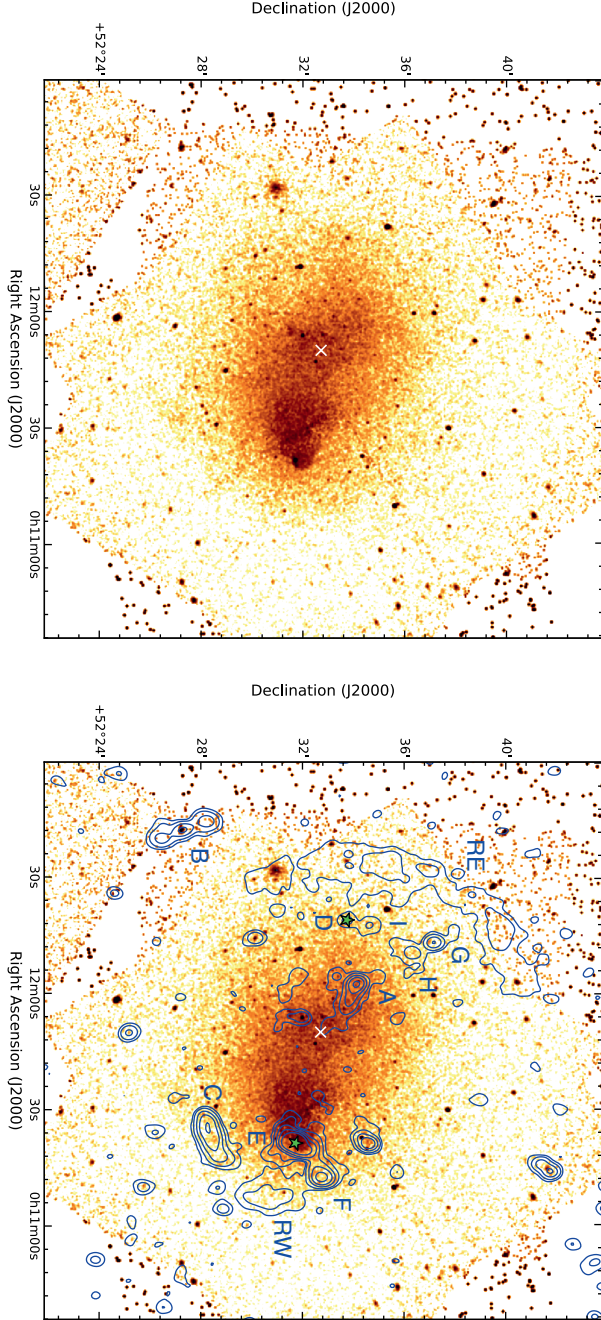
Figure 3.1: Left panel: background-subtracted, vignetting- and exposure-corrected 0.5–2.0 keV *Chandra* image of ZwCl0008 smoothed with a 2D Gaussian with $\sigma = 2''$ (i.e. 1 image pixel). Right panel: the same as the left panel with the 1.4 GHz WSRT radio contours at $4\sigma_{\mathrm{rms}} \times [1, 4, 16, \ldots]$ overlaid; the noise level of the radio map is $\sigma_{\mathrm{rms}} = 27\ \mu\mathrm{Jy\ beam^{-1}}$ (van Weeren et al., 2011b). Radio sources in the right panel have been labeled following van Weeren et al. (2011b), and the two bright central galaxies (BCGs) are identified by the two green stars. The cluster center is identified in the two panels by the white cross.

Table 3.1: *Chandra* ObsIDs list.

ObsID	Obs. Date [yyyy-mm-dd]	CCD on	Exp. Time [ks]	Filtered Exp. Time [ks]
15318	2013-06-10	0, 1, 2, 3, 6	29.0	28.9
17204	2015-03-27	0, 1, 2, 3, 6, 7	6.4	5.6
17205	2015-03-17	0,1, 2, 3, 6, 7	6.4	5.9
18242	2016-11-04	0, 1, 2, 3	84.3	83.9
18243	2016-10-26	0, 1, 2, 3, 6, 7	30.6	30.2
18244	2016-10-22	0, 1, 2, 3, 6	31.7	31.2
19901	2016-10-17	0, 1, 2, 3, 6	31.8	31.5
19902	2016-10-19	0, 1, 2, 3, 6	65.7	65.2
19905	2016-10-29	0, 1, 2, 3, 6, 7	37.8	37.6
19916	2016-11-05	0, 1, 2, 3	90.2	90.1

Note:

CCD from 0 to 3: ACIS-I; CCD from 4 to 9: ACIS-S. Back Illuminated (BI) chips: ACIS-S1 and ACIS-S3 (CCD 5 and 7, respectively).

Table 3.2: *Suzaku* observations and exposure times.

Sequence ID	Obs. Date [yyyy-mm-dd]	Exp. Time [ks]	Filtered Exp. Time [ks]
809118010	2014-07-06	119.8	98.6
809117010	2014-07-09	102.3	84.6

blank-sky files were used for background subtraction. The resulting filtered exposure time is 410.1 ks (i.e. 3.6 ks were discarded).

The final exposure corrected image was made in the 0.5–2.0 keV band by combining all the ObsIDs and using a pixel binning of a factor of four, i.e. 2″. Compact sources were detected in the 0.5–7.0 keV band with the CIAO task wavdetect using scales of 1, 2, 4, 8 pixels and cutting at the 3σ level. Those compact sources were removed from our spectral and spatial analysis.

3.2.2.   *Suzaku* **observations**

Suzaku observations of ZwCl0008 were taken on 6 and 9 July 2014, with two different pointings, to the east to the west of the cluster center (IDs: 809118010 and 809117010, respectively; see Table 3.2). Standard data reduction has been performed: data-screening and cosmic-ray cut-off ri gidity (COR2 > 6 GV to suppress the detector background have been applied (see Akamatsu et al., 2015, 2017; Urdampilleta et al., 2018, for a detailed description of the strategy). We made use of the high-resolution *Chandra* observation for the point source identification. The final cleaned exposure times are 99 and 85 ks (on the east and west pointing, respectively).

3.3. Results

3.3.1. Global properties

In the left panel in Fig. 3.1, we present the background-subtracted, vignetting- and exposure-corrected 0.5–2.0 keV *Chandra* image of ZwCl0008.

The X-ray emission shows a particularly disturbed morphology: it is elongated from east to west, confirming the merger scenario proposed in the previous studies (e.g. van Weeren et al., 2011b; Golovich et al., 2017; Molnar & Broadhurst, 2018). The bright, dense remnant core originally associated with the wester BCG lies westward from the cluster center[2]. It has been partly stripped of its material forming a tail of gas towards the north-east. It appears to have substantially disrupted the ICM of the eastern sub-cluster and shows a sharp, bullet-like surface brightness edge, similarly to the one found in the Bullet Cluster (Markevitch et al., 2002; Markevitch, 2006b) and in Abell 2126 (Russell et al., 2010, 2012). As was also pointed out by Golovich et al. (2017), the remnant core is also coincident with the BCG of the western sub-cluster (marked by a green star symbol in the right panel of Fig. 3.1). This is not the case for the eastern sub-cluster's BCG, which is clearly offset from the X-ray peak (green star in the east in the right panel in Fig. 3.1). A surface brightness discontinuity, extending about 1 Mpc, is seen in the western part of the cluster (left panel in Fig. 3.1). The location of the western edge is coincident with one of the two radio relics previously detected. However, this relic (hereafter RW, van Weeren et al., 2011b) appears to have a much smaller extent than the X-ray discontinuity. To the east, the other radio relic (hereafter RE, van Weeren et al., 2011b) is located, symmetrically to RW with respect to the cluster center. This relic is ∼ 1.4 Mpc long, but no clear association with an X-ray discontinuity has been found (see right panel in Fig. 3.1).

We determined the X-ray properties of the whole cluster by extracting the spectrum from a circular region with a radius of 0.9 Mpc (approximately R_{500}, see Golovich et al., 2017) centered between the two BCGs (see the black dashed circle in the right panel in Fig. 3.3). The cluster spectrum was fitted in the 0.7–7.0 keV energy band with `XSPEC v12.9.1u` (Arnaud, 1996). We used a `phabs*APEC` model, i.e. a single temperature (Smith et al., 2001) plus the absorption from the hydrogen column density (N_H) of our Galaxy. We fixed the abundance to $A = 0.3$ $Z_\odot$ (abundance table of Lodders et al., 2009) and $N_H = 0.311 \times 10^{22}$ cm^{-2}[3]. The value of Galactic absorption takes the total, i.e. atomic (HI) and molecular (H$_2$), hydrogen column density into account (Willingale et al., 2013). Due to the large number of counts in the cluster, the spectrum was grouped to have a minimum of 50 counts per bin, and the χ^2 statistic was adopted. Stan-

---

[2]The cluster center is taken to be equidistant between the two BCGs, i.e. RA = $0^h 11^m 50^s$.024 and DEC = +52°32′37″.98, J2000 (see white cross in Fig. 3.1).

[3]Calculation from http://www.swift.ac.uk/analysis/nhtot/
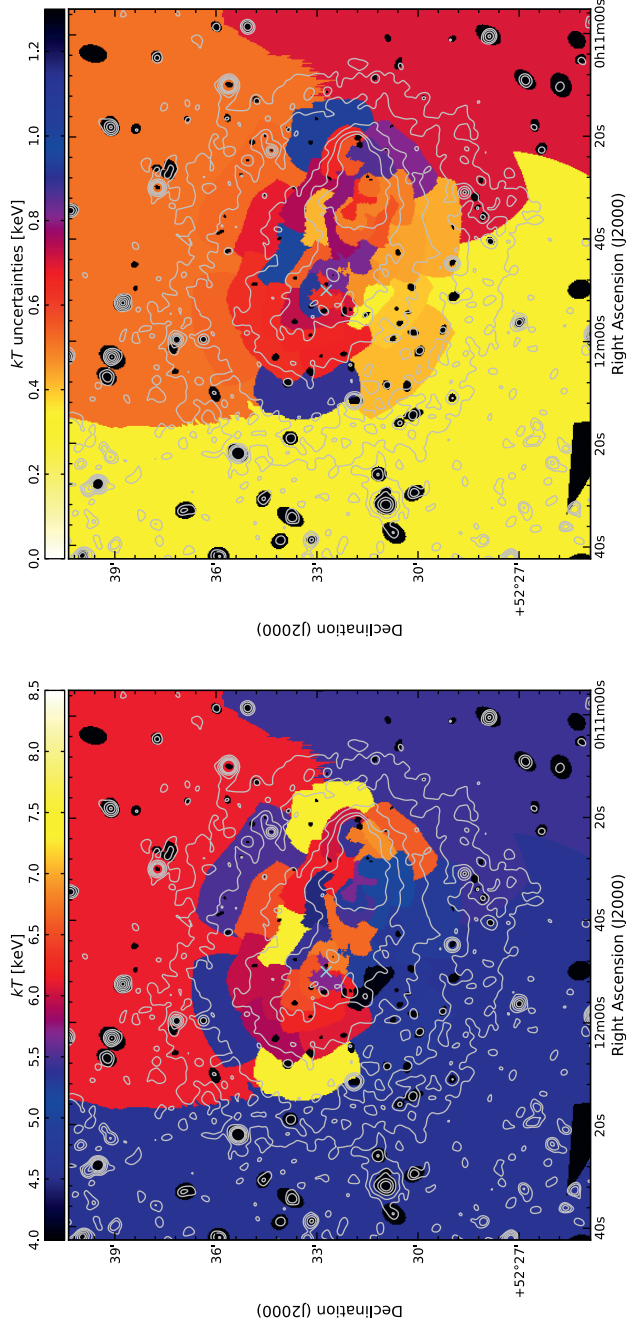
Figure 3.2: Temperature map (left) and the relative uncertainties (right) of ZwCl0008. Each region has a S/N = 40. Black ellipses represent the compact sources excluded from our spectral and spatial analysis. The cyan cross displays the cluster center (as Fig. 3.1). X-ray contours (gray) are drawn at $[1.2, 2, 2.4, 4.8, 8.2, 12] \times 10^{-6}$ photons cm^{-2} s^{-1}.

dard blank-sky background was used and subtracted from the spectrum of each ObsID.

We found a global cluster temperature and an unabsorbed luminosity[4] of $kT_{500} = 4.83 \pm 0.06$ keV and $L_{[0.1-2.4 \text{ keV}],500} = 1.12 \pm 0.09 \times 10^{44}$ erg s^{-1}, respectively. We also repeated the fit, leaving N_H free to vary (while the abundance was kept fixed). A resulting temperature of $kT_{500} = 4.50 \pm 0.10$ keV and column density of $N_H = 0.342 \pm 0.007 \times 10^{22}$ cm^{-2} were found, consistent with the previous results. Our analysis also agree with the results by Golovich et al. (2017)[5].

3.3.2. Temperature map

We used `CONTBIN` (Sanders, 2006) to create the temperature map of ZwCl 0008. We divided the cluster into individual regions with a signal-to-noise ratio (S/N) of 40. As for the calculation of the global temperature, we removed the contribution of the compact sources, and performed the fit with `XSPEC12.9.1u` in the 0.7–7.0 keV energy band. The same parameters as in Sect. 3.3.1 were used (i.e. $A = 0.3$ Z$_\odot$ and $N_H = 0.311 \times 10^{22}$ cm^{-2}), and we assumed χ^2 statistics. The resulting temperature map, and the corresponding uncertainties, are displayed in Fig. 3.2 (left and right panel, respectively).

The disturbed morphology of the cluster is highlighted by the temperature variation in the different regions. Overall, we found that the southeastern part of the cluster appears to have lower temperatures than the northwestern one ($kT_{SE} \sim 4.5$ keV and $kT_{NW} \sim 6.5$ keV). We measure a region of cold gas ($kT \sim 5.5$ keV), in coincidence with the bullet, and a hot region ($kT \sim 7.0$ keV) ahead of it, westward in the cluster outskirts. This signature is suggestive of the presence of a cold front. Unfortunately, the S/N required for the temperature map is too high for the identification of any discontinuity at the location of the western outermost edge we see in Fig. 3.1. Additional hot regions ($kT \sim 7.5$ keV) are found eastward and northwestward of the cluster center.

3.4. A search for shocks and cold front

3.4.1. Characterization of the discontinuities

The X-ray signatures described in Section 3.3.1, and displayed in Fig. 3.1, are characteristic of a cluster merger event. To confirm the presence of sur-

---

[4]Since we are fitting simultaneously different ObsID observations, we use the longest exposure ObsID (i.e. 19916, see Table 3.1) to obtain the cluster luminosity.

[5]Golovich et al. (2017) found $kT_{500} = 4.9 \pm 0.13$ keV, using $A = 0.3$ Z$_\odot$ and $N_H = 0.201 \times 10^{22}$ cm^{-2} fixed, with N_H the weighted average value from the Leiden/Argentine/Bonn (LAB) survey (Kalberla et al., 2005).
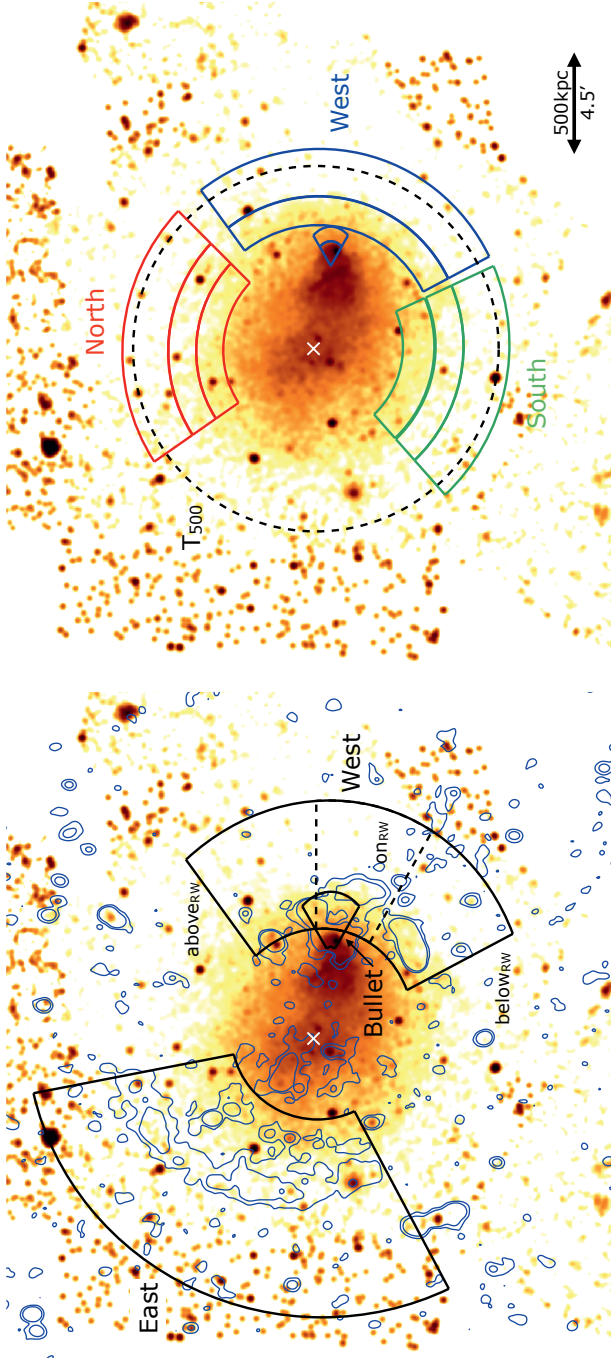
Figure 3.3: Smoothed (4'') *Chandra* 0.5–2.0 keV images showing the sectors used for extracting the surface brightness (left panel) and temperature (right panel) profiles shown in Figs. 3.5, 3.6, 3.7 and 3.8. The dashed lines in the left panel show the division for the western edge (sub-sectors above, on, and below the western relic). Radio contours in the same panel are drawn at $[1, 4] \times 3\sigma_{rms}$ levels (σ_{rms} is the same as that used in the bottom right panel in Fig. 3.1). The black dashed circle in the right panel represents the R_{500} region, from which the cluster average temperature has been obtained. The white cross represents the cluster center.

face brightness discontinuities, we analyzed the surface brightness profile in sectors around the relics. We assume that the X-ray emissivity is only proportional to the density squared ($S_X \propto n^2$), and that the underlying density profile is modeled by a broken power-law model (Markevitch & Vikhlinin, 2007, and references therein):

$$n(r) = \begin{cases} Cn_0\left(\dfrac{r}{r_{\text{edge}}}\right)^{-\alpha_1}, & r \leq r_{\text{edge}} \\[3mm] n_0\left(\dfrac{r}{r_{\text{edge}}}\right)^{-\alpha_2}, & r > r_{\text{edge}}. \end{cases} \qquad (3.1)$$

Here, $C \equiv n_1/n_2$ is the compression factor at the jump position (i.e. r_{edge}), n_0 the density immediately ahead of the putative outward-moving shock front, and α_1 and α_2 the slopes of the power-law fits. Throughout this paper, the subscripts 1 and 2 are referred to the region behind and ahead the discontinuity (see the right panel in Fig. 3.3), namely the down- and upstream regions, respectively. All parameters are left free to vary in the fit. The model is then integrated along the line of sight, assuming spherical geometry and with the instrumental and sky background subtracted. The areas covered by compact sources were excluded from the fitting (see Sect. 3.2). The strongest requirement for the surface brightness analysis is the alignment of the sectors to match the curvature of the surface brightness discontinuities. For this purpose, elliptical sectors[6] with different aperture angles have been chosen (see the left panel in Fig. 3.3). The adopted minimum number of required counts per bin are listed in Table 3.3.

According to this model, a surface brightness discontinuity is detected when $C > 1$, meaning that in the downstream region, i.e. $r \leq r_{\text{edge}}$, the gas has been compressed. In the case of a shock, there is a relation between the compression factor C and the Mach number ($\mathcal{M} = v_{\text{shock}}/c_s$, where v_{shock} is the velocity of the pre-shock gas and c_s the sound velocity in the medium[7]), via the Rankine-Hugoniot relation (Landau & Lifshitz, 1959):

$$\mathcal{M}_{S_X} = \sqrt{\frac{2C}{\gamma + 1 - C(\gamma - 1)}} + syst_{S_X}, \qquad (3.2)$$

where γ is the adiabatic index of the gas, and is assumed to be 5/3 (i.e. a monoatomic gas). The parameter $syst_{S_X}$ takes all the unknown uncertainties into account, e.g. projection effects, curvature of the sector, back-

---

[6]The "ellipticity" of the sector, e, is defined as the ratio of the maximum and minimum radius (see Table 3.3).

[7]$c_s = \sqrt{\dfrac{\gamma k T_2}{\mu m_{\text{H}}}}$, where k is the Boltzmann constant, γ the adiabatic index, $\mu = 0.6$ the mean molecular weight and m_{H} the proton mass. kT_2 is the pre-shock, i.e. unperturbed medium, temperature.

ground estimation, etc. Unfortunately, all these parameters are not easily quantified, so they are embedded in the assumption of our model.

The surface brightness analysis has been performed with PyXel[8] (Ogrean, 2017), and the uncertainties on the best-fitting parameters are determined using a Markov chain Monte Carlo (MCMC) method (Foreman-Mackey et al., 2013).

The nature of the confirmed X-ray surface discontinuities is determined by the analysis of the temperature ratio of the down- and up-stream regions, in correspondence of the edge. Shocks and cold fronts are defined to have $T_1/T_2 > 1$ and $T_1/T_2 < 1$, respectively (Markevitch & Vikhlinin, 2007). For a cold front, the jump in temperature has similar, but inverse, amplitude to the density compression. Hence, they are also characterized by pressure equilibrium across the discontinuity (i.e. $P_1/P_2 = 1$[9]). In case of shock front, the Rankine-Hugoniot jump conditions relate the temperature jump, $\mathcal{R} \equiv T_1/T_2$, to the Mach number (e.g. Landau & Lifshitz, 1959):

$$\mathcal{M}_{T_X} = \sqrt{\frac{(8\mathcal{R} - 7) + \sqrt{(8\mathcal{R} - 7)^2 + 15}}{5}} + syst_{T_X} \quad , \qquad (3.3)$$

where $\gamma = 5/3$ has been used, as for Eq. 3.2. Again, $syst_{T_X}$ takes all the unknown temperature-related uncertainties into account, such as the variation of the metal abundance (A) and the Galactic absorption (N_H) towards the cluster outskirts, background subtraction, etc. (for a more extensive description of the possible systematic uncertainties see Akamatsu et al., 2017).

Sectors for the radial temperature measurements have been chosen similarly to the ones used for the surface brightness analysis (see the right panel in Fig. 3.3), which also provides the accurate position of the edges. As for the global cluster analysis (see Sect. 3.3.1), we fit each spectrum with a single temperature, taking into account the Galactic absorption (phabs*apec). Both the abundance and hydrogen column density were fixed, at $A = 0.3$ $Z_\odot$ and $N_H = 0.311 \times 10^{22}$ cm^{-2}, respectively. Since the number of counts in cluster outskirts are usually low, the spectrum was grouped to have a minimum of 1 count per bin, and the Cash statistic (Cash, 1979) was adopted. The ACIS readout artifacts were not subtracted in our analysis. This does not affect the analysis, since the cluster is relatively faint and no bright compact source is contaminating the observations.

The spatial and spectral analysis results are shown in Sects. 3.4.2, 3.4.3 and 3.4.4 and the best-fit values reported in Tabs. 3.3 and 3.4. The corresponding MCMC "corner plots" for the distribution of the uncertainties in the fitted parameters of the surface brightness analysis are shown

---

[8] https://github.com/gogrean/PyXel

[9] $P = k n_e T$, with k the Boltzmann constant and n_e the electron density.
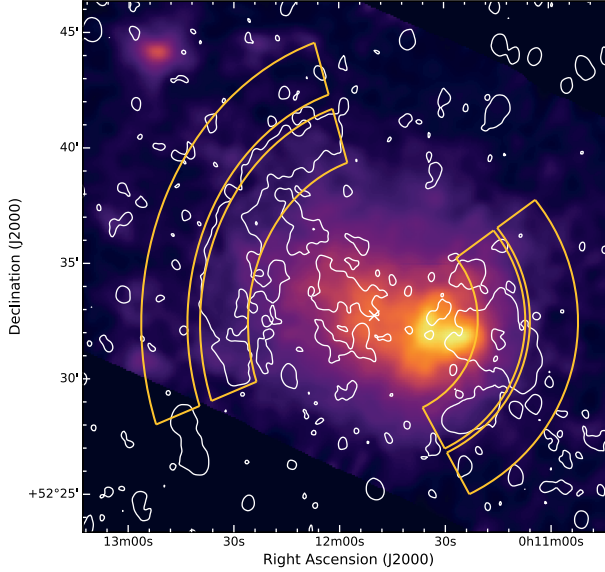
Figure 3.4: *Suzaku* 0.5–4.0 keV image of ZwCl 0008. WSRT radio contours are drawn in white at the $3\sigma_{\mathrm{rms}}$ level. Orange sectors overlaid represent the regions where the temperature measurements were extracted for the western and eastern relic (see left and right panel in Fig. 3.8, respectively). As for Fig. 3.3, the white cross represents the cluster center.

in Appendix .1. We used the distribution on the compression factor to obtain the uncertainties on $\mathcal{M}_{S_X}$, while the uncertainties on $\mathcal{M}_{T_X}$ have been calculating with 2,000 Monte Carlo realizations of Eq. 3.3.

3.4.2. The western sector

The best-fitting double power-law model finds the presence of a density jump with $C = 1.70^{+1.04}_{-0.64}$ located at $r = 6.88^{+0.15}_{-0.27}$ arcmin (i.e. ∼ 700 kpc, at the ZwCl 0008 redshift) from the cluster center (top left panel in Fig. 3.5). Assuming the Rankine-Hugoniot density jump condition, this results in a Mach number for the western edge of $\mathcal{M}_{S_X} = 1.48^{+0.50}_{-0.32}$ (Eq. 3.2), which shows a shock detection at the ∼ 90% confidence level. No significant differences have been found by varying the background level by ±5% (i.e., three times the residual fluctuation in the 9–12 keV band). The same region was also fitted with a simple power-law model, representative of the surface brightness profile at the cluster outskirts in the absence of shock discontinuities. We compared the results of the two models performing the

Bayesian Information Criterion (BIC, see Kass & Raftery, 1995) analysis, for which the model with the lower score is favored. We obtain BIC=195 (χ^2 = 186.35) and the BIC=126 (χ^2 = 104.30) for the power-law and the broken power-law model respectively, again pointing to the presence of a discontinuity at the western relic position.
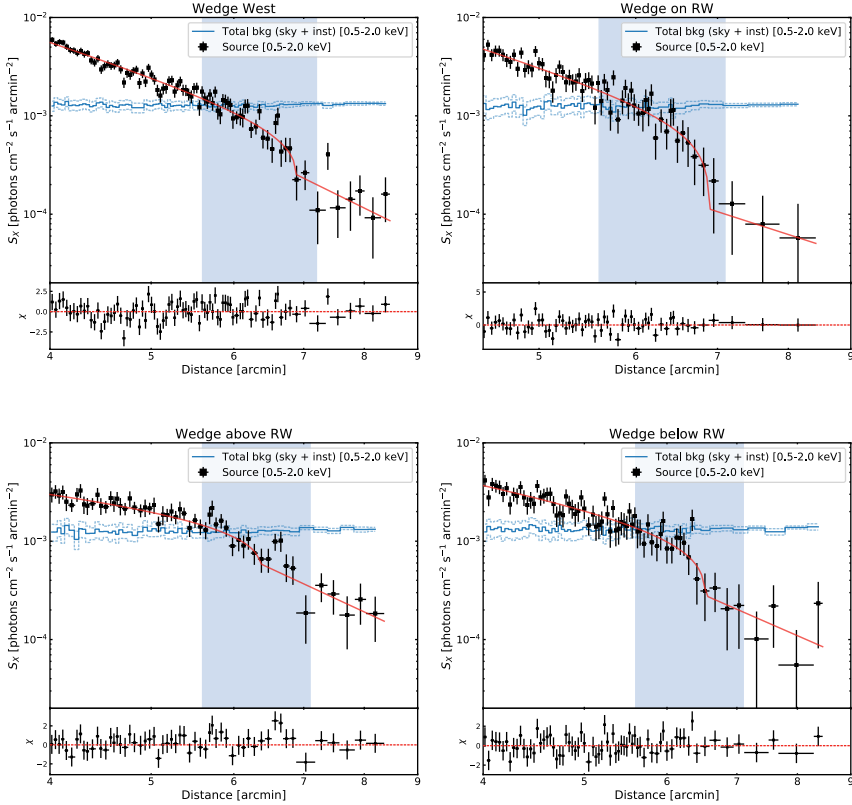

Figure 3.5: Surface brightness profiles across the western sector (top left panel) and the sub-sectors on, above and below RW (top right, bottom left and bottom right panels, respectively).The light blue rectangle identifies the position of the western radio relic. The total background level (i.e. instrumental and astrophysical) is shown by the light blue line, with the $\pm 1\sigma$ uncertainties (light blue dashed lines). On the bottom of each panel, the residuals (i.e. $\frac{S_{X,obs} - S_{X,mod}}{\Delta S_{X,obs}}$) are displayed.

The temperature profile, derived across this discontinuity, shows the presence of heated gas behind the edge and colder gas ahead of it (kT_1 = $8.55^{+1.35}_{-1.14}$ and $kT_2 = 3.01^{+1.12}_{-0.70}$ keV, respectively, see filled blue squares in

the left panel in Fig. 3.8). We obtained consistent result when we decrease the sector width by a factor of two (see empty blue squares in the left panel in Fig. 3.8). In principle, the temperature jump at the shock is also affected by the intrinsic temperature gradient of the cluster, before the shock passage (Vikhlinin et al., 2006). Following Burns et al. (2010), the expected temperature variation in our temperature bin is about 0.7 keV (see solid line in the right panel in Fig 3.8). We add this variation as a systematic uncertainty in the temperature estimation. Additional support for the presence of heated gas behind the detected edge is that we do not find significant variation of temperature in the north and south directions (see the red and green sectors in the right panel in Fig. 3.3 and temperature profile in the central panel in Fig. 3.8), where indeed there is no evidence of shocks. We also investigated possible systematic uncertainties associated with Galactic abundance (N_H) variations across the cluster, using the $E(B-V)$ reddening map at 100 μm from the NASA/IPAC Infrared Science Archive (IRSA[10]; Schlegel et al., 1998) and assuming $N_H \propto E(B-V)$. We found a mild N_H variation (e.g. $\sim 9\%$) in the west with respect to the cluster center value. The fit was then repeated, adding/subtracting this fluctuation and keeping N_H fixed, showing an increase of the temperature uncertainties of about $^{+0.9}_{-0.5}$ and $^{+0.2}_{-0.1}$ in the post- and pre-shock regions, respectively. We use the drop in the temperature at the western edge, i.e. $\mathcal{R} = 2.61^{+1.03}_{-0.69}$, to obtain the Mach number of the shock, i.e., $\mathcal{M}_{T_X} = 2.35^{+0.74}_{-0.55}$ (see Eq. 3.3).

Additional temperatures were derived in the relic sectors from the *Suzaku* observations (see orange sectors in Fig. 3.4). The abundance and Galactic absorption have been fixed at the same values as the *Chandra* observations, assuming a `phabs*apec` model and adopting the Lodders et al. (2009) abundance table. The sky background was estimated using the *ROSAT* background tool, with the intensity of the cosmic X-ray background (CXB) allowed to change by $\pm 10\%$ to explain cosmic variance. Given the high sensitivity of *Suzaku*, the spectra were grouped to have a minimum of 20 counts per bin, and the χ^2 statistic was used. The temperature estimated in the post-shock region with *Suzaku* is $kT_1 = 4.67^{+1.13}_{-0.78}$, which is lower than the one obtained with *Chandra* at the $> 90\%$ confidence level (see orange diamonds in the left panel in Fig. 3.8). We looked for possible temperature contamination from the cold front in the post-shock region, due to the limited *Suzaku* spatial resolution (i.e. ~ 2 arcmin), by reducing the width of the post-shock region to 30″: no significantly different temperature has been found. The difference in temperature in the post-shock region between *Chandra* and *Suzaku* might be explained by different instrumental calibrations. Cross-correlation studies of *XMM-Newton*/*Suzaku* (Kettula et al., 2013) and *XMM-Newton*/*Chandra* (Schellenberger et al., 2015) have shown that *Chandra* finds systematically higher temperatures, up to 20–

---

[10]https://irsa.ipac.caltech.edu/cgi-bin/bgTools/nph-bgExec

25% for cluster temperatures of 8 keV, compared with *XMM-Newton* (Schellenberger et al., 2015). On the contrary, differences between *Suzaku* and *XMM-Newton* result were found to be negligible (Kettula et al., 2013). On the other hand, the pre-shock temperature from *Suzaku* agrees well with the *Chandra* measurement (i.e. $kT_2 = 2.38^{+0.23}_{-0.21}$ and $kT_2 = 3.01^{+1.12}_{-0.70}$ keV, respectively), suggesting that standard blank sky field and background modelling give consistent results. Including also the systematic uncertainties (i.e. global temperature profile and instrumental calibrations), we found $\mathcal{M}_{T_X} = 2.02^{+0.74}_{-0.43}$ with *Suzaku*, which is within the 1σ confidence level with the *Chandra* result.

The pressure jump across the edge is $4.45^{+2.00}_{-1.47}$. Using the *Chandra* pre-shock temperature $kT_2 = 3.01^{+1.12}_{-0.70}$ keV and the Mach number given by the *Chandra* temperature profile, we obtain a shock velocity of $v_{\mathrm{shock,W}} = 1989^{+509}_{-468}$ km s^{-1}. Given the distance of the edge from the cluster center (~ 7 arcmin, i.e. ~ 780 kpc) and the shock velocity, we estimated the time since the first core passage being ~ 0.3–0.5 Gyr, older than the time found for the Bullet Cluster Markevitch (2006b) and for Abell 2146 (Russell et al., 2010), i.e. ~ 0.2 Gyr. The time we found is consistent with the one found by Golovich et al. (2017) assuming an "outbound" scenario, i.e. 0.49–1.0 Gyr.

The most remarkable aspect of ZwCl 0008 is that the western radio relic traces only part of the shock front (LLS$_{\mathrm{RW}} \approx 290$ kpc, while LLS$_{\mathrm{edge,W}} \approx$ 1 Mpc). A possible explanation is that the Mach number of the shock varies along the length of the edge and the relic forms only where $\mathcal{M}$ is high enough to accelerate electrons. To investigate this, we divided the western edge into three sub-sectors, tracing the shock above, below, and on RW (see left panel in Fig. 3.3 and Table 3.3). The corresponding surface brightness profiles are displayed in the top right, bottom right, and bottom left panels in Fig. 3.5. Due to the low S/N in the upstream region, for these sectors we additionally constrained the slope a_2 to be in the range $1 < a_2 < 3.2$. Those values have been chosen to match the slopes of the surface brightness profiles, at R_{500}, of the full cluster sample in the *Chandra–Planck* Legacy Program for Massive Clusters of Galaxies[11] (PI: C. Jones; Andrade-Santos et al., 2017, Andrade-Santos et al., in prep.). Under these assumptions, we obtain $\mathcal{M}^{\mathrm{above}}_{\mathrm{RW}} = 1.30^{+0.46}_{-0.17}$, $\mathcal{M}^{\mathrm{on}}_{\mathrm{RW}} = 2.98^{+2.62}_{-0.85}$ and $\mathcal{M}^{\mathrm{below}}_{\mathrm{RW}} = 1.70^{+0.79}_{-0.55}$ for the sub-sector above, on, and below the western relic, respectively. They are consistent to each other within the error bars, hence we cannot assert whether the Mach number is varying along the western X-ray discontinuity. Given the few counts in the pre- and post-shock regions, we were not able to perform a temperature analysis for the three separate sub-sectors.

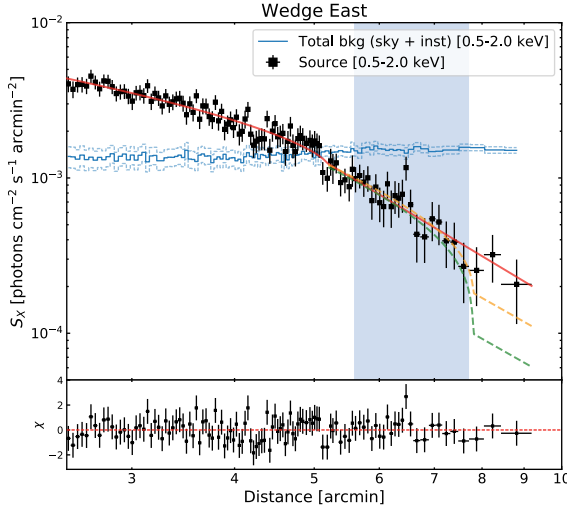[11]hea-www.cfa.harvard.edu/CHANDRA_PLANCK_CLUSTERS/

Figure 3.6: Surface brightness profile across the eastern sector. The light blue rectangle identifies the position of the eastern radio relic. The total background level (i.e. instrumental and astrophysical) is shown by the light blue line, with the $\pm 1\sigma$ uncertainties (light blue dashed lines). On the bottom, the residuals (i.e. $\frac{S_{X,obs} - S_{X,mod}}{\Delta S_{X,obs}}$) are displayed, representative of the broken power-low best-fit (red line). Models of density jumps of $C = 1.7$ and $C = 2.3$ at fixed $r_{break} = 7.8$ arcmin are also overlaid (dashed orange and green lined, respectively).

3.4.3. The eastern sector

No clear discontinuity is detected in the east. Assuming the broken power-law model, as suggested by the presence of the radio relic (RE), we found a mild jump in density (Fig. 3.6) of $C = 1.09^{+0.11}_{-0.08}$ at $5.16^{+0.26}_{-0.23}$ arcmin (i.e. ~ 550 kpc from the cluster center), suggesting simply a change of slope at this location (i.e. a King profile, see King, 1972). However, BIC scores slightly disfavor a β-model (see Cavaliere & Fusco-Femiano, 1976), rather than the broken power-law model (BIC=108 against BIC=100, respectively). Interestingly, the location of this putative X-ray discontinuity is displaced from the edge of the eastern relic (i.e. $r \sim 7.8$ arcmin) toward the cluster center. No drop has been detected at the relic location, either from the X-ray image and surface brightness profiles (Figs. 3.3 and 3.6). However, we note that this relic is located far from the cluster center, i.e. $\sim 5.6 - 7.8$ arcmin, or $\sim 610 - 900$ kpc, at the edge of the field of view (FOV) of our observation (see the right panel in Fig. 1). Hence, not all the ObsIDs cover the area ahead the eastern relic, i.e. the pre-shock region. In Fig. 3.6

we also overlay models of a density jump of C = 1.7 (i.e. $\mathcal{M}$ = 1.5, see orange dashed line) and C = 2.3 (i.e. $\mathcal{M}$ = 2.0, see green dashed line), in the region $5 \lesssim r \lesssim 9$ arcmin[12], with r_{break} fixed at the outermost edge of the eastern relic (i.e. r_{RE} = 7.8 arcmin). It is clear that a density jump of C = 2.3 is ruled out by our data. On the other hand, a density jump of C = 1.7 is still consistent with our observations. Hence, we conclude that, if present, a shock front at the location of the eastern relic should be quite weak (i.e. $\mathcal{M} \lesssim 1.5$). In agreement with this result, we obtain a temperature based Mach number from *Suzaku* of $\mathcal{M} = 1.54^{+0.65}_{-0.47}$ at the relic position (see orange sectors Fig. 3.4).
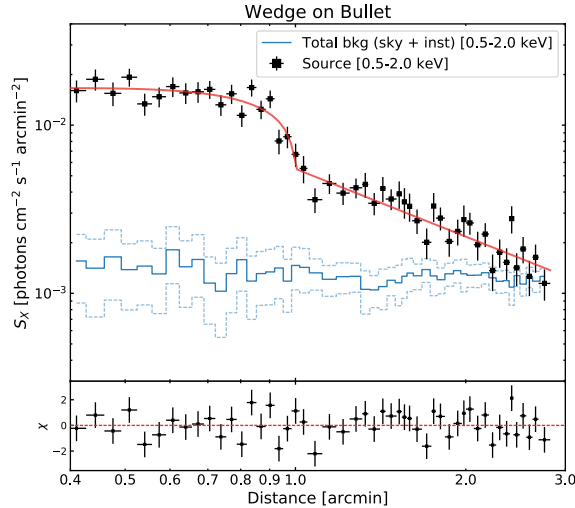

Figure 3.7: Surface brightness profile across the bullet sector. The total background level (i.e. instrumental and astrophysical) is shown by the light blue line, with the $\pm 1\sigma$ uncertainties (light blue dashed lines). On the bottom, the residuals (i.e. $\frac{S_{\text{X,obs}} - S_{\text{X,mod}}}{\Delta S_{\text{X,obs}}}$) are displayed.

3.4.4. The bullet sector

In order to match the curvature of the bullet, we chose an elliptical sector displaced from the cluster center by $\sim 3.5'$ (RA = $0^{\text{h}}11^{\text{m}}25^{\text{s}}.976$ and DEC = +52°31′58″.49, J2000). The best-fit of the surface brightness profile analysis (Fig. 3.7) results in a density jump $C = 2.06^{+0.24}_{-0.19}$ at r = 0.99 ± 0.02 arcmin from the sector center (i.e. $\sim$ 490 kpc from the cluster

---

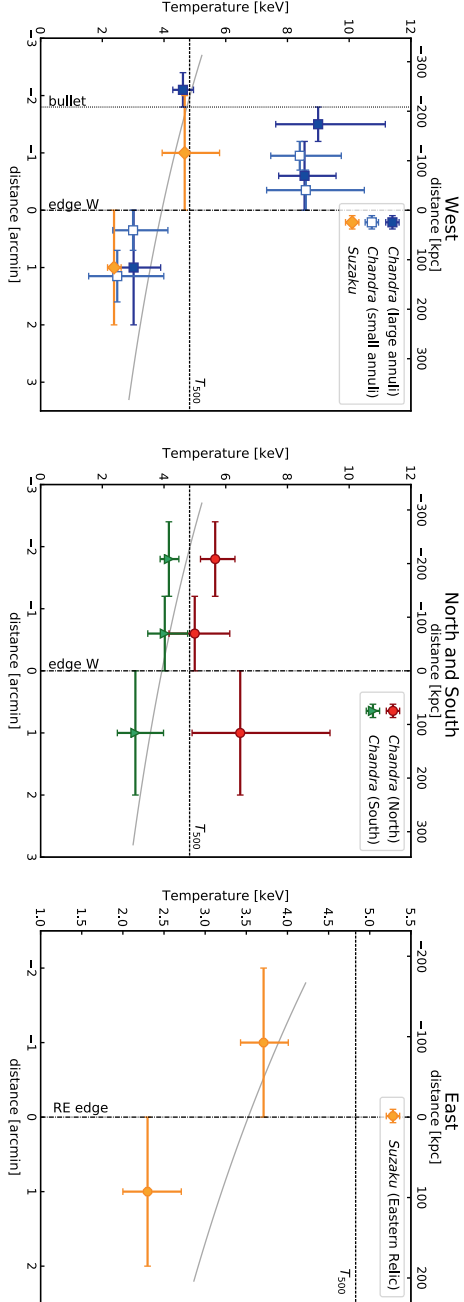[12]In this way, we avoid the change of slope at $r \sim 5$ arcmin.

Figure 3.8: Radial temperature profiles westward (left), northward and southward (central) and on the eastern relic (right). All the values have been obtained by fixing the abundance and hydrogen column density at $A = 0.3 \, Z_\odot$ and $N_H = 0.311 \times 10^{22} \, cm^2$, respectively. The horizontal dashed lines in the three panels represent the averaged temperature of the global cluster at R_{500}, obtained with *Chandra*. The vertical dot-dashed lines display the position of the western edge (left and central panel) and the edge of the eastern relic (right panel); the vertical dotted line in the left panel displays the position of the cold front. The solid gray line represents the averaged temperature profile according to Burns et al. (2010).

center, at the cluster redshift). At this location, we measure a temperature jump of $T_1/T_2 = 0.56^{+0.10}_{-0.09}$ (see Fig. 3.8). By combining the temperature and the electron density jumps, we obtain $P_1/P_2 = 1.15^{+0.25}_{-0.20}$, consistent with a constant pressure across the edge, confirming that the discontinuity is a cold front.

3.5. Discussion

At the location of a shock front, particles are thought to be accelerated via first-order Fermi acceleration, e.g. *diffusive shock acceleration* (DSA, Drury, 1983; Blandford & Eichler, 1987) and *shock drift acceleration* (SDA, Wu, 1984; Krauss-Varban & Wu, 1989) mechanisms. In particular, the SDA process has been recently invoked to solve the so-called "electron injection problem", which is particularly important in the low-$\mathcal{M}$ regime (i.e., $\mathcal{M} \lesssim 2$), giving the necessary pre-acceleration to the electron population to facilitate the DSA process (Guo et al., 2014a,b; Caprioli & Spitkovsky, 2014). The interaction between these accelerated particles and the amplified magnetic field in merging clusters produces synchrotron emission in the form of radio relics. According to the DSA theory, there is a relation between the spectral index measured at the shock location, the so-called injection spectral index α_{inj}, and the Mach number $\mathcal{M}$ of the shock (e.g. Giacintucci et al., 2008):

$$\mathcal{M}_{\text{radio}} = \sqrt{\frac{2\alpha_{\text{inj}} + 3}{2\alpha_{\text{inj}} - 1}} \,. \tag{3.4}$$

Thus for DSA, the Mach number estimated in this way is expected to agree with the one obtained from the X-ray observations. This is not always the case: a number of radio relics have been found to have higher radio Mach numbers than the one obtained via X-ray observations (e.g. Macario et al., 2011; van Weeren et al., 2016; Pearce et al., 2017). Another problem is that in some cases no radio relics have been found even in the presence of clear X-ray discontinuities (e.g. Shimwell et al., 2014). Furthermore, it is still unclear whether the DSA mechanism of thermal electrons, in case of low-$\mathcal{M}$ shocks, can efficiently accelerate particles to justify the presence of giant radio relic (e.g. Brunetti & Jones, 2014; Vazza & Brüggen, 2014; van Weeren et al., 2016; Hoang et al., 2017).

Several arguments have been proposed to address the issues described above. One possibility is that the assumption of spherical symmetry, which is at the basis of Eq. 3.2 and 3.3, is not strictly correct, and that projection effects can hide the surface brightness and temperature discontinuity, leading to smaller $\mathcal{M}$ from the X-ray compared to the one obtained from the radio analysis. Also, the Mach number might be not constant across the shock front, as it is suggested by numerical simulations (e.g. Skillman

et al., 2013), and synchrotron emission is biased to the measurement of high Mach number shocks (Hoeft & Brüggen, 2007). An alternative explanation is given by invoking the *re-acceleration* mechanism (e.g. Markevitch et al., 2005; Macario et al., 2011; Bonafede et al., 2014; Shimwell et al., 2015; Botteon et al., 2016b; Kang et al., 2017; van Weeren et al., 2017a). Indeed, several very recent observations (van Weeren et al., 2017a,b; de Gasperin et al., 2017; Di Gennaro et al., 2018) revealed that if a shock wave passes through fossil (i.e. already accelerated) plasma, such as the lobes of a radio galaxy, it could re-accelerate or re-energize the electrons and produce diffuse radio emission.

In order to best investigate the properties of shocks in ZwCl0008, in the following sections we will discuss the comparison between our new *Chandra* observations and the previous radio analysis by van Weeren et al. (2011b).

3.5.1. Radio/X-ray comparison for the western relic

The previous radio analysis of ZwCl0008 was performed at 241, 610, 1328 and 1714 MHz with the GMRT and the WSRT (van Weeren et al., 2011b). This work revealed the presence of two symmetrically located radio relics (see also right panel of Fig. 3.1). In the proximity of the western relic our *Chandra* observations indicate the presence of a shock. From the spectral index analysis[13] of RW, van Weeren et al. estimated α_{inj} = -1.0 ± 0.15, with a spectral index steepening towards the cluster center (i.e. in the shock downstream region) due to synchrotron and Inverse Compton energy losses, as expected from an edge-on merger event (see Fig. 8 in van Weeren et al., 2011b). Given the injection spectral indices and Eq. 3.4, van Weeren et al. estimated a radio Mach numbers of $\mathcal{M}_{RW}$ = $2.4^{+0.4}_{-0.2}$. This value is consistent within the uncertainties with our X-ray analysis ($\mathcal{M}_{S_X}$ = $1.48^{+0.50}_{-0.32}$ and $\mathcal{M}_{T_X}$ = $2.35^{+0.74}_{-0.55}$), consistent with the DSA scenario for the western relic's origin.

An interesting complication to this picture comes by the fact that the western relic only partly traces the shock front. Total or partial absence of relic emission in presence of clear X-ray discontinuities could be explained by having a shock strength which drops below a certain threshold, depending on the plasma beta parameter ($\beta \equiv P_{gas}/P_B$) at the shock (Guo et al., 2014a,b). Unfortunately, the net count statistics in those sectors are very poor and our estimated Mach numbers in the three sub-sectors are characterized by large error bars (see Table 3.4). Hence, we cannot assert whether $\mathcal{M}$ variations are present and justify the smaller size of RW compared to the X-ray shock extent (however, see Sect. 3.5.4). Another appealing explanation for the origin of the western relic is suggested

---

[13] α_{inj} was calculated either directly from the map, and from the volume-integrated spectral index α_{int} (i.e. $\alpha_{inj} = \alpha_{int} + 0.5$, Blandford & Eichler, 1987). The two values are consistent with each other.

Table 3.3: Wedges information (columns 1 to 4) and best-fit parameters (columns 5 to 8) from the surface brightness profiles shown in Figures 3.5, 3.6 and 3.7. A broken power-law model has been assumed (see Eq. 3.2) for each sector.

Sector	$\Delta\theta$ [degree]	Min. count per bin	e	α_1	α_2	r_{edge} [arcmin]	C
West	98	70	1.14	$2.20^{+0.10}_{-0.10}$	$3.11^{+2.40}_{-1.75}$	$6.88^{+0.15}_{-0.26}$	$1.70^{+0.91}_{-0.65}$
above RW[†]	36	50	1.14	$0.91^{+0.37}_{-0.19}$	$2.96^{+0.25}_{-0.66}$	$6.35^{+0.66}_{-0.47}$	$1.44^{+0.97}_{-0.36}$
on RW[†]	30	25	1.14	$2.38^{+0.25}_{-0.56}$	$2.50^{+0.64}_{-1.35}$	$6.89^{+0.17}_{-0.16}$	$2.99^{+0.90}_{-0.86}$
below RW[†]	32	30	1.14	$1.44^{+0.27}_{-0.33}$	$2.82^{+0.37}_{-1.37}$	$6.53^{+1.25}_{-1.09}$	$1.96^{+1.30}_{-0.94}$
East[‡]	107	70	1.14	–	–	7.8	$\lesssim 1.7$
Bullet	60	40	1.42	$-0.24^{+0.23}_{-0.29}$	$1.17^{+0.06}_{-0.07}$	$0.99^{+0.02}_{-0.02}$	$2.06^{+0.24}_{-0.19}$

Note: All the sectors are centered in the cluster center (i.e. RA = $0^h 11^m 25^s.976$ and DEC = +52°32'37''.98, J2000), with the exception of the bullet (RA = $0^h 11^m 25^s.976$ and DEC = +52°31'58''.49, J2000). The ellipticity of each sector is given by the parameter e. [†]Prior on α_2 (see Sect. 3.4.2) [‡] Model.

Table 3.4: Best-fit temperature profiles for the X-ray discontinuities. A phabs*APEC model with fixed $N_H = 0.311 \times 10^{22}$ cm^{-2} and $A = 0.3$ Z$_\odot$ has been assumed for the analysis.

Sector	Instrument	kT [keV]	$^{\text{stat}}/_{\text{dof}}$	$\mathcal{R}$	$\mathcal{M}_{T_X}$	$\mathcal{M}_{S_X}^\circ$
R_{500}	*Chandra*	4.83 ± 0.06	$4214.75/3785$	—	—	—
West	*Chandra*	$8.55^{+1.35}_{-1.14}$ (a) $3.01^{+1.12}_{-0.79}$ (b)	$3643.65/3964$ (a) $1182.10/1258$ (b)	$2.61^{+1.03}_{-0.69}$	$2.35^{+0.74}_{-0.55}$	$1.48^{+0.50}_{-0.32}$
West	*Suzaku*	$4.67^{+1.13}_{-0.78}$ (a) $2.38^{+0.23}_{-0.21}$ (b)	$47.39/54$ (a) $208.61/228$ (b)	$2.05^{+0.77}_{-0.43}$	$2.02^{+0.74}_{-0.43}$	—
above RW	*Chandra*	—	—	—	—	$1.30^{+0.46}_{-0.17}$
on RW	*Chandra*	—	—	—	—	$2.98^{+2.62}_{-0.85}$
below RW	*Chandra*	—	—	—	—	$1.70^{+0.79}_{-0.55}$
East	*Chandra*	—	—	—	—	$\lesssim 1.5^{\ddagger}$
on RE	*Suzaku*	$3.71^{+0.30}_{-0.28}$ (a) $2.30^{+0.41}_{-0.30}$ (b)	$309.86/337$ (a) $171.82/162$ (b)	$1.54^{+0.39}_{-0.26}$	$1.54^{+0.65}_{-0.47}$	—
Bullet	*Chandra*	$4.61^{+0.34}_{-0.33}$ (a) $8.99^{+2.17}_{-1.37}$ (b)	$1250.23/1602$ (a) $1059.42/1309$ (b)	$0.56^{+0.10}_{-0.09}$	—	—

Note: values at $^{(a)}$ $r \leq r_{\text{edge}}$ and $^{(b)}$ $r > r_{\text{edge}}$; $^\circ$ calculated from C in Table 3.3. ‡ Model. The uncertainties on $\mathcal{M}_{S_X}$ have been obtained from the compress factor distributions shown in Appendix .1, while the uncertainties on $\mathcal{M}_{T_X}$ have been calculated with 2,000 Monte Carlo realizations of Eq. 3.3 and including the systematic uncertainty given by the cluster temperature average profile (i.e. 0.7 keV).

by the proximity of three different radio galaxies (i.e. sources C, E and F in the right panel in Fig. 3.1) which can provide the fossil electrons for the synchrotron emission, according to the re-acceleration mechanism. In this case, the absence of diffuse radio emission associated to the relic, above and below RW, can be simply explained by the absence of underlying fossil plasma to be re-accelerated by the crossing shock wave. For the case of ZwCl 0008, there is no clear connection between the radio galaxies and RW, which is the strongest requirement to invoke the re-acceleration mechanism, together with the detection of the shock. However, such fossil plasma can be faint and characterized by a very steep spectral index, meaning that it is best detected with sensitive low- frequency observations.

3.5.2. The puzzle of the eastern radio relic

Similarly to RW, the eastern relic also displays spectral steepening towards the cluster center (see Fig. 8 in van Weeren et al., 2011b). The measured injection spectral index is $\alpha_{\mathrm{inj}} = -1.2 \pm 0.2$, which corresponds to a Mach number of $\mathcal{M} = 2.2^{+0.2}_{-0.1}$, under the assumption of DSA of thermal electrons (Eq. 3.4 and van Weeren et al., 2011a). A surface brightness discontinuity is therefore expected in the eastward outskirts of ZwCl 0008, tracing the shape of RE. Nonetheless, no discontinuity has been detected at the relic position in our *Chandra* observations.

A complication that should be taken into account is projection effects, which can hide, or at least smooth, X-ray discontinuities. Polarization analysis (Golovich et al., 2017) and numerical simulations (Kang et al., 2012) of the eastern relic showed that the merger angle in ZwCl 0008 ranges between 25 and 30°, being 0° the angle associated to a perfectly edge-on collision. This possible non-negligible inclination angle might, in principle, contribute in hiding X-ray discontinuities. Despite that, our observations suggest that, if present, the shock front in the eastern side of the cluster is rather weak, i.e. $\mathcal{M} \lesssim 1.5$, which is lower than the one found by the radio spectral index analysis. Further studies, focused on this side of the cluster, are necessary to give better constraints on the strength of the putative shock front.

3.5.3. Shock location and comparison with numerical simulations

The distribution of the ICM and the exact location of the shock fronts are essential to put constraints on the characterization of the dynamical model of the merger event. Two previous studies have been performed for ZwCl 0008, using weak lensing (Golovich et al., 2017) and N-body/hydrodynamical (Molnar & Broadhurst, 2018) simulations. Despite qualitative agreements (e.g. the identification of the most massive sub-cluster, the

small impact parameter and offset of the main cluster from the dark matter peak), different sub-cluster mass ratio and time after the first core passage have been found in two works. It is worthy to note, though, that analysis performed by Molnar & Broadhurst (2018) was based on the position of the putative shock fronts, given by the previous shallow (42 ks) X-ray observations. These were supposed to be located, in the east, at the position of the well-defined radio relic, and, in the west, further in the cluster outskirts (see Fig. 1 in Molnar & Broadhurst, 2018). Such positions led to an extremely high shock velocities (i.e $\sim$ 4000 and 5000 km s^{-1}, respectively for the western and eastern shock). This interpretation, however, does not agree with our new, deeper (410 ks), X-ray observations. We indeed detect a shock front at the western relic position, while no clear confirmation has been found at the eastern relic one (see right panel in Fig. 3.1, top left panel in Fig. 3.5 and Fig. 3.6). We can then conclude that, in cases of merging clusters with the presence of radio relics, the position of shock discontinuity cannot be arbitrary, but needs to match the position of the radio source. This information is particularly suitable for double radio relics, which describe merger events very close to the plane of the sky.

3.5.4. Shock acceleration efficiency

As described above, one of the open questions related to the DSA mechanism is whether the particles from the thermal pool can be efficiently accelerated by a low-$\mathcal{M}$ shock (e.g. $\mathcal{M} \lesssim 2$).

The acceleration efficiency, η, is defined as the amount of kinetic energy flux available at the shock that is converted into the supra-thermal and relativistic electrons, and it relates to the synchrotron luminosity L_{sync} of the radio relic according to (Brunetti & Jones, 2014):

$$\eta = \left[\frac{1}{2} \rho_2 v_{\text{shock}}^3 \left(1 - \frac{1}{C^2} \right) \frac{B^2}{B^2 + B_{\text{CMB}}^2} S \right]^{-1} \Psi(\mathcal{M}) L_{\text{sync}}, \qquad (3.5)$$

where ρ_2 is the total density in the up-stream region, v_{shock} the shock speed, C the compression factor at the shock, B the magnetic field, $B_{\text{CMB}} = 3.25(1 + z)^2$ μG the magnetic field equivalent for the Cosmic Microwave Background radiation, and S the shock surface area. Here, $\Psi(\mathcal{M})$ is a dimensionless function which takes the ratio of the energy flux injected in "all" the particles and those visible in the radio band (see Eq. 5 in Botteon et al., 2016a, for the exact mathematical description of $\Psi(\mathcal{M})$) into account.

In Fig. 3.9 we report the electron acceleration efficiency analysis for the western radio relic, for which we have the strongest evidence of the X-ray shock, as a function of the magnetic field. We assume $S = \pi \times 290^2$ kpc^2, $P_{1.4 \text{ GHz}} = 0.37 \times 10^{24}$ W Hz^{-1} (see van Weeren et al., 2011b), a total
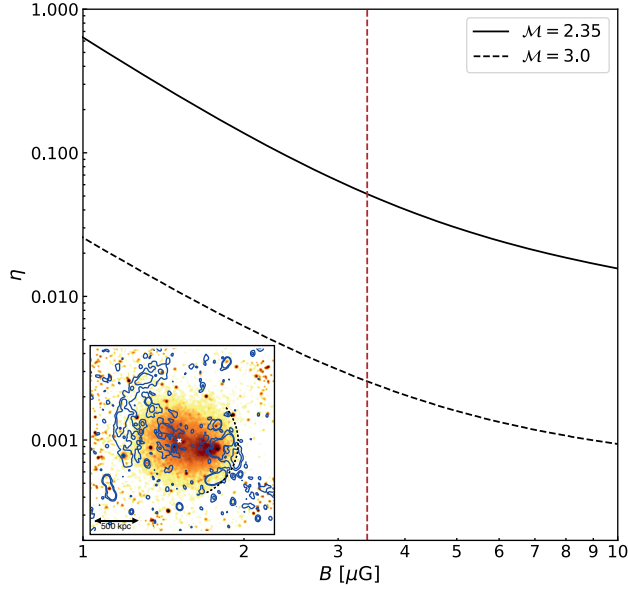
Figure 3.9: Electron acceleration efficiency as a function of magnetic field for the western relic. The vertical red dashed line shows the value of the magnetic field estimated by van Weeren et al. (2011b). The dashed arc in the inset in the bottom left corner shows the position of the shock as revealed by the surface brightness analysis (top left panel in Fig. 3.5).

pre-shock numerical density[14] $n_2 = 1.8 \times 10^{-4}$ cm^{-3}, and a shock Mach number of $\mathcal{M} = 2.35$, according to the *Chandra* measurement. Given the estimation of magnetic field of 3.4 μG (under the assumption of equipartition, see van Weeren et al., 2011b), the efficiency required for the electron acceleration due to the shock is $\eta \sim 0.05$. This would disfavor the standard DSA scenario, since efficiencies $\lesssim 10^{-3}$ are expected for weak shocks (e.g. Brunetti & Jones, 2014; Caprioli & Spitkovsky, 2014; Hong et al., 2014; Ha et al., 2018). Given the high uncertainties on our Mach number estimation, we also repeated the analysis assuming $\mathcal{M} = 3.0$ (i.e., the upper limit of our *Chandra* temperature measurement and the value we found for the sector on the western relic (on$_{RW}$), see Tab. 3.4). In this case we obtain $\eta \sim 3 \times 10^{-3}$, still consistent with the DSA framework. Future deeper X-ray observations are therefore required to reduce the uncertainties on the Mach number, and give better constraints on this point.

Finally, the radio luminosity expected for a $\mathcal{M} = 1.7$ shock[15], using our

---

[14]$\rho = \mu m_H n$

[15]the upper limit of the Mach number we measured in the sector above$_{RW}$, where no radio emission has been observed

most optimistic acceleration efficiency (η = 0.05), is $P_{1.4\ \mathrm{GHz}} \sim 10^{18}$ W Hz^{-1}. This radio power is far below our detection limit. Hence, the lack of radio emission in this sector is still consistent with a DSA scenario.

3.6.   **Summary**

In this paper we presented deep *Chandra* (410 ks) and *Suzaku* (180 ks) observations of ZwCl 0008.8+5215 (z = 0.104). This galaxy cluster was previously classified as a merging system by means of radio-optical analysis (van Weeren et al., 2011b; Golovich et al., 2017) and numerical simulations (Kang et al., 2012; Molnar & Broadhurst, 2018). The previous radio observations revealed the presence of a double radio relic in the east and in the west of the cluster (van Weeren et al., 2011b).

With the new *Chandra* observations, we find evidence for the presence of a cold front in the west part of the cluster and, about 2′ further in the cluster outskirts, a shock. For this shock, we estimate $\mathcal{M}_{S_X} = 1.48^{+0.50}_{-0.32}$ and $\mathcal{M}_{T_X} = 2.35^{+0.74}_{-0.55}$, from the surface brightness and radial temperature analysis respectively. Additionally, *Suzaku* temperature profile suggests a Mach number of $\mathcal{M}_{T_X} = 2.02^{+0.74}_{-0.43}$. Given these values, we estimate the shock velocity of $v_{\mathrm{shock,W}} = 1989^{+509}_{-468}$ km s^{-1}, and a consequent time since core passage of $\sim 0.3 - 0.5$ Gyr. The Mach number found with X-ray observations agrees with the one obtained by the radio analysis, assuming diffusive shock acceleration of thermal electrons (i.e. $\mathcal{M}_{\mathrm{RW}} = 2.4^{+0.4}_{-0.2}$, van Weeren et al., 2011b). However, given the large uncertainties on the Mach number, we cannot assert whether this is the leading mechanism for the generation of the relic. Also, it remains an open question why the radio relic does not fully trace the full extent of the X-ray shock: we measure LLS$_{\mathrm{edge,W}} \sim 1$ Mpc and LLS$_{\mathrm{RW}} \sim 290$ kpc from the X-ray and radio images, respectively. We propose that three radio galaxies, located in the proximity of the relic, might have provided the fossil plasma which has subsequently been re-accelerated. However, no clear connection between the relic and the radio galaxies has been found with the previous radio observation. Further deep and low-frequency observations will be needed to reveal, if present, diffuse and faint radio emission connecting the radio galaxies with the relic (as seen in van Weeren et al., 2017a, for the merging cluster Abell 34311-3412).

In the eastern side of the cluster, where another, longer (i.e. LLS$_{\mathrm{RE}} \sim 1.4$ Mpc), radio relic is observed, we do not find evidence for a shock. We suggest a possible combination of projection effects and position of the relic at the edge of the FOV to explain this. Form the surface brightness profile with *Chandra* we could rule out the presence of shock front with $\mathcal{M} > 1.5$, and *Suzaku* temperature measure in the post- and pre-shock regions found $\mathcal{M}_{T_X} = 1.54^{+0.65}_{-0.47}$. Both this results disagree with the radio

analysis, for which a shock with $\mathcal{M} = 2.2^{+0.2}_{-0.1}$ was derived. Further studies, focused on this radio relic, are necessary to better understand its formation scenario.

.1. MCMC corner plots

In this section we present the MCMC "corner plot" (Foreman-Mackey, 2016, 2017) for the distribution of the uncertainties in the fitted parameters for the X-ray surface brightness profile across the wedges presented in Figs. 3.5, 3.6 and 3.7. For all corner plots, contour levels are drawn at $[0.5, 1.0, 1.5, 2.0]\sigma$.
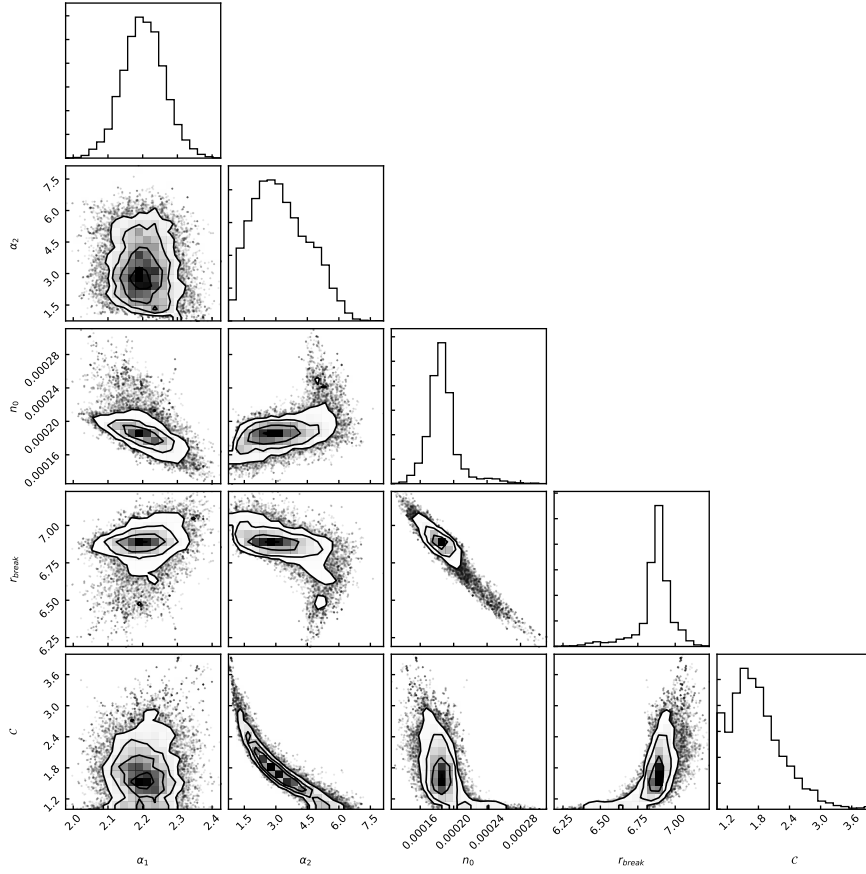
Figure .1.1: The MCMC "corner plot" for the X-ray surface brightness profile across the western edge (see top left panel in Fig. 3.5)
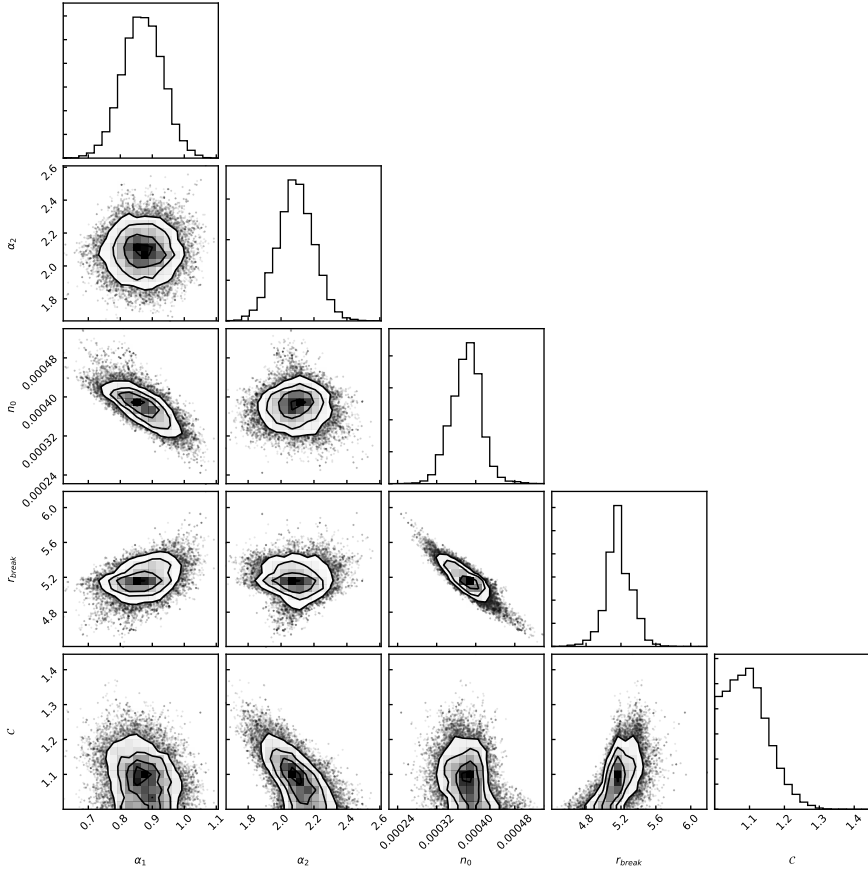
Figure .1.2: The MCMC "corner plot" for the X-ray surface brightness profile across the eastern edge (see Fig. 3.6).
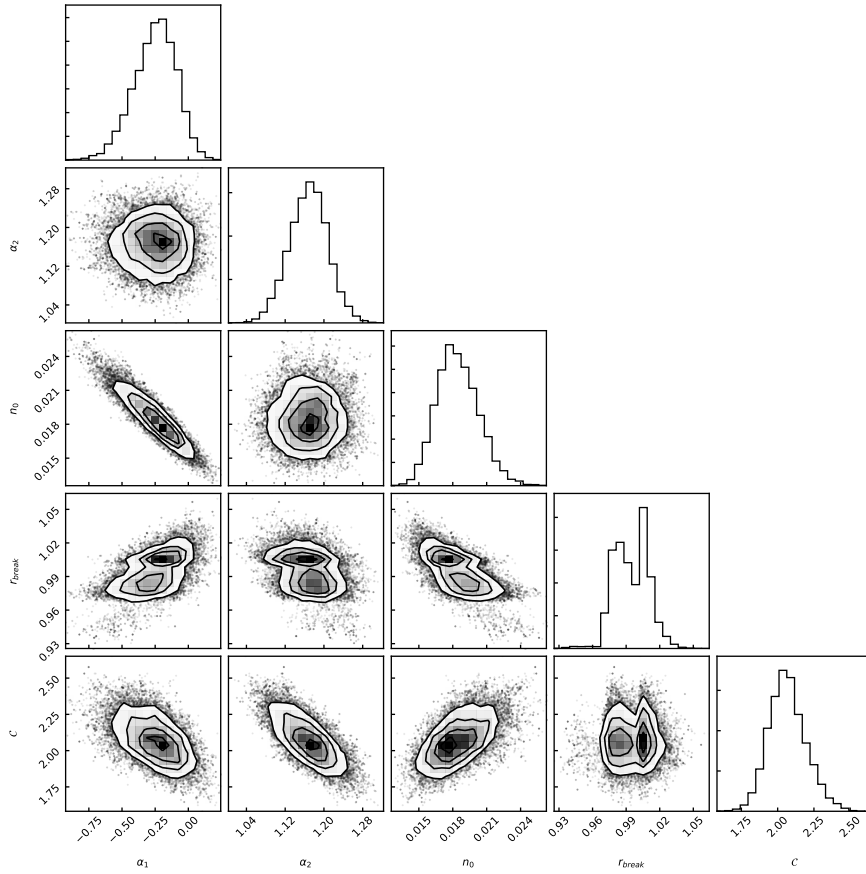
Figure .1.3: The MCMC "corner plot" for the X-ray surface brightness profile across the bullet (see Fig. 3.7)

Figure .1.4: The MCMC "corner plot" for the X-ray surface brightness profile across the wedge above the western relic (see bottom left panel in Fig. 3.5)

Figure .1.5: The MCMC "corner plot" for the X-ray surface brightness profile across the wedge on the western relic (see top right panel in Fig. 3.5)

Figure .1.6: The MCMC "corner plot" for the X-ray surface brightness profile across the wedge below the western relic (see bottom right panel in Fig. 3.5)
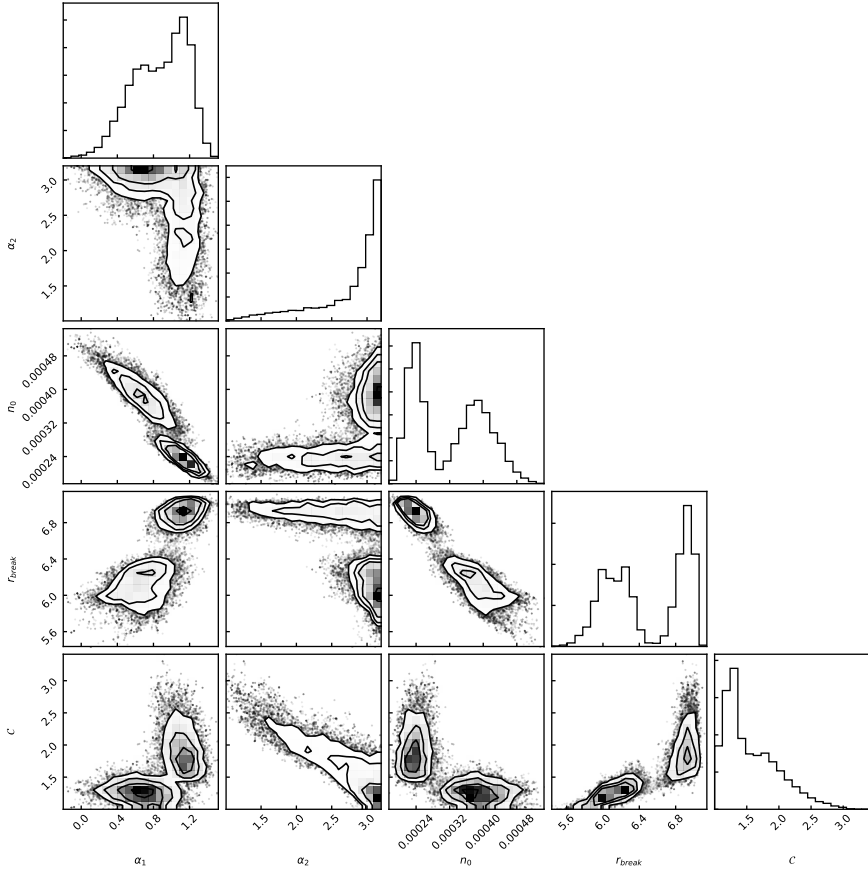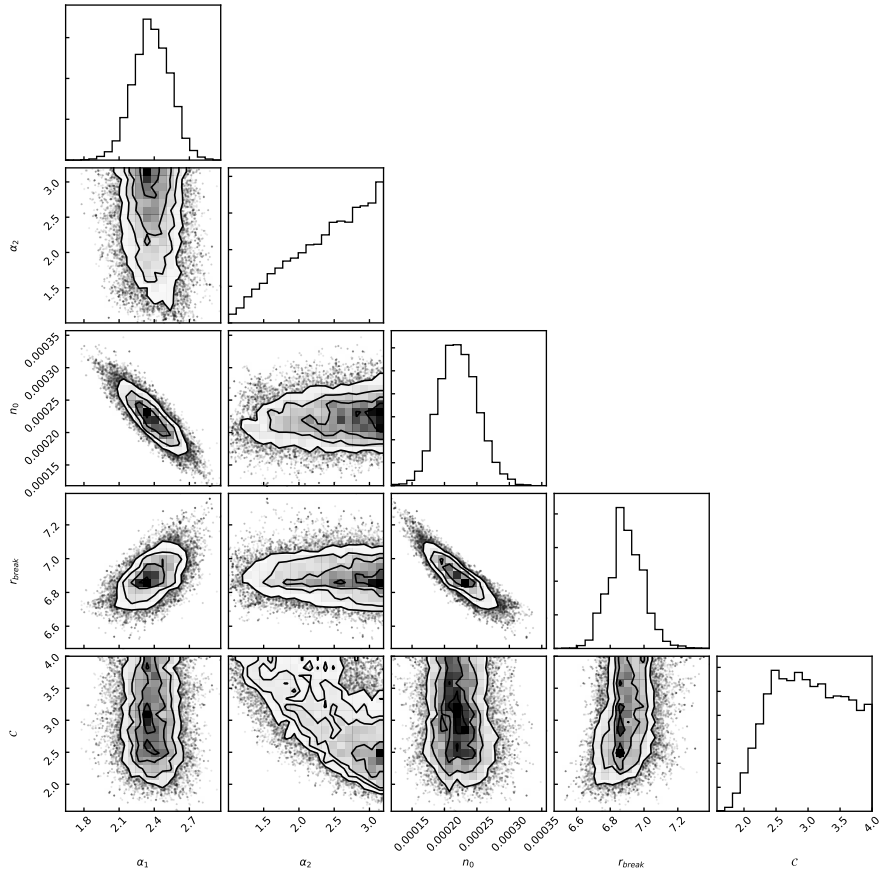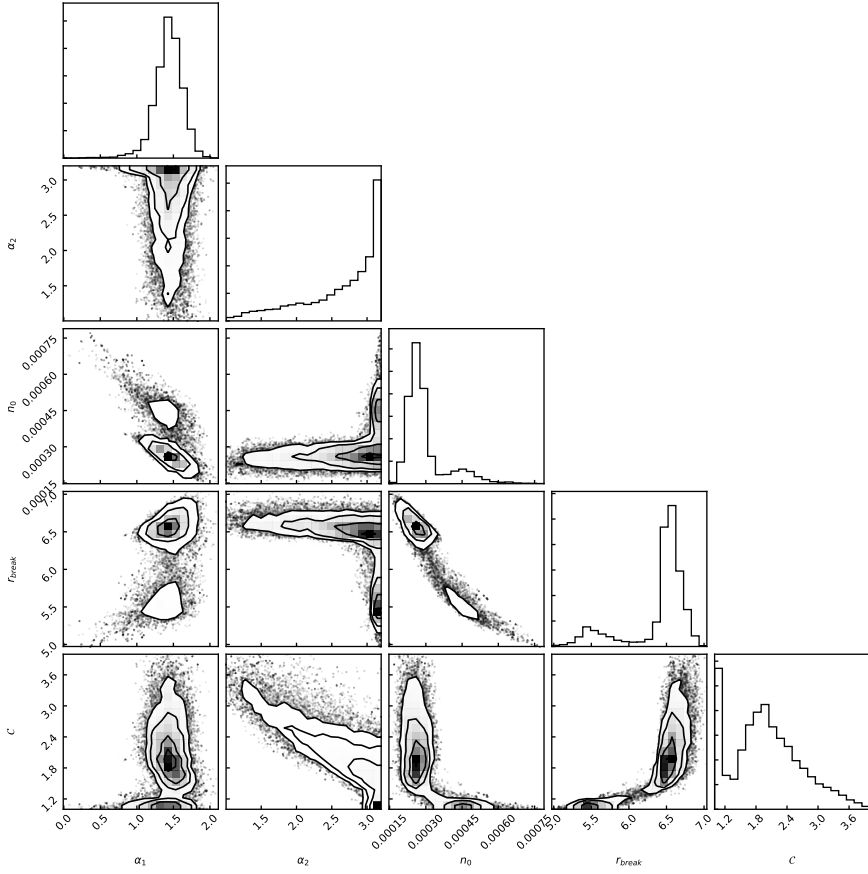
CHAPTER

4

FAST MAGNETIC FIELD AMPLIFICATION IN DISTANT GALAXY CLUSTERS

G. Di Gennaro, R.J. van Weeren, G. Brunetti, R. Cassano, M. Brüggen et al. *Nature Astronomy*, 5, 268 (2021)

Abstract. The origin and the amplification of magnetic fields during structure formation is still not understood. We report Low Frequency Array (LOFAR) observations, which reveal large-scale diffuse radio emission from galaxy clusters when the Universe was only half of its present age (i.e. $z > 0.6$). The observed synchrotron emission indicates the existence of cosmic rays and magnetic field, associated with the dilute intracluster medium. We find that the diffuse radio emission in massive, distant clusters is common, and the high radio luminosities, in spite of the strong Inverse Compton losses at high redshifts, indicates that these clusters have magnetic field strengths that are similar to those in nearby clusters. This implies that magnetic field amplification during the first phases of cluster formation is fast, which has strong implications for models of magnetogenesis.

In the present-day Universe, magnetic fields pervade galaxy clusters (Carilli & Taylor, 2002), with strengths of a few microGauss obtained from Faraday Rotation (Bonafede et al., 2010a). Evidence for cluster magnetic fields is also provided by Megaparsec-scale radio emission, namely radio halos and relics (van Weeren et al., 2019). These are commonly found in merging systems (Cassano et al., 2010b) and are characterized by a steep radio spectrum ($\alpha < -1$, where $S_\nu \propto \nu^\alpha$). It is widely believed that magnetohydrodynamical turbulence and shock-waves (re-)accelerate cosmic rays (Brunetti & Jones, 2014), producing halos and relics. The origin and the amplification of magnetic fields in clusters is not well understood. It has been proposed that turbulence drives a small-scale dynamo (Dolag et al., 2005; Subramanian et al., 2006; Ryu et al., 2008; Miniati & Beresnyak, 2015; Vazza et al., 2018; Domínguez-Fernández et al., 2019) that amplifies seed magnetic fields (primordial and/or injected by galactic outflows, as active galactic nuclei, starbursts, or winds; Donnert et al., 2018). At high redshift, radio halos are expected to be faint, due to the Inverse Compton losses and dimming effect with distance. Moreover, Faraday Rotation measurements are difficult to obtain. If detected, distant radio halos provide an alternative tool to investigate magnetic field amplification. Here, we report LOFAR observations which reveal diffuse radio emission in massive clusters when the Universe was only half of its present age, with a sample occurrence fraction of about 50%. The high radio luminosities indicate that these clusters have similar magnetic field strengths to those in nearby clusters, and suggest that magnetic field amplification is fast during the first phases of cluster formation.

To investigate this unexplored territory, we present a systematic investigation of magnetic fields in distant galaxy clusters, using the low-frequency radio telescope LOFAR (van Haarlem et al., 2013). Our observations were taken from the LOFAR Two-metre Sky Survey (LoTSS; Shimwell et al., 2019). The 120–168 MHz LoTSS survey has a spatial resolution of approximately 6″ and reaches a median sensitivity of about 70 μJy beam^{-1} (Shimwell et al., 2019). Currently, LoTSS covers about 40% of the Northern sky. The clusters were selected from the latest *Planck* Sunyaev-Zel'dovich (SZ) PSZ2 catalog (Planck Collaboration et al., 2016), at redshift above 0.6 and declination above 20 degrees. The advantage of SZ-selection is that the SZ-signal ($y \propto \int n_e T_e \, dl$, i.e. the line of sight integral of the product of the electron number density, n_e, and the electron temperature, T_e) does not suffer from redshift dimming and the integrated cluster's SZ-signal is closely related to the cluster mass ($M_{SZ,500}$). The cluster masses are taken from the *Planck* catalog, and are obtained from the integrated cluster's SZ-signal within R_{500}, where R_{500} is the radius with a density 500 times the critical density of the Universe at the given redshift.

Using this selection and taking the available LoTSS observations, we obtain a sample of 19 galaxy clusters in a redshift range of $\sim 0.6 - 0.9$ and with masses $M_{SZ,500} \sim 4 - 8 \times 10^{14}$ M$_\odot$. These objects are among
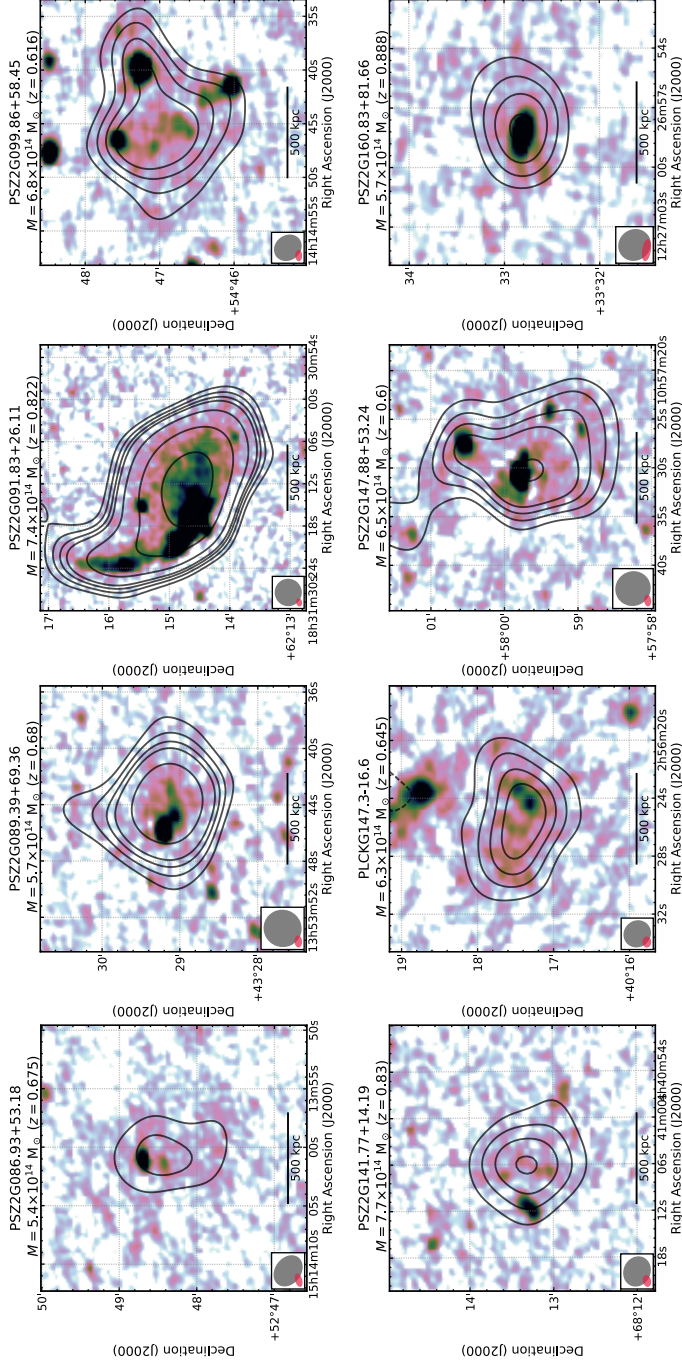
Figure 4.1: Examples of observed radio emission in our high-z galaxy cluster sample. In colorscale we show the full-resolution LOFAR images, while radio contours show the low-resolution emission after the subtraction of compact sources, displayed at the $[-2, 2, 3, 4, 5, 8, 16] \times \sigma_{\mathrm{rms}}$ level (with σ_{rms} the individual map noise; the negative contour levels are indicated with a short-dashed line style). The full- and low-resolution LOFAR beams are displayed in the bottom left corner (in pink and grey colors, respectively). In the header of each image, the galaxy cluster name, mass and redshift are reported.

Figure 4.2: X-ray images of a sub-sample of Figure 1. LOFAR radio contours are drawn as Figure 1, with the LOFAR beam displayed in the bottom left corner. The dashed white circle in each map shows the $R = 0.5R_{SZ,500}$ region, obtained from $M_{SZ,500}$. In the header of each image, the galaxy cluster name is reported.

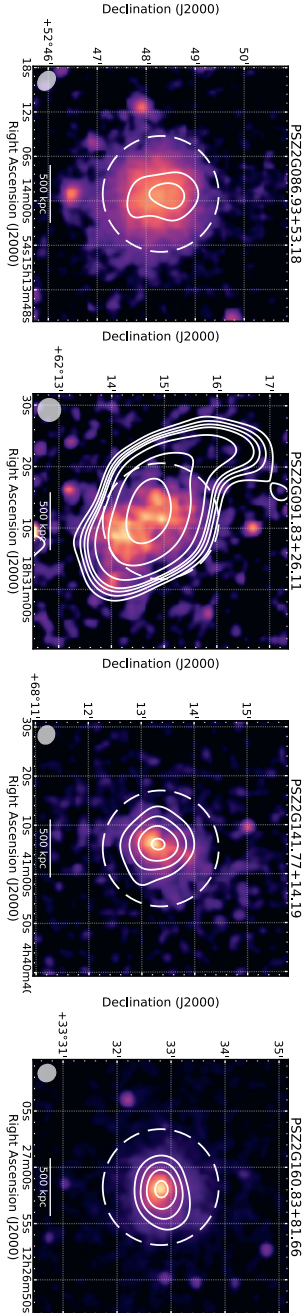the most massive structures at these redshifts. In Figure 4.1, we show a number of full-resolution (i.e. about 6″) LOFAR images of the detected diffuse radio sources from our sample, with radio contours tracing the low-resolution (approximately 15″) emission, without compact sources (for the full sample, see Figure 4.4). We find that at least nine out of the 19 clusters host diffuse radio emission (see Table 4.1). The diffuse emission is mostly centrally located in the clusters, with an overall roundish shape, and extending over scales spanning from few hundreds of kiloparsec to about one Megaparsec. In those systems that have targeted X-ray observations, the radio emission follows the thermal radiation, see Figure 4.2 (for the full sample, see Figure 4.5). We therefore classify these diffuse sources as radio halos. From the X-ray images, most clusters look dynamically disturbed. Particularly noteworthy among the clusters in our sample are PSZ2 G091.83+26.11 at $z = 0.822$, where a very bright Megaparsec-sized radio halo and relic are present, and PSZ2 G160.83+81.66 at $z = 0.888$, which hosts the most distant radio halo discovered to date, with a size of 0.7 Mpc.

Based on the radio flux density measurements and assuming $\alpha = -1.5 \pm 0.3$, we compute radio luminosities in the range $P_{1.4\text{GHz}} \sim 0.7 - 14 \times 10^{24}$ W Hz^{-1} (Table 4.1). Although most of the radiation in high-redshift halos is expected to be emitted via Inverse Compton (IC), the radio luminosities of these halos fall surprisingly within the scatter of those observed in nearby (median value $z \sim 0.2$ Cassano et al., 2013) galaxy clusters of the same mass range (see Figure 4.3a).

For synchrotron emission, the similar radio luminosities imply that the product of the number of the radio-emitting electrons and magnetic field ($N_e \times B^2$) in high-redshift clusters is similar to that in lower-redshift systems of comparable mass. Furthermore, this key observable may also suggests that both the magnetic field strength and the number of electrons in high-redshift clusters are comparable to those in low-z systems, otherwise the energetics of the halos would be very different while generating similar radio luminosities.

In re-acceleration models, the synchrotron luminosity is (Cassano et al., 2019; Brunetti & Vazza, 2020)

$$P_{\text{rad}} \propto \eta_{\text{rel}} \frac{\rho v_t^3}{L_{\text{inj}}} \frac{B^2}{B^2 + B_{\text{CMB}}^2} , \tag{4.1}$$

where $\rho v_t^3 / L_{\text{inj}}$ is the turbulent energy flux (with ρ the gas density, and v_t and L_{inj} the turbulent velocity and injection scale, respectively), η_{rel} is the fraction of the turbulent energy flux that is dissipated in the re-acceleration of seed relativistic electrons, B is the magnetic field averaged over the halo volume and $B_{\text{CMB}} = 3.25(1 + z)^2$ μG is the CMB equivalent magnetic field strength. The ratio $\frac{B^2}{B^2 + B_{\text{CMB}}^2}$ sets the fraction of non-thermal luminosity that is emitted into synchrotron radiation. The stronger en-

Table 4.1: Integrated flux density and radio luminosity of the galaxy clusters observed with LOFAR. Column 1: *Planck* cluster name. Column 2: Cluster redshift. Column 3: Largest linear size (LLS) of the diffuse radio emission. Column 4: Classification of the diffuse radio emission. Column 5: Integrated flux density of the diffuse emission (compact sources removed). Column 6: 1.4 GHz (k-corrected) radio luminosity.

Planck (PSZ) name	z	LLS [Mpc]	Classification	$S_{144\text{MHz}}$ [mJy]	$P_{1.4\text{GHz}}$ [10^{24} W Hz^{-1}]
PSZ2G045.87+57.70	0.611	–	Uncertain	–	–
PSZ2G070.89+49.26	0.610	–	–	–	–
PSZ2G084.10+58.72	0.731	–	Uncertain	–	–
PSZ2G086.28+74.76	0.699	–	Uncertain	–	–
PSZ2G086.93+53.18	0.675	0.5	Halo	7.2 ± 1.5	0.7 ± 0.4
PSZ2G087.39+50.92	0.748	–	–	–	–
PSZ2G089.39+69.36	0.680	1.0	Halo	12.5 ± 1.9	1.3 ± 0.7
PSZ2G091.83+26.11	0.822	1.2	Halo	84.3 ± 12.7	13.8 ± 8.4
		1.2	Relic	259.4 ± 38.9	–
PSZ2G092.69+59.92	0.848	–	–	–	–
PSZ2G099.86+58.45	0.616	1.2	Halo	27.8 ± 4.3	2.2 ± 1.3
PSZ2G104.74+40.42	0.690	–	Uncertain	–	–
PSZ2G126.28+65.62	0.820	0.8	Halo	8.8 ± 1.7	1.4 ± 0.6
PSZ2G127.01+26.21	0.630	–	Uncertain	–	–
PSZ2G139.00+50.92	0.600	–	–	–	–
PSZ2G141.77+14.19	0.830	0.6	Halo	8.8 ± 1.4	1.4 ± 0.7
PSZ2G141.98+69.31	0.714	–	–	–	–
PLCKG147.3–16.6	0.645	0.8	Halo	22.5 ± 3.7	$6.4 \pm 3.4^\star$
PSZ2G147.88+53.24	0.600	0.6	Halo	14.4 ± 2.3	0.9 ± 0.5
PSZ2G160.83+81.66	0.888	0.7	Halo	13.0 ± 2.1	2.7 ± 1.5

Note: Uncertainties on the 1.4 GHz radio luminosity include the flux density and spectral index uncertainties, assuming a Gaussian distribution of spectral indices ($\alpha = -1.5 \pm 0.3$), see Method. *We used the spectral index obtained combining our LOFAR observation with literature GRMT flux measurement (van Weeren et al., 2014, see the Supplementary).

ergy losses due to IC ($dE/dt \propto (1 + z)^4$) are expected to balance the effect of a potentially larger injection rate of electrons at higher redshift (due to enhanced activity of active galactic nuclei and/or star-forming galaxies). For this reason we can assume that the budget of seed particles that accumulate in the ICM at high redshift is similar to that at lower redshift (as detailed in the Methods). For a fixed budget of seed particles to re-accelerate, η_{rel} depends only on the interplay between turbulence and particles Brunetti & Jones (2014), and we assume it is independent of redshift. From the comparison of their radio luminosities, and taking into account that mergers at $z \sim 0.7 - 0.8$ generate more turbulent energy flux compared to the $z = 0.2$ sample (by a factor ~ 3, see Methods), we find

that the magnetic field in high-z halos has to be similar to that observed for local clusters, i.e. $B \geq 1$ μG. This suggests that the magnetic field amplification has been surprisingly efficient, producing a microGauss-level field in a Mpc^3 volume already at $z \sim 0.7$, i.e. within few Gyr from cluster formation (see Figure 4.3b). This result provides important insights on the origin and evolution of magnetic fields in galaxy clusters.

It is widely accepted that the small-scale turbulent dynamo plays a role in the amplification of the initial magnetic field from primordial seeds or galactic outflows (Donnert et al., 2018). Initially, the amplification operates in a kinematic regime, where the magnetic field grows exponentially with time ($B^2(t) \sim B_0^2 \exp(t\,\Gamma)$). The competition of turbulent stretching and diffusion makes this phase initially very slow, with a growth time-scale $\Gamma^{-1} = 30 L_{inj}/(\mathrm{Re}^{1/2} v_t)$ (Cho, 2014; Beresnyak & Miniati, 2016), where Re is the Reynolds number. When the magnetic and the kinetic energy densities become comparable at the viscous dissipation scale, the turbulent dynamo becomes faster and transits to a phase where the magnetic field grows linearly with time. During this phase, the magnetic field reaches equipartition with the kinetic turbulent energy at increasingly larger scales, and saturates after several eddy turnover times (several Gyrs). In this scenario, our observations then require a fast magnetic amplification during the initial exponential phase, as it needs to be much shorter than a few Gyrs. This constrains the initial field and the ICM Reynolds number, being Re $> 4 \times 10^4$ and $> 5 \times 10^3$ for $B_0 \sim 1$ nG and ~ 0.1 μG, respectively, assuming a continuous injection of turbulence with $v_t = 500$ km s^{-1} at the injection scale $L_{inj} = 1$ Mpc (Dolag et al., 2005; Donnert et al., 2018; Hitomi Collaboration et al., 2018), the ICM number density of $n = 3 \times 10^{-3}$ cm^{-3} (Markevitch & Vikhlinin, 2007), and a time available for the magnetic field amplification of ~ 3.7 Gyr (see Figure 4.3b and Methods). These values of the Reynolds number are much larger than the classical value obtained assuming Coulomb collisions (≈ 100; Brunetti & Lazarian, 2007; Cho, 2014), and would suggest that kinetic effects and instabilities play an important role in the weakly-collisional magnetized ICM (Schekochihin & Cowley, 2006). This is also in line with recent X-ray observations in the ICM of local systems that have suggested a much smaller viscosity than the isotropic value obtained only considering Coulomb collisions (Zhuravleva et al., 2019). In case of a smaller Reynolds number, our observations would require that the activity of galactic outflows and AGN in high redshift clusters is sufficient to generate microGauss fields spread on > 100 kpc scales (Xu et al., 2011). This would generate a clumpier distribution of the radio emission in the cluster volume. This can be tested with deeper observations, in combination with predictions of the spatial distribution of radio emission from cosmological magneto-hydrodynamic simulations that explore different magnetogenesis scenarios.
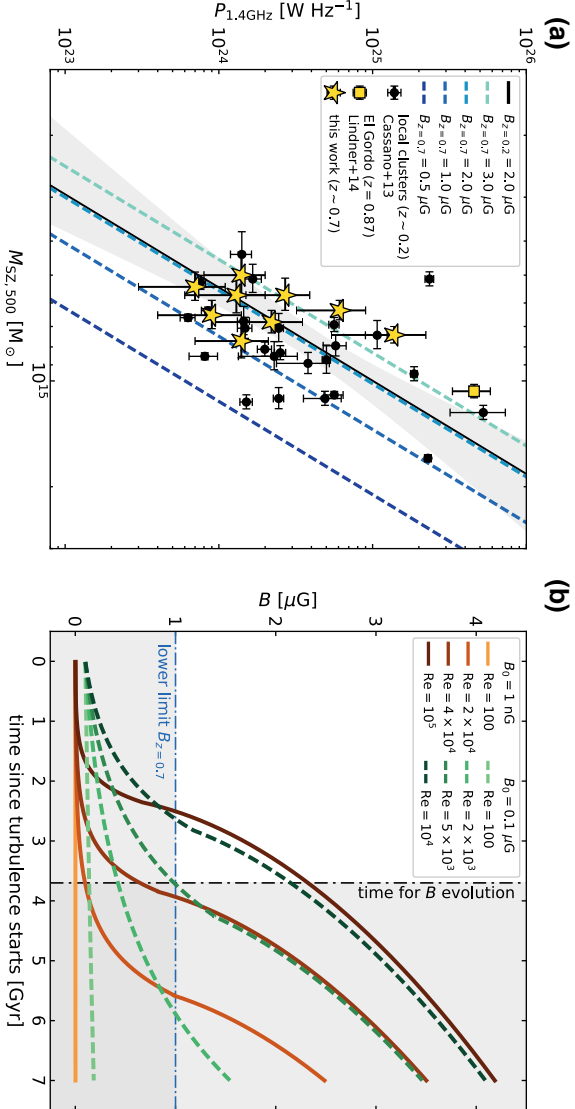
Figure 4.3: Cluster magnetic field estimation and theoretical magnetic field evolution. *Panel (a):* $P_{1.4GHz}$–M_{500} diagram for nearby (*median*(z) ~ 0.2, black dots Cassano et al., 2013) and distant (*median*(z) ~ 0.7, yellow stars) radio halos, including that in El Gordo ($z = 0.87$, Lindner et al., 2014, yellow square). Error bars on the yellow stars are obtained with 100 Monte Carlo realization of the radio luminosity, including flux density and spectral index uncertainties, while error bars on the black dots and yellow square are given by the literature. The black solid line represents the best-fit relation from the low-redshift sample, with the 95% level confidence (grey area). The blue dashed lines represent, from light to darker colors, the theoretical relations at high-z taking magnetic field strengths of 3.0, 2.0, 1.0 and 0.5 μG (assuming a typical local cluster magnetic field of 2 μG). *Panel (b):* Magnetic field growth since the start of the turbulence, based on the small-scale dynamo theory. The initial fields, B_0, are set at 1 nG (solid orange lines; from light to darker colors: Re = [100, 2×10^3, 5×10^3, 10^4]) and 0.1 μG (dashed green lines; from light to darker colors: Re = [100, 2×10^4, 4×10^4, 10^5]). The horizontal blue dot-dashed line sets the lower limit of the magnetic field strength in distant galaxy clusters (see panel (a)). The vertical black dot-dashed line shows the upper limit on the approximate time available for the magnetic field growth (see Methods).
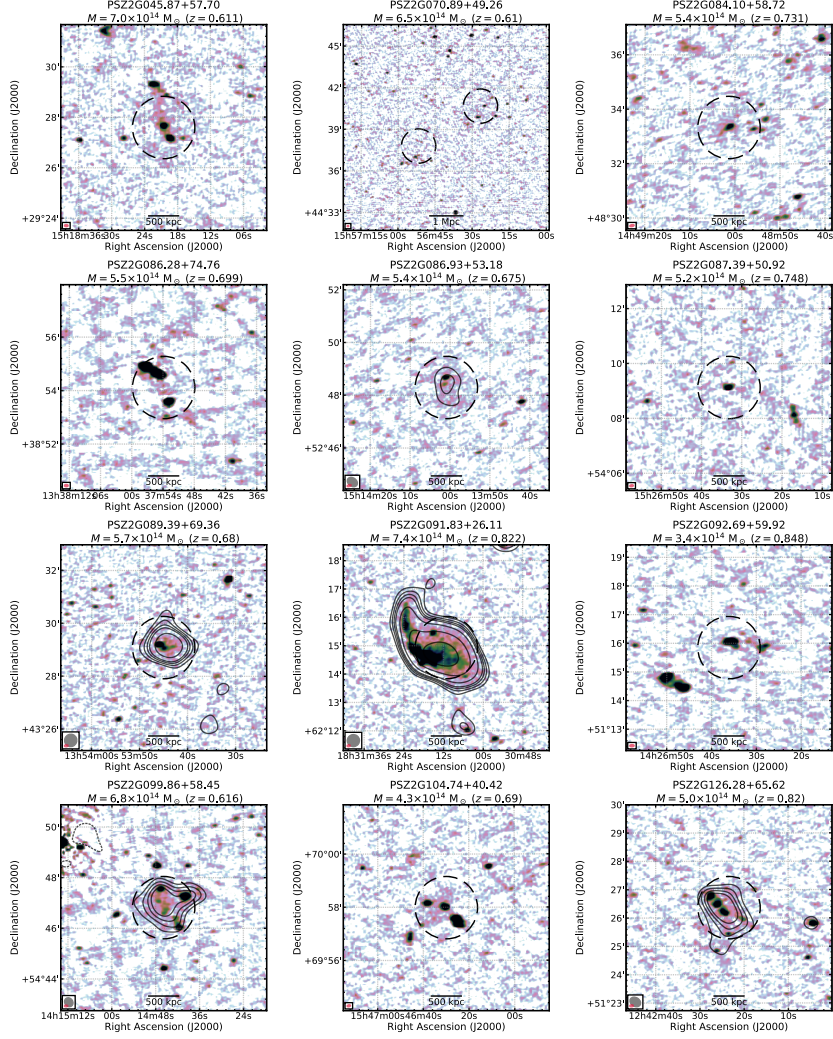
Figure 4.4: Observed radio emission in our high-z galaxy cluster sample. In colorscale we show the full-resolution LOFAR images. Low-resolution source-subtracted radio contours, displayed at the $[-2, 2, 3, 4, 5, 8, 16] \times \sigma_{\mathrm{rsm}}$ level, are shown only for clusters that host diffuse radio emission (with σ_{rsm} the individual map noise; the negative contour levels are indicated with a short-dashed line style). The full- and low-resolution LOFAR beams are displayed in the bottom left corner (in pink and grey colors, respectively). In the header of each image, the galaxy cluster name, mass and redshift are reported. The dashed black circle in each map shows the $R = 0.5R_{\mathrm{SZ},500}$ region, obtained from $M_{\mathrm{SZ},500}$.
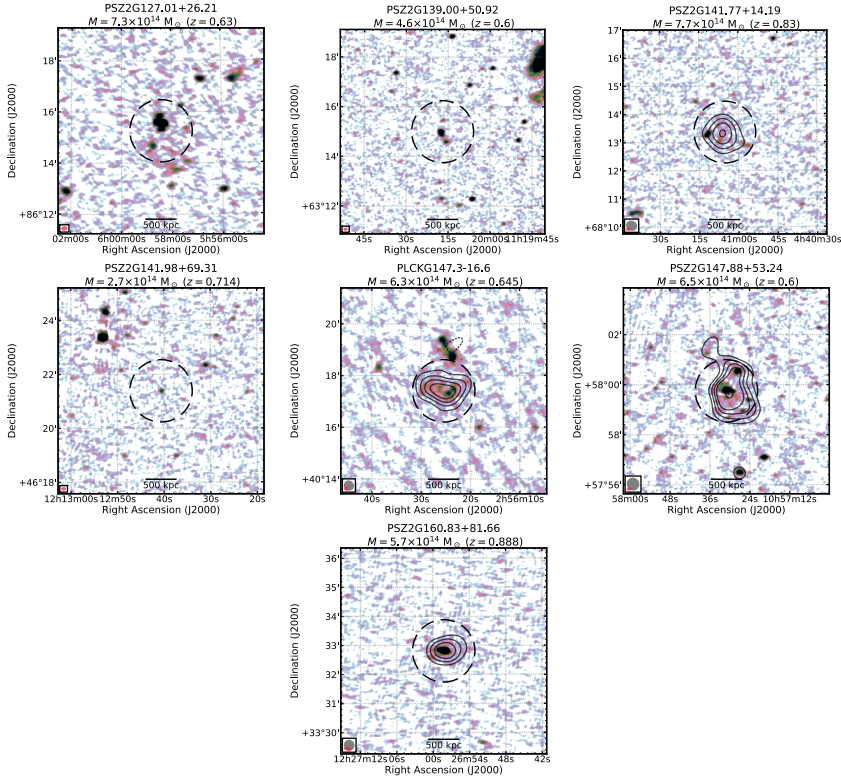
Figure 4.4: Continued

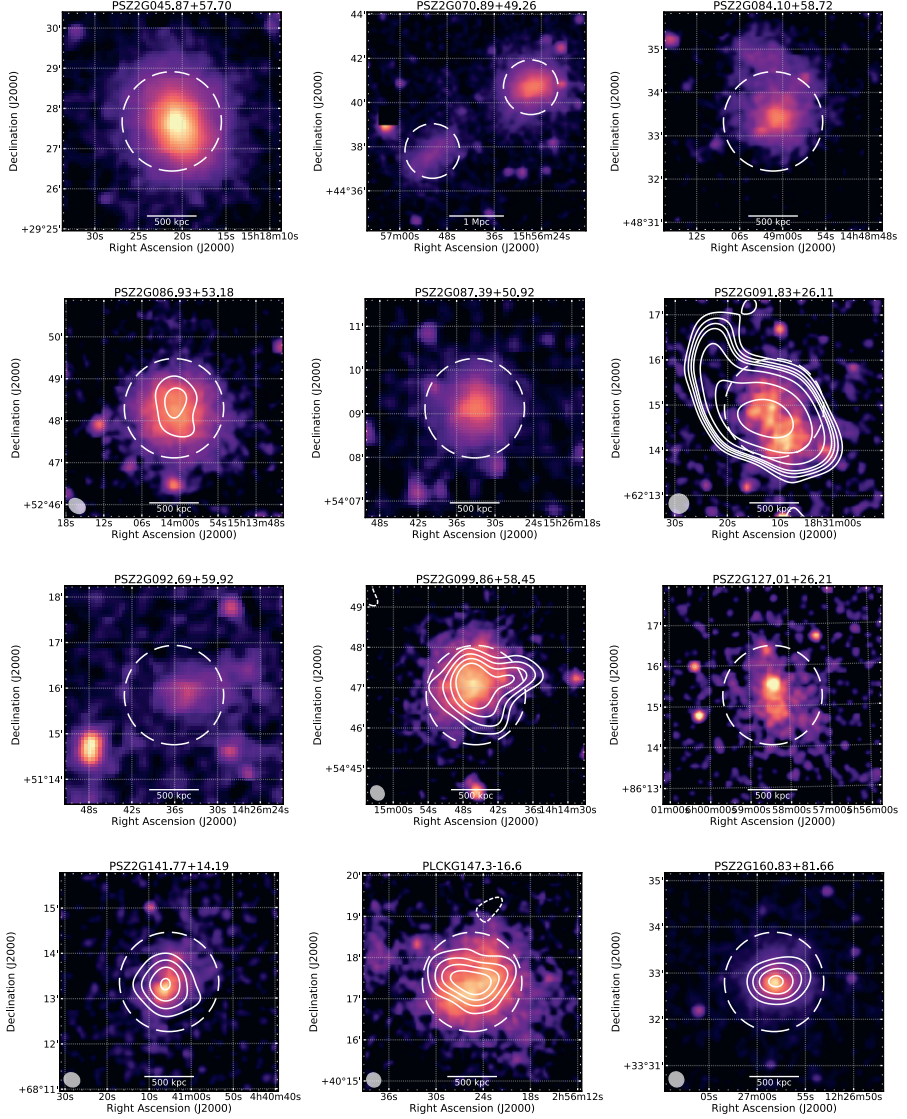**Figure 4.5: X-ray images of all the galaxy clusters in our sample.** In colorscale we show the *Chandra/XMM-Newton* images. LOFAR radio contours are drawn as Figure 1, with the LOFAR beam displayed in the bottom left corner. The dashed white circle in each map shows the $R = 0.5R_{\mathrm{SZ,500}}$ region, obtained from $M_{\mathrm{SZ,500}}$. In the header of each image, the galaxy cluster name is reported.

4.1.   Methods

Galaxy cluster sample selection

We construct our sample of high-z galaxy clusters using the latest *Planck* Sunyaev-Zel'dovich (SZ) catalog, i.e. PSZ2 (Planck Collaboration et al., 2016). This catalog provides a reliable cluster mass estimation for galaxy clusters up to $z \sim 1$. Although the exact effect of selection biases is still being debated and may overestimate the observed fraction of clusters with radio halos, there is no clear consensus in the literature that suggests the SZ sample chosen here disproportionately favours merging over relaxed clusters (Eckert et al., 2011; Rossetti et al., 2017; Andrade-Santos et al., 2017). We select all the objects at DEC $\geq 20°$, to match the part of the sky with the best LOFAR sensitivity, and $z \geq 0.6$. No mass-threshold has been applied in our cluster selection. These selection criteria result in a sample of 30 objects (see Table 4.2 in the Supplementary). The sample includes clusters where precise redshift measurements became available recently (van der Burg et al., 2016; Amodeo et al., 2018; Barrena et al., 2018; Burenin et al., 2018; Sereno et al., 2018; Streblyanska et al., 2018; Zohren et al., 2019) and a previous-discovered *Planck* cluster, i.e. PLCK G147.3–16.6 (van Weeren et al., 2014). We used the optical images from the Panoramic Survey Telescope and Rapid Response System (Pan-STARRS; Chambers et al., 2016) to refine the accuracy of the cluster center coordinates, using the brightest cluster galaxy (BCG), when detected, or approximately the center of the distribution of the galaxies. We also inspected the *Chandra* and/or *XMM-Newton* X-ray image, when available, to verify the correspondence of the cluster coordinates with the center of the thermal gas distribution. Among these 30 *Planck* clusters, 21 objects were already covered as part of the LOFAR Two-metre Sky Survey (LoTSS; Shimwell et al., 2019). From these 21 clusters one was affected by bad ionospheric observing conditions (i.e. PSZ2 G088.98+55.07) and one lays on the same line of sight of a cluster at $z = 0.3$ (i.e. PSZ2 G097.52+51.70). Those are therefore excluded from the final sample (see Figure 4.4), consisting of 19 objects at median redshift of $z = 0.7$.

LOFAR observations, data reduction, images and flux measurements

The LOFAR observations were carried out together with the LOFAR Two-metre Sky Survey (LoTSS; Shimwell et al., 2019) in the 120–168 MHz frequency range. The survey consists in 8 hours of observation for each pointing, with a field of view of $\sim 2.6°$, full resolution of about $6''$, and median noise of about 70 μJy beam^{-1}. Given the large sky coverage already achieved by the survey, our targets were often observed by more than one

pointing (see Table 4.3 in the Supplementary), which further improved our signal to noise. For each LoTSS pointing, we performed standard data reduction Shimwell et al. (2019), which includes direction-independent and dependent calibration, and imaging of the full LOFAR field of view using `prefactor` (van Weeren et al., 2016; Williams et al., 2016; de Gasperin et al., 2019), `killMS` (Tasse, 2014; Smirnov & Tasse, 2015) and `DDFacet` (Tasse et al., 2018). We additionally improved the quality of the calibration, using the products of the pipeline, subtracting all the sources outside a region of $\sim 15' \times 15'$ surrounding the target, and performing extra phase and amplitude self-calibration loops in each target sub-field. To verify the quality of the calibration, each pointing is imaged independently using `WSClean` (Offringa et al., 2014), with the wideband deconvolution mode (`channelsout=6`). For all our imaging, we employ automatic clean masks for the deconvolution. We utilize a $3\sigma_{\mathrm{rms}}$ masking threshold, with σ_{rms} the local map noise, and cleaning down to the $1\sigma_{\mathrm{rms}}$ level inside the mask. The images have a central frequency of 144 MHz, and are provided in the Figure 4.4.

All the clusters in our sample were carefully visually inspected in the full-resolution image to search for extended radio emission. To emphasize the presence of diffuse radio emission, we also produced low-resolution source-subtracted images. We first applied an uv-cut to the data, to filter out emission associated to linear sizes larger than 500 kiloparsecat the cluster redshift and to create a clean component model of the compact sources. For PSZ2 G089.39+69.36 we apply an uv-cut corresponding to 400 kpc. During this step, we employed multiscale deconvolution (Offringa & Smirnov, 2017), using scales of $[0, 4, 8, 16] \times$ pixelscale (with the pixel size of $1.5''$) to properly include and subtract somewhat extended radio galaxies. In addition, for the automatic deconvolution we lower the mask threshold to $1\sigma_{\mathrm{rms}}$ to subtract the faintest contaminating sources (see Supplementary Figure 4.6). Finally, we subtracted the compact sources model from the visibilities and tapered the uv-data to $\sim 15''$ resolution. It is important to note that in case of an extended radio galaxy, with linear size $\gtrsim 500$ kpc, this method cannot properly subtract the radio emission from the uv-data. For that reason, the extended double-lobed radio galaxy just north of PLCKG147.3–16.6 has been manually excluded and blanked in the low-resolution source-subtracted image (Figures 4.1 and 4.4).

We used these low-resolution source-subtracted images to define the largest linear size (LLS) of the diffuse radio emission, following the $2\sigma_{\mathrm{rms}}$ contour. Systems with LLS < 500 kpc were not included in our statistics. Roundish, centrally-located significantly detected sources (see the next paragraph) that follow the ICM distribution were classified as radio halos; elongated, peripheral structures were classified as radio relics. We did not identify clear examples of fossil radio plasma sources (i.e. "radio phoenices"), these typically have small sizes (i.e. 200 kpc or smaller), irregular shapes, and are not centered on the cluster center (de Gasperin

et al., 2017; Mandal et al., 2020). Similarly, we did not find clear examples of "mini-halos", as these diffuse sources usually have LLS smaller than 500 kpc and are located in dynamically relaxed systems (Giacintucci et al., 2017). Uncertain classifications, due to contamination from extended radio galaxies in the cluster region and/or ambiguous shapes, were excluded from our final statistical analysis. If we measure the LLS following the $3\sigma_{\mathrm{rms}}$ contour, we would classify 8 radio halos instead of 9 (see Table 4.4 in the Supplementary).

To determine the integrated flux densities for the radio halos, we first measured the total cluster radio flux densities (i.e. compact sources and diffuse emission) from the low-resolution image, following the $2\sigma_{\mathrm{rms}}$ radio contour to fully cover the extension of the diffuse radio emission (see Figure 4.4). In Table 4.4, we also report the integrated flux density measurements following the $3\sigma_{\mathrm{rms}}$ radio contour. We then mathematically subtracted the flux densities of the compact sources within the cluster region, measured in the full-resolution uv-cut image, to obtain the flux density associated to the diffuse radio sources (Cassano et al., 2019). For PSZ2 G091.83+21.16, which also hosts a bright radio relic, we visually separated it from the radio halo region (see Figure 4.6 in the Supplementary). The uncertainties on the flux densities are estimated adding in quadrature the σ_{rms} statistical uncertainty, the 15% systematic error associated to the LOFAR flux scale calibration, f_{cal} (Shimwell et al., 2019), and the uncertainty due to the source subtraction in the cluster region, σ_{sub} (Cassano et al., 2013), according the following Equation:

$$\Delta S = \sqrt{(f_{\mathrm{cal}}S_{144\mathrm{MHz}})^2 + \sigma_{\mathrm{rms}}^2 N_{\mathrm{beam,h}} + \sigma_{\mathrm{sub}}^2} . \qquad (4.2)$$

Here, $\sigma_{\mathrm{sub}}^2 = \sum_i \sigma_{\mathrm{rms}}^2 N_{\mathrm{beam,s}_i}$, and $N_{\mathrm{beam,h}}$ and $N_{\mathrm{beam,s}_i}$ are the number of beams covering the halo and the subtracted i sources, respectively. Uncertainties associated to possibly missed faint compact sources are not included, but these should be smaller than the systematic error associated to the LOFAR flux scale calibration.

We confirmed the presence of diffuse radio emission when the measured integrated radio flux density is larger than five times the flux uncertainty, i.e. $\frac{S_{144\mathrm{MHz}}}{\Delta S} \geq 5$ (see Column 5 in Table 4.1). Flux density measurements directly obtained from the low-resolution source-subtracted images are also provided in the Supplementary.

Finally, we calculated the k-corrected radio luminosity at 1.4 GHz:

$$P_{1.4\mathrm{GHz}} = 4\pi D_L^2 \frac{S_{1.4\mathrm{GHz}}}{(1+z)^{\alpha+1}} , \qquad (4.3)$$

with D_L the luminosity distance assuming standard ΛCDM cosmology (i.e. $H_0 = 70$ km s^{-1} Mpc^{-1}, $\Omega_m = 0.3$, and $\Omega_\Lambda = 0.7$) and $S_{1.4\mathrm{GHz}} = S_{144\mathrm{MHz}}\left(\frac{1.4\mathrm{GHz}}{144\mathrm{MHz}}\right)^\alpha$. Since the spectral indices of the radio halos are not

measured, we assume a Gaussian distribution of spectral indices α with mean value -1.5 and scatter 0.3 for computing the radio luminosity. These values were chosen to encompass the typical range of spectral indices found in radio halos (van Weeren et al., 2019), and to take into account that they could be steeper than local systems (Cassano et al., 2006). Only for PLCK G147.3–16.6, we used the spectral index obtained combining our observations with the GMRT literature data (van Weeren et al., 2014, see Supplementary). The radio luminosities are listed in Table 4.1, whose uncertainties are obtained by performing Monte Carlo simulations including the flux density uncertainties and the spectral index uncertainty.

X-ray observations and data reduction

Twelve clusters among our LOFAR sample have also *Chandra* and/or *XMM-Newton* observations (see Figure 4.5 and Table 4.5 in the Supplementary).

Chandra data were reduced using the `chav` software package (`http://hea-www.harvard.edu/~alexey/CHAV/`) with `CIAO` `v4.6` and applying the `CALDB` `v4.7.6` calibration files (Vikhlinin et al., 2005). The processing includes the application of gain maps to calibrate photon energies, filtering out counts with ASCA grade 1, 5, or 7 and bad pixels, and a correction for the position-dependent charge transfer inefficiency (CTI). Periods with count rates with a factor of 1.2 above and 0.8 below the mean count rate in the 6–12 keV band were also removed. Standard blank-sky files were used for background subtraction. The final exposure-corrected images were made in the 0.5–2.0 keV band using a pixel binning of a factor of 4 (i.e 2″) and combining the different ObsIDs together where relevant (i.e., PSZ2 G160.83+81.66).

XMM-Newton observations were reduced using version 17.0.0 of the dedicated Science Analysis System (SAS). After converting the observation data files to unfiltered event lists, we extracted light curves in bins of 100 seconds in the energy ranges 10–12 keV for the MOS and 10–14 keV for the pn detectors onboard. Good time intervals were created excluding periods when the mean count rates in these light curves were different from the corresponding mean by more than 2 standard deviations. Images were extracted in the 0.4–7.0 keV band, using only the highest quality (FLAG==0) single to quadruple MOS events (PATTERN≤12) and single to double pn events (PATTERN≤4). Images were weighted by the respective exposure maps for each detector and combined, accounting for a factor ~2.5 difference between the typical expected count rates for MOS and pn at a given source flux (due to the slightly different effective areas and the fact that the light focused by two of the XMM-Newton telescopes is split evenly between the MOS and RGS detectors). Since we are interested mostly in the morphology of high-redshift, thus relatively compact, clusters positioned

close to the aim point, the effects of vignetting and instrumental particle background are minimal and have not been corrected for this analysis.

Turbulent energy flux at high redshift

According to re-acceleration models, relativistic electrons in radio halos are re-accelerated by turbulence. Assuming that turbulence in the ICM is mainly injected by cluster mergers, then the turbulence injection rate is $\rho v_i^3 / L_{\text{inj}}$ (Cassano & Brunetti, 2005), with v_i the impact velocity between the two merging clusters, ρ the cluster mean density and L_{inj} the injection scale of turbulence (which can be assumed to be of the same order of the cluster size, about 1 Mpc at both $z = 0.2$ and $z = 0.7$). The relative impact velocity of two subclusters with virial masses M_v and ΔM_v which collide (at a distance R_v between the centers) starting from an initial distance d_0 with zero velocity is given by Sarazin (2002):

$$v_i \simeq \sqrt{2G\frac{(M_v + \Delta M_v)}{R_v}\left(1 - \frac{1}{\eta_v}\right)}. \tag{4.4}$$

Here, $d_0 = \eta_v R_v$, $\eta_v \simeq 4\left(\frac{M_v + \Delta M}{M_v}\right)^{1/3}$, and R_v is the virial radius of the main cluster, i.e., the radius at which the ratio between the average density in the cluster and the mean cosmic density at the redshift of the cluster is given by Kitayama & Suto (1996):

$$\Delta_c(z) = 18\pi^2(1 + 0.4093\,\omega(z)^{0.9052}), \tag{4.5}$$

where $\omega(z) \equiv \Omega_f(z)^{-1} - 1$ with:

$$\Omega_f(z) = \frac{\Omega_{m,0}(1 + z)^3}{\Omega_{m,0}(1 + z)^3 + \Omega_\Lambda}. \tag{4.6}$$

The virial mass, M_v, and the virial radius are thus related by:

$$R_v = \left[\frac{3M_v}{4\pi\Delta_c(z)\rho_m(z)}\right]^{1/3} \tag{4.7}$$

where $\rho_m(z) = 2.78\times10^{11}\,\Omega_{m,0}\,(1+z)^3\,h^2\,\text{M}_\odot\,\text{Mpc}^{-3}$ is the mean mass density of the Universe at redshift z. The ratio of the gas density at high and low redshift can be assumed to scale as the ratio of the two virial densities, i.e., $\frac{\rho_{v,z=0.7}}{\rho_{v,z=0.2}} = \frac{M_{v,z=0.7}}{\left(R_{v,z=0.7}\right)^3} \times \frac{\left(R_{v,z=0.2}\right)^3}{M_{v,z=0.2}}$. In the case $M_{v,z=0.7} = M_{v,z=0.2}$, the density ratio becomes simply proportional to $\left(R_{v,z=0.2}/R_{v,z=0.7}\right)^3$. Specifically, considering both at low and high-z $M_v \simeq 1.0 \times 10^{15}\,\text{M}_\odot$ and $\Delta M_v \simeq M_v/3$, the above equations give a ratio $\left(v_{i,z=0.7}/v_{i,z=0.2}\right)^3 \sim 1.5$ and $\rho_{v,z=0.7}/\rho_{v,z=0.2} \sim 2.2$. The

resulting ratio of turbulent energy flux derived at high and low redshift is then ~ 3.3.

The above calculation is approximate, because we only took kinematic effects and ΛCDM cosmology into account. We thus also use simulations in Cassano & Brunetti (2005) to calculate the injection of turbulence during simulated cluster merging histories, and derived the turbulent energy injected in the volume swept by the infalling subcluster. We found that in this case the distributions of the turbulent energy fluxes derived for clusters with $M_v \simeq 0.9 - 1.4 \times 10^{15} \, M_\odot$ in the two redshift ranges $0.2 - 0.3$ and $0.7 - 0.8$ differ by a factor of $\sim 3 - 4$, in a good agreement with the simpler derivation reported above.

Radiative lifetime and electrons acceleration in high-z clusters

In the paper we have assumed that η_{rel}, i.e. the fraction of turbulent energy flux that is absorbed by relativistic electrons (Eq. 4.1), is constant with redshift. This depends on the energy budget of the population of re-accelerated seed electrons, and on the microphysics of the nonlinear interaction between turbulence and particles. The latter is assumed to be redshift-independent (e.g. Brunetti & Lazarian, 2007). Thus, a constant η_{rel} implies a similar energy budget of the seed electrons that are accumulated in high- and low-z ICM.

More specifically, we used Eq. 4.1 to infer a lower limit to the ratio of the magnetic field in high- and low-z radio halos, thus our conclusions may change in the case that clusters at higher redshift host a population of seed electrons with a much larger energy budget. In this section we show that this possibility is very unlikely, as the higher injection rate of electrons in the ICM expected from high-redshift sources is balanced by the stronger electron energy losses.

The budget of seed electrons that accumulate in the ICM can be estimated as $N_e \propto Q_e \times T_{\mathrm{max}}$ (with Q_e the injection rate and T_{max} the maximum electron lifetime). The lifetime of relativistic electrons in the ICM, which is determined by the energy losses due to Coulomb interaction with the thermal plasma and to Inverse Compton scattering with the CMB photons and synchrotron losses, can be expressed as (Brunetti & Jones, 2014):

$$T = 4 \left\{ \frac{1}{3} \tilde{\gamma} \beta_z + \frac{\tilde{n}}{\tilde{\gamma}} \left[1.2 + \frac{1}{75} \ln \left(\frac{\tilde{\gamma}}{\tilde{n}} \right) \right] \right\}^{-1}, \qquad (4.8)$$

where we put $\tilde{\gamma} = \gamma/300$, $\tilde{n} = n/10^{-3}$, $\beta_z = \left(\frac{B}{3.2} \right)^2 + (1+z)^4$. Here, γ is the Lorentz factor, n the number density in cm^{-3} and B the magnetic field strength in μG. This lifetime increases with the energy γ of relativistic

electrons at lower energy, it reaches a maximum and then decreases as a function of γ.

The maximum of T is obtained for $\bar{\gamma} \approx \sqrt{\frac{3\bar{n}}{\beta_z}}$. For $B < B_{\mathrm{CMB}}$, it is determined by the combination of IC and Coulomb losses. Replacing this in Eq. 4.8 gives the typical lifetime of relativistic electrons that can be accumulated in the ICM on cluster lifetime and then re-accelerated during mergers:

$$T_{\mathrm{max}}\,[\mathrm{Gyr}] = 4 \left\{ \frac{\beta_z}{3}\sqrt{\frac{3\bar{n}}{\beta_z}} + \bar{n}\sqrt{\frac{\beta_z}{3\bar{n}}} \right\}^{-1} . \tag{4.9}$$

Considering that between $z = 0.2$ and $z = 0.7$ the virial density (and hence the thermal gas density n) increases by a factor of ~ 2, the maximum lifetime ratio for electrons radiating at these two redshifts is ~ 2.7, considering $B \sim 1 - 2\ \mu$G.

Several sources can inject electrons in the ICM including AGN, galaxies (galactic winds, GW) and cosmological shocks. Most of the energy of the relativistic plasma of GW and shocks is in the form of supra-thermal and relativistic protons with only a negligible fraction in the form of electrons (e.g. Brunetti & Jones, 2014).

AGN are thought to be the dominant sources of relativistic electrons in the ICM (e.g. Brunetti & Jones, 2014); this hypothesis is also supported by recent LOFAR observations, where sources of fossil radio plasma from old AGN-electrons are commonly found in galaxy clusters (de Gasperin et al., 2017; Mandal et al., 2020). The injection rate of electrons from a number of AGN in clusters, N_{AGN}, is $Q_e \sim N_{\mathrm{AGN}}n_{\mathrm{rel}}V/\Theta$, where n_{rel} is the number density of radio-emitting electrons in the jets and lobes, V is the volume of the radio plasma and Θ is the AGN life-time. The number density of radio-emitting electrons in the AGN lobes can be estimated assuming equipartition between particles and magnetic fields, i.e. $n_{\mathrm{rel}} \propto \sqrt{L_{\mathrm{syn}}/V}$, with L_{syn} the AGN synchrotron luminosity. This gives $Q_e \propto \sqrt{L_{\mathrm{syn}}V}N_{\mathrm{AGN}}/\Theta$. The linear size of radio galaxies is observed to decline with redshift, probably due to the higher density of the medium in which radio lobes and jets expand (Neeser et al., 1995; Blundell et al., 1999). Thus we attempt to account for the expected change of V with redshift assuming approximate pressure equilibrium of the lobes with the surrounding medium. This would imply $P_{\mathrm{ICM}} \propto n_{\mathrm{rel}} \propto \sqrt{L_{\mathrm{syn}}/V}$ and consequently $Q_e \propto L_{\mathrm{syn}}N_{\mathrm{AGN}}/(P_{\mathrm{ICM}}\Theta) \approx \rho_L(1+z)^3/(P_{\mathrm{ICM}}\Theta)$, where ρ_L is the luminosity density of radio AGN per comoving-volume. The luminosity density increases by a factor $\sim 2 - 2.5$ from $z \sim 0.2$ to $z \sim 0.7$ (Smolčić et al., 2017, their Fig. 5). The increase of P_{ICM} with redshift can be estimated using virial quantities, i.e. $P_{\mathrm{ICM}} \propto n_{\mathrm{ICM}}T_{\mathrm{ICM}} \propto \frac{M_v}{R_v^3}\frac{M_v}{R_v}$, implying that pressure increases by a factor ~ 2.5 from $z \sim 0.2$ to $z \sim 0.7$ for clusters with the same virial mass. We find that Q_e is only about 2-3 times larger in clusters at $z \sim 0.7$ if we assume that

the life-time of AGN does not change much with redshift. Combining this result with the maximum lifetime of the radiating electrons, that is ~ 2.7 times longer at lower redshift, suggests that the budget of seed electrons at low and high redshift is similar.

Seed electrons in the ICM can also be generated by the decay chain of inelastic proton-proton collisions (e.g. Brunetti & Lazarian, 2011; Pinzke et al., 2017). The importance of this channel depends on the energy budget of CR in the ICM, which is poorly known. A relevant contribution of re-accelerated secondary particles to radio halos is still allowed by current gamma-ray limits from FERMI-LAT (e.g. Brunetti et al., 2017). For this reason, we also compare the budget of secondary electrons accumulated in galaxy clusters at low and high redshift considering cosmological shocks as the main sources of relativistic protons. In this case, numerical simulations suggest the ratio of CR to thermal ICM pressures ($X = P_{\mathrm{CR}}/P_{\mathrm{ICM}}$) in high-$z$ clusters is generally smaller than that at low redshift (e.g. Vazza & Brüggen, 2014). The ratio of the energy budget of secondary electrons at high and low redshift can be approximately estimated as:

$$\frac{N_{e,z=0.7}}{N_{e,z=0.2}} \sim \frac{X_{z=0.7}}{X_{z=0.2}} \frac{n_{\mathrm{ICM},z=0.7} P_{\mathrm{ICM},z=0.7}}{n_{\mathrm{ICM},z=0.2} P_{\mathrm{ICM},z=0.2}} \frac{T_{\max,z=0.7}}{T_{\max,z=0.2}} , \qquad (4.10)$$

implying $N_{e,z=0.7}/N_{e,z=0.2} \sim 0.4 - 1.8$ if we assume typical CR pressure ratios measured in simulations, i.e. ~ 0.2 – 1 (Vazza et al., 2012b; Vazza & Brüggen, 2014, Figs. 14 and Fig. 12 respectively), and the ratios between physical quantities as derived above: $T_{\max,z=0.7}/T_{\max,z=0.2} \sim 1/2.7$, $P_{\mathrm{ICM},z=0.7}/P_{\mathrm{ICM},z=0.2} \sim 2.5$ and $n_{\mathrm{ICM},z=0.7}/n_{\mathrm{ICM},z=0.2} \sim 2$. Similarly to the case of AGN, this implies that the budget of secondary particles that is available at higher redshift is very similar to that at low redshift.

Reynolds number estimation

In Figure 4.3b we have used a simple model of magnetic field amplification to infer combined constraints on the initial magnetic field and on the Reynolds number. We follow the method as outlined in Beresnyak (2012). We assume that the amplification initially operates in a kinematic regime, where the magnetic field grows exponentially with time:

$$B^2(t) \sim B_0^2 \exp(t\,\Gamma) , \qquad (4.11)$$

where the time-scale of the magnetic growth is $\Gamma^{-1} \sim 30 L_d/\delta v_d$. This depends on the turbulent eddy turnover time at the viscous dissipation scale, $L_d \sim L_{\mathrm{inj}} \mathrm{Re}^{-3/4}$, $\delta v_d \sim v_t (L_d/L_{\mathrm{inj}})^{1/3}$. The factor ~ 30 is derived from simulations (Cho, 2014; Beresnyak & Miniati, 2016), and accounts for the less effective stretching of the field lines due to the turbulent diffusion. When the

magnetic and the kinetic energy densities become comparable at the viscous dissipation scale ($B(t)^2/8\pi \sim 1/2\rho\delta v_d^2$), the turbulent dynamo transits to a phase where the magnetic field grows linearly with time. This phase is known as the non-linear regime because the magnetic field (Reynolds stress) becomes dynamically important. From Eq. 4.11, this transition occurs at a time:

$$t_* \sim 60\frac{L_{\text{inj}}}{v_t}\text{Re}^{-1/2}\ln\left(\frac{B_*}{B_0}\right) \qquad (4.12)$$

where $B_* \sim \sqrt{4\pi\rho}\,v_t\text{Re}^{-1/4}$. According to simulations, in the non-linear regime, i.e. for time $t \geq t_*$, we assume that a constant fraction of the turbulent kinetic energy flux, η_B, is channeled into magnetic field energy ($\eta_B = 0.05$, Beresnyak, 2012). Therefore, the evolution of the magnetic field with time is:

$$B^2(t) \sim B_*^2 + 4\pi\frac{\rho v_t^3}{L_{\text{inj}}}\eta_B(t - t_*)\,. \qquad (4.13)$$

In the calculations shown in Figure 4.3b, we assume a continuous injection of turbulence with $v_t = 500$ km s^{-1} at the injection scale $L_{\text{inj}} = 1$ Mpc, and $n = \rho/m_p = 3\times10^{-3}$ cm^{-3} (with m_p the proton mass). We note that a situation of continuous injection of turbulence with these parameters is appropriate for a dynamically active and massive cluster (Dolag et al., 2005; Donnert et al., 2018; Hitomi Collaboration et al., 2018; Markevitch & Vikhlinin, 2007) and consequently calculations would overestimate the magnetic field strength if extrapolated for a time scale that is much larger than that of a typical merger.

An important parameter in the model is the time when the turbulent dynamo starts, as it fixes the time available for magnetic field amplification up to the epoch of observation. Here, we assume that the turbulent dynamo starts when the clusters have formed a quarter of their mass. This implies that the time available for the amplification is of about 3.7 Gyr (Fakhouri et al., 2010; Giocoli et al., 2012). Assuming a turbulent velocity of $v_t = 500$ km s^{-1} at an earlier stage in the cluster life-time is optimistic, as the cluster would be too small. Since the turbulent energy flux is proportional to v_t^3, the effect of much weaker turbulence at earlier epochs is not relevant for the magnetic field evolution. Conversely, if we assume that the dynamo started later in the cluster life-time, e.g. when it has assembled half of its mass, it results in more stringent Reynolds numbers, since the time available for the amplification is shorter (about 2.7 Gyr). Lower turbulent velocities and lower number densities would imply higher values of the Reynolds number. On the other hand, higher turbulent velocities would imply a smaller value of Re. However, even if we consider $v_t = 800$ km s^{-1} (Dolag et al., 2005; Donnert et al., 2018), i.e. the case of a large turbulent pressure of about 30–40% the ICM pressure, we obtain Reynolds numbers

that are only three times smaller than the case with $v_t = 500$ km s^{-1}. We also mention that in real clusters turbulence is induced in a medium that is highly stratified due to gravity (Roh et al., 2019). In this case, the transport of magnetised turbulent eddies toward the outskirts could make the turbulent dynamo slightly less efficient than in our model, implying that our constraints on the Reynolds number are conservative.

4.2. Supplementary

Physical properties of the galaxy clusters in the sample

Here, we report the properties of the galaxy clusters selected from the *Planck* sample (Table 4.2).

LOFAR images

In this section we present the LOFAR full resolution source-subtracted images of the clusters in our sample (Figure 4.6). The radio contours of the subtracted radio galaxies overlaid, starting from $3\sigma_{\mathrm{rms}}$, with σ_{rms} the noise of the full-resolution uv-cut map, spaced by a factor of 2. The dashed contours display the $-3\sigma_{\mathrm{rms}}$ contour level.

Below we provide a brief description of the galaxy clusters (ObsIDs list is reported in Table 4.3).

- PSZ2 G045.87+57.70 ($z = 0.611$) shows extended diffuse radio emission in the north-south direction, which is unresolved in the east-west direction. For this reason, and since it is not located in the cluster center, we classify this emission as "uncertain". The X-ray emission also looks elongated in the north-south direction.

- PSZ2 G070.89+49.26 ($z = 0.610$) is actually a double cluster (Planck Collaboration et al., 2015). In both systems, there is no evidence of diffuse radio emission (see Figure 4.4).

- PSZ2 G084.10+58.72 ($z = 0.731$) does not show clear presence of extended diffuse emission in the full resolution image. The X-ray emission suggests a dynamically disturbed system.

- An extended, probably foreground, radio galaxy contaminates the radio emission from PSZ2 G086.28+74.76 ($z = 0.699$). We cannot classify this cluster hosting diffuse radio emission. No X-ray observations are available.

- PSZ2 G086.93+53.18 ($z = 0.675$) is the faintest candidate halos in our sample. We find hints of diffuse radio emission on the $2\sigma_{\mathrm{rms}}$

Table 4.2: List of galaxy clusters from Planck SZ Catalog with DEC $\geq 20°$ and $z \gtrsim 0.6$

PSZ name	z	RA$_{J2000}$ [deg]	DEC$_{J2000}$ [deg]	M$_{SZ,500}$ [10^{14} M$_\odot$]	LOFAR	Chandra	XMM	Ref.
PSZ2G032.31+66.07	0.609	219.35404	+24.3986	5.6 ± 0.8				(a,g,i)
PSZ2G045.87+57.70	0.611	229.58737	+29.46957	7.0 ± 0.7			✓	(a)
PSZ2G066.34+26.14	0.630	270.277	+39.86853	4.8 ± 0.7	✓			(a,g,i)
PSZ2G069.39+68.05	0.762	215.40979	+38.35494	–				(a,d,g)
PSZ2G070.89+49.26	0.610	239.21558	+44.63012	6.5 ± 0.7		✓		(a)
PSZ2G073.31+67.52	0.609	215.16250	+39.91500	6.7 ± 0.6				(a)
PSZ2G084.10+58.72	0.731	222.25554	+48.55556	5.4 ± 0.6	✓	✓		(a)
PSZ2G085.95+25.23	0.782	277.6164	+56.8823	5.4 ± 0.6	✓			(a,b,i)
PSZ2G086.28+74.76	0.699	204.47446	+38.90189	$5.3^{+0.7}_{-0.8}$	✓			(a,g,i)
PSZ2G086.93+53.18	0.675	228.50446	+52.81074	5.4 ± 0.5	✓			(a)
PSZ2G087.39+50.92	0.748	231.63821	+54.15210	$5.2^{+0.5}_{-0.6}$	✓	✓		(a)
PSZ2G088.98+55.07	0.702	224.74384	+52.81730	4.9 ± 0.6	✓	✓		(a)
PSZ2G089.39+69.36	0.680	208.43748	+43.48476	5.7 ± 0.7	✓			(a)
PSZ2G091.83+26.11	0.822	277.78430	+62.24770	7.4 ± 0.4	✓			(a,b)
PSZ2G092.69+59.92	0.848	216.65041	+51.26417	4.5 ± 0.5	✓	✓		(a,d,i)
PSZ2G097.52+51.70	0.700	223.8588	+58.85514	5.2 ± 0.5	✓	✓		(a)
PSZ2G099.86+58.45	0.616	213.6909	+54.78029	6.8 ± 0.5	✓		✓	(a,e,f)
PSZ2G100.22+33.81	0.620	258.43971	+69.36335	–				(a,g)
PSZ2G104.74+40.42	0.690	236.6082	+69.95975	$4.3^{+0.5}_{-0.6}$	✓			(a,c)
PSZ2G106.15+25.75	0.630	284.25043	+74.93208	4.6 ± 0.7	✓			(a,h)
PSZ2G108.27+48.66	0.674	52.79720	+65.65932	4.9 ± 0.5	✓	✓		(a,c)
PSZ2G126.28+65.62	0.820	190.5975	+51.43944	5.0 ± 0.7	✓	✓		(a,d,i)
PSZ2G126.57+51.61	0.815	187.4492	+65.35361	5.8 ± 0.6				(a,d,i)
PSZ2G127.01+26.21	0.630	89.6057	+86.2544	$7.3^{+0.8}_{-0.9}$		✓		(a)
PSZ2G139.00+50.92	0.600	170.070701	+63.24996	$4.6^{+0.7}_{-0.8}$	✓			(a,g,i)
PSZ2G141.77+14.19	0.830	70.27167	+68.22275	7.7 ± 0.9	✓	✓		(a,h)
PSZ2G141.98+69.31	0.714	183.16929	+46.35641	$4.1^{+0.9}_{-0.9}$	✓			(a,g,i)
PLCKG147.3−16.6	0.645	44.105898	+40.290140	6.3 ± 0.4	✓		✓	(a,b,j)
PSZ2G147.88+53.24	0.600	164.37923	+57.99591	6.5 ± 0.6	✓	✓		(a,g,i)
PSZ2G160.83+81.66	0.888	186.74267	+33.54682	$5.7^{+0.6}_{-0.7}$	✓	✓	✓	(a)

References: (a) Planck Collaboration et al. (2016); (b) Amodeo et al. (2018), (c) Barrena et al. (2018), (d) Burenin et al. (2018), (e) Cassano et al. (2019), (f) Sereno et al. (2018), (g) Streblyanska et al. (2018), (h) van der Burg et al. (2016), (i) Zohren et al. (2019), (j) van Weeren et al. (2014).

level, located southward of the BCG. The X-ray emission is spherically symmetric within the $R = 0.5R_{500}$ region.

- PSZ2 G087.39+50.92 ($z = 0.748$) does not show extended radio emission. The X-ray image suggests this is a dynamically relaxed system.

- PSZ2 G089.39+69.36 ($z = 0.680$) hosts a bright radio halo with a size of about 1 Mpc. No X-ray observations are available for this cluster.

- PSZ2 G091.83+26.11 ($z = 0.822$) hosts the brightest radio halo in our sample ($S_{144\mathrm{MHz}} = 84.3 \pm 12.7$ mJy). Moreover, it also hosts an elongated 1.2 Mpc arc-like radio source. No clear optical counterparts is found for this source. The brightest region of this arc is also visible in a short Very Large Array (VLA) observation, which also allowed us to define the relic region for the flux density measurements (see the blue polygon in Figure 4.7). Future spectral index and polarization studies would help to verify the different contributions of the halos and relic. Combining our LOFAR flux density measurements with that of the VLA yields an integrated spectral index of $\alpha \sim -1.6$ (also see the following Section). The steep spectral index, the lack of clear optical counterparts and the elongated shape, strongly suggest we are observing a radio relic. Shallow X-ray observations also show disturbed thermal emission, elongated in the north-south direction, suggesting that the cluster is in a merging state (second panel in Figure 4.2). The radio relic is located parallel to the putative merger axis, and not perpendicularly to it as it is usually observed in low-redshift systems. This suggests a merger that is more complex than a head-on binary merger.

- PSZ2 G092.69+59.92 ($z = 0.848$) does not show extended radio emission. The dynamical state of this cluster is unclear from the X-ray image.

- The radio halo in PSZ2 G099.86+58.45 ($z = 0.616$) was recently studied (Cassano et al., 2019), combining LOFAR, VLA and *XMM-Newton* observations. The cluster is thought to undergo a merger event. Additionally, it has been claimed (Sereno et al., 2018) that this cluster is located in a particularly high-density environment, which might have favored the formation of the halo.

- PSZ2 G104.74+40.42 ($z = 0.690$) shows hints of presence of extended radio emission. After subtracting the flux density of the radio galaxies in the cluster volume, the resulting diffuse radio emission result to be $S_{144\mathrm{MHz}} < 5\Delta S$, hence it is classified as "uncertain" detection. No X-ray observations are available.

- Although the radio emission is dominated by three radio galaxies, PSZ2 G126.28+65.62 ($z = 0.820$) shows evidence of diffuse radio emission, spanning a region of about 800 kpc. No X-ray observations are available.

- All the radio emission detected in PSZ2 G127.01+26.21 ($z = 0.630$) is associated with the radio galaxies. The X-ray emission is peaked on the BCG, appearing elongated in the north-south direction.

- A small double-lobed radio galaxy is observed in the center of PSZ2 G139.00+50.92, without hints of diffuse emission. No X-ray observations are available.

- The radio halo in PSZ2 G141.77+14.19 extends over 600 kpc. The X-ray emission appears very disturbed and elongated in the northwest-southeast direction.

- PSZ2 G141.98+69.31 ($z = 0.714$) does not show extended radio emission. No X-ray observations are available.

- Diffuse radio emission in PLCK G147.3–16.6 ($z = 0.645$) extends in the east-west direction over 800 kpc. Optical and X-ray data suggest the cluster is undergoing a merger event. The radio halo was earlier discovered using GMRT observations (van Weeren et al., 2014). Using the GMRT and LOFAR halo flux densities, we calculate an integrated spectral index $\alpha = -0.77 \pm 0.15$. This value is flatter than what we assume for the other radio halos in our sample, but it is consistent, within the uncertainties, with other literature radio halos (Feretti et al., 2012). Further studies on the spectral index of this source are however needed.

- The radio emission in PSZ2 G147.88+53.24 ($z = 0.600$) has a largest size of about 600 kpc. The emission encompasses the BCG in the south-west direction. No X-ray observations are available for this cluster.

- PSZ2 G160.83+81.66, at $z = 0.888$, represents the highest redshift object of our sample. Diffuse radio emission is detected extending over 700 kpc centered around the central BCG. The radio emission follows the thermal gas emission (see last panel in Figure 4.2). This is the most distant radio halo discovered so far. Deep X-ray observations (Maughan et al., 2007) suggest this cluster has a relaxed morphology (see also last panel in Figure 4.2). However, no signs of central cooling have been found from an X-ray temperature analysis, suggesting a possible earlier merger event (Maughan et al., 2007). In agreement with this, a weak lensing analysis revealed a bimodal mass distribution (Jee & Tyson, 2009).
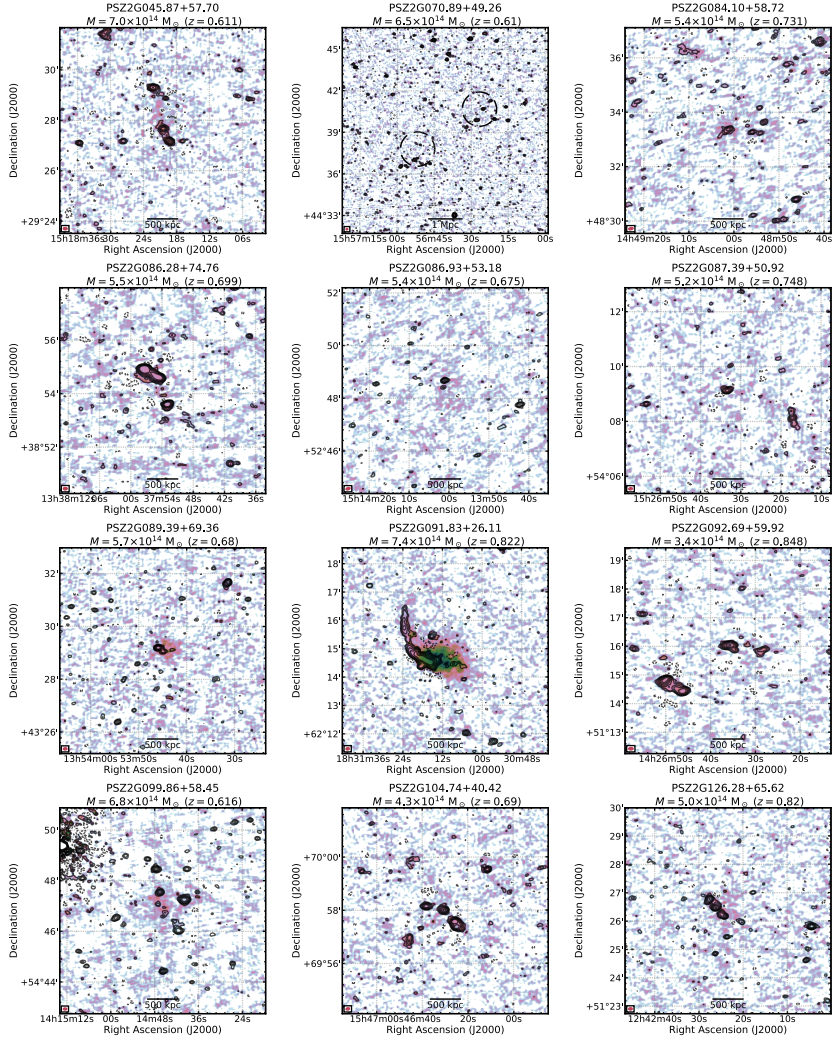
Figure 4.6: Observed diffuse radio emission in our high-z galaxy cluster sample. In colorscale we show the full-resolution LOFAR images of the clusters in our sample after the subtraction of the compact sources. Radio contours show the subtracted compact sources, at the same resolution. The contour levels are drawn at $2\sigma_{\mathrm{rms}} \times [-1, 1, 2, 4, \dots]$, with σ_{rms} the noise level of the full-resolution uv-cut image (with the short-dashed line displaying the negative contour). In the header of each image, the galaxy cluster name, mass and redshift are reported. The dashed black circle in each map shows the $R = 0.5R_{\mathrm{SZ},500}$ region, obtained from $M_{\mathrm{SZ},500}$.
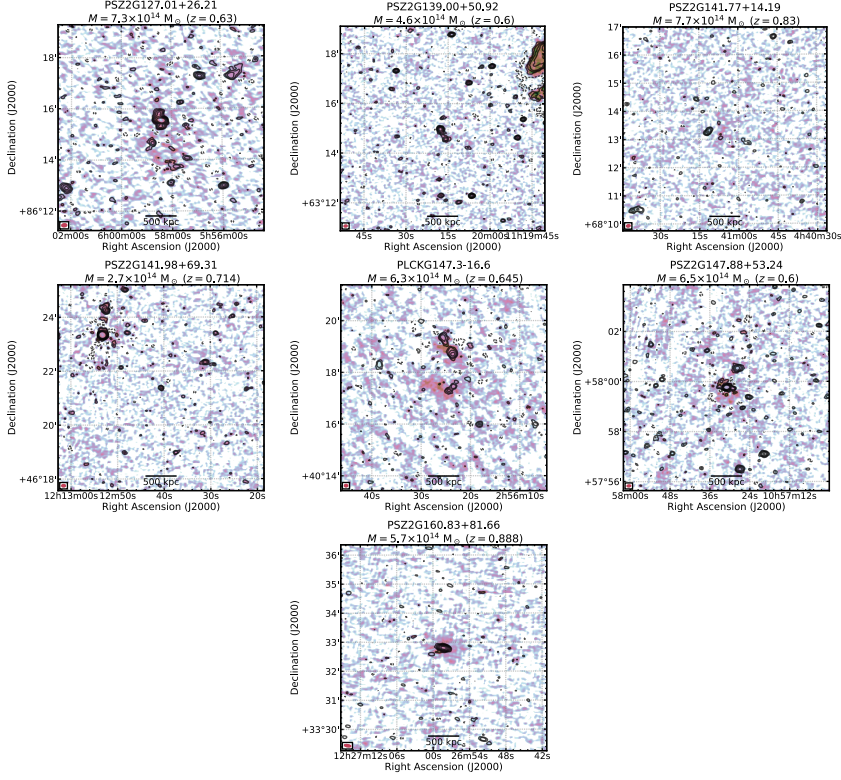
Figure 4.6: Continued.

Additional flux density measurements

In Table 4.1 we reported the flux density measurements and the largest linear size of the candidate radio halos obtained following the $2\sigma_{\mathrm{rms}}$ radio contour in the low-resolution source-subtracted image. Here, we report the same analysis but following the $3\sigma_{\mathrm{rms}}$ radio contour (see Table 4.4). Moreover, we also provide flux density measurements from the low-resolution source-subtracted images, following both the 2 and $3\sigma_{\mathrm{rms}}$ radio contours. The uncertainty on the flux densities are calculated as Equation 2 but, in this case, the term σ^2_{sub} refers to the uncertainty due to the source subtraction in the *uv* plane, i.e. a fraction (about 3%) of the total flux of the subtracted radio galaxies (see Cassano et al., 2013; Hoang et al., 2017).

Table 4.3: ObsIDs list of the LOFAR observations.

PSZ name	ObsID(s)
PSZ2G045.87+57.70	P230+27, P228+30, P231+30
PSZ2G070.89+49.26	P236+45, P240+45
PSZ2G084.10+58.72	P221+47,P223+50,P225+47
PSZ2G086.28+74.76	P203+37, P204+40
PSZ2G086.93+53.18	P227+55, P227+53, P231+53
PSZ2G089.39+69.36	P207+45, P209+42
PSZ2G091.83+26.11	P275+60, P281+63, P275+63, P280+60
PSZ2G092.69+59.92	P214+52, P215+50, P219+52, P219+50
PSZ2G099.86+58.45	P209+55, P214+55
PSZ2G104.74+40.42	P240+70, P232+70
PSZ2G126.28+65.62	P33Hetdex08, P29Hetdex19, P30Hetdex06
PSZ2G127.01+26.21	P098+84, P113+87, P066+87
PSZ2G139.00+50.92	P168+62, P168+65
PSZ2G141.77+14.19	P075+69, P072+67, P068+69
PSZ2G141.98+69.31	P20Hetdex17, P23Hetdex20, P19Hetdex17
PLCKG147.3–16.6	P044+39, P045+41, P042+41
PSZ2G147.88+53.24	P166+60, P165+57
PSZ2G160.83+81.66	P185+35, P188+35, P188+32, P185+32

Additional radio maps and integrated spectral index for PSZ2 G091.83+26.11

PSZ2 G091.83+26.11 was observed with the Very Large Array (VLA), in the 1–2 GHz frequency band, in the B-array configuration on the 22nd of March 2015 (project code: 15A-270). The total time on source is about 40 minutes. Standard VLA data reduction (Di Gennaro et al., 2018) has been performed on the dataset with CASA v5.3 (McMullin et al., 2007). Applied corrections included the antenna delays, bandpass, cross-hand delays, and polarisation leakage and angles using the primary calibrators 3C286 and 3C147. These calibration solutions were applied to the target, and self-calibration was performed to refine the amplitudes and phases. The final image was produced using w-projection (Cornwell et al., 2005, 2008), Briggs weighting with robust=0 and nterms=3 (Rau & Cornwell, 2011). The correction for the primary beam attenuation has also been applied. The final image resolution is $3.8'' \times 3.0''$, with a noise of $\sigma_{\rm rms} = 50.7\ \mu$Jy beam^{-1}. Only the brightest part of the relic is visible in this observation (Supplementary Figure 3). We measured a radio flux density of $S_{1.5\mathrm{GHz}} \sim 5.5$ mJy. Combined LOFAR-VLA images yields an integrated spectral index of $\alpha \sim -1.6$. The lack of short baselines and short on-source integration time,

Table 4.4: Integrated flux density and radio luminosity of the galaxy clusters observed with LOFAR. Column 1: *Planck* cluster name. Column 2: Cluster redshift. Column 3: Largest linear size (LLS), following the 2 and $3\sigma_{rms}$ radio contours. Columns 4 and 5: The integrated flux density and radio luminosity measurements, following the $2\sigma_{rms}$ and $3\sigma_{rms}$ contours (from Figure 4.4), and, for both, the values using the flux-subtraction (see Method) and the uv-subtraction (see above) strategies.

Planck (PSZ2) name	z	LLS [Mpc] $2\sigma_{rms}$	LLS [Mpc] $3\sigma_{rms}$	Classification	$S_{144\mathrm{MHz}}$ [mJy] $2\sigma_{rms}$ flux sub	$S_{144\mathrm{MHz}}$ $2\sigma_{rms}$ uv-sub	$S_{144\mathrm{MHz}}$ $3\sigma_{rms}$ flux sub	$S_{144\mathrm{MHz}}$ $3\sigma_{rms}$ uv-sub	$P_{1.4\mathrm{GHz}}$ [10^{24} W Hz^{-1}] $2\sigma_{rms}$ flux sub	$P_{1.4\mathrm{GHz}}$ $2\sigma_{rms}$ uv-sub	$P_{1.4\mathrm{GHz}}$ $3\sigma_{rms}$ flux sub	$P_{1.4\mathrm{GHz}}$ $3\sigma_{rms}$ uv-sub
PSZ2G045.87+57.70	0.611	–	–	Uncertain	–	–	–	–	–	–	–	–
PSZ2G070.89+49.26	0.610	–	–	Uncertain	–	–	–	–	–	–	–	–
PSZ2G084.10+58.72	0.731	–	–	Uncertain	–	–	–	–	–	–	–	–
PSZ2G086.28+74.76	0.699	–	–	Uncertain	–	–	–	–	–	–	–	–
PSZ2G086.93+53.18	0.675	0.5	0.3	Halo/Uncertain	7.2 ± 1.5	7.9 ± 1.6	4.3 ± 0.8	5.2 ± 1.0	0.7 ± 0.4	0.8 ± 0.5	0.5 ± 0.2	0.5 ± 0.3
PSZ2G087.39+50.92	0.748	–	–	Uncertain	–	–	–	–	–	–	–	–
PSZ2G089.39+69.36	0.680	1.0	0.9	Halo	12.5 ± 1.9	11.9 ± 1.7	10.3 ± 1.5	10.1 ± 1.5	1.3 ± 0.7	1.1 ± 0.6	1.0 ± 0.6	0.9 ± 0.5
PSZ2G091.83+26.11	0.822	1.2	1.2	Halo	84.3 ± 12.7	73.0 ± 9.0	83.9 ± 11.4	72.8 ± 9.0	13.8 ± 8.4	12.4 ± 5.5	12.6 ± 5.6	11.8 ± 4.0
				Relic	259.4 ± 38.9	–	–	–	–	–	–	–
PSZ2G092.69+59.92	0.848	1.2	1.0	Halo	27.8 ± 4.3	21.5 ± 3.6	21.0 ± 3.2	17.6 ± 3.0	2.2 ± 1.3	1.7 ± 0.9	1.6 ± 1.0	1.4 ± 0.9
PSZ2G099.86+58.45	0.616	–	–	Uncertain	–	–	–	–	–	–	–	–
PSZ2G104.74+40.42	0.690	–	–	Uncertain	–	–	–	–	–	–	–	–
PSZ2G126.28+65.62	0.820	0.8	0.8	Halo	8.8 ± 1.7	9.2 ± 1.8	5.5 ± 1.1	6.3 ± 1.2	1.4 ± 0.6	1.7 ± 0.9	0.9 ± 0.4	1.4 ± 0.9
PSZ2G127.01+26.21	0.630	–	–	Uncertain	–	–	–	–	–	–	–	–
PSZ2G139.00+50.92	0.600	–	–	Uncertain	–	–	–	–	–	–	–	–
PSZ2G141.77+14.19	0.830	0.6	0.5	Halo	8.8 ± 1.4	9.0 ± 1.6	4.7 ± 0.8	6.4 ± 1.2	1.4 ± 0.7	1.6 ± 0.7	0.7 ± 0.4	1.1 ± 0.6
PSZ2G141.98+69.31	0.714	–	–	Uncertain	–	–	–	–	–	–	–	–
PLCKG147.3−16.6	0.645	0.8	0.8	Halo	22.5 ± 3.7	23.2 ± 3.9	19.0 ± 3.0	19.4 ± 3.8	6.4 ± 3.4	6.7 ± 2.7	4.9 ± 1.7	5.9 ± 2.0
PSZ2G147.88+53.24	0.600	0.6	0.6	Halo	14.4 ± 2.3	11.8 ± 2.3	11.1 ± 1.7	10.0 ± 2.1	0.9 ± 0.5	0.7 ± 0.5	0.8 ± 0.4	0.8 ± 0.6
PSZ2G160.83+81.66	0.888	0.7	0.5	Halo	13.0 ± 2.1	10.6 ± 2.0	10.2 ± 1.6	7.9 ± 1.6	2.7 ± 1.5	2.2 ± 1.1	1.9 ± 1.0	1.7 ± 0.6

means that the radio halo cannot be detected.

Figure 4.7: VLA-LOFAR comparison of PSZ2G091.83+26.11. In colorscale we show the 1–2 GHz B-array VLA radio image of the cluster. The full-resolution LO-FAR radio contours are displayed at $3\sigma_{\mathrm{rms}} \times [-1, 1, 2, 4, \dots]$ level, with σ_{rms} the map noise and negative contours displayed with the short-dashed line, as comparison. The VLA and LOFAR beams are displayed in the bottom left corner, in pink and black respectively. The blue and red boxes show the regions where the flux densities were extracted, for the relic and the halo respectively.

X-ray observations and images

Here we list the summary (Supplementary Table 4.5) of the clusters with X-ray observations. For those clusters which had both *Chandra* and *XMM-Newton* observations, we only show the best case, i.e., a compromise between high resolution and exposure time.

Table 4.5: Supplementary Table 4: ObsIDs list of the X-ray observations.

PSZ name	Satellite	ObsID(s)	Total exposure time [ks]
PSZ2G045.87+57.70	*XMM-Newton*	0693661101	32
PSZ2G070.89+49.26	*XMM-Newton*	0693661301	50
PSZ2G084.10+58.72	*XMM-Newton*	783880901	86
PSZ2G086.93+53.18	*XMM-Newton*	0783880701	81
PSZ2G087.39+50.92	*XMM-Newton*	0783881201	22
PSZ2G091.83+26.11	*Chandra*	18285	23
PSZ2G092.69+59.92	*XMM-Newton*	0783880401 0783881901	107
PSZ2G099.86+58.45	*XMM-Newton*	0693660601 0693662701 0723780301	63
PSZ2G127.01+26.21	*Chandra*	18286	16
PSZ2G141.77+14.19	*Chandra*	18289	21
PLCKG147.3–16.6	*XMM-Newton*	0679181301	10
PSZ2G160.83+81.66	*Chandra*	3180 5014	67

CHAPTER

5

DOWNSTREAM DEPOLARIZATION IN THE SAUSAGE RELIC: A 1–4 GHZ VERY LARGE ARRAY STUDY

Abstract. Radio relics are elongated sources related to shocks driven by galaxy cluster merger events. Although these objects are highly polarized at GHz frequencies ($\gtrsim$ 20%), high-resolution studies of their polarization properties are still lacking. We present the first high-resolution and high-sensitivity polarimetry study of the merging galaxy cluster CIZA J2242.8+5301 in the 1–4 GHz frequency band. We use the *QU*-fitting approach to model the Stokes *I*, *Q* and *U* emission, obtaining best-fit intrinsic polarization fraction (p_0), intrinsic polarization angle (χ_0), Rotation Measure (RM) and wavelength-dependent depolarization (σ_{RM}) maps of the cluster. Our analysis focuses on the northern relic (RN). For the first time in a radio relic, we observe a decreasing polarization fraction in the downstream region. Our findings are possibly explained by geometrical projections and/or by decreasing of the magnetic field anisotropy towards the cluster center. From the amount of depolarization of the only detected background radio galaxy, we estimate a turbulent magnetic field strength of $B_{turb} \sim$ 5.6 μGauss in the relic. Finally, we observe Rotation Measure fluctuations of about 30 rad m^{-2} around at the median value of 140.8 rad m^{-2} at the relic position.

5.1. Introduction

Radio relics are synchrotron sources generally located in the outskirts of merging galaxy clusters. They are elongated, often arc-shaped, and not associated with any optical counterparts. It is now accepted that these sources trace particles (re)accelerated due to the propagation of shock waves generated by a cluster-cluster merger event (see Brunetti & Jones, 2014; van Weeren et al., 2019, for a theoretical and observational review). Being synchrotron sources, radio relics are also tracers of the magnetic field in cluster outskirts. Numerical simulations (e.g. Dolag et al., 1999; Brüggen et al., 2005; Vazza et al., 2018), as well as observations (e.g. Govoni & Feretti, 2004b; Bonafede et al., 2010a), show that the magnetic field intensity declines with radius (and hence with particle density) in clusters, with central values of a few μGauss (Bonafede et al., 2010a). On the other hand, it is expected that, during a cluster merger, the un-ordered magnetic fields in the intracluster medium (ICM) are compressed, amplified and aligned with the propagating shock plane, generating strongly linearly polarized emission ($\gtrsim$ 20%, see Ensslin et al., 1998). The exact mechanism leading to magnetic field amplification at shocks is not completely understood (see Donnert et al., 2018, for a recent review). For the typical low Mach numbers of cluster merger shocks ($\mathcal{M} = 1 - 3$), the amplification factor appears to be too small to explain the magnetic field strength measured in relics simply via shock compression, as it is for supernovae remnants (Iapichino & Brüggen, 2012; Donnert et al., 2017). Recently, new high-resolution (i.e., 32 kpc) numerical simulations by Wittor et al. (2019) show that the polarized emission from relics should strongly depend on the properties of the upstream magnetic field, with laminar gas flow generating parallel alignment of the electric vectors. Determining the polarization properties of radio relics thus plays a crucial role in the understanding of these sources, as well as the properties of the ICM.

While studies of magnetic fields of radio galaxies, in the field and in galaxy clusters, have been performed (e.g. Bicknell et al., 1990; Govoni et al., 2006; O'Sullivan et al., 2012, 2018; Bonafede et al., 2010b; Frick et al., 2011; Farnsworth et al., 2011; Orrù et al., 2015), very little information is known on the magnetic field structure in radio relics, with few observational studies performed so far (Bonafede et al., 2010a; van Weeren et al., 2010, 2012; Bonafede et al., 2013; Ozawa et al., 2015; Pearce et al., 2017; Stuardi et al., 2019). In this paper, we present a detailed polarization analysis, performed with the Jansky Very Large Telescope (VLA), of the well-studied merging galaxy cluster CIZAJ2242.8+5301 (hereafter CIZAJ2242) at $z = 0.192$ (Kocevski et al., 2007).

The cluster is the result of the collision of two equal-mass sub-clusters (Dawson et al., 2015; Jee et al., 2015), with a small inclination of the merger axis to the plane of the sky (i.e. $|i| \lesssim 10°$, van Weeren et al., 2011a). The cluster hosts two main radio relics, in the north and in the south,

several tailed radio galaxies and several patches of diffuse emission (see Di Gennaro et al., 2018). High-frequency studies, up to 30 GHz, showed a possible steepening in the integrated radio spectrum[1] from ~ -1.0 to ~ -1.6 at $\nu > 2.5$ GHz (Stroe et al., 2016), in contrast with the simple picture of a single power-law spectrum predicted from the standard acceleration model (i.e. diffusive shock acceleration, DSA; Ensslin et al., 1998). Possible explanations were given by Kang & Ryu (2016), who suggested a model where a shock passed through a region containing fossil electrons, by Donnert et al. (2016), who suggested the presence of exponential magnetic field amplification in the downstream region (being the shock located at the outermost edge of the relic), and by Basu et al. (2016), who proposed a non-negligible contribution from the Sunyaev-Zel'dovich (SZ) effect (also supported by single-dish observations, see Loi et al., 2017). Single-dish observations revealed that this relic is strongly polarized (up to 60% at 8.35 GHz, Kierdorf et al., 2017), although the poor resolution (i.e. $90''$) strongly limited their analysis. From the relic width (55 kpc) and X-ray downstream velocity (about 1000 km s^{-1}), van Weeren et al. (2010) estimated magnetic field strengths of 5 or 1.2 μGauss.

The paper is organized as follows: in Sect. 5.2 we describe the data reduction and the imaging procedures; in Sect. 5.3 we present the *QU* fitting approach; we highlight the effect of the Galactic Rotation Measure in Sect. 5.4; the results and discussion are given in Sect. 5.5 and 5.6; we end with the conclusion in Sect. 5.7. Throughout the paper, we assume a flat ΛCDM cosmology with $H_0 = 70$ km s^{-1} Mpc^{-1}, $\Omega_{\mathrm{m}} = 0.3$ and $\Omega_\Lambda = 0.7$, which gives a conversion factor of 3.22 kpc/$''$ and a luminosity distance of ≈ 944 Mpc, at the cluster's redshift ($z = 0.192$, Kocevski et al., 2007).

5.2. Observations and data reduction

We made use of the same 1–4 GHz VLA observations presented in Di Gennaro et al. (2018), to which we refer for a detailed description of the data reduction. The observations were made with all the four array configurations (namely, A, B, C and D), some of them split into sub-datasets (see Table 1 in Di Gennaro et al., 2018). Due to the large angular size of the cluster, and the limited field of view (FOV) at 2–4 GHz, we observed three separate pointings in this frequency range. We briefly summarize the data reduction strategy below.

First, we Hanning smoothed the data, and removed radio frequency interference (RFI) with the *tfcrop* mode from the `flagdata` task in `CASA`. Then, we calibrated the antenna delays, bandpass, cross-hand delays, and polarization leakage and angles using the primary calibrators 3C138, 3C147, and/or 3C48. For the polarization leakage calibration, we can

---

[1]The radio spectrum is defined as $S_\nu \propto \nu^\alpha$, with α the spectral index.

Table 5.1: Datacube information. Columns 1 to 3: Gaussian uv-taper, weighting and robust parameters for the imaging. Column 4: final resolution of the datacubes. Column 5: total number of channels in the 1–2 and 2–4 GHz bands. Column 6: channel width in MHz in the 1–2 and 2–4 GHz bands. Column 7: noise map for the Stokes I, Q and U datacubes.

uv-taper ["]	weighting	robust	resolution ["×"]	#channels		$\Delta\nu$ [MHz]		$\sigma_{\rm rms}$[1.26–3.60GHz] [μJy beam^{-1}]		
				1–2 GHz	2–4 GHz	1–2 GHz	2–4 GHz	I	Q	U
2.5	uniform	N/A	2.7×2.7	104	75	4	16	12.1	11.2	11.3
2.5	Briggs	0	4.55×4.55	104	75	4	16	8.9	10.1	10.0
5	Briggs	0	7×7	104	136	4	8	7.9	5.1	5.2
10	Briggs	0	13×13	104	136	4	8	18.2	5.1	5.4

Note: The noise levels in the last column have been calculated as standard deviation of the datacube, in a central, "empty" region of the cluster. For the 2.5″-tapered images, we only produced stamps of the single sources, hence we report the map noise locally to RN.

only make use of an unpolarized source[2], hence we discarded all the sub-datasets where 3C48 was the only calibrator (for further details, see Di Gennaro et al., 2018). We determined the global cross-hand delay solutions (`gaintype='KCROSS'`) from the polarized calibrator 3C138, taking a RL-phase difference of $-10°$ (both L- and S-band) and polarization fractions of 7.5% and 10.7% (L- and S-band respectively). We used 3C147 to calibrate the polarization leakage terms (`poltype='Df'`), and 3C138 to calibrate the polarization angle (`poltype='Xf'`). The solution tables were applied on the fly to determine the complex gain solution for the secondary calibrator J2202+4216. Additional RFI removal was performed, using the *tfcrop* and *rflag* modes (in `CASA`) and `AOFlagger` (Offringa et al., 2010), before and after applying the calibration tables to the target field, respectively. The data were averaged by a factor of two in time and a factor of four in frequency. This reflects a frequency resolution (i.e. channel width) of $\Delta\nu = 4$ and $\Delta\nu = 8$ MHz, at 1–2 and 2–4 GHz respectively. The only exception is the 2.5″-tapered dataset at 2–4 GHz, for which we average by a factor of eight, i.e. $\Delta\nu = 16$ MHz. Finally, self-calibration was performed to refine the amplitude and phase calibration on the target.

To retrieve the images for all the Stokes parameters (i.e., *I*, *Q* and *U*) at each channel $\Delta\nu$, as required for a detailed polarization analysis, we employed the `WSClean` (Offringa et al., 2014). Images were produced with different weightings (i.e. `Briggs` and `uniform`), and uv-tapers (i.e., 2.5″, 5″ and 10″). Bad spectral windows and channels were discarded from the final analysis. For the Stokes-*Q* and -*U* images, we also used the options `-join-channels`, `-join-polarizations` and `-squared-channel-joining`, which prevent the *Q*-, *U*-flux to be averaged out to zero[3]. After imaging, channel images that where too noisy or low-quality were removed. In the end, a total of 240 channels, for the 5″- and 10″-tapered images, and 179 channels, for the 2.5″-tapered images, were used. This results in a final frequency coverage of 1.26–3.60 GHz. The single-channel images were re-gridded to the same pixel grid and convolved to the same resolution (see Tab 5.1). Finally, all the single images were primary-beam corrected, by taking the beam variation with the frequency taken into account[4], and merged into a single datacube for each Stokes parameter. Errors in the single channel images were estimated using the rms noise level from a central, empty, region of the cluster (at 7″ and 13″ resolution) or locally for the sources of interest (at 4.5″ and 2.7″ resolution).

---

[2]In principle, a calibrator with enough parallactic angle coverage can also be used for the leakage calibration. This kind of calibrator was not available in our observations.

[3]https://sourceforge.net/p/wsclean/wiki/RMSynthesis/

[4]The beam shapes have been obtained with `CASA` v. 5.3.

5.3. Polarization theory and modelling approach

The linear polarization emission can be described in terms of Stokes parameters for the total intensity, I, and the orthogonal components, Q and U:

$$P(\lambda^2) = p(\lambda^2)I(\lambda^2)\exp[2i\chi(\lambda^2)] = Q(\lambda^2) + iU(\lambda^2)\,, \qquad (5.1)$$

and λ is the observing wavelength. Here, $p(\lambda^2)$ is the fractional (or degree of) polarization and $\chi(\lambda^2)$ is the polarization angle, which are wavelength-dependent quantities that can be written as:

$$p(\lambda^2) = \frac{P(\lambda^2)}{I(\lambda^2)} = \frac{\sqrt{Q^2(\lambda^2) + U^2(\lambda^2)}}{I(\lambda^2)} \qquad (5.2)$$

and

$$\chi(\lambda^2) = \frac{1}{2}\arctan\left(\frac{U(\lambda^2)}{Q(\lambda^2)}\right)\,. \qquad (5.3)$$

The passage of the polarized radiation through a foreground magneto-ionic medium, such as the ICM, results in a rotation of polarization plane via the Faraday effect according to

$$\chi(\lambda^2) = \chi_0 + \mathrm{RM}\lambda^2\,, \qquad (5.4)$$

where χ_0 is the intrinsic polarization angle and RM is the Faraday rotation measure. This is defined as:

$$\mathrm{RM} = 0.81\int_{\mathrm{source}}^{\mathrm{observer}} n_e B_\parallel dl \quad [\mathrm{rad\ m^{-2}}]\,, \qquad (5.5)$$

where n_e is the electron density (in $\mathrm{cm^{-3}}$), $B_\parallel$ the magnetic field (in μGauss) along the line of sight, l the path length through the magneto-ionic medium (in pc), and with the sign of the equation defined positive for a magnetic field pointing towards the observer.

The traditional way to retrieve the intrinsic polarization angle χ_0 is to observe χ at several wavelengths, and linearly fit Eq. 5.4. The long-standing problem of this approach is the lack of a sufficient number of $\chi(\lambda^2)$ measurements. In this work, this issue is overcome by the large number of channel images with high signal-to-noise (S/N) of our wide-band observations (see Sect. 5.3.1).

Several models of the polarized signal, in the presence of Faraday rotation, are known. In the simplest scenario, Eq. 5.1 can be written as:

$$P(\lambda^2) = p_0 I\exp[2i(\chi_0 + \mathrm{RM}\lambda^2)]\,, \qquad (5.6)$$

with p_0 the intrinsic polarization fraction. This corresponds to the physical situation of a single Faraday screen in the foreground. In this case, $d\chi/d\lambda^2$ and $p(\lambda)$ are constant.

Observations have shown that radio relics depolarize at frequencies $\lesssim 1$ GHz (Brentjens, 2011; Pizzo et al., 2011; Ozawa et al., 2015). Common depolarization mechanisms are external and internal Faraday rotation dispersion (EFD and IFD, respectively; see Sokoloff et al., 1998, for the detailed parametrization of those mechanisms). EFD occurs when variations in the magnetic field direction are not resolved in the single beam (Burn, 1966; Tribble, 1991). For a Gaussian distribution of RM, the observed polarization is parameterized as:

$$P(\lambda^2) = p_0 I \exp(-2\sigma_{\mathrm{RM}}^2 \lambda^4) \exp[2i(\chi_0 + \mathrm{RM}\lambda^2)] \,, \tag{5.7}$$

where σ_{RM} is the dispersion about the mean RM across the beam on the sky.

On the other hand, IFD occurs when the emitting source and the Faraday screen (i.e. the rotating layer) are mixed. In this case, depolarization is due to the random direction of the plane of polarization through the emitting region, and it can be parametrized as:

$$P(\lambda^2) = p_0 I \left[\frac{1 - \exp(-2\varsigma_{\mathrm{RM}}^2 \lambda^4)}{2\varsigma_{\mathrm{RM}}^2 \lambda^4} \right] \exp[2i(\chi_0 + \mathrm{RM}\lambda^2)] \,, \tag{5.8}$$

where ς_{RM} is the internal dispersion of the random field.

5.3.1. *QU*-modelling approach

Stokes $Q(\lambda^2)$ and $U(\lambda^2)$ fitting has been used in literature to determine the polarization properties of a magneto-ionic layer (e.g. O'Sullivan et al., 2012; Ozawa et al., 2015; Anderson et al., 2016). In this approach, $Q(\lambda^2)$ and $U(\lambda^2)$ were fitted simultaneously with cosine and sine models, while $I(\lambda^2)$ was fitted with a log-parabolic model (see also Massaro et al., 2004), which represents a curved spectrum, as suggested by Stroe et al. (2016) and given the large bandwidth used:

$$I_\nu = I_0 \nu^{a+b \log(\nu/\nu_{\mathrm{ref}})} \,, \tag{5.9}$$

where we fixed the reference frequency ν_{ref} to 1 GHz.

In this model, b is the curvature parameter and the spectral index is calculated as the log-derivative, i.e. $\alpha = a + 2b \log(\nu/\nu_{\mathrm{ref}})$. For each channel image in the $I(\lambda^2)$, $Q(\lambda^2)$ and $U(\lambda^2)$ datacubes, the uncertainties were computed by adding in quadrature the relative (spatial) map noise and 5% of the Stokes I, Q and U flux in each channel. Here, the 5% represents a spatially-independent intrinsic scatter which takes into account the flux variations between the single-frequency channel maps. The origin of this scatter is not fully clear, but it is probably related to bandpass calibration and/or deconvolution uncertainties.
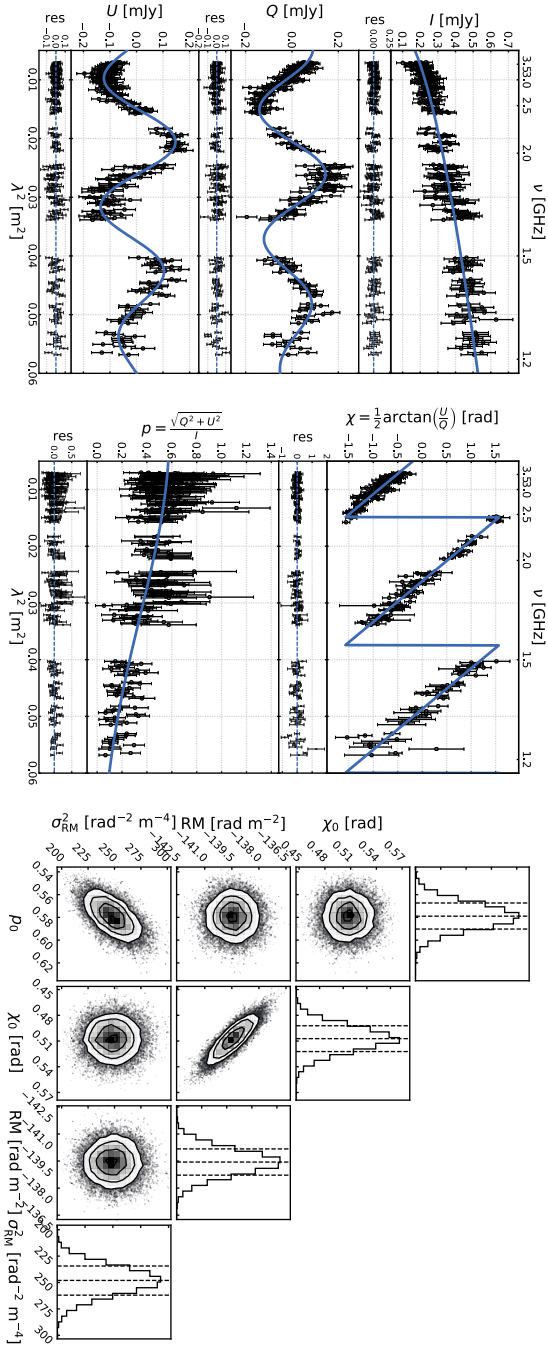
Figure 5.1: Result of the QU fit assuming the external depolarization model (EDF, Eq. 5.7) on a single pixel of the northern relic. Left panel: Fits on Stokes I, Q and U fluxes. Central panel: Resulting fractional polarization, $p(\lambda^2)$, and polarization angle, $\chi(\lambda^2)$, estimated from Eqs. 5.2 and 5.3, respectively. Right panel: Corner plot for the distribution of the uncertainties in the fitted polarization parameters (i.e. p_0, χ_0, RM and σ_{RM}^2): contour levels are drawn at $[0.5, 1.0, 1.5, 2.0]\sigma$, with σ the 68% statistical uncertainty (see dashed lines in the 1D histogram).

We fitted our data with the Markov Chain Monte Carlo (MCMC) method[5] (Foreman-Mackey et al., 2013) to explore the best-set of model parameters (Ozawa et al., 2015). During the fitting procedure, all the parameters (i.e. I_0, a and b for Stokes I, and p_0, χ_0, RM and σ_{RM}^2 for the combined Stokes Q and U) were left free to vary through the full parameter space. In the fitting, we constrained p_0, χ_0 and σ_{RM}^2 (or $\varsigma_{\mathrm{RM}}^2$) to the following physical conditions:

$$\begin{cases} 0 \leq p_0 \leq 1 \\ 0 \leq \chi_0 < \pi \\ \sigma_{\mathrm{RM}}^2 \geq 0 \text{ or } \varsigma_{\mathrm{RM}}^2 \geq 0 \,, \end{cases} \tag{5.10}$$

and we assumed a single-RM component model (see also Appendix .1)). The upper limit for the polarization angle is set to π because the polarization vectors have no preferred direction. In this convention, $\chi_0 = 0$ and $\chi_0 = \pi/2$ give the north/south and east/west directions, respectively. We chose to include depolarization in our fit as our observations showed a decrease in polarization fraction towards longer λ^2. It is worth noting that the p_0 value obtained from the MCMC fit could be an underestimation of the intrinsic polarization fraction, because of the limited λ^2 coverage, and possible misalignment of the intrinsic polarization angle χ_0 from different emitting sites along the line of sight. Hereafter, we refer to p_0 as the best-fit intrinsic polarization fraction. The uncertainties on the best-fitting parameters were determined with the MCMC analysis. The results of the fitting procedure using the EFD model on a representative single pixel in the cluster northern relic are displayed in Fig. 5.1. Similar result were found using the IDF model (Eq. 5.8), except for ς_{RM} which is higher due to the different functional way it describes the depolarization.

5.4.   Rotation Measure from our Galaxy

The best-fit Rotation Measure value obtained could, in principle, give information on the magnetic field structure of the diffuse radio emission in the cluster (Eq. 5.5). However, in order to have a reliable estimation of the RM associated with the ICM, the contribution of the foreground Galactic RM needs to be estimated and removed from the calculations.

The Galactic coordinates of CIZAJ2242 are $l = 104°$ and $b = -5°$, meaning that the cluster lies on close to the Galactic plane. Hence, the RMs of the cluster sources are strongly affected by the Faraday rotation from our Galaxy. Using the map of the Galactic contribution to Faraday rotation provided by Oppermann et al. (2015)[6], we found an average contribution

---

[5]The initial guesses for the parameters were obtained with the least square method (*scipy.optimize.leastsq* in Python).

[6]https://wwwmpa.mpa-garching.mpg.de/ift/faraday/2014/index.html

Table 5.2: Averaged RM values of the sources labelled in Fig. 5.2 observed in the
1–2 GHz frequency range. The "uncertainty" on RM is represented by the standard
deviation of the RM pixel distribution within the source.

Source	RA_{J2000}	DEC_{J2000}	$\langle RM \rangle \pm std(RM)$
	[^{h} ^{m} ^{s}]	[° ′ ″]	[rad m^{-2}]
1	22 44 31.5	+53 00 39.0	-113.0 ± 5.4
2	22 42 12.4	+52 47 56.5	-43.9 ± 3.6
3	22 42 05.2	+52 59 32.0	$+1.2 \pm 8.1$
4	22 41 22.1	+53 02 15.5	-71.7 ± 7.2
5	22 41 00.1	+53 04 15.7	-77.4 ± 5.1
6	22 41 33.1	+53 11 07.7	-155.9 ± 1.4
7	22 43 02.2	+53 19 42.2	-76.0 ± 8.5
8	22 43 37.5	+53 09 15.5	-137.2 ± 5.0
9	22 41 22.9	+52 52 54.3	-81.1 ± 6.7
10	22 43 05.2	+53 17 33.8	-92.0 ± 6.4

Note: Source 3 and source 8 are labelled as source A and N in Fig. 5.3, respectively

of about -65 ± 57 rad m^{-2} in a region of 20′ around the cluster center co-
ordinates. However, the current available Galactic RM map is affected by
very poor angular resolution (i.e. ~ 10′/pixel), which is comparable with
the cluster size (~ 15′). For this reason, we lack detailed information on
the RM variations on the cluster/sub-cluster scale.

We investigated the RM values of compact sources within the field of
view of our observations, but outside the cluster region. In this way, we
exclude the contribution of the ICM on the RM estimation. Since the size of
the primary beam depends on the frequency as FOV $\propto \nu^{-1}$, and we want to
maximize the area where we search for polarized sources, we only used the
1–2 GHz observations. We found a total of 10 sources in the 1–2 GHz FOV
(~ 18′, see Fig. 5.2). Their Rotation Measure values, listed in Table 5.2, are
consistent with the average Galactic RM value found by Oppermann et al.
(2015), with a median value of about -80 rad m^{-2} and standard deviation
of about 42 rad m^{-2}. Moreover, we found that sources close to each other
(i.e., sources 4 and 5, and sources 7 and 10) have similar RM, suggesting
that the Galactic foreground might remain approximately constant in that
region, on those spatial scales (3′ – 5′, i.e. few hundreds of kpc, at the
cluster distance). However, we find a strong variation from in RM north
to south and east to west, although without a clear trend. It remains
therefore difficult to quantify a unique Rotation Measure value from the
Galactic foreground, and to subtract it from our measured RM values for
the cluster sources. For this reason, in the following maps and plots we
report the best-fit RM value, including the Galactic contribution.
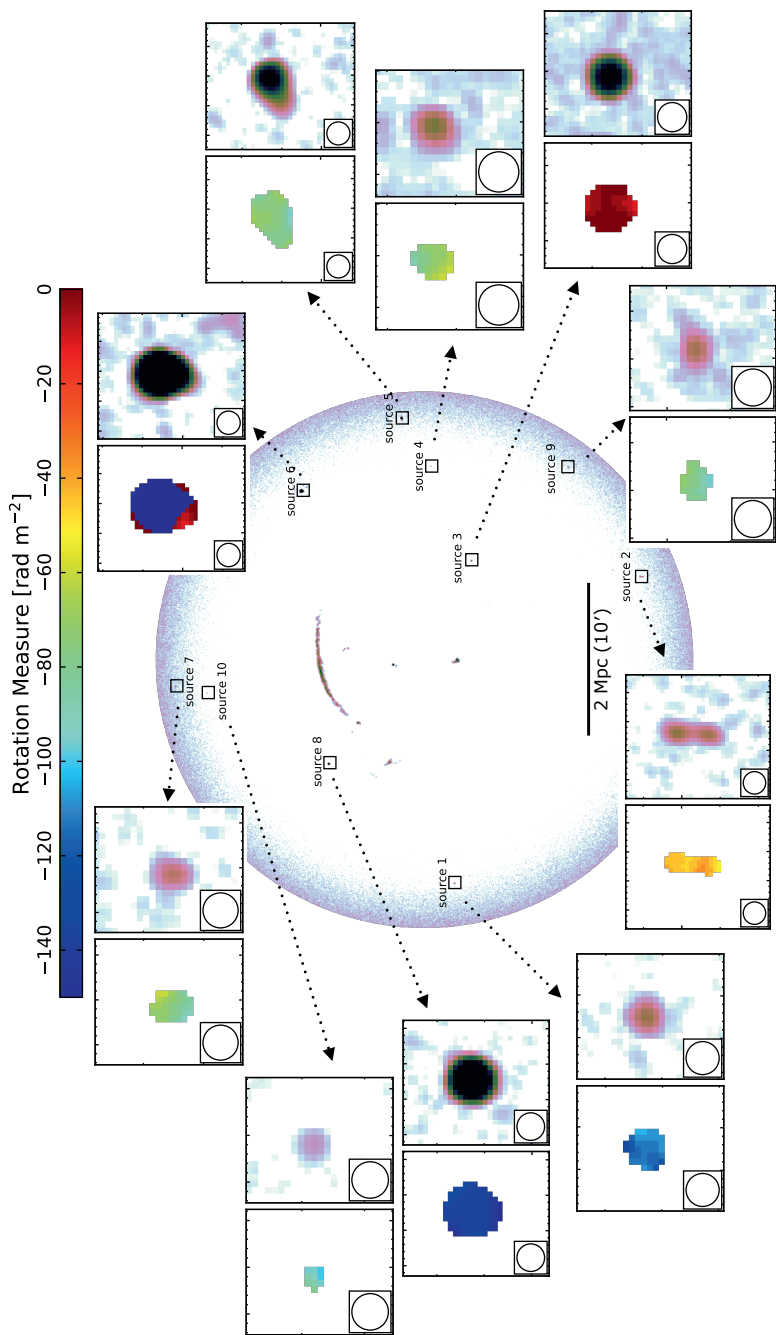
Figure 5.2: Total polarized emission of the 1–2 GHz field of view (FOV ~ 18' in radius) to search for polarized radio galaxies outside CIZAJ2242. A zoom on those sources is shown in the insets, where the Rotation Measure and the total intensity are displayed in the left and right panel, respectively. The RM colorscale is fixed for all the sources. The averaged RM values of those sources are listed in Table 5.2.

5.5. Results

5.5.1. Polarized flux densities and fractions

We obtained the total averaged polarization images in the 1.26–3.60 GHz band by means of the RM-Synthesis technique (Brentjens & de Bruyn, 2005), using the `pyrmsynth` tool[7]. In Fig. 5.3 and in the top panel of Fig. 5.4, we show the total averaged polarization images of the entire cluster at 7″ resolution and of the northern relic at 2.7″ resolution, at the effective frequencies of 2.3 and 2.0 GHz, respectively. We retrieve the polarized intensity at the canonical frequencies, i.e. 1.5 and 3.0 GHz (i.e. at wavelength of 0.2 and 0.1 m, respectively), using the fit results of Eq. 5.7 as described in Section 5.3.1. In Table 6.4 we report the polarized and total flux densities, the correspondent factional polarization (Eq. 5.3), and the amount of depolarization $DP_{1.5GHz}^{3.0GHz} = 1 - (p_{1.5GHz}/p_{3.0GHz})$[8], for the diffuse radio sources in the cluster.

We detect significant polarized emission both from the numerous radio galaxies and from the diffuse radio sources. The brightest polarized structure of the cluster is the northern relic (RN), with integrated polarized flux densities of $P_{3.0GHz} = 17.0 \pm 0.9$ and $P_{1.5GHz} = 19.4 \pm 1.0$ mJy (Table 6.4). The relic presents a similar continuous shape as detected in total intensity emission (see radio contours in Fig. 5.3). At 2.7″ resolution (i.e. the highest resolution available in our observations), the polarized emission traces the relic's filamentary structure observed already in the total intensity (see top panel in Fig. 5.4 in this manuscript and Fig. 7 in Di Gennaro et al., 2018). Hints of polarized emission at 13″ resolution are seen also from the very faint relic northward of RN, i.e. R5, with high degree of polarization at both 3.0 and 1.5 GHz (i.e. about 35% and 30%).

Particularly bright in polarization is also the relic located eastward of RN, i.e. R1 ($P_{3.0GHz} = 1.5 \pm 0.1$ and $P_{1.5GHz} = 2.6 \pm 0.1$ mJy). The relic labelled as R4 shows a particularly high degree of polarization at both 3.0 and 1.5 GHz (∼ 50%), with negligible wavelength-dependent depolarization. On the contrary, the relic westward of RN, i.e. R3, undergoes strong depolarization from 3.0 to 1.5 GHz ($DP_{1.5GHz}^{3.0GHz} \sim 80\%$).

Faint polarized emission is observed in the southern relic (RS), at 13″ resolution. Here, the emission only comes from two out of the five "arms" that were detected in Di Gennaro et al. (2018), i.e. only RS1 and RS2. This is not completely a surprise, as these two "arms" are also the brightest in total intensity (see Di Gennaro et al., 2018).

No polarized emission is detected for the diffuse sources R2 and I. Finally, we detect polarized emission from the radio galaxies in and around the cluster (i.e. A, B, C, D, E, F, H, J, K1, M, N and O), whose degree of

---

[7] https://github.com/mrbell/pyrmsynth
[8] In this convention, $DP_{1.5GHz}^{3.0GHz} = 0$, i.e. $p_{1.5GHz} = p_{3.0GHz}$, means no depolarization, while $DP_{1.5GHz}^{3.0GHz} = 1$, i.e. $p_{1.5GHz} \sim 0$, means full depolarization.

Table 5.3: Polarized (P_ν) and total intensity (I_ν) flux densities, and integrated polarization fraction (p_ν) for the diffuse radio sources labelled in Fig. 5.3 at $\nu = 1.5$ and 3.0 GHz. The depolarization fraction between the two frequencies is shown in the last column.

Source	resolution [''×'']	$P^{(a)}_{3.0\text{GHz}}$ [mJy]	$I_{3.0\text{GHz}}$ [mJy]	$p^{(b)}_{3.0\text{GHz}}$	$P^{(a)}_{1.5\text{GHz}}$ [mJy]	$I_{1.5\text{GHz}}$ [mJy]	$p^{(b)}_{1.5\text{GHz}}$	$DP^{3.0\text{GHz}}_{1.5\text{GHz}}$
RN	7×7	17.0±0.9	45.5±2.3	0.37	19.4±1.0	105.2±5.3	0.18	0.51
RS1+RS2	13×13	1.2±0.1	5.7±0.3	0.22	2.3±0.1	11.2±0.6	0.20	0.06
R1	7×7	1.5±0.1	6.4±0.3	0.28	2.6±0.1	13.2±0.7	0.19	0.15
R2	13×13	–	3.7±0.2	–	–	7.6±0.4	–	–
R3	7×7	0.9±0.05	3.9±0.2	0.23	0.5±0.02	10.1±0.5	0.05	0.77
R4	7×7	0.7±0.04	1.5±0.1	0.47	1.5±0.1	3.4±0.2	0.46	0.03
R5	13×13	0.5±0.03	1.5±0.1	0.35	1.0±0.1	3.2±0.2	0.31	0.12
I	13×13	–	1.6±0.2	–	–	3.5±0.3	–	–

Note: [a] Uncertainties are of the same order of those on the total intensity which are given by $\sqrt{(\zeta I_\lambda)^2 + \sigma^2_{\text{rms},I}}\, N_{\text{beam}}$ ($\zeta = 0.05$ is the calibration uncertainty, $\sigma_{\text{rms},I}$ is the Stokes I noise map and $N_{\text{beam}} = A_{\text{source}}/A_{\text{beam}}$ is the number of beam in the source where we measure the flux). [b] Uncertainties are dominated by the precision on the leakage calibration (0.5%, https://science.nrao.edu/facilities/vla/docs/manuals/obsguide/modes/pol).
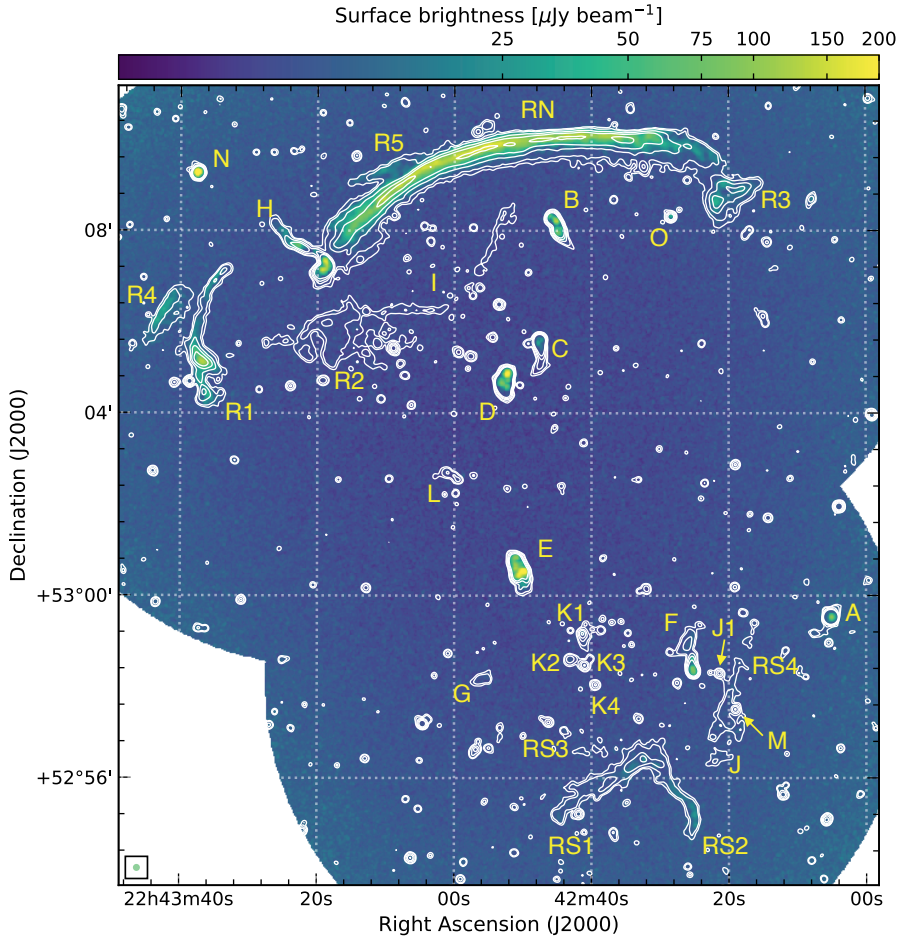
Figure 5.3: Total averaged polarized emission for CIZAJ2242 in the 1.26–3.60 GHz band (effective frequency of 2.3 GHz) at 7″ resolution. This image is not corrected for the Ricean bias. The radio contours are from the averaged total intensity image, in the same frequency band and at the same resolution, with contours drawn at levels of $3\sigma_{\mathrm{rms}} \times \sqrt{[1, 4, 16, 64, 256, \ldots]}$, with $\sigma_{\mathrm{rms}} = 4.2$ μJy beam^{-1}. Sources are labelled following Fig. 2 in Di Gennaro et al. (2018).

polarization at 1.5 and 3.0 GHz ranges between 1–10%, consistently with other similar objects (e.g. O'Sullivan et al., 2012).
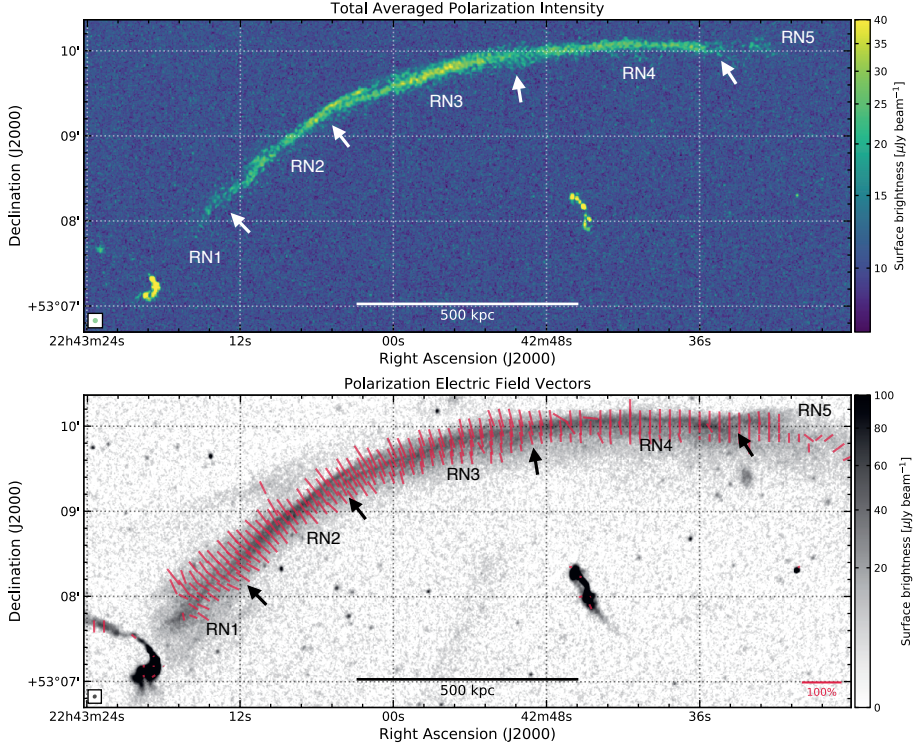
Figure 5.4: Top panel: High-resolution (2.7″×2.7″) total averaged polarized image in the 1.26–3.60 GHz band (effective frequency of 2.0 GHz) zoomed on the northern relic ($\sigma_{Q,\mathrm{rms}[1.26-3.60\mathrm{GHz}]}$ = 11.2 and $\sigma_{U,\mathrm{rms}[1.26-3.60\mathrm{GHz}]}$ = 11.3 μJy beam^{-1}). As for Fig. 5.3, this image is not corrected for the Ricean bias. Bottom panel: High-resolution (2.1″×1.8″) Stokes I observation in the 1–2 GHz band (Di Gennaro et al., 2018) with the polarization electric field vectors at 2.7″ resolution, corrected for Faraday Rotation, displayed in red; the length of the vectors is proportional to the intrinsic polarization fraction (scale in the bottom right corner). White and black arrows in the two panels indicate the points where the relic breaks into separate filaments, following Fig. 7 in Di Gennaro et al. (2018).

5.5.2. Intrinsic fractional polarization, intrinsic polarization angle, RM and depolarization maps

In Fig. 5.5 we show a comparison between the total intensity and total averaged polarization maps of the northern relic at 7″ resolution (panels (a) and (b), respectively), best-fit intrinsic and 1.5 GHz polarization fractions (p_0 and $p_{1.5\mathrm{GHz}}$, panels (c) and (d) respectively), Rotation Measure (RM, panel (e)) and external wavelength-dependent depolarization (σ_{RM}, panel
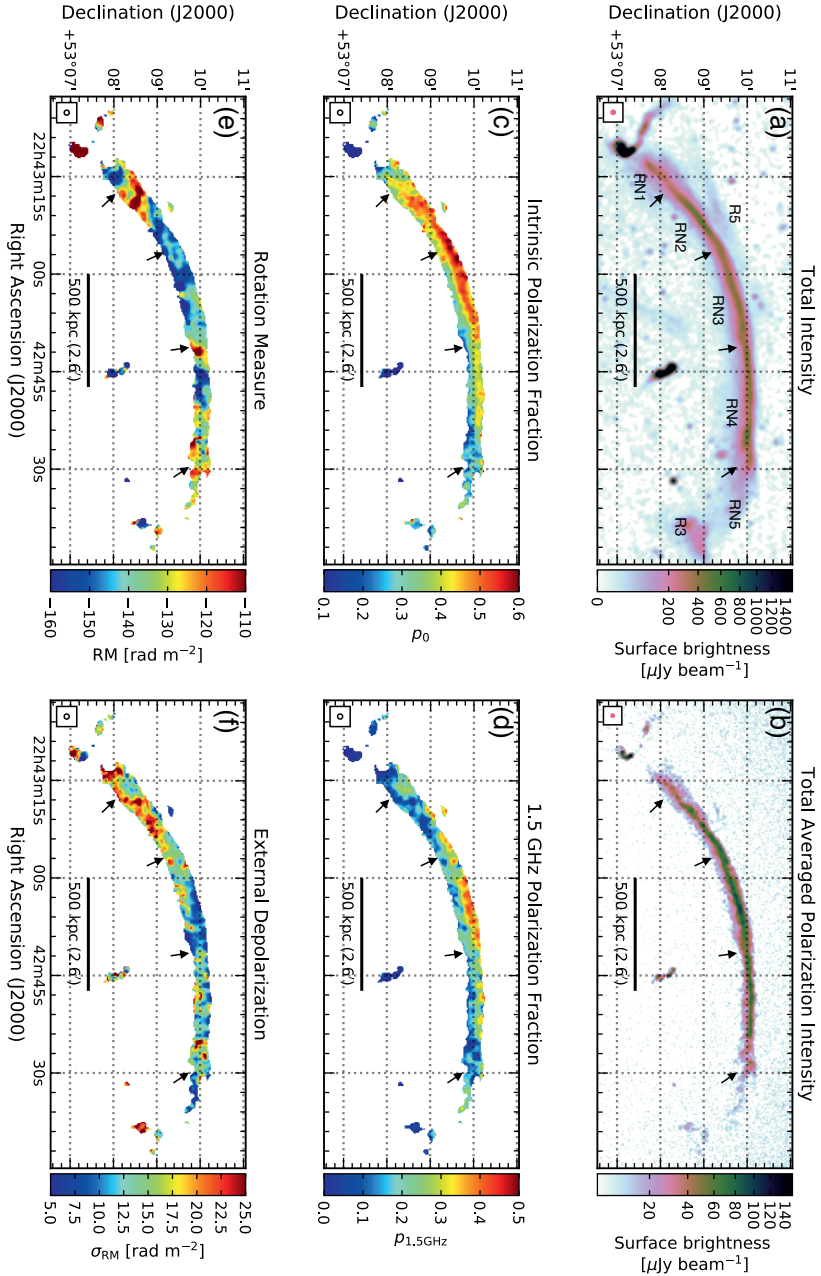
Figure 5.5: Panels (a) and (b): 1–4 GHz Stokes *I* emission of the northern relic (Di Gennaro et al., 2018) and correspondent 1.26–3.60 GHz averaged polarized emission (not corrected for the Ricean bias) at ∼ 5″ resolution. Panels (c), (d), (e), and (f): intrinsic polarization fraction, polarization fraction at 1.5 GHz, Rotation Measure and External Depolarization maps at 7″ resolution. Black arrows in the plots are located at same physical coordinates, and indicate the points where the relic breaks into separate filaments (see also Fig. 5.4 in this manuscript and Fig. 7 in Di Gennaro et al., 2018). Uncertainty maps corresponding to panels (c) to (f) are displayed in Appendix .2.

(f)) maps. The polarization best-fit parameter maps of the full cluster at 13″ resolution is shown in Fig. 5.6. These result from the QU-fitting approach for the case of the External depolarization (Eq. 5.7) for each pixel with averaged polarized emission above $f \times \sigma_{\mathrm{rms},P}$. Here, $\sigma_{\mathrm{rms},P}$ is obtained at the given resolution as the root mean squared level of the averaged polarized emission measured in a central, "empty" region of the cluster. We use $f = 2$ for the 2.5″-tapered images with `weighting='uniform'` and $f = 3$ for all the other resolutions and `weighting='Briggs'`. The corresponding uncertainty maps are displayed in Appendix .2.

The northern relic (RN) shows very high best-fit intrinsic polarization fraction values at the outermost edge, with the eastern side up to 60% and the western side up to 40% polarized. We also note a radial decreasing of p_0 towards the cluster center. The intrinsic polarization angles approximately follow the shock normal, which is assumed to be perpendicular to the Stokes I edge, supporting the scenario where the magnetic field is aligned after the shock passage (see also bottom panel in Fig. 5.4). The angles remain aligned also in the downstream region. The Rotation Measure value is not constant along the relic, it spans east to west from RM ~ -150 rad m^{-2} to RM ~ -130 rad m^{-2}, respectively, with median value of about -141 rad m^{-2}. Given the large distance from the cluster center (i.e. ~ 1.5 Mpc), where the contribution of the ICM is likely low, we suggest that this median value is mostly associated with the Galactic foreground (see Sect. 5.4). The variations in RM across the northern relic (~ 30 rad m^{-2}, have a dominant scale of $\sim 15″ - 30″$, and we cannot distinguish, with the available data, whether this is due to fluctuations in our Galaxy or in the ICM (see Sect. 5.6.5). Similar east-west RM and p_0 variations were reported with Effelsberg observations at 4.85 and 8.35 GHz (Kierdorf et al., 2017). To the contrary, the RM value measured in the western side of the relic (RM ~ -130 rad m^{-2}) differs from what has been found by the Sardina Radio Telescope at 6.6 GHz (RM ~ -400 rad m^{-2}, Loi et al., 2017). No north-south best-fit intrinsic polarization gradient across the relic's width was found by either Kierdorf et al. (2017) or Loi et al. (2017), although their observations suffer from much lower resolution (i.e., 90″ and 2.9′, respectively) which smoothed out any possible downstream gradient. Interestingly, we measure RM values of about -100 rad m^{-2} where the relic breaks in the RN1-RN2 and RN3-RN4 filaments (see panel (e) in Fig. 5.5). Finally, we do not find any particular east-west trend in the σ_{RM} behavior, with an overall value of $\sigma_{\mathrm{RM}} \sim 15 - 20$ rad m^{-2} (see panel (f) in Fig. 5.5). These values differ from the high-frequency observations, as Kierdorf et al. (2017) did not measure any depolarization for the northern relic.

The radio relic R4 is characterized by a very high best-fit intrinsic polarization fraction ($\sim 55\%$), while it is lower for R1, R3 and R5 ($\sim 20\%$). No clear gradients have been observed for these sources, except for R3 which shows hints of increasing values of p_0 towards the cluster center. The RM values are rather constant across R1 and R4, RM ~ -142 rad

m^{-2}, consistent with the one found for source N: since this radio galaxy is located outside of the cluster, its Rotation Measure is likely associated with the screen of our Galaxy rather than the ICM. Also, R1 and R4 have a very small values of σ_{RM}, again consistent with their spatial position in the cluster, in a region of low ICM density.
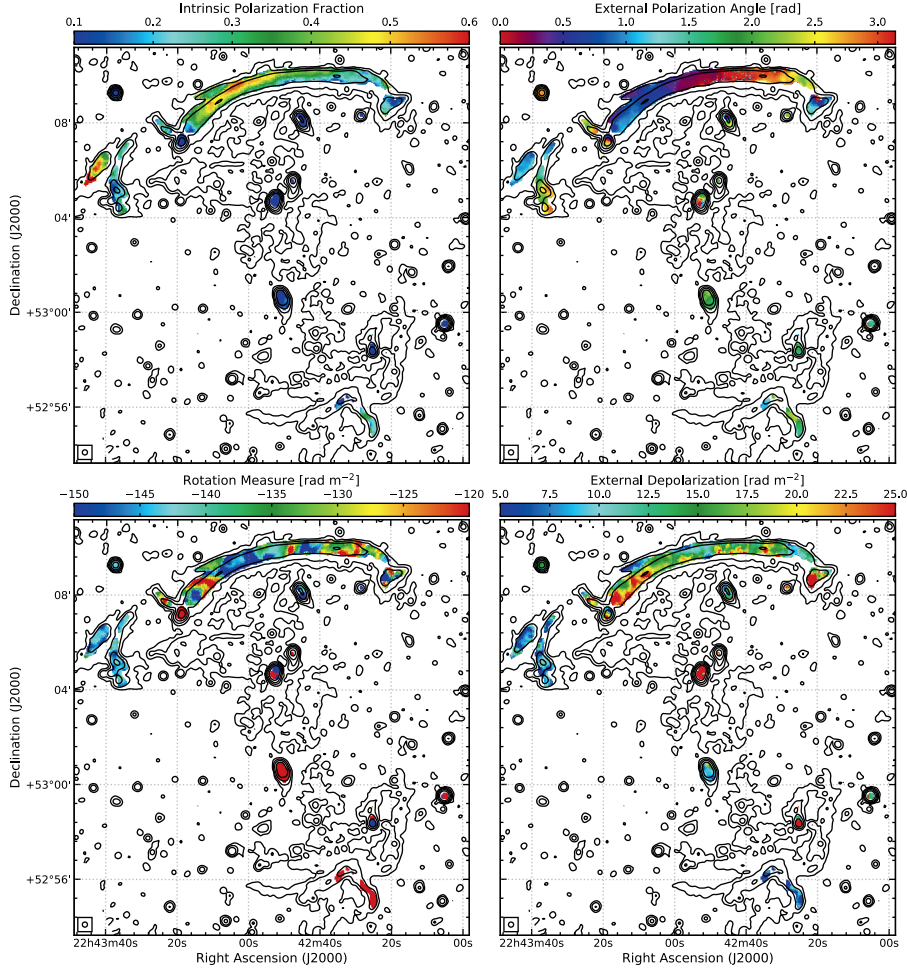

Figure 5.6: From top left to bottom right: intrinsic polarization fraction (p_0), intrinsic angle (χ_0), Rotation Measure (RM) and depolarization (σ_{RM}) maps of CIZAJ2242 at 13″ resolution. Stokes I radio contours at the same resolution are drawn in black at levels of $3\sigma_{\mathrm{rms}} \times \sqrt{[1, 4, 16, 64, 256, \ldots]}$, with $\sigma_{\mathrm{rms}} = 6.2\ \mu$Jy beam^{-1} (Di Gennaro et al., 2018). Negative and positive uncertainty maps are displayed in Appendix .2.

In the southern relic (RS), we measure a relatively low best-fit intrinsic polarization fraction of $\sim 10 - 25\%$. Across RS1 and RS2, the Rotation Measure spans from ~ -90 to ~ -80 rad m^{-2}. As for the northern relic, since RS is located in the cluster outskirts, we speculate that most of its RM is due to the Galaxy. The discrepancy between RM$_{RN}$ and RM$_{RS}$ can be either due to our Galaxy, whose RM variation is very uncertain (Sect. 5.4), or to a different combination of $n_e B_\parallel$ along the line of sight northward and southward the cluster ICM (see Eq. 5.5).

Finally, the polarized radio galaxies in the cluster field present different values of Rotation Measure. This possibly reflects the combination of their different position in the ICM with the Galactic contribution, although their intrinsic RM cannot be fully excluded. Among them, sources D and C are particularly interesting. They are located, in projection, in the cluster center and we measure a large difference in RM in the source's lobes, with the northwestern being negative (i.e. ~ -600 and ~ -200 rad m^{-2}, for source D and C respectively) and the southeastern being positive (i.e. $\sim +300$ and $\sim +250$ rad m^{-2}, for source D and C respectively). Such an extreme variation of RM in the lobes of the two radio galaxies probably originates in the radio galaxies themselves, although some effects might also be associated with the large amount of ICM traversed by the polarized emission. However, for these sources we find that a single-RM model does not properly fit the data, even within a single resolution element (i.e. a single pixel, see Appendix .1). We therefore suggest the presence of a complex RM structure, as is observed also in other radio galaxies (e.g. O'Sullivan et al., 2012). This study is, however, beyond the scope of this paper.

5.6.   Discussion

Radio relics are thought to trace merger-induced shock waves which (re-)accelerate electrons and compress and amplify the cluster magnetic fields (e.g., Ensslin et al., 1998). While several studies have been performed to investigate the mechanism to produce the highly-relativistic electrons in radio relics (e.g. Brunetti & Jones, 2014; Fujita et al., 2015; Donnert et al., 2016; Kang et al., 2017), studies of their magnetic field properties have been challenging, mostly because depolarization effects are stronger at low frequencies (i.e. $\lesssim 1$ GHz).

The northern radio relic in CIZAJ2242, i.e. the Sausage relic, is well-known to be highly polarized, hence it represents one of the best target for detailed polarization studies. Here, we present the first analysis of the radial and longitudinal polarization properties of the relic in the post-shock region on ten-kpc scales (i.e. $\sim 8 - 40$ kpc). Additionally, we investigate possible correlations between the polarization parameters and look for the presence of possible underlying trends among them by calculating the running median along the x-axis, with moving boxes of 20 win-

dows. The uncertainties are calculated as $\sigma_\pm/\sqrt{N}$, with $\sigma_+ = y_{0.50} - y_{0.16}$ and $\sigma_- = y_{0.84} - y_{0.50}$ (with $y_{0.16}$, $y_{0.50}$ and $y_{0.84}$ the 16%, 50%, i.e. the median, and 84% of the distribution, respectively), and N the number of windows (Lamee et al., 2016). The existence of a correlation was then evaluated by means of the Pearson coefficient, r_p (Pearson, 1895), where we define $|r_p| \leq 0.3$ as no/very weak correlation, $0.3 < |r_p| \leq 0.7$ as weak/moderate correlation, and $|r_p| > 0.7$ as strong correlation. We also report the Spearman coefficient, r_s, which assesses whether the relationship is monotonic (i.e. $|r_s| \leq 0.3$: no/very weakly monotonic ; $0.3 < |r_s| \leq 0.7$: weakly/moderately monotonic ; $|r_s| > 0.7$: strongly monotonic).

The following discussion is focused on the Sausage relic. In Sect. 5.6.1 we present the radial profiles of the best-fit polarization parameters; in Sect. 5.6.2 we discuss possible explanation for the profile found for the best-fit p_0; in Sect. 5.6.3 we look at the contribution of the turbulent magnetic field in the post-shock region; in Sect. 5.6.4 we investigate the limitation of the observing bandwidth coverage; finally, in Sect. 5.6.5 we look at the RM fluctuation in the relic.

5.6.1. Polarization parameters radial profiles

We repeated the QU fit using Eq. 5.7 in beam-sized boxes (i.e. $7''$, resulting in a linear size of about 20 kpc at the cluster redshift, see legend in Figs. 5.7 and 5.8, and Fig. .3.1) covering the filament RN3, which we consider to be representative part of the relic (see Fig. 5.5). For each single radial annulus (i.e. same-colored markers in Figs. 5.7 and 5.8), the polarization parameters have a similar trend along the filament (i.e. east to west, Fig. 5.7), with the exception for the Rotation Measure which shows a variation of about 30 rad m^{-2}. On the other hand, a clear north-south trend is visible for the best-fit intrinsic polarization fraction. It drops about 35–40%, from an average value of $\langle p_0 \rangle_{d=0\text{kpc}} = 0.40 \pm 0.04$ at the shock position to $\langle p_0 \rangle_{d=66\text{kpc}} = 0.28 \pm 0.06$ in the innermost downstream annulus (top panel in Fig. 5.7). The same trend is also observed for the polarization fraction at 1.5 GHz (Fig. 5.8). At this wavelength, the drop is even larger, about 60% (from $\langle p_{1.5\text{GHz}} \rangle_{d=0\text{kpc}} = 0.35 \pm 0.04$ to $\langle p_{1.5\text{GHz}} \rangle_{d=66\text{kpc}} = 0.24 \pm 0.09$). A similar but opposite trend is observed for the external wavelength-dependent depolarization: here we found higher values towards the downstream region (from $\langle \sigma_{\text{RM}} \rangle_{d=0\text{kpc}} = 10.1 \pm 0.2$ to $\langle \sigma_{\text{RM}} \rangle_{d=66\text{kpc}} = 13.9 \pm 0.8$ rad m^{-2}, bottom panel in Fig. 5.7). Hints of these radial trends are also seen in the entire relic (Fig. 5.9; see Appendix .3 for a view on the beam-sized boxes where we performed the QU fit). In this case, the radial information is obtained by looking at the spectral index, $\alpha_{3.0\text{GHz}}^{150\text{MHz}}$, since steeper values are located further in the downstream region where synchrotron and Inverse Compton energy losses increase (e.g., Di Gennaro et al., 2018). We calculated $\alpha_{3.0\text{GHz}}^{150\text{MHz}}$ using the LOFAR (150 MHz), GMRT (610 MHz) and VLA (1.5 and 3.0 GHz) maps described in Hoang et al. (2017), van Weeren et al.
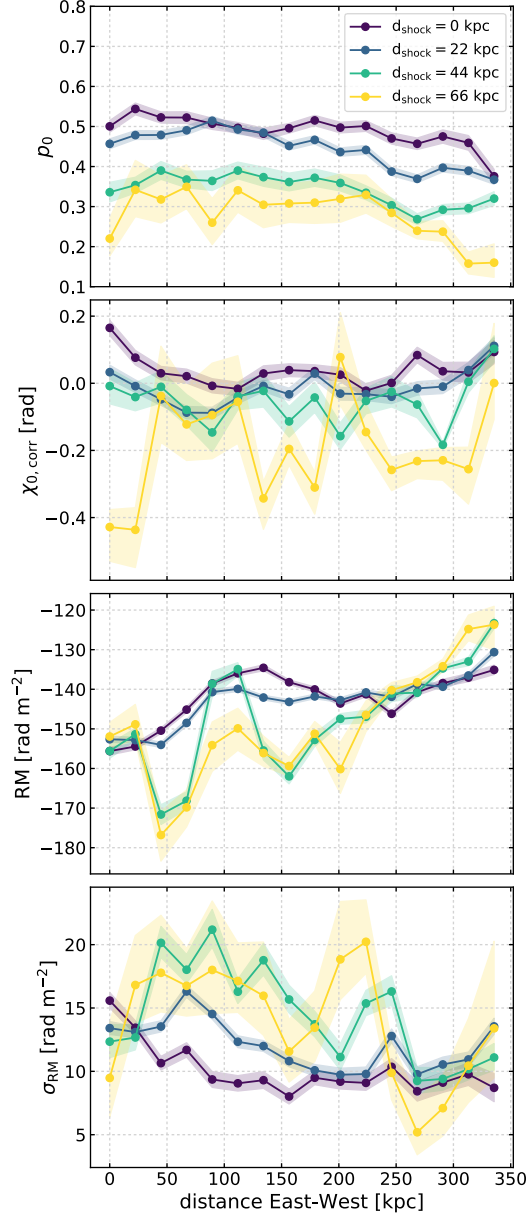
Figure 5.7: From top to bottom: East-West profiles on the RN3 filament for the best-fit intrinsic polarization fraction (p_0), intrinsic polarization angle corrected for the shock normal ($\chi_{0,\mathrm{corr}}$), Rotation Measure (RM) and depolarization (σ_{RM}) using the External Faraday Rotation dispersion model (Eq. 5.7). Different colors represent different distances from the shock (d_{shock}, see legend), being the shock located at the outermost edge of the relic, and the correspondent shaded areas show the uncertainties on the measurements.
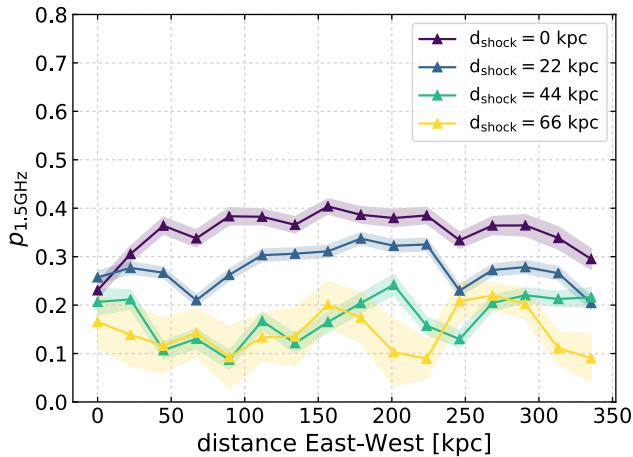
Figure 5.8: As the top panel in Fig. 5.7, but for the polarization fraction at 1.5 GHz.

(2010) and Di Gennaro et al. (2018), respectively. We found Pearson and Spearman rank coefficients of $r_p = -0.28$ and $r_s = -0.28$ for the $p_0-\alpha_{3.0GHz}^{150MHz}$ distribution, and $r_p = 0.16$ and $r_s = 0.24$ for the $\sigma_{RM}-\alpha_{3.0GHz}^{150MHz}$ distribution. These measurements show, for the first time, that the northern relic in CIZAJ2242 suffers from both wavelength- and radial-dependent depolarization.

Finally, no clear downstream variations are seen for the intrinsic polarization angle corrected for the shock normal in the plane of the sky[9] ($\chi_{0,corr} = \chi_0 - n$, second panel in Fig. 5.7) and for the Rotation Measure (third panel in Fig. 5.7; see also Sect. 5.6.5).

5.6.2. On the downstream depolarization

In the following sections, we discuss two possible explanations for the observed radial profile of the polarization fraction. In particular, we investigate the role of wavelength-dependent depolarization and Faraday Rotation (Sect. 5.6.2) and include a three-dimensional modelling of the relic (Sect. 5.6.2).

---

[9]Uncertainties on $\chi_{0,corr}$ are determined included the uncertainties on χ_0 (~ 0.01 rad, from the fitting procedure using MCMC) and on n within the beam region (~ 0.02 rad at 7″ resolution).
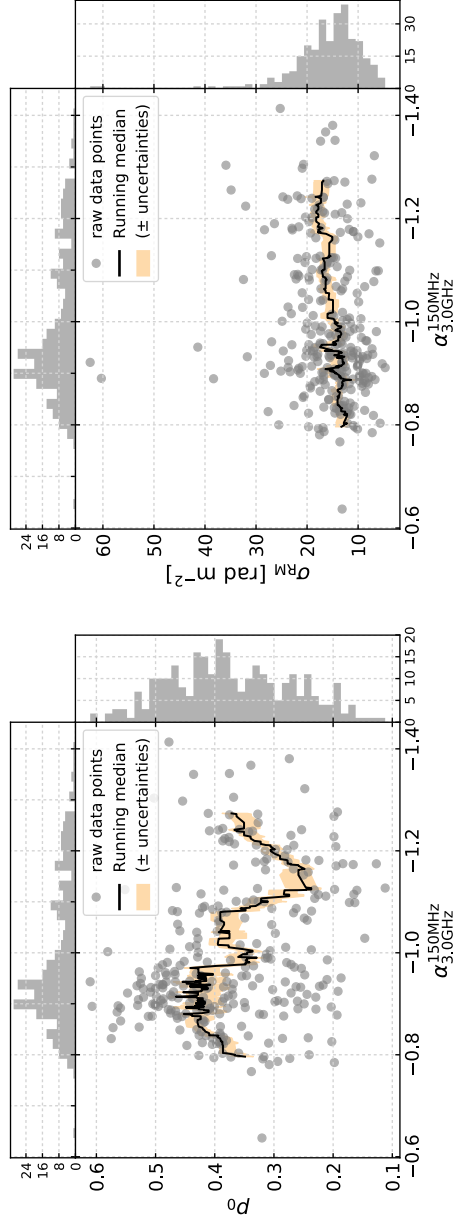
Figure 5.9: Distributions of the intrinsic polarization fraction and external wavelength-dependent depolarization as a function of the spectral index (grey circles in the left and right panel, respectively). The grey histograms show the projected distribution of the y- and x-axis quantities along each axis. The black solid line shows the running median of p_0 and σ_{RM} calculated using 20 windows in the $\alpha_{3.0\mathrm{GHz}}^{150\mathrm{MHz}}$ space, while the yellow area represents the correspondent uncertainties.
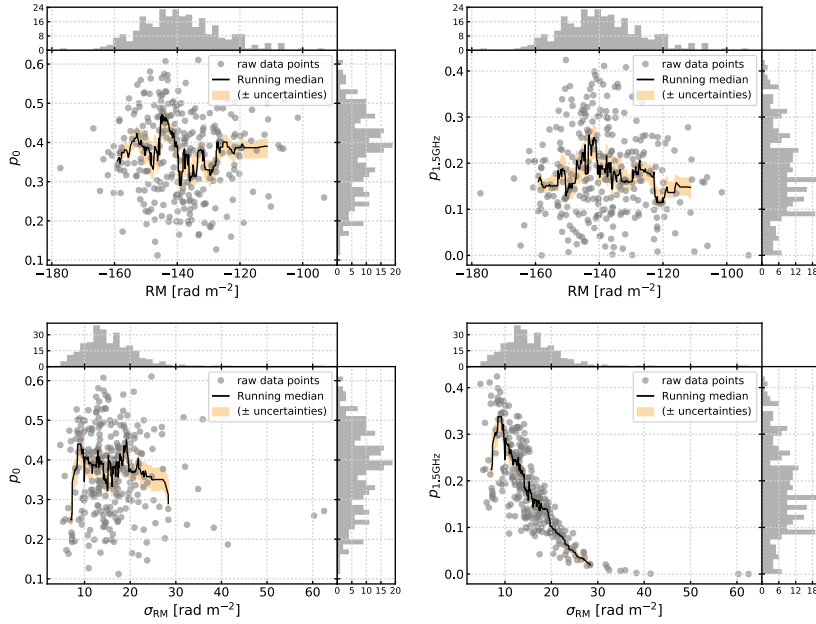
Figure 5.10: Distributions of the intrinsic and 1.5 GHz polarization fractions (left and right column respectively) as a function of the absolute relative Rotation Measure and external wavelength-dependent depolarization (grey circles in the top and bottom panels, respectively). The grey histograms show the projected distribution of the y- and x-axis quantities along each axis. For both columns, the solid black line represents the running median of the y-axis variable (i.e. p_0 and $p_{1.5\mathrm{GHz}}$) calculated using 20 windows in the space of the x-axis variable (i.e. RM and σ_{RM}). The yellow shaded area represents the uncertainty on the running median.

Wavelength-dependent depolarization and Faraday Rotation effects

A naive explanation for the downstream depolarization is the effect of a complex magneto-ionic layer that might differently rotate the polarization vectors in different parts of the relic. According to this scenario, the bottom panel in Fig. 5.7 and the right panel in Fig. 5.9 both suggest a mild increasing contribution of the external wavelength-dependent depolarization in the downstream region.

We investigated the relation between the best-fit intrinsic polarization fraction and the measured Rotation Measure and external wavelength-dependent depolarization (left column in Fig. 5.10). In both cases, we do not see particular trends, nor underlying fluctuations from the analysis of the running median. Both the Pearson and Spearman rank coefficients confirm the visual inspection, being $r_p = -0.06$ and $r_s = -0.09$

Table 5.4: Pearson (r_p) and Spearman (r_s) rank correlation coefficients of the running median in Figs. 5.9 and 5.10.

Parameters	r_p	r_s
p_0–RM	−0.06	−0.09
p_0–σ_{RM}	−0.06	−0.01
$p_{1.5GHz}$–RM	−0.07	−0.04
$p_{1.5GHz}$–σ_{RM}	−0.73	−0.82
p_0–$\alpha_{3.0GHz}^{150MHz}$	−0.28	−0.28
σ_{RM}–$\alpha_{3.0GHz}^{150MHz}$	0.16	0.24

for the p_0–RM distribution and r_p = −0.06 and r_s = −0.01 for the p_0–σ_{RM} one (see Table 5.4). We therefore conclude that our best-fit intrinsic polarization fraction is independent from external factors, as the Faraday Rotation and the wavelength-dependent depolarization. On the other hand, an anti-correlation in the $p_{1.5GHz}$–σ_{RM} distribution is observed (r_p = −0.73 and r_s = −0.82). No correlation has been found for the $p_{1.5GHz}$–RM one (r_p = −0.07 and r_s = −0.04). These suggest that only the wavelength-dependent depolarization affects the polarization fraction at lower frequencies.

Relic three-dimensional shape

For a power law electron energy distribution with slope $\delta = 1 - 2\alpha$, i.e. $dN(E)/dE \propto E^{-\delta}$, in a region with homogeneous magnetic field the intrinsic polarisation amounts to (Rybicki & Lightman, 1986):

$$p_0 = \frac{3\delta + 3}{3\delta + 7}. \tag{5.11}$$

Therefore, if the slope of the electron distribution varies across the relic the intrinsic polarisation will also vary. According to the standard scenario for relic formation, electrons are (re-)accelerated at the shock front, with a power law energy distribution, and cool subsequently due to synchrotron and Inverse Compton energy losses. Locally, the resulting electron spectrum may show a break, even if the sum of all these spectra is a power law again, (see Di Gennaro et al., 2018, for a detailed spectral analysis of the relic). The locally curved spectra thus show a different intrinsic degree of polarization than the overall relic. From Eq. 5.11, the downstream region with the aged electron population would have a higher intrinsic polarisation fraction (orange line in Fig. 5.11).

Although the decreasing radial profile of the best-fit polarization degree seems to be in contrast with the above description, the complex shape of
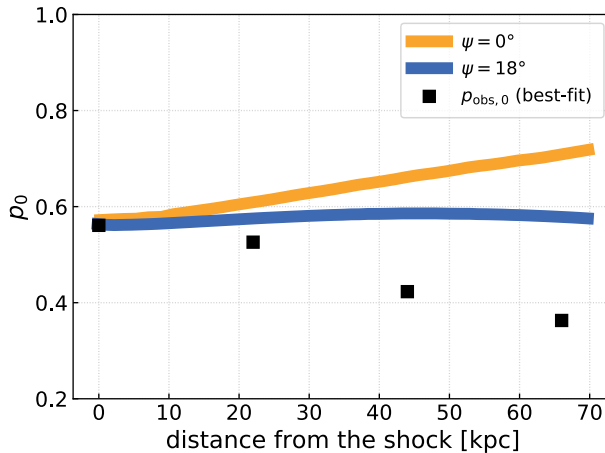
Figure 5.11: Theoretical profiles of the intrinsic polarization fraction in the post-shock region assuming a shock wave perfectly aligned with the plane of the sky (i.e. $\psi = 0°$, orange line) and assuming an opening angle for the relic of $\psi = 18°$ (Di Gennaro et al., 2018, blue line). Black squares represent the best-fit intrinsic polarization fraction values obtained from a smaller sector of RN3 (i.e. where we could assume constant polarization parameters in the east-west direction).

the shock front and the downstream region may impact the polarization, for instance by an inhomogeneous intrinsic polarisation fractions and by large differences in the path through the magnetized ICM from the emission to the observer. In this context, to reproduce a correct projected intrinsic polarization profile, it is necessary to take into account a realistic shape of the shock front, which has to include the contribution of its inclination with respect to the line of sight (M. Hoeft et al. in prep.).

Following Di Gennaro et al. (2018), we created a toy model assuming that the shock front is a spherically symmetric cap in the plane determined by the line of sight and the cluster center, with a curvature radius of 1.5 Mpc and opening angle of $2\psi = 36°$ (see also Fig. 10 in Kierdorf et al., 2017). The alignment of electric field vectors with the shock normal (bottom panel in Fig. 5.4) implies that the magnetic field is dominantly tangled on scales smaller than the resolution of the observations (i.e. 2.7″). If the polarization angle reflects the structure of the magnetic field, we can assume a shock-compression scenario to explain the polarization properties of the relic (Ensslin et al., 1998). In this scenario, an upstream isotropically tangled magnetic field is compressed by the shock front resulting in a downstream anisotropically tangled field, causing polarized synchrotron emission. In the specific case of RN, we adopt a shock Mach number of 3.7 which corresponds to an intrinsic polarization fraction of 58%, when the

shock is observed perfectly edge on. This value matches the maximum p_0 we estimated in the relic (see panel (c) in Fig. 5.5). The emission of different parts of the shock front is summed up, taking into account the angle between the shock normal and the line of sight, $90° - \psi$. The more this angle deviates from $90°$ the lower the intrinsic polarization becomes. Since those parts of the shock which deviate more from $90°$ are shifted further downstream with respect to the outermost edge of the relic, the intrinsic polarization fraction decreases towards the downstream. For our model parameters, these two effects, namely the downstream increase in polarization due to the aging of the electrons population and the decrease due to the shift of those parts of the shock which are not seen perfectly edge on, cancel out, resulting in an almost constant theoretical p_0 profile. This, however, still deviates from our observations (see blue line and black squares in Fig. 5.11).

It is worth noting that we have used here a very simplified geometrical model that, for instance, does not explain the east-west p_0 variation we observed in the relic. Moreover, it does not include the effect of emitting regions at different Faraday depths in the relic downstream. According to the spherical model described above, at a distance of 60 kpc of the outer edge, the emission from the "back side" of the cluster travels about 800 kpc through the magnetised ICM, which causes additional downstream depolarization. Interestingly, no evidence of multiple-RM components in the downstream region are observed in our data (see Appendix .1). This suggests either that the relic cannot be described simply by a smooth spherical cap (e.g. overlapping filamentary structures) or we might be actually observing only the front/back side of the radio relic. On the other hand, the geometrical projections involve a number of adjustable parameters (see, e.g. Kang et al., 2012). Hence, a detailed modeling, which should include the shock shape, its downstream spectral and polarized characteristics and its physical properties (such as the Mach number distribution, e.g. Ha et al., 2018; Botteon et al., 2020), is complicated and needs to be further examined.

5.6.3. Turbulent magnetic field in the post-shock region

In the presence of both ordered and random magnetic field, Eq. 5.11 can be written as (Sokoloff et al., 1998; Govoni & Feretti, 2004b):

$$p_0 = \frac{3\delta + 3}{3\delta + 7} \frac{1}{1 + \left(\frac{B_{\mathrm{rand}}}{B_{\mathrm{ord}}}\right)^2} , \qquad (5.12)$$

where B_{ord} represents the magnetic field component that is aligned with the shock surface and B_{rand} represents the isotropic magnetic field component. Thus, the ratio $B_{\mathrm{rand}}/B_{\mathrm{ord}}$ describes the order of isotropy of the magnetic field distribution.
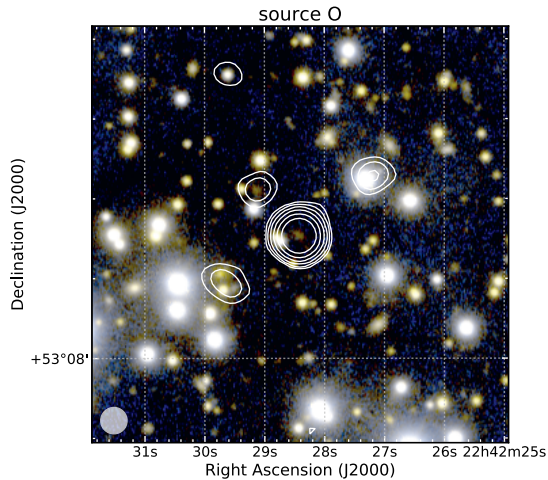
Figure 5.12: Subaru *g-gi-i* optical image of source O (Dawson et al., 2015; Jee et al., 2015). 1–4 GHz total intensity radio contours at 2.5″ resolution are overlaid at levels of $3\sigma_{\mathrm{rms}} = \sqrt{(1, \ 4, \ 16, \dots)}$, with $\sigma_{\mathrm{rms}} = 5.6 \ \mu\mathrm{Jy \ beam}^{-1}$ the map noise (Di Gennaro et al., 2018).

In the northern relic of CIZAJ2242, the polarization angle seems to follow well the shock normal (see bottom panel in Fig. 5.4), and no change is observed in the downstream region (second panel in Fig. 5.7). This suggests that the component of the magnetic field parallel to the polarization angle is approximately constant in the downstream region. However, our measurements are limited by the observing resolution, which can hide the presence of tangled magnetic field on smaller scales and lead to a decreasing polarization fraction. If this is the case, from Eq. 5.12, we can relate the radial decrease of p_0 with the decrease of the degree of anisotropy in the downstream region (i.e. the ratio $B_{\mathrm{rand}}/B_{\mathrm{ord}}$ increases). Given the averaged values found in the RN3 filament, i.e. $\langle p_0 \rangle_{d=0\mathrm{kpc}} \sim 0.49$ and $\langle p_0 \rangle_{d=66\mathrm{kpc}} \sim 0.28$, and assuming $\delta = 3$ (i.e. $\alpha = -1$) we find that the ratio $B_{\mathrm{rand}}/B_{\mathrm{ord}}$ should increase of about 40% in the downstream region. Shock propagation in the ICM generates vorticity which boosts turbulence and amplify the magnetic field (e.g., Ryu et al., 2008). Behind the shock, turbulence behaves more or less as a "decaying" turbulence, (see, e.g., Porter et al., 2015; Donnert et al., 2018), which might lead to the decreasing degree of anisotropy. Further studies are needed, however, upon this point.

The turbulent magnetic field B_{turb} is related to the wavelength-dependent depolarization, according to (Sokoloff et al., 1998; Kierdorf et al., 2017):

$$\sigma_{\mathrm{RM}} = 0.81 \sqrt{\frac{1}{3}} \langle n_e \rangle B_{\mathrm{turb}} \sqrt{\frac{L\Lambda}{f}} \, , \qquad\qquad (5.13)$$

where $\langle n_e \rangle$ is the average electron density in cm^{-3}, f is the volume filling factor of the Faraday-rotating gas, L is the path length through the thermal gas and Λ is the turbulence scale, both in pc unit. In the cluster area, only source O is a background polarized radio galaxy (see Fig. 5.12). From our QU fit, we found that the amount of the external depolarization for this source is very similar to that in RN, i.e. $\sigma_{\mathrm{RM}} \sim 22$ rad m^{-2} (see panel (f) in Fig. 5.5 and bottom left panel in Fig. 5.6). Given the proximity of source O and RN and assuming that there is no contribution to the depolarization from source O itself and from the Galactic plane, we can use this σ_{RM} in Eq. 5.13 to obtain an approximate estimation of the tangled magnetic field in the northern relic, being $B_{\mathrm{turb}} \sim 5.6$ μGauss. Here, we used $\langle n_e \rangle = 10^{-4}$ cm^{-3} (Ogrean et al., 2014), $L = 350$ kpc[10], $f = 0.5$ (Govoni & Feretti, 2004b; Murgia et al., 2004) and $\Lambda = 8$ kpc[11], i.e. the linear scale of our best resolution observation (i.e. 2.7″). Note that the estimated B_{turb} is consistent with the upper value of the total magnetic field strength quoted by van Weeren et al. (2010), leading to a ratio of magnetic and the thermal pressures $P_{\mathrm{mag}}/P_{\mathrm{th}} \sim 0.11$ (Akamatsu et al., 2015).

5.6.4. Effect of the limited frequency-band coverage

The basic assumption of the QU-fitting approach is that, given observations in a wide band $\Delta\lambda^2 = \lambda^2_{\mathrm{max}} - \lambda^2_{\mathrm{min}}$ and assuming a theoretical model, one can extrapolate the intrinsic polarization parameters, p_0 and χ_0, at the ideal wavelength $\lambda \rightarrow 0$ where no wavelength-dependent effects (e.g. depolarization or Faraday Rotation) occur. The wider $\Delta\lambda^2$ and lower λ^2_{min} the better one can validate the theoretical model. However, due to the lack of high-resolution information at higher frequencies we cannot exclude the possibility of the existence of a more complex model to describe the polarized emission in RN. For example, Ozawa et al. (2015) found a step-like fractional polarization profile in the radio relic in Abell 2256, with the fractional polarization increase occurring above 3.0 GHz. However, it is important to note that the presence of more complex models would result in a strong deviation from the Burn model in the downstream region, where a larger amount of magnetized plasma (i.e. the ICM) is crossed. Despite the low S/N, however, we see that the Burn approximation still holds in this region. Finally, $\Delta\lambda^2$ also sets the amount of wavelength-dependent

---

[10]The path length of the magnetized plasma crossed by the polarized emission is $L \approx 2\sqrt{2d_s\,r_s}$, where $d_s = 10$ kpc and $r_s = 1.5$ Mpc are the intrinsic width of the shock and its distance from the cluster center, respectively (see Kierdorf et al., 2017).

[11]This is about one order of magnitude smaller than what is commonly used for galaxy clusters (i.e. 100 kpc, see Iapichino & Brüggen, 2012).
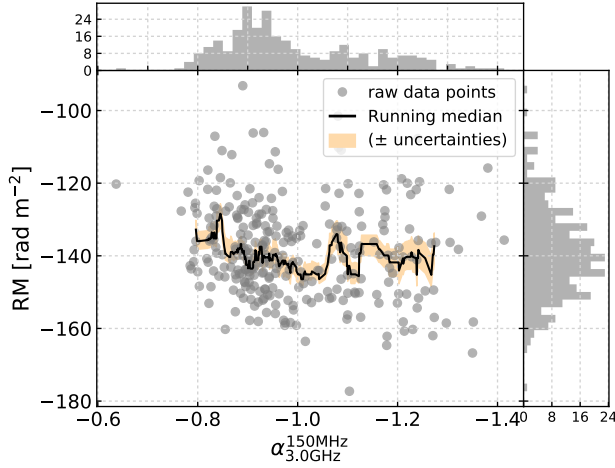
Figure 5.13: Distributions of the absolute relative Rotation Measure as a function of the spectral index (grey circles). The grey histograms show the projected distribution of the y- and x-axis quantities along each axis. The black solid line shows the running median of RM in the $\alpha_{3.0\text{GHz}}^{150\text{MHz}}$ space using 20 windows. The yellow area represents the uncertainties on the running median.

depolarization detectable. Given our observing band, it would be rather difficult to determine $p(\lambda^2)$ if $\sigma_{\text{RM}} \geq 100$ rad m^{-2}.

Interestingly, if we extract the profiles of the polarization parameters using an Internal Faraday Rotation Dispersion model (i.e. Eq. 5.8), we found consistent p_0, χ_0 and RM profiles as those we found using the External Depolarization model, and a larger amount of internal depolarization ς_{RM}, in agreement with the mathematical differences of the two formulas. This means that, with the current data in hand, we cannot distinguish between an External or Internal depolarization model for the northern relic in CIZAJ2242. Lower-wavelength wide-band observations (i.e. C- and X-band, 4–8 and 8–12 GHz respectively) might then help to infer the nature of the polarized emission of the northern relic in CIZAJ2242.

5.6.5. Investigation for intrinsic RM fluctuations

We found very weak/no correlations between RM and the spectral index and between RM and the external wavelength-dependent depolarization (Figs. 5.13 and 5.14, respectively). The absence of correlation in the latter case is expected in case of external beam depolarization (Govoni & Feretti, 2004b).

In Sect. 5.4, we show evidence for strong Rotation Measure variation
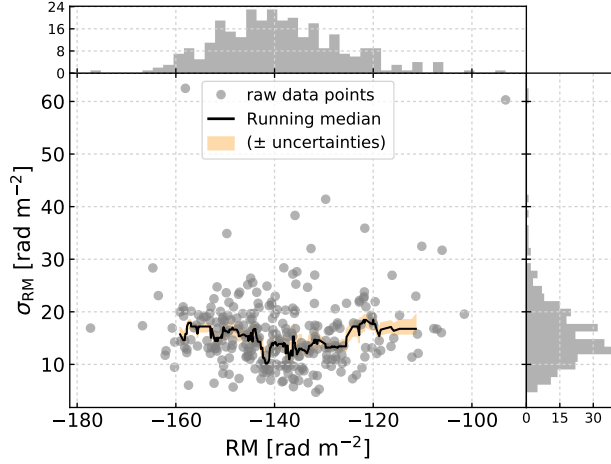
Figure 5.14: Distribution of the external wavelength-dependent depolarization as a function of the absolute relative Rotation Measure (grey circles). The grey histograms show the projected distribution of the y- and x-axis quantities along each axis. The black solid line shows the running median of σ_{RM} in the RM space calculated using 20 windows. The yellow area represents the uncertainties on the running median.

of the Galactic foreground, over angular scales of $3' - 5'$, by investigating the RM values in radio galaxies outside the cluster. Along the northern relic, a variation of 30 rad m^{-2} around the median value of 140.8 rad m^{-2} is also found on much smaller scales (i.e. $15'' - 30''$, see Fig. 5.5). At the cluster position ($l = 104°$ and $b = -5°$), strong variation from the Galactic plane is expected (van Eck, priv. comm.), although detailed studies are still missing. If the detected RM variation is entirely due to the Galactic plane, this would show for the first time that Galactic RM variation is also present on relatively small scales.

Alternatively, this variation could be due to the ICM, and to the magnetic field close to the relic. As shown in Figs. 5.5 and 5.6, the strongest RM fluctuations are measured at the connection of two pairs of filaments, i.e. RN1–RN2 and RN3–RN4, where we measure on average ΔRM $\sim$ 30 rad m^{-2} (see panel (e) in Fig. 5.5). If this is entirely due to the ICM, given the relation between RM and $B_{\parallel}$ (Eq. 5.5), we can constrain the magnetic field variation in the relic, being $\Delta B_{\parallel} \sim 1$ μGauss, where we have used $n_e = 10^{-4}$ cm^{-3} and $L = 350$ kpc. Assuming a global value of 5 μGauss (van Weeren et al., 2010), we obtain a magnetic field variation of roughly 20%. In case of weaker global magnetic field, i.e. 1.2 μGauss (van Weeren et al., 2010), variations increase up to 80%.

Table 5.5: Pearson (r_p) and Spearman (r_s) rank correlation coefficients of the running median in Figs. 5.13 and 5.14.

Parameters	r_p	r_s
RM–$\alpha_{3.0\text{GHz}}^{150\text{MHz}}$	−0.14	−0.17
σ_{RM}–RM	0.08	−0.05

5.7. Conclusions

In this work, we have presented a polarimetric study of the merging galaxy cluster CIZA J2242.8+5301 ($z = 0.1921$) in the 1–4 GHz frequency range with the Jansky Very Large Array. We used the *QU*-fitting approach to obtain information on the polarization parameters, i.e. intrinsic polarization fraction (p_0), intrinsic polarization angle (χ_0), Rotation Measure (RM) and depolarization (σ_{RM}), for the full cluster at 2.7″, 4.5″, 7″ and 13″ resolution. This work mainly focused on the most prominent source in CIZA J2242.8+5301, i.e., the northern radio relic (RN). Below, we summarize the main results of our work:

- CIZA J2242.8+5301 is bright in polarized light, with the emission coming from several sources, both diffuse and associated with radio galaxies. In particular, at the highest resolution available (i.e. 2.7″) the northern relic mimics the filamentary structure seen in total intensity emission (Di Gennaro et al., 2018).

- In agreement with previous studies (van Weeren et al., 2010; Kierdorf et al., 2017), we found a high degree of intrinsic polarization in RN, with the eastern side having a higher value than the western one (i.e. $p_{0,\text{east}} \sim 0.55$ and $p_{0,\text{west}} \sim 0.35$, with p_0 the best-fit values from the *QU*-fit).

- The polarization vectors strongly align with the shock surface also in high resolution observation (i.e. 2.7″), implying that the magnetic field is dominantly tangled on scales smaller than ~ 8 kpc.

- For the first time we were able to investigate the polarization parameters in the relic post-shock region on ten-kpc scales. We found that both the best-fit intrinsic and 1.5 GHz polarization fractions (i.e. p_0 and $p_{1.5\text{GHz}}$) decrease towards the cluster center. While, for the latter, a strong contribution of the external wavelength-dependent depolarization is present, the downstream depolarization profile for p_0 does not correlate with RM and σ_{RM}.

- We speculate that complex geometrical projections and/or relic shape could possibly explain the p_0 downstream depolarization, although

detailed modelings should be further worked. We also note that the decrease of the degree of magnetic field anisotropies (i.e. B_{ord}/B_{rand}) by about 40% might explain the depolarization.

- We detect only one polarized background radio galaxy, i.e. source O. Its σ_{RM} is similar to the average value in the northern relic, and allows us to set an approximate value on the turbulent cluster magnetic field of about 5.6 μGauss.

- Different Rotation Measures are observed in the northern and southern relics ($RM_{RN} \sim -140$ and $RM_{RS} \sim -80$ rad m^{-2}, respectively). This could be either due to variation of the foreground Galactic Faraday Rotation or to a different contribution of $n_e B_\parallel$ in the ICM along the line of sight.

- Rotation Measure fluctuations of about 30 rad m^{-2} on physical scales of about $3' - 5'$ are observed at the location of the northern relic. With the current data in hand we cannot determine whether this is due to Galactic plane or to magnetic field local to the relic. In the former case, this will be the first evidence of small-scale Galactic RM fluctuations. In the latter case, we estimate a magnetic field variation of about 1 μGauss.

Recently, the polarization properties of radio relics were investigated by Wittor et al. (2019) and Roh et al. (2019) using numerical simulations. Although they were able to reproduce some properties of observed relics, such as the global observed degree of polarization, they found that it is difficult to explain the high degree polarization (up to $\sim$ 60 %) and the uniformity of the intrinsic polarization angle of the Sausage relic. Incorporating realistic modelings, as well as matching the spatial resolution for simulations and observations, would be crucial steps for the understanding of the observed polarization properties of relics and the connection to the underlying magnetic field.

and RPK acknowledge support from the Smithsonian Institution and the
Chandra High Resolution Camera Project through NASA contract NAS8-
03060. This research made use of APLpy, an open-source plotting package
for Python (Robitaille & Bressert, 2012).

.1. *QU*-fit plots

In Fig. 5.1 we show an example of the *QU*-fitting results on a single
pixel with high S/N at the shock location. In Fig. .1.1, we show the same
results but applied on a pixel in the relic downstream. Despite the lower
S/N, a single-RM component *QU* fit still provides a good match to our data.
In Figs. .1.2, we show the Faraday spectrum on these two pixels, obtained
with pyrmsynth. The RM cube ranges from –4000 to +4000 rad m^{-2}, with
a FWHM of 60 rad m^{-2}. The two symmetric side-lobes we see next to each
peak are likely due to interference in the Faraday spectra, as we do not use
the RM-CLEAN option (see footnote 2 in Brentjens, 2011).

.2. Uncertainty maps on the polarization parameters

In this section, we show the p_0, RM and σ_{RM} negative and positive uncer-
tainty maps correspondent to Fig. 5.5(d), (e) and (f) (right and left column
in .2.1), and the $p_{1.5\mathrm{GHz}}$ uncertainty maps (Fig. .2.2). We also present the
polarization parameter uncertainty (negative and positive) maps of the full
cluster at 13″ resolution (Figs. .2.3 and .2.4). The map of the polariza-
tion fraction at 1.5 GHz and its correspondent uncertainty map of the full
cluster at 7″ resolution is displayed in Fig. .2.5).

.3. Annuli on RN3 and grid used for the correlation analysis

Here, we display the regions where we performed the *QU*-fit. The boxes
shown in Fig. .3.1 generate the profiles in Figures 5.7 and 5.8. The boxes
shown in Fig. .3.2 generate Figures 5.9, 5.10, 5.13 and 5.14. Each box
has the same size of the restoring beam, i.e. 7″×7″ (about 22×22 kpc^2 at
the cluster redshift). The polarized flux in each box is above a threshold
of $3\sigma_{\mathrm{rms},P}$ (see Sect. 5.3).
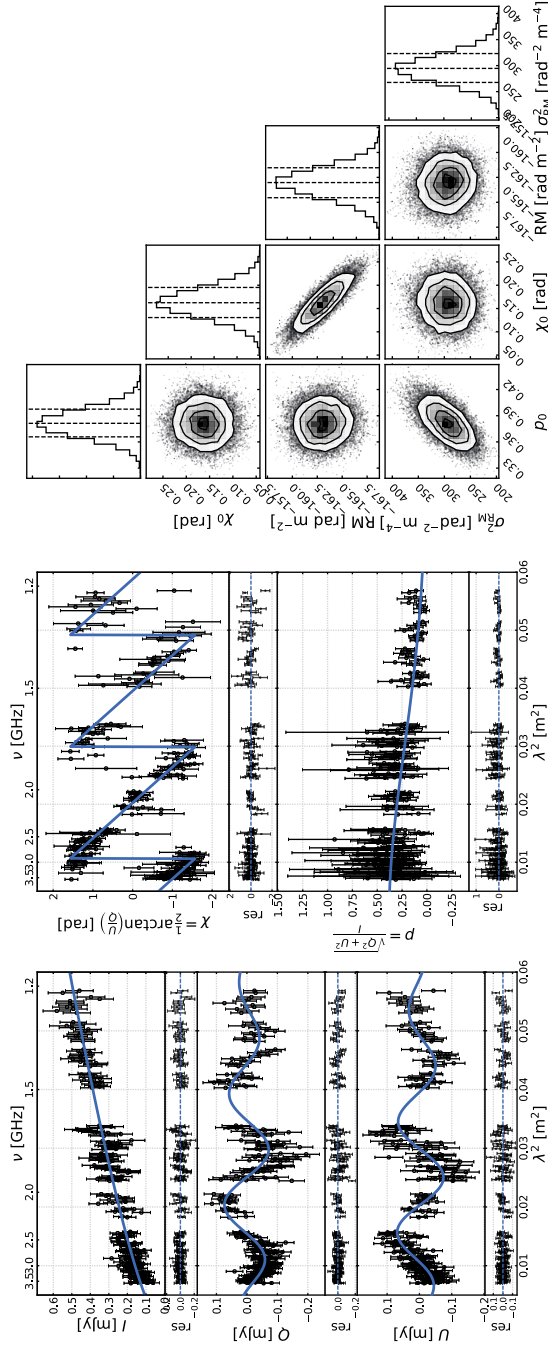
Figure .1.1: As Fig. 5.1 but for a pixel further in the RN downstream region.
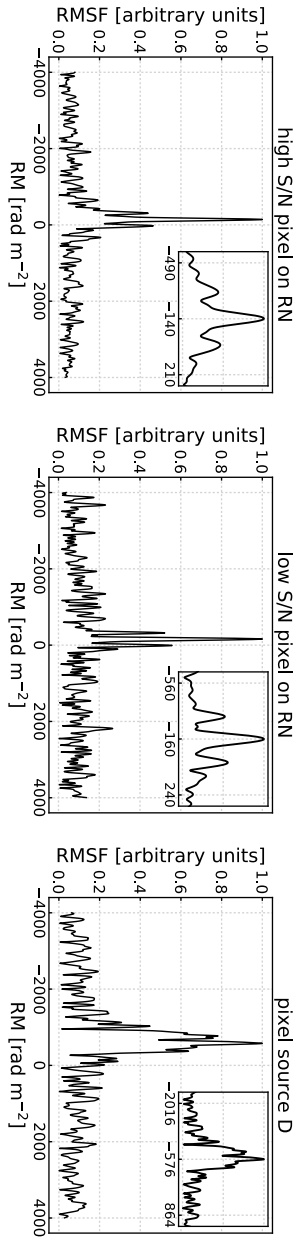
Figure .1.2: Faraday spectrum on the pixels displayed in Figs. 5.1 (left panel) and .1.1 (central panel). In the right panel, the Faraday spectrum of a high S/N pixel in source D is shown. The inset in the two plots shows the zoom on the Faraday peak.
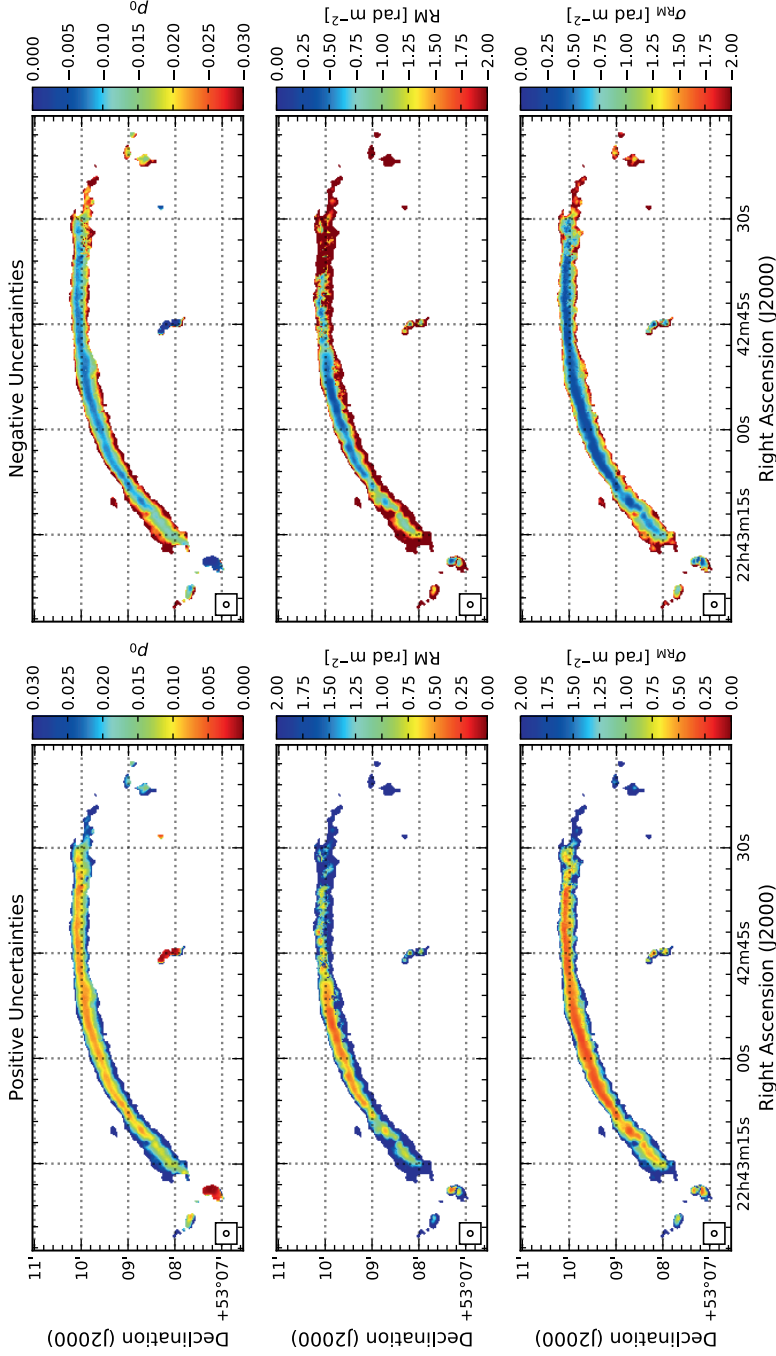
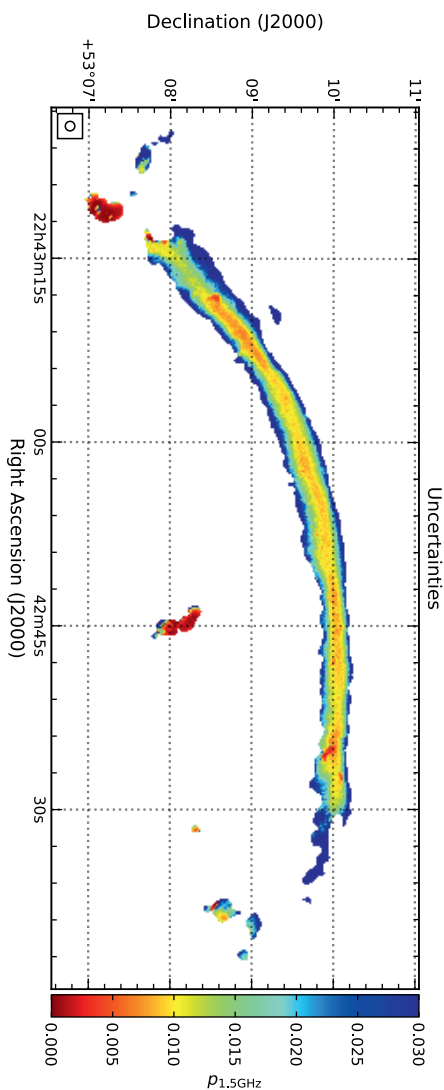**Figure .2.1:** Positive (left column) and negative (right column) uncertainty maps corresponding to panels (c), (e) and (f) in Fig. 5.5.

Figure .2.2: 1.5 GHz polarization fraction uncertainty map (panel (d) in Fig. 5.5).
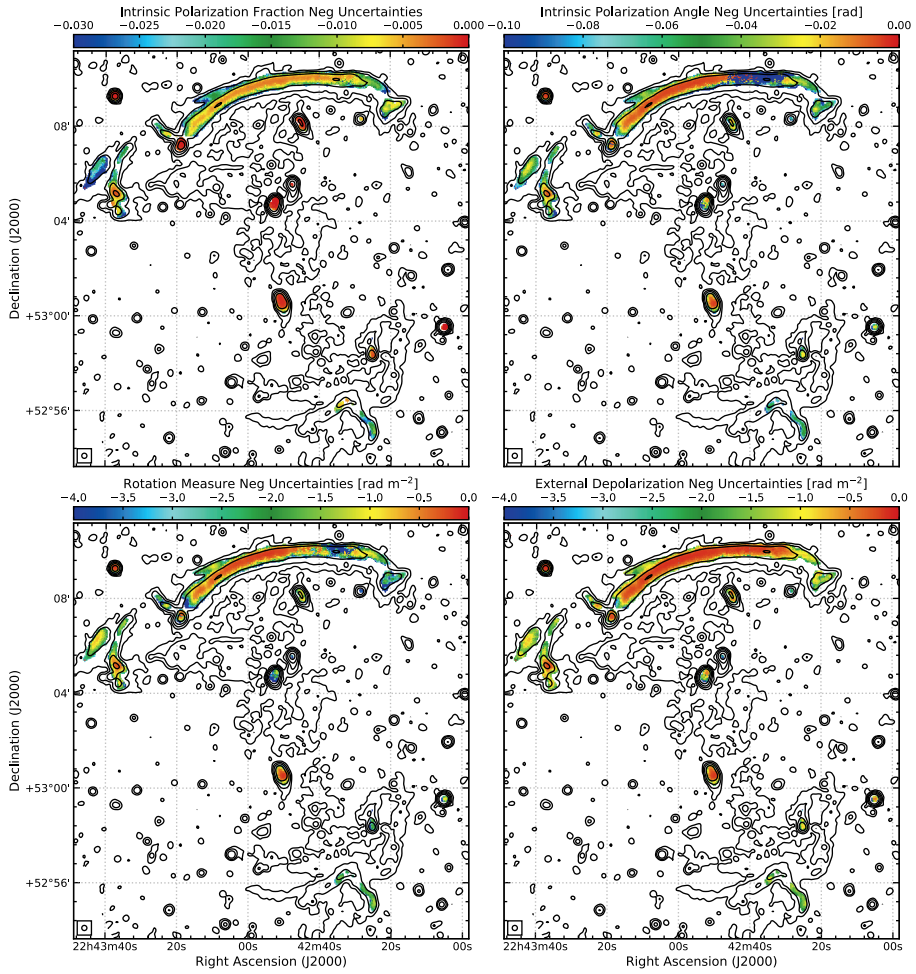
Figure .2.3: Negative uncertainty maps corresponding to Fig. 5.6.
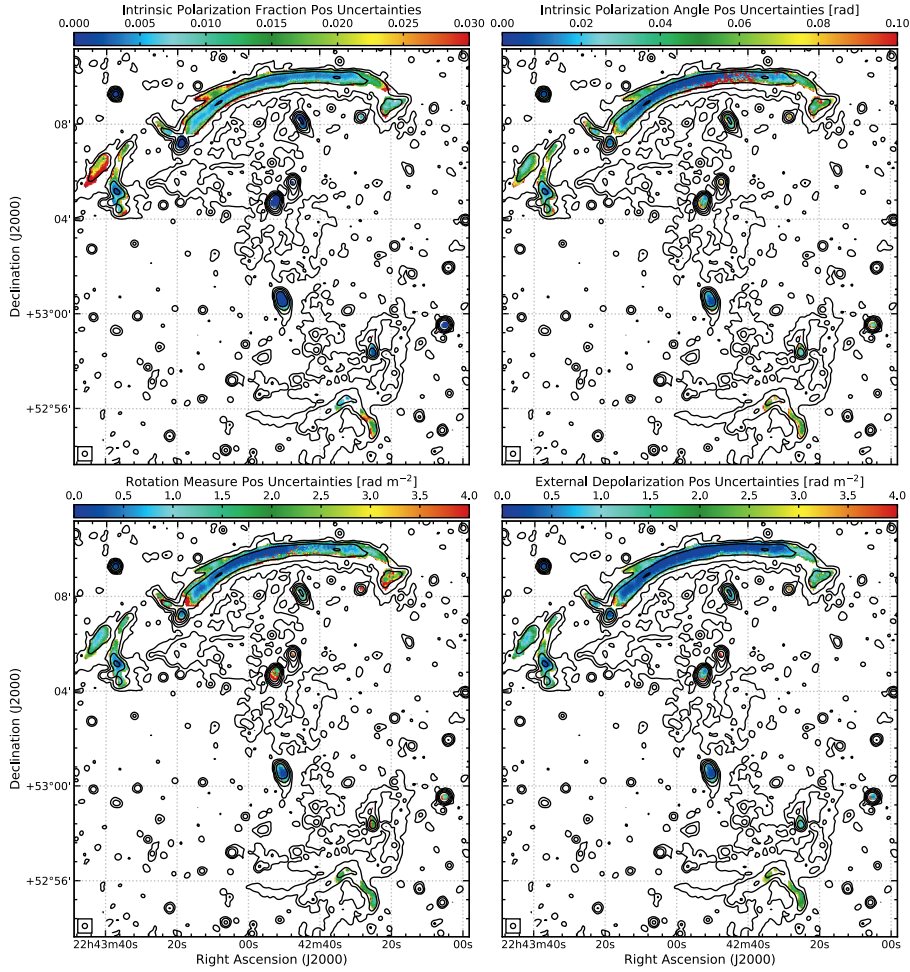
Figure .2.4: Positive uncertainty maps corresponding to Fig. 5.6.
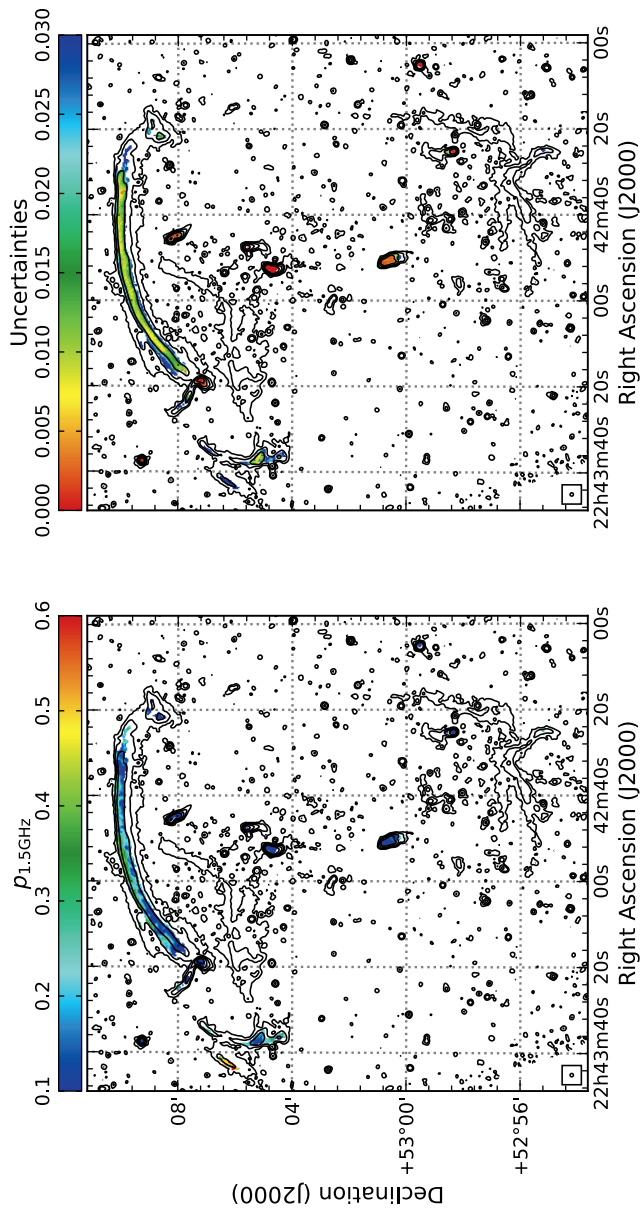
Figure .2.5: Polarization fraction map at 1.5 GHz (left panel) and correspondent error map (right panel) of CIZAJ2242 at 7″ resolution. Stokes I radio contours at the same resolution are drawn in black at level of $3\sigma_{rms}\sqrt{1, 4, 16, 64, \ldots}$, with $\sigma_{rms} = 4.2 \ \mu Jy \ beam^{-1}$ (Di Gennaro et al., 2018).
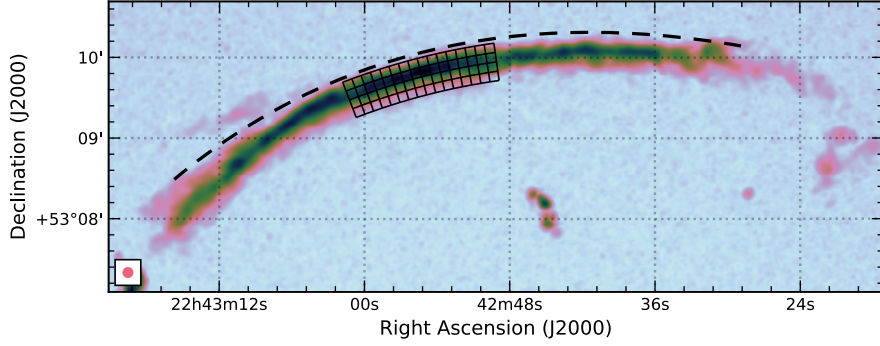
Figure .3.1: Total averaged polarization image at 7″ resolution of the northern relic with the boxes used to investigate the presence correlation among the polarization parameters in Figs. 5.7 and 5.8. The position of the shock (i.e. $d_{\text{shock}} = 0$ kpc) is displayed by the black dashed line.
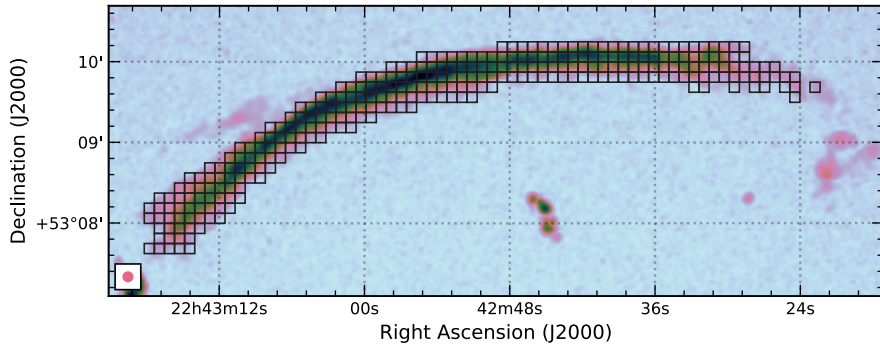
Figure .3.2: Total averaged polarization image at 7″ resolution of the northern relic with the boxes used to investigate the presence correlation among the polarization parameters in Figs. 5.10 and 5.14.

CHAPTER

6

A LOFAR-UGMRT SPECTRAL INDEX STUDY OF DISTANT RADIO HALOS

G. Di Gennaro, R.J. van Weeren, R. Cassano, G. Brunetti, M. Brüggen et al. *Astronomy & Astrophysics*, to be submitted.

Abstract. Radio halos are Mpc-scale diffuse radio sources located at the centres of merging galaxy clusters. The common mechanism invoked to explain their origin is the re-acceleration of relativistic particles driven by large-scale turbulence. Current re-acceleration models predict that a significant number of halos at high redshift should be characterised by very steep spectra ($\alpha < -1.5$), due to strong Inverse Compton energy losses. In this paper, we investigate the spectral index properties of a sample of nine clusters selected from the second Planck Sunyaev-Zel'dovic catalogue showing diffuse radio emission with the Low Frequency Array (LOFAR) in the 120–168 MHz band. We analysed upgraded Giant Metrewave Radio Telescope (uGMRT) observations in Band 3 and 4, i.e. 250–500 and 550-900 MHz respectively. These observations were combined with existing LOFAR data to produce spectral index maps and to retrieve the cluster spectral properties.We find diffuse radio emission in the uGMRT observations for five of the nine high-z radio halos previously discovered with LOFAR. For those, we measure spectral indices in the range of -1 to -1.4. For the uGMRT non-detections, we estimated upper limits on the spectral index of < -1.5. We also find only one candidate relic. Despite the poor statistics, we find evidence that a significant fraction of massive and merging clusters at high redshift host radio halos with very steep spectra. This is consistent with theoretical predictions, although larger statistical samples are necessary to test models.

6.1. Introduction

In the framework of the ΛCDM cosmological model, galaxy clusters form and grow via accretion of less massive systems (e.g. galaxy groups or small galaxy clusters, see Press & Schechter, 1974; Springel et al., 2006). These events release up to 10^{64} erg in the intracluster medium (ICM) in a few Gyrs. A fraction of this energy is dissipated by shocks and turbulence into the amplification of magnetic fields and (re)acceleration of particles, producing diffuse radio emission in the form of *radio halos* and *radio relics* (see Brunetti & Jones, 2014; van Weeren et al., 2019, for recent theoretical and observational reviews). Due to their intrinsic low surface brightness (~ 1 μJy arcsec^{-2} at 1.4 GHz), halos and relics are difficult to detect. In addition, they are characterised by steep spectra (i.e. $\alpha < -1$, with $S_\nu \propto \nu^\alpha$), hence they are better observed at low radio frequencies (i.e. below GHz).

Radio halos are cluster-size structures that generally follow the distribution of the thermal cluster emission (i.e. the ICM). Their currently favoured formation scenario involves the re-acceleration of electrons via turbulence induced by cluster merger events (e.g. Brunetti et al., 2001; Petrosian, 2001; Donnert et al., 2013). In support of this scenario, radio halos are preferentially detected in dynamically disturbed clusters. The non-detection of γ-rays emission from galaxy clusters, at the level expected (e.g. Reimer et al., 2003; Ackermann et al., 2010a; Prokhorov & Churazov, 2014b; Brunetti et al., 2017; Adam et al., 2021), strongly disfavours hadronic models. The results of proton-proton collisions can generate secondary electrons which then emit synchrotron radiation (e.g. Brunetti & Lazarian, 2011; Pinzke et al., 2017; Brunetti et al., 2017)

Radio relics are elongated structures, generally located in the cluster outskirts. It is widely believed that these are associated with propagating shock waves caused by mergers (e.g. Rottgering et al., 1997; Ensslin et al., 1998; Giacintucci et al., 2008; van Weeren et al., 2010; Pearce et al., 2017; Hoang et al., 2018; Di Gennaro et al., 2018). This is also supported by the detection of strongly polarised emission at the relic position (e.g. van Weeren et al., 2010; Di Gennaro et al., 2021b), which suggests amplification and compression of magnetic fields. Nonetheless, the nature of the (re)acceleration mechanism is still unclear (e.g. Vazza & Brüggen, 2014). Standard Fermi type-I acceleration mechanisms (e.g. Drury, 1983; Ensslin et al., 1998; Brunetti & Jones, 2014) sometimes require an unrealistic shock efficiency to justify the relic radio brightness, due to the low Mach number of the shocks ($\mathcal{M} \lesssim 2$, e.g. Hoang et al., 2017; Di Gennaro et al., 2019; Botteon et al., 2020). Re-acceleration of pre-existing relativistic plasma at the shock has been therefore proposed (e.g. Markevitch et al., 2005; Bonafede et al., 2014; Kang et al., 2017; van Weeren et al., 2017a). Examples which can are considered to indicate on-going re-acceleration are still limited to a few cases (e.g. van Weeren et al., 2017a; Di Gennaro et al., 2018).

Most of the statistical studies of diffuse radio emission are limited to the local Universe (i.e. $z \sim 0.2$; e.g. Cassano et al., 2013; Kale et al., 2015; Cuciti et al., 2021b,a). A handful of clusters up to $z \sim 0.5$ hosting diffuse radio emission have been recently reported in Giovannini et al. (2020). At high redshifts ($z \geq 0.6$), only a few exceptional clusters have been studied so far (e.g. "El Gordo" at $z = 0.87$, Lindner et al. 2014, PLCK G147.3-16.6 at $z = 0.645$, van Weeren et al. 2014 and PSZ2 G099.86+58.45 at $z = 0.616$ Cassano et al. 2019). All these observations were firstly carried out at GHz frequencies, and eventually followed up at lower frequencies (i.e. ~ 100 MHz) to investigate the spectral characteristic of the observed radio halos. This approach however misses a large fraction of (ultra-)steep spectrum halos, because radio halos with $\alpha < -1.5$ are hardly detected at GHz frequencies.

Recently, in Di Gennaro et al. (2021a) we have presented the first statistical study of a sample of distant ($z \geq 0.6$) galaxy clusters, selected from the second Planck Sunyaev-Zel'dovic (SZ) catalog (Planck Collaboration et al., 2016) and observed with the LOFAR Two-Metre Sky Survey (LoTSS; Shimwell et al., 2017, 2019). We observed that 9 out of 19 clusters host diffuse radio emission. The radio halos are located in dynamically disturbed clusters, based on available X-ray observations (Chandra and/or XMM-Newton). Assuming turbulent re-acceleration, from the radio luminosities we estimated magnetic field strengths similar to nearby ($z \sim 0.2$) systems, in the same mass range. According to the turbulent re-acceleration scenario, a large fraction of distant radio halos should have steep integrated spectral indices ($\alpha < -1.5$) due to the increasing synchrotron and Inverse Compton (IC) losses. We have followed up those clusters hosting diffuse radio emission in Di Gennaro et al. (2021a) with the upgraded Giant Metrewave Radio Telescope (uGMRT). This represents the first high-frequency follow up of halos detected at low frequencies. The observed sample is listed in Table 6.1.

Throughout the paper, we assume a standard ΛCDM cosmology, with $H_0 = 70$ km s^{-1} Mpc^{-1}, $\Omega_m = 0.3$ and $\Omega_\Lambda = 0.7$.

6.2. Observations and data Reduction

6.2.1. LOFAR

We use the same dataset presented in Di Gennaro et al. (2021a). The sample was observed together with LoTSS (Shimwell et al., 2017, 2019), which consists of the 8 hours of observation for each pointing (see Table 6.2). We performed standard LOFAR data reduction, which includes direction-independent and direction-dependent calibration and imaging of the full LOFAR field of view using `prefactor` (van Weeren et al., 2016; Williams et al., 2016; de Gasperin et al., 2019), `killMS` (Tasse, 2014; Smirnov

Table 6.1: Physical properties of the galaxy clusters.

Cluster name	z	RA_{J2000} [deg]	Dec_{J2000} [deg]	$M_{SZ,500}$ [10^{14} M$_\odot$]	kpc/″
PSZ2 G086.93+53.18	0.675	228.50446	+52.81074	5.4 ± 0.5	7.125
PSZ2 G089.39+69.36	0.680	208.43748	+43.48470	5.7 ± 0.7	7.148
PSZ2 G091.83+26.11	0.822	277.78430	+62.24770	7.4 ± 0.4	7.676
PSZ2 G099.86+58.45	0.616	213.6909	+54.78029	6.8 ± 0.5	6.845
PSZ2 G126.28+65.62	0.820	190.5975	+51.43944	5.0 ± 0.7	7.670
PSZ2 G141.77+14.19	0.830	70.27167	+68.22275	7.7 ± 0.9	7.700
PLCK G147.3−16.6	0.645	44.105898	+40.290140	6.3 ± 0.4	6.988
PSZ2 G147.88+53.24	0.600	164.37923	+57.99591	6.5 ± 0.6	6.762
PSZ2 G160.83+81.66	0.888	186.74267	+33.54682	$5.7^{+0.6}_{-0.7}$	7.865

The cluster masses, $M_{SZ,500}$, are taken from the Planck-SZ catalog (Planck Collaboration et al., 2016).

Table 6.2: Radio observation details.

Cluster name	Telescope	Project	Observation date [dd-mm-yyyy]	Observation length† [h]	Frequency coverage [MHz]	Configuration
PSZ2 G086.93+53.18	LOFAR	P227+53	19-02-2015	8.33	120–168	HBA Dual Inner
		P231+53	19-02-2015			
	uGMRT	38_054	30-08-2020	6	550–900	Band 4
PSZ2 G089.39+69.36	LOFAR	P207+45	07-05-2015	8.33	120–168	HBA Dual Inner
		P209+42	05-03-2015			
	uGMRT	38_054	25-08-2020	6	250–500	Band 3
PSZ2 G091.83+26.11	LOFAR	P275+63	22-08-2016	8.33	120–168	HBA Dual Inner
		P280+60	18-01-2019			
	uGMRT	36_039	05-05-2019	5	250–500	Band 3
	uGMRT	36_039	29-05-2019	5	550–900	Band 4
PSZ2 G099.86+58.45	LOFAR	P209+55	30-04-2015	8.33	120–168	HBA Dual Inner
		P214+52	12-05-2015			
		P214+55	12-05-2015			
	uGMRT	38_054	30-08-2020	6	550–900	Band 4
PSZ21 G126.28+65.62	LOFAR	P29Hetdex19	26-06-2014	8.33	120–168	HBA Dual Inner
		P30Hetdex06	30-05-2014			
		P33Hetdex08	19-06-2014			
	uGMRT	38_054	10-07-2020	6	550–900	Band 4
PSZ2 G141.77+14.19	LOFAR	P068+69	08-09-2017	8.33	120–168	HBA Dual Inner
	uGMRT	36_039	07-05-2019	5	550–900	Band 4
PLCK G147.3−16.6	LOFAR	P044+39	29-11-2017	8.33	120–168	HBA Dual Inner
	uGMRT	38_054	20-06-2020	6	550–900	Band 3
	uGMRT	38_054	16-06-2020	6	550–900	Band 4
PSZ2 G147.88+53.24	LOFAR	P165+57	11-05-2015	8.33	120–168	HBA Dual Inner
		P166+60	13-10-2017			
	uGMRT	38_054	20-06-2020	6	550–900	Band 4
PSZ2 G160.83+81.66	LOFAR	P185+32	11-12-2019	8.33	120–168	HBA Dual Inner
		P185+35	23-02-2017			
		P188+32	18-08-2017			
		P188+35	28-03-2019			
	uGMRT	38_054	12-08-2020	6	550–900	Band 4

†The observation length includes also the time on the calibrators.

& Tasse, 2015) and `DDFacet` (Tasse et al., 2018, 2021). Additionally, we performed extra phase and amplitude self-calibration loops to improve the quality of the calibration, using the products of the pipeline[1] and subtracting all of the sources outside of a region of $15' \times 15'$ surrounding the target (van Weeren et al., 2020). Final imaging was done with `WSClean` (Offringa et al., 2014; Offringa & Smirnov, 2017) with the wideband deconvolution mode (`channelsout=6`). The images have a central frequency of 144 MHz. The systematic uncertainty due to residual amplitude errors is set to 15% (Shimwell et al., 2019).

6.2.2. uGMRT

The clusters presented in this work have been observed with the uGMRT in Band 3 (250–550 MHz) and/or Band 4 (550–900 MHz). The total length of the observation is 6 hours, except for PSZ2 G091.83+26.11 and PSZ2 G141.77+14.19 which have been observed for 5 hours (see Table 6.2). Data were recorded in 2048 frequency channels with an integration time of 4 s in full Stokes mode. We used 3C286, 3C147 and 3C48 as primary calibrators, depending on the target. To process the data, we run the Source Peeling and Atmospheric Modeling (`SPAM`, Intema et al., 2009) on 6 sub-bands, of 33.3 MHz bandwidth each for the Band 3, and on 4 sub-bands, of 50.0 MHz bandwidth each for the Band 4. For each Band, the sub-bands are then imaged together using `WSClean`, at the common frequency of 400 and 650 MHz, for Band 3 and 4 respectively. The systematic uncertainties due to residual amplitude errors are set to 8% and 5%, for the observations in Band 3 and 4 respectively (Chandra et al., 2004).

6.3. Results

6.3.1. Images and integrated flux densities

For all clusters, we produced the final deep images using `WSClean`, with `weighting=` 'Briggs' and `robust=-0.5`. Only for the LOFAR images, we applied an inner uv-cut of 80λ (van Weeren et al., 2020). The final noise levels range between $\sim 50 - 150$ μJy beam^{-1}, $\sim 20 - 60$ μJy beam^{-1} and $\sim 7 - 12$ μJy beam^{-1} for the 144, 400 and 650 MHz full-resolution images, respectively (see Tab. 6.3). This means that the 650 MHz observations are about three times deeper than the LOFAR ones for the compact sources detection, i.e. assuming a typical spectral index $\alpha = -0.8$. For steep-spectra sources, i.e. $\alpha = -1.5$ the sensitivities of the two arrays are similar. The low resolution images, for both the LOFAR and uGMRT observations, were produced by applying a Gaussian taper at different resolutions to down weight the visibilities from longer baselines. We display all the images in

---

[1]`https://github.com/mhardcastle/ddf-pipeline`

Table 6.3: Imaging parameters and image properties of the cluster sample.

Cluster name	Central Frequency [MHz]	Resolution [″×″]	uv min [λ]	uv-taper [″]	$\sigma_{\rm rms}$ [μJy beam^{-1}]
PSZ2 G086.93+53.18	144	9.5 × 4.5	80	–	91.8
		26.0 × 26.0	80	15	239.4
	650	3.8 × 3.4	–	–	8.6
		26.0 × 26.0	–	15	45.5
PSZ2 G089.39+69.36	144	8.3 × 4.8	80	–	64.3
		29.0 × 29.0	80	15	138.2
	400	6.4 × 5.1	–	–	57.2
		29.0 × 29.0	–	15	47.0
PSZ2 G091.83+26.11	144	6.8 × 4.5	80	–	92.1
		14.0 × 14.0	160	6	188.4
	400	13.8 × 6.2	–	–	64.6
		14.0 × 14.0	160	–	94.6
	650	4.4 × 2.8	–	–	11.4
		14.0 × 14.0	160	6	38.9
PSZ2 G099.86+58.45	144	8.0 × 4.4	80	–	66.3
		18.0 × 18.0	180	10	153.2
	650	5.0 × 2.6	–	–	8.2
		18.0 × 18.0	180	10	33.7
PSZ2 G126.28+65.62	144	7.6 × 4.5	80	–	52.3
		25.0 × 25.0	80	15	117.6
	650	7.6 × 2.5	–	–	9.8
		25.0 × 25.0	–	15	39.9
PSZ2 G141.77+14.19	144	7.6 × 5.0	80	–	119.6
		17.0 × 17.0	150	10	171.0
	650	6.4 × 3.3	–	–	9.7
		17.0 × 17.0	150	10	21.3
PLCK G147.3–16.6	144	7.6 × 5.9	80	–	152.8
		17.0 × 17.0	150	10	315.6
	400	8.0 × 4.1	–	–	22.3
		17.0 × 17.0	150	10	58.1
	650	3.4 × 3.0	–	–	7.3
		17.0 × 17.0	150	10	25.5
PSZ2 G147.88+53.24	144	8.6 × 4.6	80	–	61.7
		14.0 × 14.0	100	6	123.4
	650	5.6 × 2.6	–	–	8.5
		14.0 × 14.0	100	6	19.5
PSZ2 G160.83+81.66	144	13.1 × 4.6	80	–	138.2
		22.0 × 22.0	80	10	221.3
	650	4.5 × 2.6	–	–	9.2
		22.0 × 22.0	–	10	22.7

Figures 6.1 to 6.9. Among the nine clusters presented in this work, five of them show extended diffuse radio emission in the uGMRT observations.

To obtain the flux densities of the radio halos, we produced source-subtracted images. We applied a *uv*-cut to the data, to filter out emission associated with sources of linear sizes larger than 500 kpc at the cluster redshift, and to create a clean component model of the compact sources. Given the smaller sizes of the halo, for the LOFAR image of PSZ2 G089.39+69.36 we employed an inner *uv*-cut of 400 kpc. During this step, we employed multiscale deconvolution using scales of $[0, 4, 8, 16] \times$ pixelscale (with the pixel size of $1.5''$, $2''$ and $1''$ for the 144, 400 and 650 MHz images, respectively) to include and subtract the diffuse emission from the radio galaxies. For the automatic deconvolution, we used a mask threshold of $1\sigma_{\mathrm{rms}}$ to subtract the faintest contaminating sources. Finally, we subtracted the compact source models from the visibilities, and tapered the *uv*-data with different Gaussian tapers (i.e. $6''$ and $10''$). For an extended radio galaxy with a linear size $\gtrsim 500$ kpc, we cannot properly subtract the radio emission from the *uv*-data (Di Gennaro et al., 2021a). This is the case for the candidate radio relic in PSZ2 G091.83+26.11 and for the radio galaxy northward of PLCK G147.3–16.6, which have been manually excluded from the radio halo region.

We measure the radio halo flux densities for each cluster from the same regions, in the LOFAR and uGMRT images, encompassing the full extent of the diffuse radio emission. Uncertainties on the halo flux densities are obtained by taking into account the systematic uncertainties due to residual amplitude errors (f), the map noise level and the uncertainty of the source subtraction in the *uv* plane (σ_{sub}, i.e. few percent of the residual flux from compact sources):

$$\Delta S_\nu = \sqrt{(f S_\nu)^2 + N_{\mathrm{beam}}\sigma_{\mathrm{rms}}^2 + \sigma_{\mathrm{sub}}^2} \, . \tag{6.1}$$

In those systems with no detection of diffuse emission in the uGMRT images, we derived upper limits as $\sigma_{\mathrm{rms}}\sqrt{N_{\mathrm{beam}}}$, with N_{beam} the number of beams covering the halo region and σ_{rms} the map noise level. The resulting flux densities, both measured and upper limits, are listed in Table 6.4.

6.3.2. Spectral index maps and integrated spectral indices

To produce the spectral index maps of those clusters with diffuse radio emission in both LOFAR and uGMRT observations, we made images with a common inner *uv*-cut to compensate for the different interferometer *uv*-coverage. To emphasise the presence of the radio halo, we also applied a Gaussian taper. The images were then convolved to the same resolution, and re-gridded to the same pixel grid (i.e. the LOFAR image). The effective final resolutions and the noise levels of each image are listed in Table

6.3. For the clusters with observations at three frequencies, we used the same procedure used in Di Gennaro et al. (2018), where a second-order polynomial fit was used in the case of significant curvature (i.e. above the 2σ threshold, where σ is the uncertainty associated with the second-order term). In this case, the spectral index was calculated at 400 MHz, i.e. the median of the total band. We blanked all the pixels below the $2\sigma_{\mathrm{rms}}$ threshold for each frequency, with σ_{rms} the noise level reported in Table 6.3. The spectral index uncertainty maps are obtained via 150 Monte Carlo simulations of the first-/second-order polynomial fit. We assumed that the uncertainty of each flux given by the sum in quadrature of the noise map and the systematic flux uncertainties, i.e. $\sqrt{(fS_\nu)^2 + \sigma_{\mathrm{rms}}^2}$. For the clusters with observations at only two frequencies, we calculate the spectral index analytically, with an uncertainty of:

$$\Delta\alpha = \frac{1}{\ln\frac{\nu_1}{\nu_2}}\sqrt{\left(\frac{\Delta S_1}{S_1}\right)^2 + \left(\frac{\Delta S_2}{S_2}\right)^2}. \tag{6.2}$$

For the clusters hosting no diffuse radio emission in the uGMRT observations, we derived upper limits on the integrated spectral indices, according to

$$\alpha = \log\left(\frac{S_{144} - \Delta S_{144}}{S_{\mathrm{uGMRT}}}\right)/\log\left(\frac{144~\mathrm{MHz}}{\nu_{\mathrm{uGMRT}}}\right), \tag{6.3}$$

where the subscript 'uGMRT' refers to the Band 4 or 3.

6.3.3.   Individual clusters

In this subsection we provide a brief description of each cluster, at the three observing frequencies.

PSZ2 G086.93+53.18

This is the faintest radio halo detected in the LOFAR observations ($S_{144} = 5.6 \pm 1.1$ mJy), with a largest linear size $\mathrm{LLS}_{144} = 0.4 - 0.5$ Mpc. No diffuse radio emission is visible at 650 MHz, despite the better depth of the observation (see Fig. 6.1). From the same halo region, we derive an upper limit for the flux of $S_{650} < 0.5$ mJy, corresponding to an upper limit on the spectral index of $\alpha < -1.5$.

PSZ2 G089.39+69.36

A Mpc-scale radio halo is found in the LOFAR observations ($S_{144} = 10.0\pm 1.6$ mJy, $\mathrm{LLS}_{144} = 1$ Mpc). No diffuse radio emission is observed in the 400 MHz image (Fig. 6.2). We derive an upper limit for the flux of $S_{400} < 1.2$ mJy, corresponding to an upper limit on the spectral index of $\alpha < -1.9$.
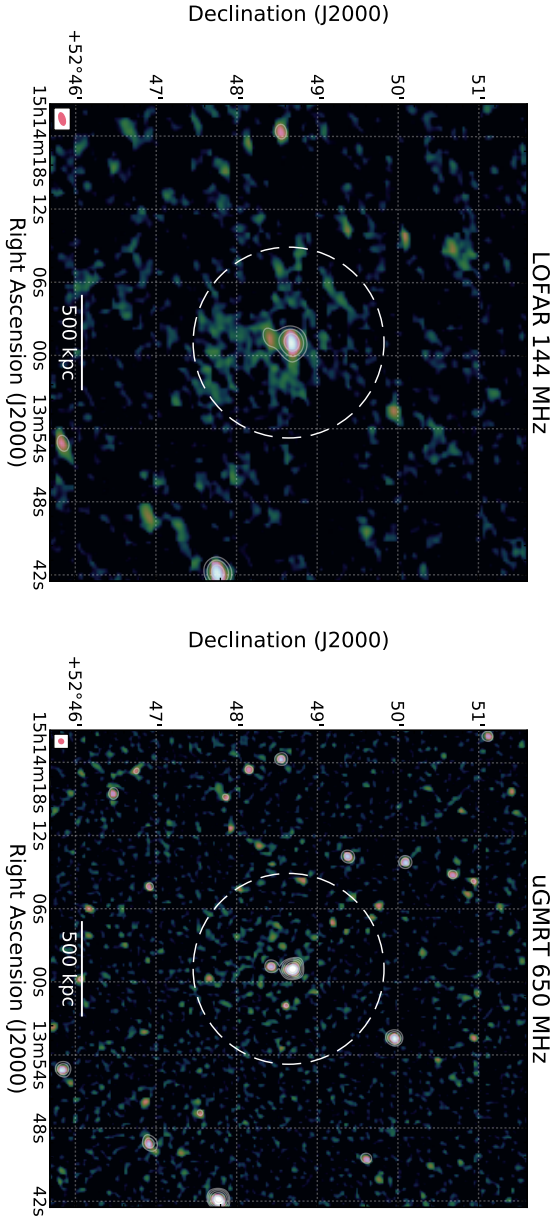
Figure 6.1: PSZ2 G086.93+53.18. Full-resolution images (weighting='Briggs' and robust=−0.5) at 144 MHz (left) and 650 MHz (right). White-coloured radio contours are drawn at levels of 2.5$\sigma_{\rm rms} \times [-1, 1, 2, 4, 8, 16, 32]$, with $\sigma_{\rm rms}$ the noise level at each frequency (see Table 6.3. The negative contour level is drawn with a dashed white line. The dashed white circle in each map shows the $R = 0.5R_{\rm SZ,500}$ region, obtained from $M_{\rm SZ,500}$.
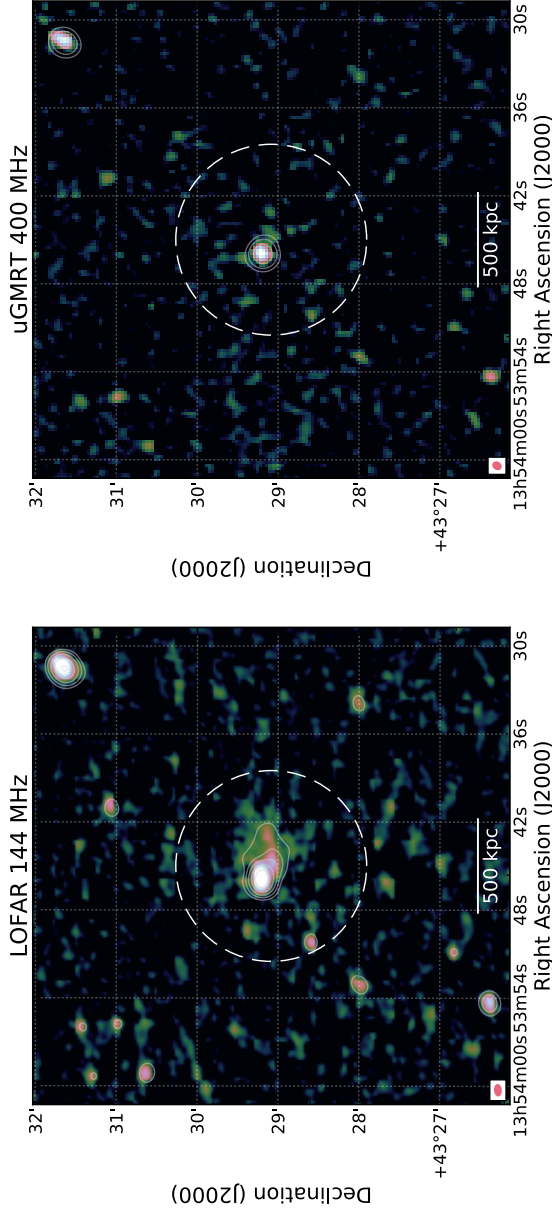
Figure 6.2: PSZ2 G089.39+69.36. Full-resolution images (weighting='Briggs' and robust=−0.5) at 144 MHz (left) and 400 MHz (right). White-coloured radio contours are drawn at levels of $2.5\sigma_{rms} \times [−1, 1, 2, 4, 8, 16, 32]$, with σ_{rms} the noise level at each frequency (see Table 6.3). The negative contour level is drawn with a dashed white line. The dashed white circle in each map shows the $R = 0.5R_{SZ,500}$ region, obtained from $M_{SZ,500}$.

PSZ2 G091.83+26.11

The radio halo in this cluster is the brightest in our sample, at all three frequencies (see Fig. 6.3). The largest linear size of the radio halos is the same in both the LOFAR and uGMRT observations, i.e. about 1.2 Mpc. The 650 MHz observation is the deepest of the three frequencies, where we also see some substructures in the halo. We measure a flux density of S_{144} = 65.4 ± 9.9 mJy, S_{400} = 23.9 ± 2.0 mJy and S_{650} = 14.5 ± 0.8 mJy for the LOFAR, uGMRT Band 3 and uGMRT Band 4 observations. These correspond to integrated spectral indices of α_{650}^{144} = −1.00 ± 0.11, α_{400}^{144} = −0.99 ± 0.17 and α_{650}^{400} = −1.03 ± 0.21. These values are consistent with a single power-law spectral shape. The spectral index map shows a somewhat steeper spectral index in the central part of the cluster, with α_{400} between ∼ −1.2 and ∼ −1.4. Northward, the spectral index flattens, with α_{650}^{144} ∼ −0.75, in correspondence of sources C and D.

In the east and southeast direction, the elongated source that was classified as a candidate radio relic in Di Gennaro et al. (2021a) maintains its morphology. This source can be divided into two pieces. One (R1), located east the cluster centre, is a faint patchy filament that is 80″ long and 8″ wide, corresponding to 640×60 kpc^2 at the cluster redshift. The other (R2), located southeastward, is brighter and extends for about 40″ (i.e. 300 kpc at the cluster redshift). Interestingly, its morphology resembles a double-lobe radio galaxy at 650 MHz. However, no optical counterpart is visible from the available PanSTARRS (Panoramic Survey Telescope and Rapid Response System; Chambers et al., 2016) optical image (see Appendix .1). However, we note that the optical image is rather shallow, and might miss faint galaxies. Possibly, R2 combines the emission of a radio relic and a double-lobe radio galaxy. Observations with the Karl-Jansky Very Large Telescope (VLA) in the 1–4 GHz band will help in the classification of this elongated piece of emission. In particular, the polarisation characteristics will be crucial and will be presented in forthcoming work (Di Gennaro et al., in prep). We measure the flux density for the candidate radio relic from the low-resolution images (i.e. $14'' \times 14''$), considering the full length of the source (i.e. R1+R2). Since at this resolution the compact sources B, C and D are embedded in the candidate relic, we measured their flux densities from the full-resolution image and we subtracted them arithmetically from the total flux density. We obtain S_{144} = 274.8 ± 45.6 mJy, S_{400} = 76.6 ± 6.5 mJy and S_{650} = 36.3 ± 2.1 mJy, corresponding to α_{650}^{144} = −1.34 ± 0.12 (α_{400}^{144} = −1.25 ± 0.18 and α_{650}^{400} = −1.54 ± 0.21). The spectral index map shows hints of steepening for R2 (up to α_{400} ∼ −2), which is typical of radio relics (e.g. Di Gennaro et al., 2018; Rajpurohit et al., 2018b). This is not observed for R1. Next to the candidate relic, source B is characterised by a very steep spectrum (α_{400} ∼ −2).
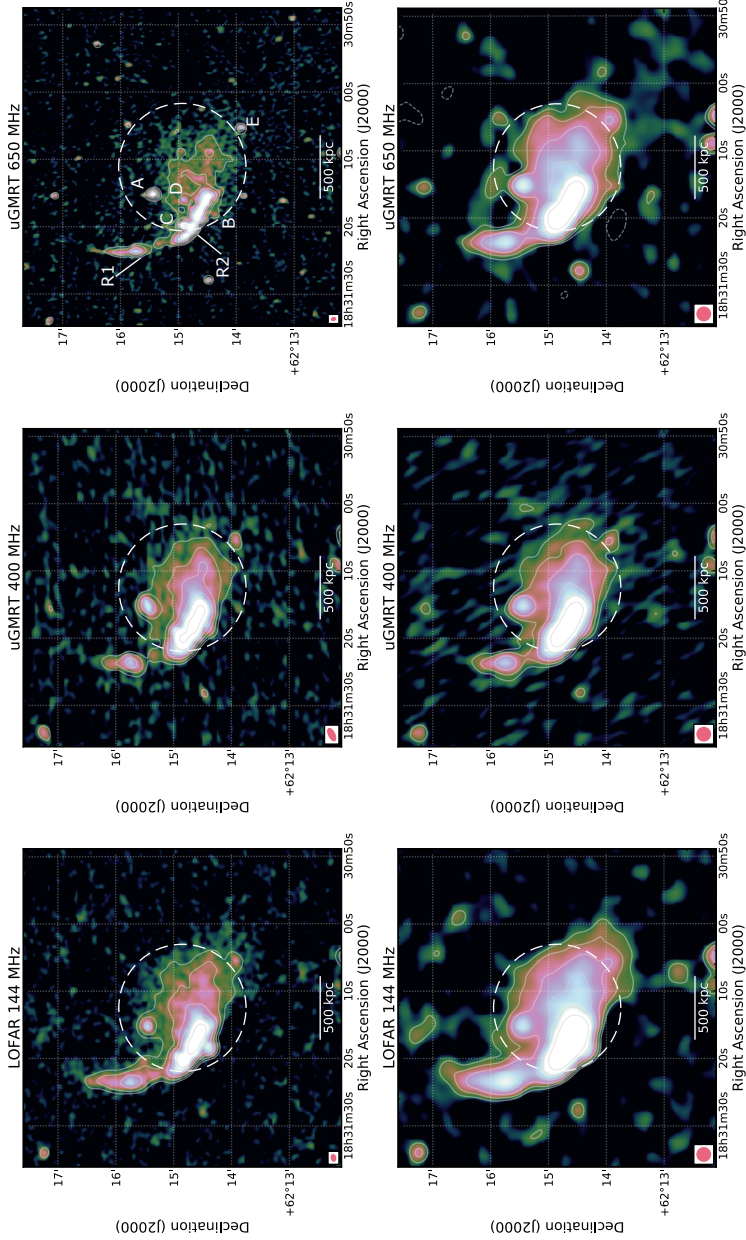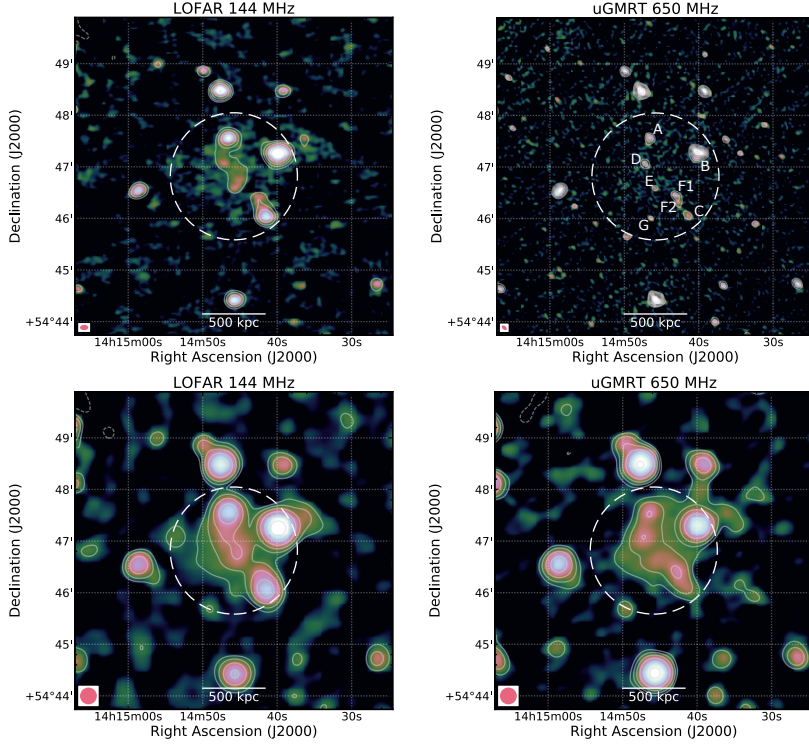
Figure 6.3: PSZ2 G091.83+26.11. Top and bottom rows: Full-resolution and 14″ images (weighting='Briggs' and robust=-0.5) at 144 MHz (left), 400 MHz (middle) and 650 MHz (right). White-coloured radio contours are drawn at levels of $2.5\sigma_{rms} \times [-1, 1, 2, 4, 8, 16, 32]$, with σ_{rms} the noise level at each frequency (see Table 6.3. The negative contour level is drawn with a dashed white line. The dashed white circle in each map shows the $R = 0.5R_{SZ,500}$ region, obtained from $M_{SZ,500}$.
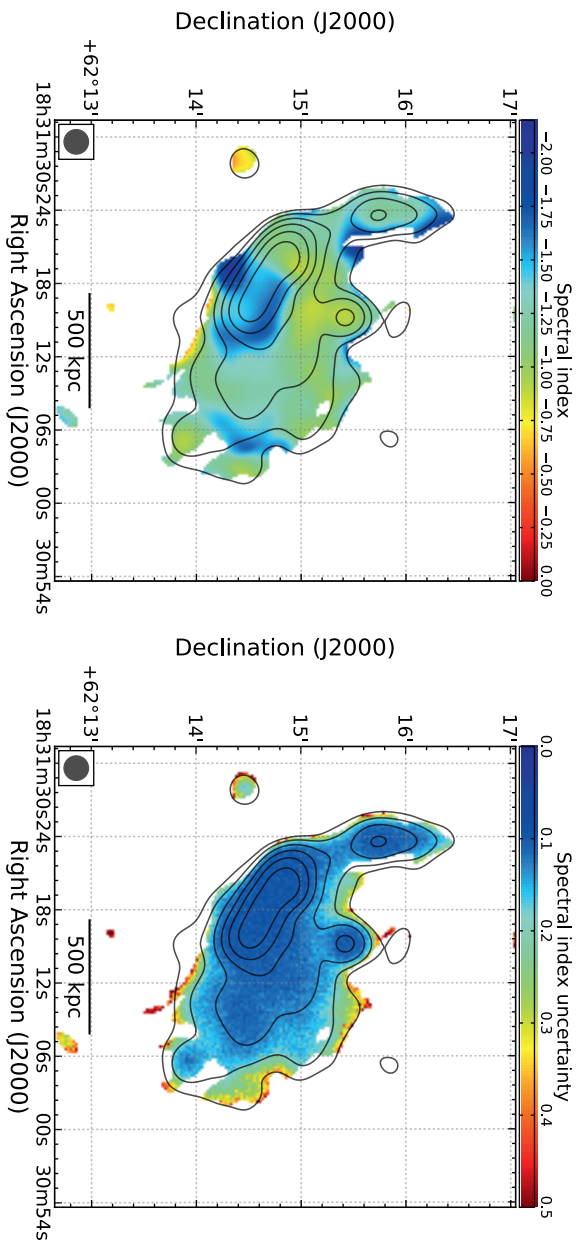
Figure 6.3: Continued. Spectral index map between 144, 400 and 650 MHz at 14″ resolution, and correspondent uncertainty map (left and right panels, respectively). uGMRT radio contours at 650 MHz are drawn in black, at the levels $3\sigma_{rms} \times [-1, 1, 2, 4, 8, 16, 32]$, with σ_{rms} the noise level (see Table 6.3).

Figure 6.4: PSZ2 G099.86+58.45. Top and bottom rows: Full-resolution and 18″ images (`weighting='`Briggs' and `robust=-0.5`) at 144 MHz (left) and 650 MHz (right). White-coloured radio contours are drawn at levels of $2.5\sigma_{\rm rms}\times[-1, 1, 2, 4, 8, 16, 32]$, with $\sigma_{\rm rms}$ the noise level at each frequency (see Table 6.3). The negative contour level is drawn with a dashed white line. We followed Cassano et al. (2019) for the source labelling (their source 1, 2 and 3 became D, E and F1+F2, respectively). The dashed white circle in each map shows the $R = 0.5R_{\rm SZ,500}$ region, obtained from $M_{\rm SZ,500}$.

PSZ2 G099.86+58.45

We detect diffuse radio emission in the 650 MHz observations, similar to what is visible at 144 MHz (Fig. 6.4, $\rm LLS_{144} = 1.2$ and $\rm LLS_{650} = 0.95$ Mpc). We measure a flux density of $S_{144} = 18.1\pm2.9$ mJy and $S_{650} = 4.0\pm0.4$ mJy for the LOFAR and uGMRT Band 4 observations. This corresponds to an integrated spectral index of $\alpha_{650}^{144} = -1.00 \pm 0.13$. The spectral index map in Fig. 6.4 shows steeper values at the cluster centre (i.e. $\alpha_{650}^{144} \sim -1.6$) and flatter at the cluster outskirts (i.e. $\alpha_{650}^{144} \sim -0.9$) For this cluster, also L-band VLA observations are available (Cassano et al., 2019). In these observations, hints of a halo are present only at the $2\sigma_{\rm rms}$ level (with
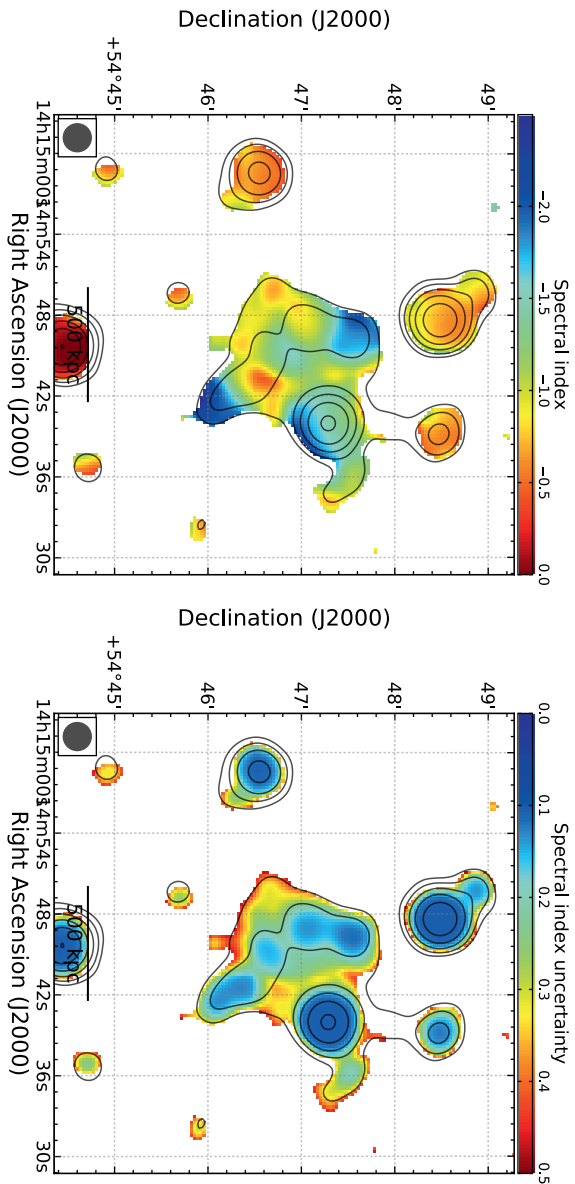
Figure 6.4: Continued. Spectral index map between 144 and 650 MHz at 18″ resolution, and correspondent uncertainty map (left and right panels, respectively). uGMRT radio contours at 650 MHz are drawn in black, at the levels $3\sigma_{\rm rms} \times$ [−1, 1, 2, 4, 8, 16, 32], with $\sigma_{\rm rms}$ the noise level (see Table 6.3).

$\sigma_{\mathrm{rms,VLA}}$ = 20 μJy beam^{-1}). We repeated the flux measurement, covering the same region of the LOFAR halo, finding a flux of S_{1500} ~ 1.0 ± 0.4 mJy, in agreement with the flux density reported in Cassano et al. (2019). This VLA flux density suggests a mild steepening towards GHz frequencies, with α_{1500}^{650} ~ −1.7 ± 0.5.

As for PSZ2 G091.83+26.11, also in this cluster we detect ultra-steep spectra from source A (α_{600}^{144} ~ −1.7) and source C (α_{650}^{144} ~ −2.5), as was also mentioned by Cassano et al. (2019).

PSZ2 G126.28+65.62

No diffuse radio emission is found in the uGMRT 650 MHz observations (see right panel Fig. 6.5, LLS_{144} = 0.8 Mpc). We measure S_{144} = 6.8 ± 1.1 mJy and derive an upper limit of S_{650} < 0.5 mJy for the radio halos, corresponding to an upper limit on the spectral index of α < −1.6.

PSZ2 G141.77+14.19

Hints of the presence of diffuse emission are present in the uGMRT 650 MHz data, around sources D, E, F and G (see right panel Fig. 6.6, LLS_{144} = 0.6 and LLS_{650} = 0.55 Mpc). We measure a flux density of S_{144} = 6.5 ± 1.2 mJy and S_{650} = 1.2 ± 0.1 mJy from the same halo region. This corresponds to a spectral index of α_{650}^{144} = −1.12 ± 0.13, and it agrees with the values found in the spectral index map.

PLCK G147.3–16.6

Observations at 610 MHz with the GMRT were published by van Weeren et al. (2014), where a radio halo was discovered. With the new wide-band GMRT observations we confirm the presence of a Mpc-size radio halo at both 400 and 650 MHz (Fig. 6.7). Interestingly, in the two uGMRT observations, the diffuse emission appears to be larger than the LOFAR image (LLS_{144} = 0.8, LLS_{400} = 1 and LLS_{650} = 1 Mpc). However, we note that this observation is less deep, probably due to a bad ionosphere. The flux densities encompassed in the area covered by the halo in the LOFAR images are S_{144} = 21.0 ± 3.7 mJy, S_{400} = 5.4 ± 0.6 mJy and S_{650} = 2.8 ± 0.3 mJy for the 144 MHz, 400 MHz and 650 MHz observations. Increasing the region to cover the full extension of the halo in in the uGMRT images, we obtain S_{144} = 26.6 ± 4.4 mJy, S_{400} = 10.0 ± 0.9 mJy and S_{650} = 5.6 ± 0.4 mJy. We note that the 650 MHz flux we report is slightly below the one found by van Weeren et al. (2014). This is probably due to a better subtraction of the contribution of the compact sources with the deeper wide-band observations. Given the integrated flux densities, we obtain spectral indices of α_{650}^{144} = −1.34±0.15, α_{400}^{144} = −1.33±0.20 and α_{650}^{400} = −1.35±0.37, in the small area, and α_{650}^{144} = −1.03 ± 0.12, α_{400}^{144} = −0.96 ± 0.19 and α_{650}^{400} = −1.19 ± 0.23,
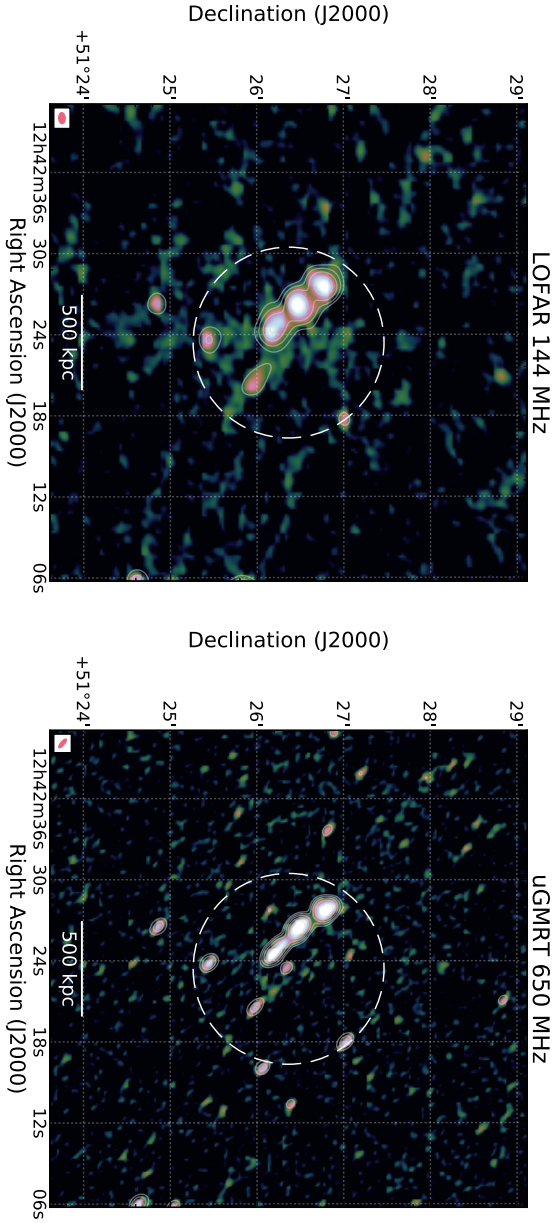
Figure 6.5: PSZ2 G126.28+65.62. Full-resolution images (weighting='Briggs' and robust=-0.5) at 144 MHz (left) and 650 MHz (right). White-coloured radio contours are drawn at levels of $2.5\sigma_{rms} \times [-1, 1, 2, 4, 8, 16, 32]$, with σ_{rms} the noise level at each frequency (see Table 6.3. The negative contour level is drawn with a dashed white line. The dashed white circle in each map shows the $R = 0.5R_{SZ,500}$ region, obtained from $M_{SZ,500}$.
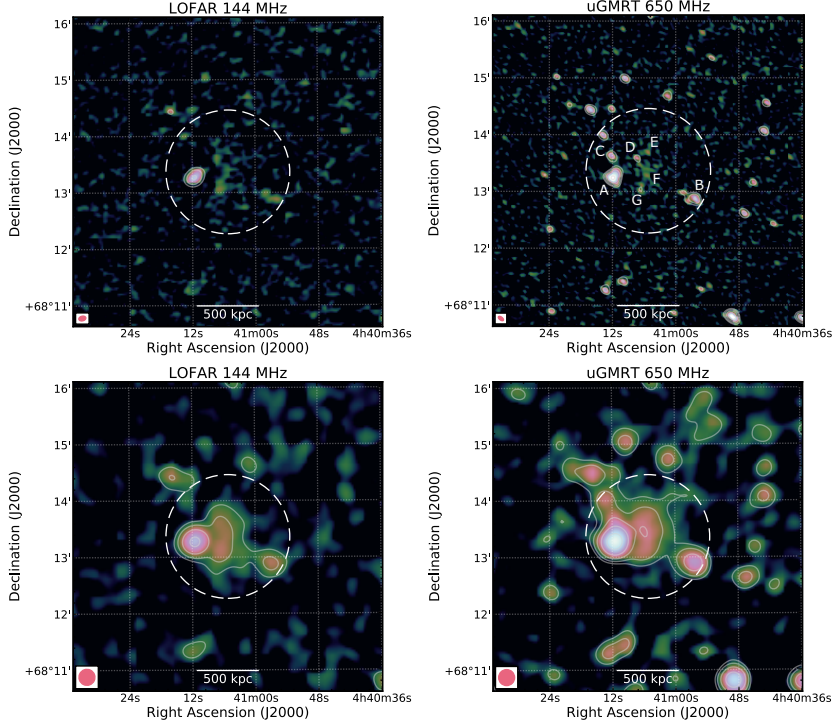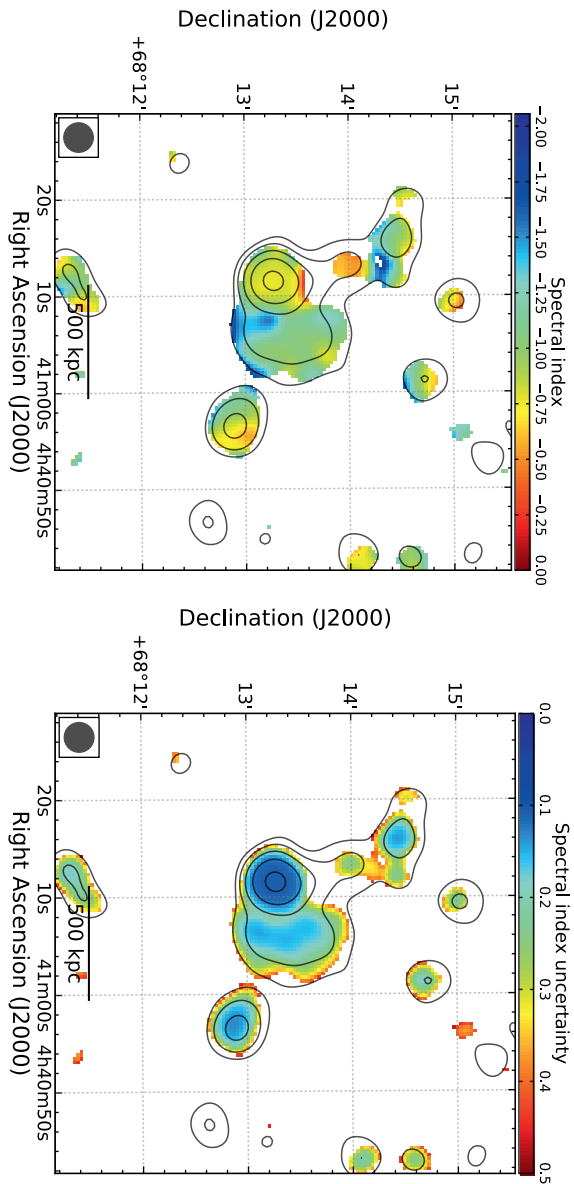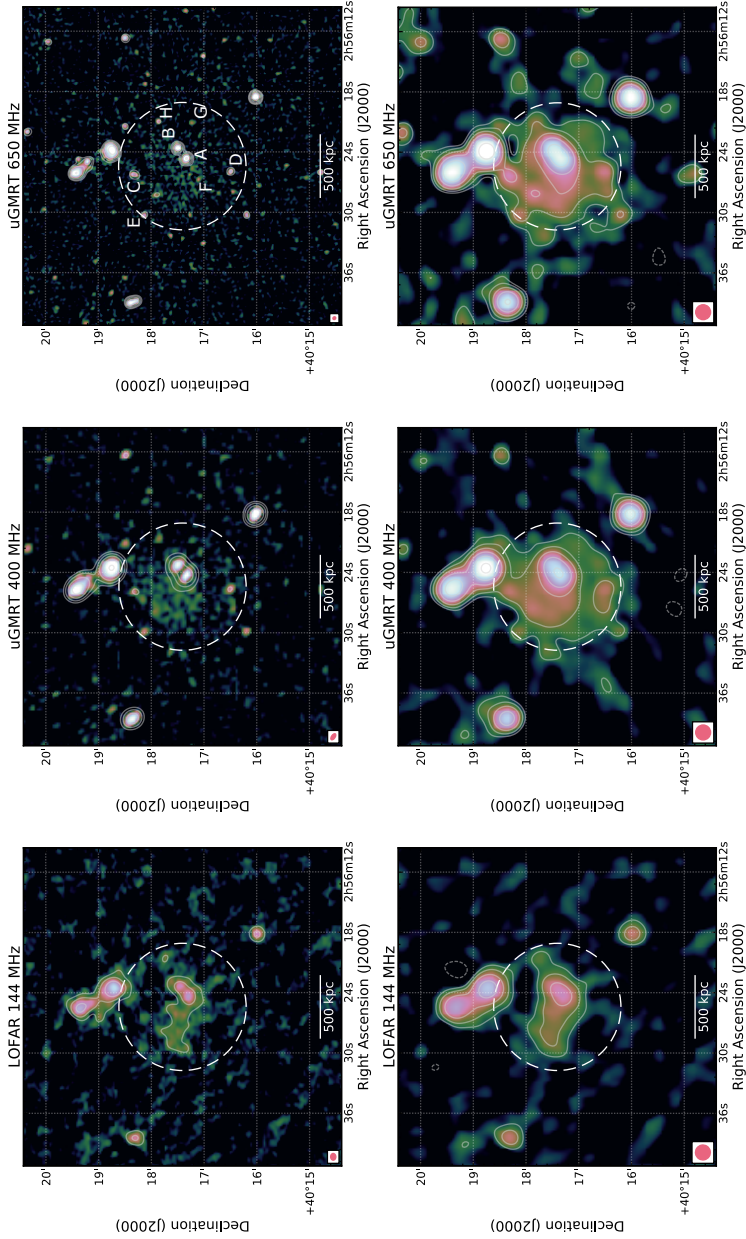
Figure 6.6: PSZ2 G141.77+14.19 . Top and bottom rows: Full-resolution and 17″ images (`weighting='Briggs'` and `robust=-0.5`) at 144 MHz (left) and 650 MHz (right). White-coloured radio contours are drawn at levels of $2.5\sigma_{\rm rms} \times [-1, 1, 2, 4, 8, 16, 32]$, with $\sigma_{\rm rms}$ the noise level at each frequency (see Table 6.3). The negative contour level is drawn with a dashed white line. The dashed white circle in each map shows the $R = 0.5 R_{\rm SZ,500}$ region, obtained from $M_{\rm SZ,500}$.

in the big area. These values are consistent with a single power-law distribution. The spectral index map in Fig. 6.7 shows steeper spectral index in the halo centre, with $\alpha_{400} \sim -1.4$, in agreement with the integrated spectral indices in the small halo region.

PSZ2 G147.88+53.24

A Mpc-size diffuse radio emission at 144 MHz was reported in Di Gennaro et al. (2021a) (LLS$_{144}$ = 0.6 Mpc). This is also confirmed by deep observations at the same frequency (Osinga et al., 2021). Hints of diffuse radio emission are visible in the 650 MHz image (see Fig. 6.8, LLS$_{650}$ = 0.5 Mpc). Excluding sources D, E, F and G from the halo region, we measure S_{144} = 8.2 ± 1.3 mJy and S_{650} = 1.1 ± 0.2 mJy, for the LOFAR and uGMRT

Figure 6.6: Continued. Spectral index map between 144 and 650 MHz at 17″ resolution, and correspondent uncertainty map (left and right panels, respectively). uGMRT radio contours at 650 MHz are drawn in black, at the levels $3\sigma_{rms} \times [-1, 1, 2, 4, 8, 16, 32]$, with σ_{rms} the noise level (see Table 6.3).
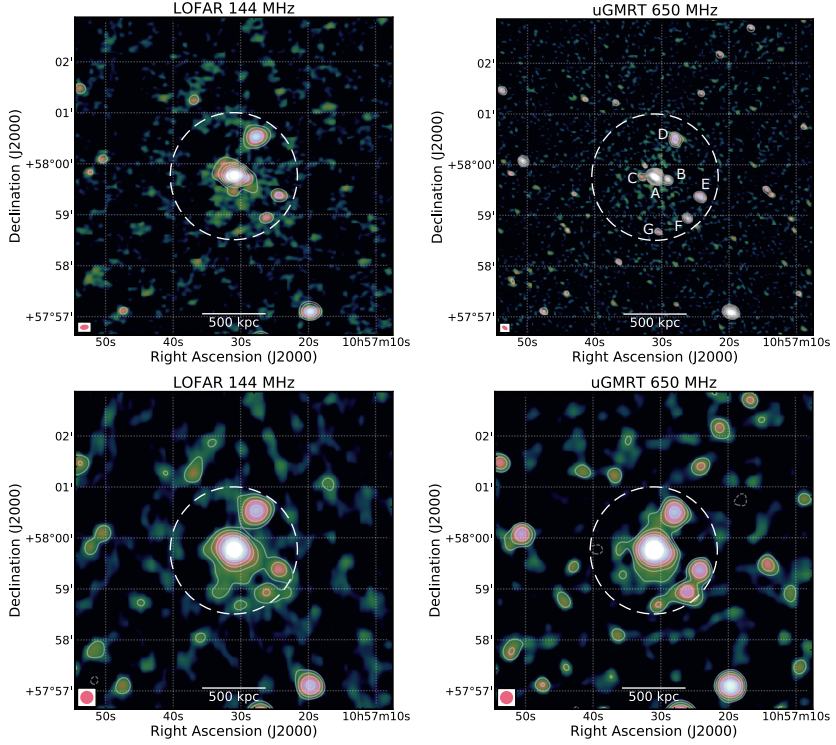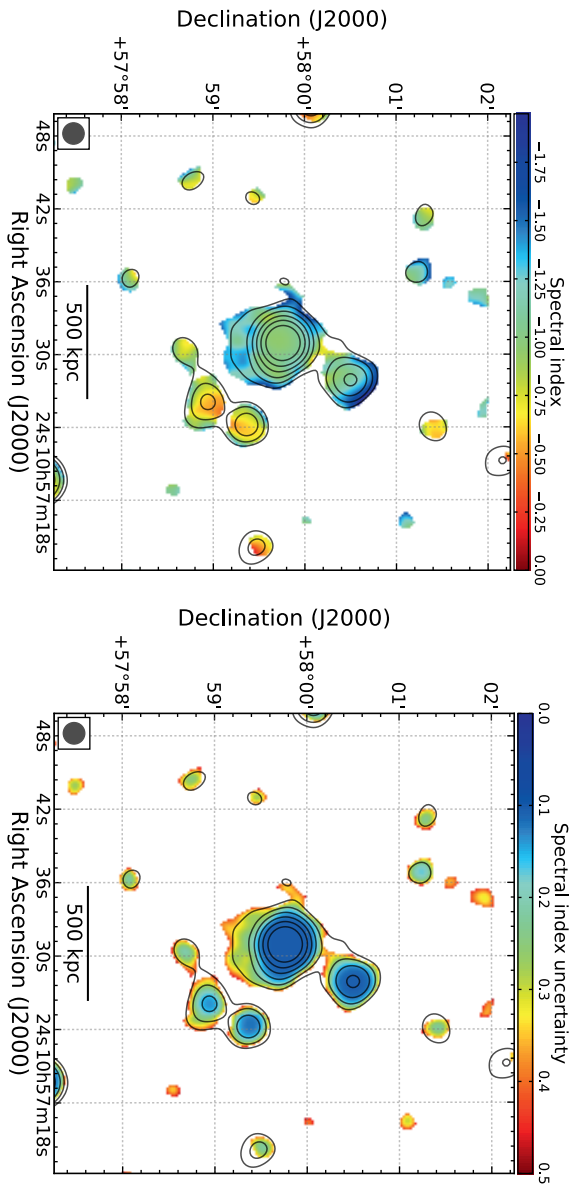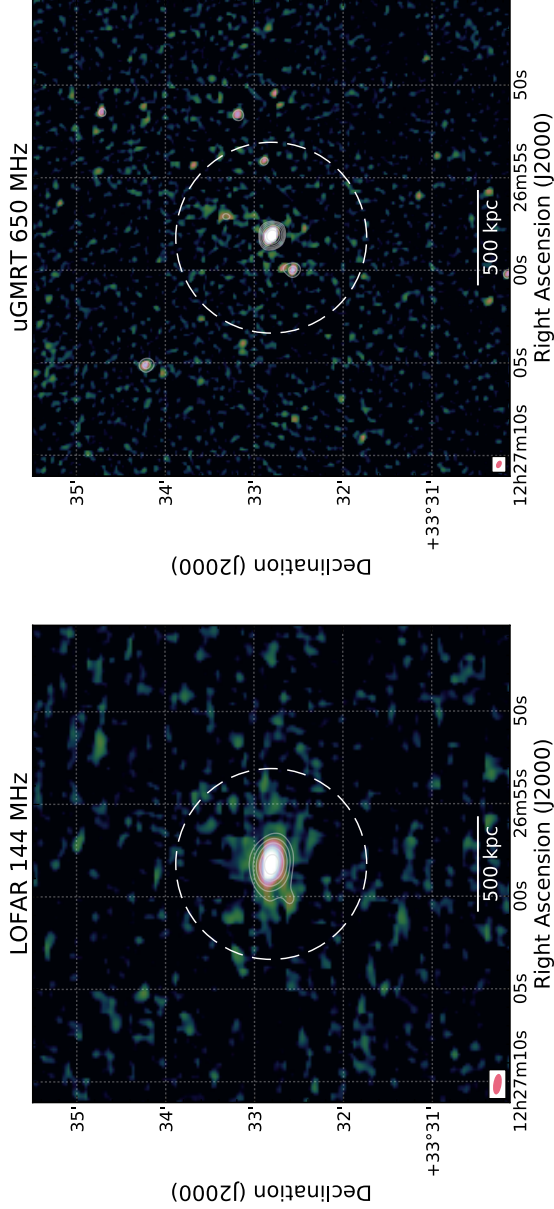
Figure 6.7: PLCK G147.3−16.6. Top and bottom rows: Full-resolution and 17″ images (weighting='Briggs' and robust=−0.5) at 144 MHz (left), 400 MHz (middle) and 650 MHz (right). White-coloured radio contours are drawn at levels of $2.5\sigma_{rms} \times [-1, 1, 2, 4, 8, 16, 32]$, with σ_{rms} the noise level at each frequency (see Table 6.3). The negative contour level is drawn with a dashed white line. We followed van Weeren et al. (2014) for the source labelling. The dashed white circle in each map shows the $R = 0.5R_{SZ,500}$ region, obtained from $M_{SZ,500}$.
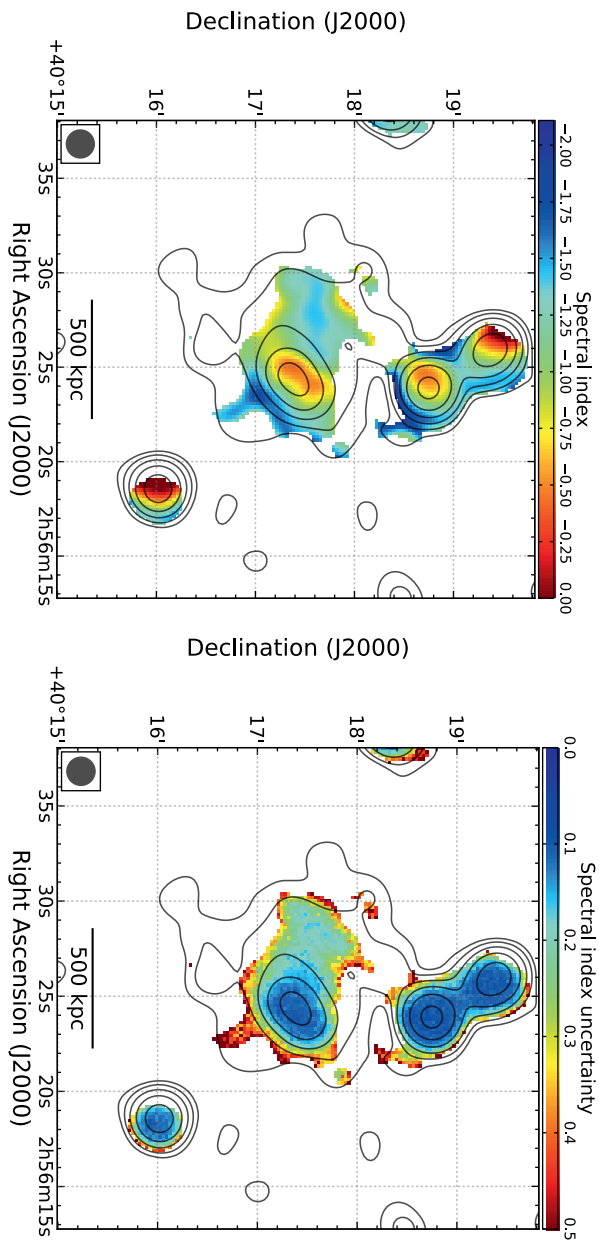
Figure 6.7: Continued. Spectral index map between 144, 400 and 650 MHz at 17″ resolution, and correspondent uncertainty map (left and right panels, respectively). uGMRT radio contours at 650 MHz are drawn in black, at the levels $3\sigma_{\rm rms} \times [-1, 1, 2, 4, 8, 16, 32]$, with $\sigma_{\rm rms}$ the noise level (see Table 6.3).

Figure 6.8: PSZ2 G147.88+53.24. Top and bottom rows: Full-resolution and 14″ images (`weighting='Briggs'` and `robust=-0.5`) at 144 MHz (right) and 650 MHz (left). White-coloured radio contours are drawn at levels of $2.5\sigma_{\mathrm{rms}} \times [-1, 1, 2, 4, 8, 16, 32]$, with σ_{rms} the noise level at each frequency (see Table 6.3). The negative contour level is drawn with a dashed white line. The dashed white circle in each map shows the $R = 0.5R_{\mathrm{SZ,500}}$ region, obtained from $M_{\mathrm{SZ,500}}$.

Figure 6.8: Continued. Spectral index map between 144 and 650 MHz at 14″ resolution, and correspondent uncertainty map (left and right panels, respectively). uGMRT radio contours at 650 MHz are drawn in black, at the levels $3\sigma_{\rm rms} \times [-1, 1, 2, 4, 8, 16, 32]$, with $\sigma_{\rm rms}$ the noise level (see Table 6.3).

Figure 6.9: PSZ2 G160.83+81.66. Full-resolution images (weighting='Briggs' and robust=−0.5) at 144 MHz (left) and 650 MHz (right). White-coloured radio contours are drawn at levels of $2.5\sigma_{rms} \times [-1, 1, 2, 4, 8, 16, 32]$, with σ_{rms} the noise level at each frequency (see Table 6.3. The negative contour level is drawn with a dashed white line. The dashed white circle in each map shows the $R = 0.5R_{SZ,500}$ region, obtained from $M_{SZ,500}$.

Band 4 observation respectively. This corresponds to a spectral index of $\alpha_{650}^{144} = -1.33 \pm 0.17$. The spectral index map for PSZ2 G147.88+53.24 is mostly dominated by the central compact source (i.e. source A, see Fig. 6.8), which is characterised by a spectral index $\alpha_{650}^{144} \sim -1$. Just south of it, we detect steeper spectral index values ($\alpha_{650}^{144} \sim -1.2$) that can be associated with the radio halo.

PSZ2 G160.83+81.66

This cluster represents the most distant radio halo found so far, at a redshift of 0.888 ($S_{144} = 8.5 \pm 1.5$ mJy, $LLS_{144} = 0.7$ Mpc). No diffuse radio emission is visible at 650 MHz, where we determine an upper limit of 0.4 mJy, corresponding to an upper limit on the spectral index of $\alpha < -1.9$.

6.4. Discussion

Investigating the spectral index properties of distant radio halos is crucial to understand the mechanism of particle acceleration in these radio sources. So far, spectral studies in radio halos have been carried out starting from high-frequency observations (i.e. ~ GHz), which were then followed up at lower frequencies. However, this approach tends to miss a large fraction of steep-spectra sources, simply because they are not detected in the GHz observations. This issue is particularly important for high-redshift clusters, as a large fraction of these halos, especially the low-mass systems, should have a steep spectral index ($\alpha < -1.5$, see Cassano & Brunetti, 2005; Cassano et al., 2006). This is due to the larger contribution of Inverse Compton energy losses (i.e. $dE/dt_{IC} \propto (1+z)^4$) that is expected to hamper the acceleration of high-energy electrons. As a consequence, the ensuing synchrotron luminosity should be reduced. The increasing area of the LOFAR Two-Meter Sky Survey (LoTSS) will help avoid this bias towards flat-spectra halos. This survey at low frequencies is expected to observe a large number of previously undiscovered radio halos (e.g. Cassano et al., 2010a; van Weeren et al., 2020), which can be followed up at higher frequencies.

In Di Gennaro et al. (2021a) we presented the first statistical study of diffuse radio emission with LOFAR (120–168 MHz) of a sample of 19 distant ($z \geq 0.6$) galaxy clusters selected from the Planck SZ catalog (Planck Collaboration et al., 2016). In this work, we present a follow-up study at higher frequencies of the nine radio halos detected in the LOFAR observations. Our observations were carried out with the uGMRT, mainly at 550–900 MHz (Band 4), but for two clusters (i.e. PSZ2 G091.83+26.11 and PLCK G147.3–16.6) we also have observations at 250-550 MHz (Band 3). At these higher frequencies, we find the presence of diffuse radio emission in five of the nine clusters discovered in LOFAR. These are PSZ2 G091.83+26.11,

Table 6.4: Flux densities and largest linear sizes (LLS) of the radio halos in our sample.

Cluster name	S_{144} [mJy]	LLS_{144} [Mpc]	S_{400} [mJy]	LLS_{400} [Mpc]	S_{650} [mJy]	LLS_{650} [Mpc]	α_{650}^{144}
PSZ2 G086.93+53.18	5.6 ± 1.1	0.4–0.5	–	–	< 0.5	N/A	< −1.5
PSZ2 G089.39+69.36	10.0 ± 1.6	1.0	< 1.2	N/A	–	–	< −1.9
PSZ2 G091.83+26.11	65.4 ± 9.9	1.2	23.9 ± 2.0	1.2	14.5 ± 0.8	1.2	−1.00 ± 0.11
PSZ2 G099.86+58.45	18.1 ± 2.9	1.2	–	–	4.0 ± 0.4	1.0	−1.00 ± 0.13
PSZ2 G126.28+65.62	6.8 ± 1.1	0.8	–	–	< 0.5	N/A	< −1.6
PSZ2 G141.77+14.19	6.5 ± 1.2	0.6	–	–	1.2 ± 0.1	0.55	−1.12 ± 0.13
PLCK G147.3−16.6	21.0 ± 3.7	0.8	5.4 ± 0.6	1.0	2.8 ± 0.3	1.0	−1.34 ± 0.20
PSZ2 G147.88+53.24	8.2 ± 1.3	0.6	–	–	1.1 ± 0.2	0.5	−1.33 ± 0.17
PSZ2 G160.83+81.66	8.5 ± 1.5	0.7	–	–	< 0.4	N/A	< −1.9

The LOFAR flux densities agree within 1σ with the values reported in Di Gennaro et al. (2021a). The flux densities reported for PLCK G147.3–16.6 refer to the small halo region. For PSZ2 G089.39+69.36 the upper limit on the spectral index is calculated between 144 and 400 MHz.
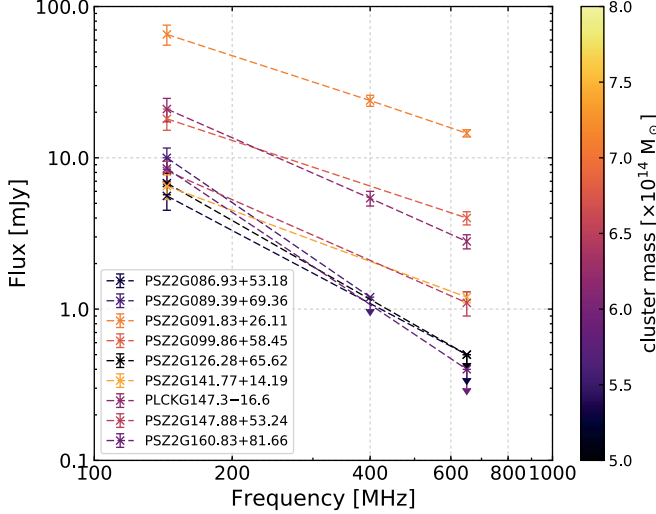
Figure 6.10: Radio spectra of the clusters in our sample (Table 6.4). The arrows show the upper limits on the fluxes.

PSZ2 G099.86+58+45, PSZ2 G141.77+14.19, PLCK G147.3–16.6 and PSZ2 G147.88+53.24. While we note that these clusters are also the most massive objects in our sample, with $M_{500,SZ} \sim 6 - 8 \times 10^{14}$ M$_\odot$, the low-mass clusters in our sample (i.e. $M_{500,SZ} = 5-6 \times 10^{14}$ M$_\odot$; PSZ2 G086.93+53.18, PSZ2 G089.39+69.36, PSZ2 G126.28+65.62 and PSZ2 G160.83+81.66), do not show diffuse radio emission at the uGMRT frequencies (Fig. 6.10).

For the uGMRT-detected radio halos, we measure integrated spectral indices between –1 and –1.3. These values are similar to what has been found for classical halos in local clusters (e.g Giovannini et al., 2009; Feretti et al., 2012; van Weeren et al., 2019). For the non-detections, given the upper limits on the flux densities obtained in the region covering the radio halo detected in LOFAR (see Tab. 6.4), we were able to determine an upper limits on the spectral index, being $\alpha < -1.5$. We also note that for those targets with three observing frequencies (PSZ2 G091.83+26.11 and PLCK G147.3–16.6), no spectral curvature is present. This means that the break frequency ν_s has to be at higher frequencies (i.e. $\nu_s > 650$ MHz). Hints of spectral steepening are indeed suggested with archival 1.4 GHz VLA observations of PSZ2 G099.86+58.45 (Cassano et al., 2019).

6.4.1. Comparison with theoretical models

Although our sample is not designed to test the occurrence of radio halos in high-redshift systems (because of its small size and low complete-

ness), we can compare our results with model expectations. According to re-acceleration models, the possibility to detect diffuse radio emission depends on the break frequency ν_s of the synchrotron spectra. Therefore, halos can be observed only at $\nu \leq \nu_s$ with ν the observing frequency. Following the procedure in Cassano et al. (2019), we estimated the probability to form a radio halo as a function of the cluster mass, at a median redshift of $z = 0.7$, with a break frequency of $\nu_s \geq 140$ MHz and $\nu_s \geq 600$ MHz (see Fig. 6.11). The formation probability includes the cluster merger history (merger trees) the generation of turbulence, particle acceleration (including energy losses) and the resulting cluster synchrotron spectrum. In these models the turbulent energy, acceleration rate and magnetic field are considered constant in the halo volume (i.e. homogeneous models, Cassano et al., 2010a). Here we consider magnetic field strengths of 2 and 5 μGauss (solid and dashed lines in Fig. 6.11), which match the range of results in Di Gennaro et al. (2021a). The highest value on the magnetic field strength is set based on the value which maximises the lifetime of relativistic electrons at the system redshift, i.e. $B = B_{CMB}/\sqrt{3}$ (where $B_{CMB} = 3.25(1 + z)^2$ μGauss is the magnetic field strength equivalent to that of the Cosmic Microwave Background). We assumed that the radio emission encompasses a region $R_H = 400$ kpc, i.e. the median size of the halos in our sample (see Tab. 6.4). The uncertainty of the estimated fraction of halos is obtained via 1000 Monte Carlo extractions of galaxy cluster samples from the pool of simulated merger trees (Cassano et al., 2010a, see red and yellow shaded areas in Fig. 6.11). We find that, in the mass interval of our sample $M_{500} = 5.0 - 8.0 \times 10^{14}$ M$_\odot$, and assuming $B = 5$ μGauss, the probability to observe a radio halo with steepening frequency $\nu_s \geq 140$ MHz is between the 60% and 30% (Fig. 6.11 red line), while it decreases down to 13–30% for $\nu_s \geq 600$ MHz (Fig. 6.11 yellow line), with a clear dependence on cluster mass. This agrees with our observations, where we detect a radio halo in about 50% of the total sample (9/19) at 144 MHz (Di Gennaro et al., 2021a) and in about 30% (5/19) at 650 MHz. The expected fractions of halos assuming $B = 2$ μGauss are consistent with the uncertainties given by the Monte Carlo simulations (see dashed lines in Fig. 6.11).

These expectations imply the presence of a population of ultra-steep spectra radio halos (USSRH) with $140 \leq \nu_s < 600$ MHz, which will be missed by observations at frequencies larger than 600 MHz, due to their ultra-steep radio spectra. In top panel of Fig.6.11, we show the fraction of these USSRH with respect to the total number of radio halos expected at 140 MHz, f_{USSRH}, as a function of the cluster mass, assuming $B = 5$ μGauss and $B = 2$ μGauss (solid and dashed lines, respectively). Given the mass range of our clusters, i.e. $M_{500} = 5.0$–8.0×10^{14} M$_\odot$, we expect that 50–60% ($B = 5$ μGauss) or 65–60% ($B = 2$ μGauss) of these to be ultra-steep (i.e. $\alpha < -1.5$). Despite the low statistics, the estimate using higher magnetic

fields is in good agreement with our observations, where we estimate 45–55% of USSRH (see Tab. 6.4). Increasing the number of distant radio halos will help in better determining the magnetic field levels in these clusters.

6.4.2. Occurrence of radio relics at high redshift

According to the predictions by Nuza et al. (2012), about 800 radio relics should have been observed at $0.5 < z < 1$ in the full LoTSS survey. However, Nuza et al. (2017) showed in a follow-up work that the majority of these relics, predicted in the simulations, would have small angular extensions ($\lesssim 2'$ when the image is smoothed with a 45" beam). If such a population of relics does exist, it would be challenging to recognise the corresponding radio features in surveys like LoTSS and classify them correctly. The results by Nuza et al. (2017) indicate that relics as extended as the one in PSZ2 G091.83+26.11 and sufficiently bright to be detected are rare in distant clusters.

In our total sample of 19 clusters at $z \geq 0.6$ we found one candidate radio relic, in PSZ2 G091.83+26.11. This source has a linear size larger than 1 Mpc. Although our sample is not complete and is rather small, we are likely observing the most violent mergers in the distant Universe (i.e. $M > 5 \times 10^{14}$ M$_\odot$) and we would have expected to detect more relics. At $z > 0.5$, five additional radio relics, namely PLCK G004.5-19.5 ($z = 0.52$, DEC $= -33°$, Albert et al., 2017), MACS J1149.5+2223 ($z = 0.544$, Bonafede et al., 2012, Bruno et al., subm.), MACS J0717.5+3745 ($z = 0.546$, Bonafede et al., 2014; Rajpurohit et al., 2021), MACS J0025.4-1222 ($z = 0.584$, DEC $= -12°$, Riseley et al., 2017), ACT-CL J0102-4915 ("el Gordo"; $z = 0.87$, DEC $= -49°$; Lindner et al., 2014), and two candidate radio relics, namely ACT-CL J0014.9-0057 ($z = 0.533$, DEC $= -1°$, Knowles et al., 2019) and ACT-CL J0046.4-3912 ($z = 0.592$, DEC $= -39°$, Knowles et al., 2021) are known in the literature[2]. Among these, MACS J0717.5+3745, MACS J1149.5+2223 and ACT-CL J0046.4-3912 host relics with linear sizes of about 1 Mpc. The small number of detections available to date does not allow a clear comparison with the current models. Despite that, the findings we present in this paper will be crucial to develop more stringent predictions on the magnetic properties of the ICM at the location of the shock, acceleration efficiency and seed populations when the first structure formed (Brüggen & Vazza, 2020).

6.5. Conclusions

In this paper, we presented follow-up observations of the high-redshift Planck-SZ clusters hosting diffuse radio sources presented in Di Gennaro

---

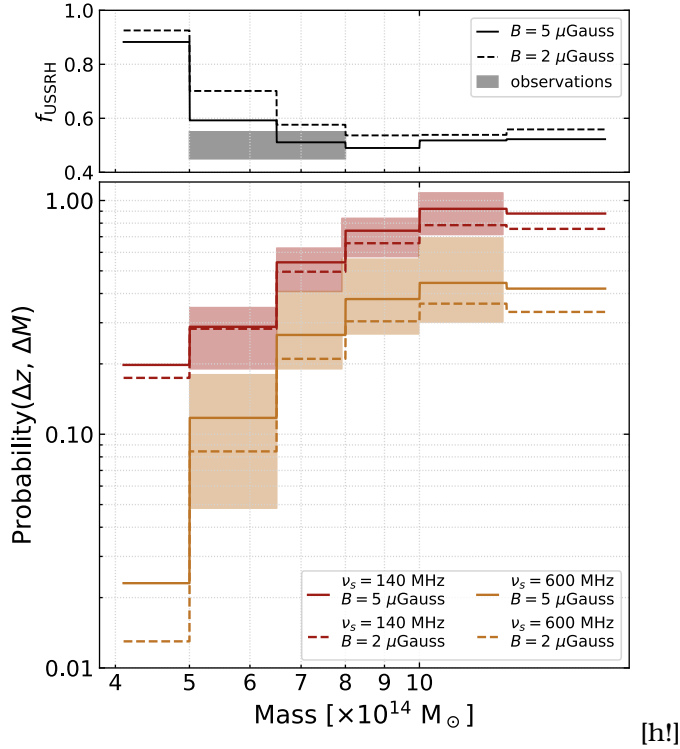[2]Only MACS J1149.5+2223 and MACS J0717.5+3745 are observed with LOFAR.

Figure 6.11: Probability of forming radio halos with $\nu_s > 140$ and $\nu_s > 600$ MHz (red and yellow lines, respectively) as a function of the cluster virial mass in the redshift range 0.6–0.7. Magnetic fields of $B = 5\ \mu$Gauss and $B = 2\ \mu$Gauss are assumed (solid and dashed lines, respectively). The shadowed regions represent the 1σ uncertainty derived through Monte Carlo calculations. Top panel: Expected fraction of USSRH visible at 144 MHz with steepening frequency $\nu_s < 600$ MHz as a function of the cluster virial mass, assuming $B = 5\ \mu$Gauss and $B = 2\ \mu$Gauss (solid and dashed lines, respectively). The shadowed area indicates the observed fraction of USSRH in our sample.

et al. (2021a). Our observations were taken with the upgraded GMRT (uGMRT) in Band 4 (550–900 MHz) and, for two clusters (i.e. PSZ2 G091.83+ 26.11 and PLCK G147.3–16.6) also in Band 3 (250–500 MHz)[3]. These observations were combined with LOFAR data at 144 MHz. Below we summarise our findings.

- About the 50% (5/9) of the clusters presented show the presence of a radio halo in the uGMRT observations, up to $\nu = 650$ MHz.

- For these systems, we measure integrated spectral indices between -1 and -1.4. We note that these clusters are also the most massive in our sample, and at these redshifts ($M > 6 \times 10^{14}$ M$_\odot$), which imply also more energetic merger events.

- For the clusters that host a radio halo in the LOFAR images but are not detected in the uGMRT ones, we estimate upper limits on the spectral indices of $\alpha < -1.5$, in line with the predictions of re-acceleration models (Cassano et al., 2010a).

- Although our sample is not complete, the fraction of cluster hosting halos and the spectral indices agree with the expectations from theoretical models of re-acceleration (Cassano & Brunetti, 2005; Cassano et al., 2006, 2010a).

- We find only one candidate radio relic in this sample of distant clusters, in PSZ2 G091.83+26.11. This is possibly contaminated by a double radio galaxy, although no optical counterparts have been observed in the PanSTARRS data. Future polarisation analysis with the VLA will provide further information on the nature of this radio source.

Observing distant diffuse radio emission is crucial for the investigation of the magnetic field evolution over cosmic time, and Universe magnetogenesis. Given the small size of the sample presented in this work, comparison with cosmological simulations are difficult. Upcoming observations with the X-ray satellite eROSITA (Extended Roentgen Survey Imaging Telescope Array; Merloni et al., 2012, 2020) will help find new distant galaxy clusters, that can be easily followed up with radio low-frequency observations.

---

[3]PSZ2 G089.39+69.36 was observed only in Band 3.

.1 Optical-Radio overlays for PSZ2 G091.83+26.11

Here we present the optical *irg* image of PSZ2 G091.83+26.11, taken from the PanSTARRS archive[4] (Chambers et al., 2016). We overlay the

---

[4]https://ps1images.stsci.edu/cgi-bin/ps1cutouts

radio contours of the uGMRT 650 MHz image, after removing the contri-
bution of the halo emission, to investigate possible optical counterparts
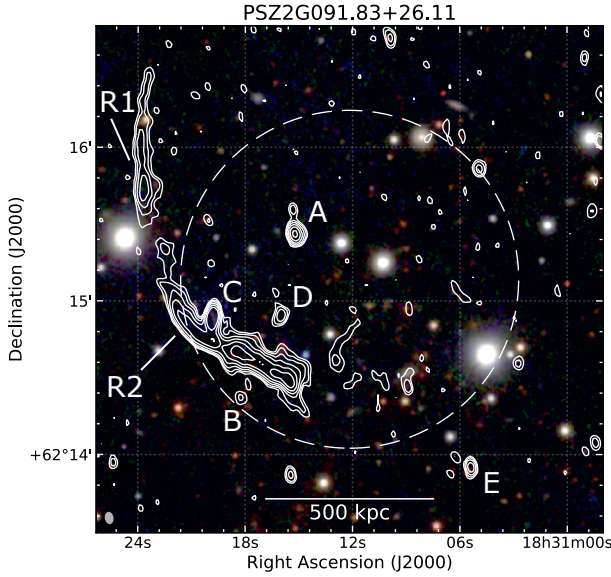that generate the radio emission of the candidate radio relic.

Figure .1.12: PanSTARRS optical *irg* image of PSZ2 G091.83+26.11. Radio con-
tours at 650 MHz without the contribution of the radio halo (i.e. with the *uv*-cut
at 500 kpc) are overlaid in white. The white dashed circle represents R_{500} region.
Labels follow Fig. 6.3.

BIBLIOGRAPHY

Ackermann, M., Ajello, M., Albert, A., et al. 2014, ApJ, 787, 18

Ackermann, M., Ajello, M., Albert, A., et al. 2016, ApJ, 819, 149

Ackermann, M., Ajello, M., Allafort, A., et al. 2010a, ApJ, 717, L71

Ackermann, M., Ajello, M., Allafort, A., et al. 2010b, ApJ, 717, L71

Adam, R., Goksu, H., Brown, S., Rudnick, L., & Ferrari, C. 2021, A&A, 648, A60

Akamatsu, H., Mizuno, M., Ota, N., et al. 2017, A&A, 600, A100

Akamatsu, H., van Weeren, R. J., Ogrean, G. A., et al. 2015, A&A, 582, A87

Albert, J. G., Sifón, C., Stroe, A., et al. 2017, A&A, 607, A4

Amodeo, S., Mei, S., Stanford, S. A., et al. 2018, ApJ, 853, 36

Anderson, C. S., Gaensler, B. M., & Feain, I. J. 2016, ApJ, 825, 59

Andrade-Santos, F., Jones, C., Forman, W. R., et al. 2017, ApJ, 843, 76

Andrade-Santos, F., van Weeren, R. J., Di Gennaro, G., et al. 2019, ApJ, 887, 31

Andreon, S. & Huertas-Company, M. 2011, A&A, 526, A11

Arnaud, K. A. 1996, in Astronomical Society of the Pacific Conference Series, Vol. 101, Astronomical Data Analysis Software and Systems V, ed. G. H. Jacoby & J. Barnes, 17

Arnaud, M. 2009, A&A, 500, 103

Arnaud, M., Pratt, G. W., Piffaretti, R., et al. 2010, A&A, 517, A92

Bagchi, J., Durret, F., Neto, G. B. L., & Paul, S. 2006, Science, 314, 791

Barrena, R., Streblyanska, A., Ferragamo, A., et al. 2018, A&A, 616, A42

Bartalucci, I., Mazzotta, P., Bourdin, H., & Vikhlinin, A. 2014, A&A, 566, A25

Basu, K., Vazza, F., Erler, J., & Sommer, M. 2016, A&A, 591, A142

Baumgartner, V. & Breitschwerdt, D. 2009, Astronomische Nachrichten, 330, 898

Beresnyak, A. 2012, Phys. Scr, 86, 058201

Beresnyak, A. & Miniati, F. 2016, ApJ, 817, 127

Bicknell, G. V., Cameron, R. A., & Gingold, R. A. 1990, ApJ, 357, 373

Biffi, V., Planelles, S., Borgani, S., et al. 2018, MNRAS, 476, 2689

Blandford, R. & Eichler, D. 1987, Phys. Rep., 154, 1

Blasi, P. & Colafrancesco, S. 1999, Astroparticle Physics, 12, 169

Bleem, L. E., Bocquet, S., Stalder, B., et al. 2020, ApJS, 247, 25

Blundell, K. M., Rawlings, S., & Willott, C. J. 1999, AJ, 117, 677

Bocquet, S., Dietrich, J. P., Schrabback, T., et al. 2019, ApJ, 878, 55

Bonafede, A., Brüggen, M., van Weeren, R., et al. 2012, MNRAS, 426, 40

Bonafede, A., Cassano, R., Brüggen, M., et al. 2017, MNRAS, 470, 3465

Bonafede, A., Feretti, L., Murgia, M., et al. 2010a, A&A, 513, A30

Bonafede, A., Feretti, L., Murgia, M., et al. 2010b, arXiv e-prints, arXiv:1009.1233

Bonafede, A., Giovannini, G., Feretti, L., Govoni, F., & Murgia, M. 2009, A&A, 494, 429

Bonafede, A., Intema, H. T., Brüggen, M., et al. 2014, ApJ, 785, 1

Bonafede, A., Vazza, F., Brüggen, M., et al. 2013, MNRAS, 433, 3208

Botteon, A., Brunetti, G., van Weeren, R. J., et al. 2020, ApJ, 897, 93

Botteon, A., Gastaldello, F., Brunetti, G., & Dallacasa, D. 2016a, MNRAS, 460, L84

Botteon, A., Gastaldello, F., Brunetti, G., & Dallacasa, D. 2016b, MNRAS, 460, L84

Brentjens, M. A. 2011, A&A, 526, A9

Brentjens, M. A. & de Bruyn, A. G. 2005, A&A, 441, 1217

Briggs, D. S. 1995, in Bulletin of the American Astronomical Society, Vol. 27, American Astronomical Society Meeting Abstracts, 1444

Brown, S. & Rudnick, L. 2011, MNRAS, 412, 2

Brüggen, M., Ruszkowski, M., Simionescu, A., Hoeft, M., & Dalla Vecchia, C. 2005, ApJ, 631, L21

Brüggen, M. & Vazza, F. 2020, MNRAS, 493, 2306

Brunetti, G., Giacintucci, S., Cassano, R., et al. 2008, Nature, 455, 944

Brunetti, G. & Jones, T. W. 2014, International Journal of Modern Physics D, 23, 1430007

Brunetti, G. & Lazarian, A. 2007, MNRAS, 378, 245

Brunetti, G. & Lazarian, A. 2011, MNRAS, 410, 127

Brunetti, G., Setti, G., Feretti, L., & Giovannini, G. 2001, MNRAS, 320, 365

Brunetti, G. & Vazza, F. 2020, Phys. Rev. Lett., 124, 051101

Brunetti, G., Zimmer, S., & Zandanel, F. 2017, MNRAS, 472, 1506

Burenin, R. A., Bikmaev, I. F., Khamitov, I. M., et al. 2018, Astronomy Letters, 44, 297

Burn, B. J. 1966, MNRAS, 133, 67

Burns, J. O., Skillman, S. W., & O'Shea, B. W. 2010, ApJ, 721, 1105

Caprioli, D. & Spitkovsky, A. 2014, ApJ, 783, 91

Carilli, C. L. & Taylor, G. B. 2002, ARA&A, 40, 319

Cash, W. 1979, ApJ, 228, 939

Cassano, R., Botteon, A., Di Gennaro, G., et al. 2019, ApJ, 881, L18

Cassano, R. & Brunetti, G. 2005, MNRAS, 357, 1313

Cassano, R., Brunetti, G., Röttgering, H. J. A., & Brüggen, M. 2010a, A&A, 509, A68

Cassano, R., Brunetti, G., & Setti, G. 2006, MNRAS, 369, 1577

Cassano, R., Ettori, S., Brunetti, G., et al. 2013, ApJ, 777, 141

Cassano, R., Ettori, S., Giacintucci, S., et al. 2010b, ApJ, 721, L82

Cavaliere, A. & Fusco-Femiano, R. 1976, A&A, 49, 137

Chambers, K. C., Magnier, E. A., Metcalfe, N., et al. 2016, arXiv e-prints, arXiv:1612.05560

Chandra, P., Ray, A., & Bhatnagar, S. 2004, ApJ, 612, 974

Cho, J. 2014, ApJ, 797, 133

Coles, P. & Chiang, L.-Y. 2000, Nature, 406, 376

Cornwell, T. J., Golap, K., & Bhatnagar, S. 2005, in Astronomical Society of the Pacific Conference Series, Vol. 347, Astronomical Data Analysis Software and Systems XIV, ed. P. Shopbell, M. Britton, & R. Ebert, 86

Cornwell, T. J., Golap, K., & Bhatnagar, S. 2008, IEEE Journal of Selected Topics in Signal Processing, 2, 647

Cuciti, V., Brunetti, G., van Weeren, R., et al. 2018, A&A, 609, A61

Cuciti, V., Cassano, R., Brunetti, G., et al. 2021a, A&A, 647, A51

Cuciti, V., Cassano, R., Brunetti, G., et al. 2021b, A&A, 647, A50

Dallacasa, D., Brunetti, G., Giacintucci, S., et al. 2009, ApJ, 699, 1288

Dawson, W. A., Jee, M. J., Stroe, A., et al. 2015, ApJ, 805, 143

de Gasperin, F., Dijkema, T. J., Drabent, A., et al. 2019, A&A, 622, A5

de Gasperin, F., Intema, H. T., Shimwell, T. W., et al. 2017, ArXiv e-prints

de Gasperin, F., Ogrean, G. A., van Weeren, R. J., et al. 2015, MNRAS, 448, 2197

de Gasperin, F., van Weeren, R. J., Brüggen, M., et al. 2014, MNRAS, 444, 3130

Di Gennaro, G., van Weeren, R. J., Andrade-Santos, F., et al. 2019, ApJ, 873, 64

Di Gennaro, G., van Weeren, R. J., Brunetti, G., et al. 2021a, Nature Astronomy, 5, 268

Di Gennaro, G., van Weeren, R. J., Hoeft, M., et al. 2018, ApJ, 865, 24

Di Gennaro, G., van Weeren, R. J., Rudnick, L., et al. 2021b, ApJ, 911, 3

Dolag, K., Bartelmann, M., & Lesch, H. 1999, A&A, 348, 351

Dolag, K., Grasso, D., Springel, V., & Tkachev, I. 2005, JCAP, 2005, 009

Domínguez-Fernández, P., Vazza, F., Brüggen, M., & Brunetti, G. 2019, MNRAS, 486, 623

Donnert, J., Dolag, K., Brunetti, G., & Cassano, R. 2013, MNRAS, 429, 3564

Donnert, J., Vazza, F., Brüggen, M., & ZuHone, J. 2018, Space Sci. Rev., 214, 122

Donnert, J. M. F., Beck, A. M., Dolag, K., & Röttgering, H. J. A. 2017, MNRAS, 471, 4587

Donnert, J. M. F., Stroe, A., Brunetti, G., Hoang, D., & Roettgering, H. 2016, MNRAS, 462, 2014

Drury, L. O. 1983, Reports on Progress in Physics, 46, 973

Ebeling, H., Edge, A. C., Mantz, A., et al. 2010, MNRAS, 407, 83

Eckert, D., Molendi, S., & Paltani, S. 2011, A&A, 526, A79

Ensslin, T. A., Biermann, P. L., Klein, U., & Kohle, S. 1998, A&A, 332, 395

Enßlin, T. A. & Brüggen, M. 2002, MNRAS, 331, 1011

Enßlin, T. A. & Gopal-Krishna. 2001, A&A, 366, 26

Fakhouri, O., Ma, C.-P., & Boylan-Kolchin, M. 2010, MNRAS, 406, 2267

Farnsworth, D., Rudnick, L., & Brown, S. 2011, AJ, 141, 191

Feretti, L., Giovannini, G., Govoni, F., & Murgia, M. 2012, A&A Rev., 20, 54

Finoguenov, A., Sarazin, C. L., Nakazawa, K., Wik, D. R., & Clarke, T. E. 2010, ApJ, 715, 1143

Foreman-Mackey, D. 2016, The Journal of Open Source Software, 2016

Foreman-Mackey, D. 2017, corner.py: Corner plots, Astrophysics Source Code Library

Foreman-Mackey, D., Hogg, D. W., Lang, D., & Goodman, J. 2013, PASP, 125, 306

Forman, W., Jones, C., & Tucker, W. 1982, in Bulletin of the American Astronomical Society, Vol. 14, 904

Frick, P., Sokoloff, D., Stepanov, R., & Beck, R. 2011, MNRAS, 414, 2540

Fruscione, A., McDowell, J. C., Allen, G. E., et al. 2006, in Proc. SPIE, Vol. 6270, Society of Photo-Optical Instrumentation Engineers (SPIE) Conference Series, 62701V

Fujita, Y., Takizawa, M., Yamazaki, R., Akamatsu, H., & Ohno, H. 2015, ApJ, 815, 116

Ghizzardi, S., Rossetti, M., & Molendi, S. 2010, A&A, 516, A32

Giacintucci, S., Markevitch, M., Cassano, R., et al. 2017, ApJ, 841, 71

Giacintucci, S., Venturi, T., Macario, G., et al. 2008, A&A, 486, 347

Giocoli, C., Tormen, G., & Sheth, R. K. 2012, MNRAS, 422, 185

Giovannini, G., Bonafede, A., Feretti, L., et al. 2009, A&A, 507, 1257

Giovannini, G., Cau, M., Bonafede, A., et al. 2020, A&A, 640, A108

Gladders, M. D. & Yee, H. K. C. 2005, ApJS, 157, 1

Goldreich, P. & Sridhar, S. 1997, ApJ, 485, 680

Golovich, N., Dawson, W. A., Wittman, D. M., et al. 2019a, ApJS, 240, 39

Golovich, N., Dawson, W. A., Wittman, D. M., et al. 2019b, ApJ, 882, 69

Golovich, N., van Weeren, R. J., Dawson, W. A., Jee, M. J., & Wittman, D. 2017, ApJ, 838, 110

Govoni, F. & Feretti, L. 2004a, International Journal of Modern Physics D, 13, 1549

Govoni, F. & Feretti, L. 2004b, International Journal of Modern Physics D, 13, 1549

Govoni, F., Murgia, M., Feretti, L., et al. 2006, A&A, 460, 425

Govoni, F., Murgia, M., Xu, H., et al. 2013, A&A, 554, A102

Guo, X., Sironi, L., & Narayan, R. 2014a, ApJ, 794, 153

Guo, X., Sironi, L., & Narayan, R. 2014b, ApJ, 797, 47

Ha, J.-H., Ryu, D., & Kang, H. 2018, ApJ, 857, 26

Hilton, M., Sifón, C., Naess, S., et al. 2021, ApJS, 253, 3

Hitomi Collaboration, Aharonian, F., Akamatsu, H., et al. 2016, Nature, 535, 117

Hitomi Collaboration, Aharonian, F., Akamatsu, H., et al. 2018, PASJ, 70, 9

Hoang, D. N., Shimwell, T. W., Stroe, A., et al. 2017, MNRAS, 471, 1107

Hoang, D. N., Shimwell, T. W., van Weeren, R. J., et al. 2018, MNRAS, 478, 2218

Hoeft, M. & Brüggen, M. 2007, MNRAS, 375, 77

Hong, S. E., Ryu, D., Kang, H., & Cen, R. 2014, ApJ, 785, 133

Huang, N., Bleem, L. E., Stalder, B., et al. 2020, AJ, 159, 110

Iapichino, L. & Brüggen, M. 2012, MNRAS, 423, 2781

Intema, H. T., van der Tol, S., Cotton, W. D., et al. 2009, A&A, 501, 1185

Jaffe, W. J. 1977, ApJ, 212, 1

Jaffe, W. J. & Perola, G. C. 1973, A&A, 26, 423

Jee, M. J., Stroe, A., Dawson, W., et al. 2015, ApJ, 802, 46

Jee, M. J. & Tyson, J. A. 2009, ApJ, 691, 1337

Johnson, A. R., Rudnick, L., Jones, T. W., Mendygral, P. J., & Dolag, K. 2020, ApJ, 888, 101

Jones, C. & Forman, W. 1984, ApJ, 276, 38

Jones, T. W., Nolting, C., O'Neill, B. J., & Mendygral, P. J. 2017, Physics of Plasmas, 24, 041402

Kalberla, P. M. W., Burton, W. B., Hartmann, D., et al. 2005, A&A, 440, 775

Kale, R., Dwarakanath, K. S., Bagchi, J., & Paul, S. 2012, MNRAS, 426, 1204

Kale, R., Venturi, T., Giacintucci, S., et al. 2015, A&A, 579, A92

Kang, H. 2015, Journal of Korean Astronomical Society, 48, 9

Kang, H. & Ryu, D. 2011, ApJ, 734, 18

Kang, H. & Ryu, D. 2013, ApJ, 764, 95

Kang, H. & Ryu, D. 2015, ApJ, 809, 186

Kang, H. & Ryu, D. 2016, ApJ, 823, 13

Kang, H., Ryu, D., & Jones, T. 2017, in International Cosmic Ray Conference, Vol. 301, 35th International Cosmic Ray Conference (ICRC2017), 283

Kang, H., Ryu, D., & Jones, T. W. 2012, ApJ, 756, 97

Kardashev, N. S. 1962, Soviet Ast., 6, 317

Kass, R. E. & Raftery, A. E. 1995, Journal of the American Statistical Association, 90, 773

Katz-Stone, D. M., Rudnick, L., & Anderson, M. C. 1993, ApJ, 407, 549

Kettula, K., Nevalainen, J., & Miller, E. D. 2013, A&A, 552, A47

Kierdorf, M., Beck, R., Hoeft, M., et al. 2017, A&A, 600, A18

King, I. R. 1972, ApJ, 174, L123

Kitayama, T. & Suto, Y. 1996, ApJ, 469, 480

Klein, U. & Fletcher, A. 2015, Galactic and Intergalactic Magnetic Fields

Knowles, K., Baker, A. J., Bond, J. R., et al. 2019, MNRAS, 486, 1332

Knowles, K., Pillay, D. S., Amodeo, S., et al. 2021, MNRAS, 504, 1749

Kocevski, D. D., Ebeling, H., Mullis, C. R., & Tully, R. B. 2007, ApJ, 662, 224

Komissarov, S. S. & Gubanov, A. G. 1994, A&A, 285, 27

Kraichnan, R. H. & Nagarajan, S. 1967, Physics of Fluids, 10, 859

Krauss-Varban, D. & Wu, C. S. 1989, J. Geophys. Res., 94, 15367

Lamee, M., Rudnick, L., Farnes, J. S., et al. 2016, ApJ, 829, 5

Landau, L. D. & Lifshitz, E. M. 1959, Fluid mechanics

Leahy, D. A. & Roger, R. S. 1998, ApJ, 505, 784

Lindner, R. R., Baker, A. J., Hughes, J. P., et al. 2014, ApJ, 786, 49

Lodders, K., Palme, H., & Gail, H.-P. 2009, Landolt Börnstein, 712

Loi, F., Murgia, M., Govoni, F., et al. 2017, MNRAS, 472, 3605

Loi, F., Murgia, M., Vacca, V., et al. 2020, MNRAS, 498, 1628

Lovisari, L., Forman, W. R., Jones, C., et al. 2017, ApJ, 846, 51

Macario, G., Markevitch, M., Giacintucci, S., et al. 2011, ApJ, 728, 82

Mandal, S., Intema, H. T., van Weeren, R. J., et al. 2020, A&A, 634, A4

Markevitch, M. 2006a, in ESA Special Publication, Vol. 604, The X-ray Universe 2005, ed. A. Wilson, 723

Markevitch, M. 2006b, in ESA Special Publication, Vol. 604, The X-ray Universe 2005, ed. A. Wilson, 723

Markevitch, M., Gonzalez, A. H., David, L., et al. 2002, ApJ, 567, L27

Markevitch, M., Govoni, F., Brunetti, G., & Jerius, D. 2005, ApJ, 627, 733

Markevitch, M., Sarazin, C. L., & Vikhlinin, A. 1999, ApJ, 521, 526

Markevitch, M. & Vikhlinin, A. 2007, Phys. Rep., 443, 1

Markevitch, M., Vikhlinin, A., & Forman, W. R. 2003, in Astronomical Society of the Pacific Conference Series, Vol. 301, Matter and Energy in Clusters of Galaxies, ed. S. Bowyer & C.-Y. Hwang, 37

Markevitch, M., Vikhlinin, A., & Mazzotta, P. 2001, ApJ, 562, L153

Massaro, E., Perri, M., Giommi, P., & Nesci, R. 2004, A&A, 413, 489

Maughan, B. J., Jones, C., Jones, L. R., & Van Speybroeck, L. 2007, ApJ, 659, 1125

Mazzotta, P., Markevitch, M., Forman, W. R., et al. 2001, arXiv e-prints, astro

McMullin, J. P., Waters, B., Schiebel, D., Young, W., & Golap, K. 2007, in Astronomical Society of the Pacific Conference Series, Vol. 376, Astronomical Data Analysis Software and Systems XVI, ed. R. A. Shaw, F. Hill, & D. J. Bell, 127

Medezinski, E., Umetsu, K., Okabe, N., et al. 2016, ApJ, 817, 24

Merloni, A., Nandra, K., & Predehl, P. 2020, Nature Astronomy, 4, 634

Merloni, A., Predehl, P., Becker, W., et al. 2012, arXiv e-prints, arXiv:1209.3114

Miley, G. 1980, ARA&A, 18, 165

Miller, T. B., Chapman, S. C., Aravena, M., et al. 2018, Nature, 556, 469

Miniati, F. & Beresnyak, A. 2015, Nature, 523, 59

Mohan, N. & Rafferty, D. 2015, PyBDSM: Python Blob Detection and Source Measurement, Astrophysics Source Code Library

Molnar, S. M. & Broadhurst, T. 2017, ApJ, 841, 46

Molnar, S. M. & Broadhurst, T. 2018, ApJ, 862, 112

Mullin, L. M., Riley, J. M., & Hardcastle, M. J. 2008, MNRAS, 390, 595

Murgia, M., Govoni, F., Feretti, L., et al. 2004, A&A, 424, 429

Nandra, K., Barret, D., Barcons, X., et al. 2013, arXiv e-prints, arXiv:1306.2307

Neeser, M. J., Eales, S. A., Law-Green, J. D., Leahy, J. P., & Rawlings, S. 1995, ApJ, 451, 76

Nuza, S. E., Gelszinnis, J., Hoeft, M., & Yepes, G. 2017, MNRAS, 470, 240

Nuza, S. E., Hoeft, M., van Weeren, R. J., Gottlöber, S., & Yepes, G. 2012, MNRAS, 420, 2006

Offringa, A. R., de Bruyn, A. G., Biehl, M., et al. 2010, MNRAS, 405, 155

Offringa, A. R., McKinley, B., Hurley-Walker, N., et al. 2014, MNRAS, 444, 606

Offringa, A. R. & Smirnov, O. 2017, MNRAS, 471, 301

Ogrean, G. 2017, in American Astronomical Society Meeting Abstracts, Vol. 229, American Astronomical Society Meeting Abstracts, 438.08

Ogrean, G. A., Brüggen, M., Röttgering, H., et al. 2013, MNRAS, 429, 2617

Ogrean, G. A., Brüggen, M., van Weeren, R., et al. 2014, MNRAS, 440, 3416

Ogrean, G. A., van Weeren, R. J., Jones, C., et al. 2016, ApJ, 819, 113

Okabe, N., Akamatsu, H., Kakuwa, J., et al. 2015, PASJ, 67, 114

Oppermann, N., Junklewitz, H., Greiner, M., et al. 2015, A&A, 575, A118

Orrú, E., Murgia, M., Feretti, L., et al. 2007, A&A, 467, 943

Orrù, E., van Velzen, S., Pizzo, R. F., et al. 2015, A&A, 584, A112

Osinga, E., van Weeren, R. J., Boxelaar, J. M., et al. 2021, A&A, 648, A11

O'Sullivan, S. P., Brown, S., Robishaw, T., et al. 2012, MNRAS, 421, 3300

O'Sullivan, S. P., Lenc, E., Anderson, C. S., Gaensler, B. M., & Murphy, T. 2018, MNRAS, 475, 4263

Overzier, R. A. 2016, A&A Rev., 24, 14

Owen, F. N., Rudnick, L., Eilek, J., et al. 2014, ApJ, 794, 24

Ozawa, T., Nakanishi, H., Akahori, T., et al. 2015, PASJ, 67, 110

O'Neill, B. J., Jones, T. W., Nolting, C., & Mendygral, P. J. 2019, The Astrophysical Journal, 887, 26

Pacholczyk, A. G. 1970, Radio astrophysics. Nonthermal processes in galactic and extragalactic sources

Pearce, C. J. J., van Weeren, R. J., Andrade-Santos, F., et al. 2017, ApJ, 845, 81

Pearson, K. 1895, Proceedings of the Royal Society of London Series I, 58, 240

Peebles, P. J. E. 1980, The large-scale structure of the universe

Perley, R. A. & Butler, B. J. 2013, ApJS, 206, 16

Petrosian, V. 2001, ApJ, 557, 560

Pfrommer, C. & Jones, T. W. 2011, ApJ, 730, 22

Pierre, M., Pacaud, F., Juin, J. B., et al. 2011, MNRAS, 414, 1732

Pierre, M., Valtchanov, I., Altieri, B., et al. 2004, JCAP, 2004, 011

Pinzke, A., Oh, S. P., & Pfrommer, C. 2017, MNRAS, 465, 4800

Pizzo, R. F., de Bruyn, A. G., Bernardi, G., & Brentjens, M. A. 2011, A&A, 525, A104

Planck Collaboration, Ade, P. A. R., Aghanim, N., et al. 2016, A&A, 594, A27

Planck Collaboration, Ade, P. A. R., Aghanim, N., et al. 2015, A&A, 582, A29

Porter, D. H., Jones, T. W., & Ryu, D. 2015, ApJ, 810, 93

Press, W. H. & Schechter, P. 1974, ApJ, 187, 425

Prokhorov, D. A. & Churazov, E. M. 2014a, A&A, 567, A93

Prokhorov, D. A. & Churazov, E. M. 2014b, A&A, 567, A93

Rajpurohit, K., Hoeft, M., van Weeren, R. J., et al. 2018a, ApJ, 852, 65

Rajpurohit, K., Hoeft, M., van Weeren, R. J., et al. 2018b, ApJ, 852, 65

Rajpurohit, K., Vazza, F., Hoeft, M., et al. 2020, A&A, 642, L13

Rajpurohit, K., Wittor, D., van Weeren, R. J., et al. 2021, A&A, 646, A56

Rau, U. & Cornwell, T. J. 2011, A&A, 532, A71

Reimer, O., Pohl, M., Sreekumar, P., & Mattox, J. R. 2003, ApJ, 588, 155

Riseley, C. J., Scaife, A. M. M., Wise, M. W., & Clarke, A. O. 2017, A&A, 597, A96

Robitaille, T. & Bressert, E. 2012, APLpy: Astronomical Plotting Library in Python, Astrophysics Source Code Library

Roettiger, K., Burns, J. O., & Stone, J. M. 1999, ApJ, 518, 603

Roh, S., Ryu, D., Kang, H., Ha, S., & Jang, H. 2019, ApJ, 883, 138

Rossetti, M., Gastaldello, F., Eckert, D., et al. 2017, MNRAS, 468, 1917

Rottgering, H. J. A., Wieringa, M. H., Hunstead, R. W., & Ekers, R. D. 1997, MNRAS, 290, 577

Rudnick, L. 2001, in Astronomical Society of the Pacific Conference Series, Vol. 250, Particles and Fields in Radio Galaxies Conference, ed. R. A. Laing & K. M. Blundell, 372

Rudnick, L. & Katz-Stone, D. 1996, Powerful diagnostics of Cygnus A's relativistic electrons, ed. C. L. Carilli & D. E. Harris, 158

Rudnick, L. & Owen, F. N. 2014, ApJ, 785, 45

Rumsey, C., Perrott, Y. C., Olamaie, M., et al. 2017, MNRAS, 470, 4638

Russell, H. R., McNamara, B. R., Sanders, J. S., et al. 2012, MNRAS, 423, 236

Russell, H. R., Sanders, J. S., Fabian, A. C., et al. 2010, MNRAS, 406, 1721

Rybicki, G. B. & Lightman, A. P. 1986, Radiative Processes in Astrophysics

Ryu, D., Kang, H., Cho, J., & Das, S. 2008, Science, 320, 909

Sanders, J. S. 2006, MNRAS, 371, 829

Sanders, J. S., Fabian, A. C., & Taylor, G. B. 2005, MNRAS, 356, 1022

Sarazin, C. L. 2002, The Physics of Cluster Mergers, ed. L. Feretti, I. M. Gioia, & G. Giovannini, Vol. 272, 1–38

Schekochihin, A. A. & Cowley, S. C. 2006, Physics of Plasmas, 13, 056501

Schekochihin, A. A. & Cowley, S. C. 2007, Turbulence and Magnetic Fields in Astrophysical Plasmas, ed. S. Molokov, R. Moreau, & H. K. Moffatt, 85

Schellenberger, G., Reiprich, T. H., Lovisari, L., Nevalainen, J., & David, L. 2015, A&A, 575, A30

Schlegel, D. J., Finkbeiner, D. P., & Davis, M. 1998, ApJ, 500, 525

Sereno, M., Giocoli, C., Izzo, L., et al. 2018, Nature Astronomy, 2, 744

Shimwell, T. W., Brown, S., Feain, I. J., et al. 2014, MNRAS, 440, 2901

Shimwell, T. W., Luckin, J., Brüggen, M., et al. 2016, MNRAS, 459, 277

Shimwell, T. W., Markevitch, M., Brown, S., et al. 2015, MNRAS, 449, 1486

Shimwell, T. W., Röttgering, H. J. A., Best, P. N., et al. 2017, A&A, 598, A104

Shimwell, T. W., Tasse, C., Hardcastle, M. J., et al. 2019, A&A, 622, A1

Simionescu, A., Nakashima, S., Yamaguchi, H., et al. 2019, MNRAS, 483, 1701

Simionescu, A., Werner, N., Urban, O., et al. 2012, ApJ, 757, 182

Skillman, S. W., Xu, H., Hallman, E. J., et al. 2013, ApJ, 765, 21

Slee, O. B., Roy, A. L., Murgia, M., Andernach, H., & Ehle, M. 2001, AJ, 122, 1172

Smirnov, O. M. & Tasse, C. 2015, MNRAS, 449, 2668

Smith, R. K., Brickhouse, N. S., Liedahl, D. A., & Raymond, J. C. 2001, ApJ, 556, L91

Smolčić, V., Novak, M., Delvecchio, I., et al. 2017, A&A, 602, A6

Sokoloff, D. D., Bykov, A. A., Shukurov, A., et al. 1998, MNRAS, 299, 189

Springel, V., Frenk, C. S., & White, S. D. M. 2006, Nature, 440, 1137

Streblyanska, A., Barrena, R., Rubiño-Martín, J. A., et al. 2018, A&A, 617, A71

Stroe, A., Harwood, J. J., Hardcastle, M. J., & Röttgering, H. J. A. 2014, MNRAS, 445, 1213

Stroe, A., Shimwell, T., Rumsey, C., et al. 2016, MNRAS, 455, 2402

Stroe, A., van Weeren, R. J., Intema, H. T., et al. 2013, A&A, 555, A110

Stuardi, C., Bonafede, A., Wittor, D., et al. 2019, MNRAS, 2080

Subramanian, K. 2016, Reports on Progress in Physics, 79, 076901

Subramanian, K., Shukurov, A., & Haugen, N. E. L. 2006, MNRAS, 366, 1437

Sunyaev, R. A. & Zeldovich, Y. B. 1972, Comments on Astrophysics and Space Physics, 4, 173

Tasse, C. 2014, A&A, 566, A127

Tasse, C., Hugo, B., Mirmont, M., et al. 2018, A&A, 611, A87

Tasse, C., Shimwell, T., Hardcastle, M. J., et al. 2021, A&A, 648, A1

Thierbach, M., Klein, U., & Wielebinski, R. 2003, A&A, 397, 53

Tribble, P. C. 1991, MNRAS, 250, 726

Urdampilleta, I., Akamatsu, H., Mernier, F., et al. 2018, A&A, 618, A74

Urdampilleta, I., Mernier, F., Kaastra, J. S., et al. 2019, A&A, 629, A31

Urry, C. M. & Padovani, P. 1995, PASP, 107, 803

van der Burg, R. F. J., Aussel, H., Pratt, G. W., et al. 2016, A&A, 587, A23

van Haarlem, M. P., Wise, M. W., Gunst, A. W., et al. 2013, A&A, 556, A2

van Weeren, R. J., Andrade-Santos, F., Dawson, W. A., et al. 2017a, Nature Astronomy, 1, 0005

van Weeren, R. J., Brüggen, M., Röttgering, H. J. A., & Hoeft, M. 2011a, MNRAS, 418, 230

van Weeren, R. J., Brunetti, G., Brüggen, M., et al. 2016, ApJ, 818, 204

van Weeren, R. J., de Gasperin, F., Akamatsu, H., et al. 2019, Space Sci. Rev., 215, 16

van Weeren, R. J., Hoeft, M., Röttgering, H. J. A., et al. 2011b, A&A, 528, A38

van Weeren, R. J., Intema, H. T., Lal, D. V., et al. 2014, ApJ, 781, L32

van Weeren, R. J., Ogrean, G. A., Jones, C., et al. 2017b, ApJ, 835, 197

van Weeren, R. J., Röttgering, H. J. A., Bagchi, J., et al. 2009, A&A, 506, 1083

van Weeren, R. J., Röttgering, H. J. A., Brüggen, M., & Hoeft, M. 2010, Science, 330, 347

van Weeren, R. J., Röttgering, H. J. A., Intema, H. T., et al. 2012, A&A, 546, A124

van Weeren, R. J., Shimwell, T. W., Botteon, A., et al. 2020, arXiv e-prints, arXiv:2011.02387

Vazza, F. & Brüggen, M. 2014, MNRAS, 437, 2291

Vazza, F., Brüggen, M., Gheller, C., & Brunetti, G. 2012a, MNRAS, 421, 3375

Vazza, F., Brüggen, M., van Weeren, R., et al. 2012b, MNRAS, 421, 1868

Vazza, F., Brunetti, G., Brüggen, M., & Bonafede, A. 2018, MNRAS, 474, 1672

Vazza, F., Jones, T. W., Brüggen, M., et al. 2017, MNRAS, 464, 210

Venturi, T., Giacintucci, S., Brunetti, G., et al. 2007, A&A, 463, 937

Vikhlinin, A., Kravtsov, A., Forman, W., et al. 2006, ApJ, 640, 691

Vikhlinin, A., Markevitch, M., Murray, S. S., et al. 2005, ApJ, 628, 655

Vogelsberger, M., Genel, S., Springel, V., et al. 2014, MNRAS, 444, 1518–1547

Walker, S. A., ZuHone, J., Fabian, A., & Sanders, J. 2018, Nature Astronomy, 2, 292–296

Wilber, A., Brüggen, M., Bonafede, A., et al. 2019, A&A, 622, A25

Wilber, A., Brüggen, M., Bonafede, A., et al. 2018, MNRAS, 473, 3536

Williams, W. L., van Weeren, R. J., Röttgering, H. J. A., et al. 2016, MNRAS, 460, 2385

Willingale, R., Starling, R. L. C., Beardmore, A. P., Tanvir, N. R., & O'Brien, P. T. 2013, MNRAS, 431, 394

Willis, J. P., Canning, R. E. A., Noordeh, E. S., et al. 2020, Nature, 577, 39

Willis, J. P., Clerc, N., Bremer, M. N., et al. 2013, MNRAS, 430, 134

Wittor, D., Hoeft, M., Vazza, F., Brüggen, M., & Domínguez-Fernández, P. 2019, MNRAS, 490, 3987

Wittor, D., Vazza, F., & Brüggen, M. 2017, MNRAS, 464, 4448

Wu, C. S. 1984, J. Geophys. Res., 89, 8857

Xu, H., Li, H., Collins, D. C., Li, S., & Norman, M. L. 2011, ApJ, 739, 77

Zhuravleva, I., Churazov, E., Schekochihin, A. A., et al. 2019, Nature Astronomy, 3, 832

Zohren, H., Schrabback, T., van der Burg, R. F. J., et al. 2019, MNRAS, 488, 2523

ZuHone, J. A., Miller, E. D., Bulbul, E., & Zhuravleva, I. 2018, The Astrophysical Journal, 853, 180

ZuHone, J. A. & Roediger, E. 2016, Journal of Plasma Physics, 82

NEDERLANDSE SAMENVATTING

Clusters van sterrenstelsels zijn de grootste objecten in het heelal die door de zwaartekracht bij elkaar worden gehouden. Ze kunnen een grootte bereiken van miljoenen lichtjaren ($\gtrsim$ 1 Megaparsec) en een massa van honderden biljoenen zonsmassa's ($\gtrsim 10^{14}$ M$_\odot$). Clusters bestaan uit duizenden sterrenstelsels, die slechts een klein percentage van de totale massa van deze objecten vertegenwoordigen. Het grootste deel van het zichtbare licht wordt geproduceerd door deeltjes (elektronen en protonen) die de ruimte tussen sterrenstelsels vullen, het zogenaamde *intracluster medium* (ICM). Het ICM is zichtbaar bij röntgengolflengten (Fig. 6.14). Volgens de huidige theorie groeien clusters van melkwegstelsels door botsingen met andere clusters of groepen melkwegstelsels, en worden verondersteld de laatste structuren te zijn die zich in het heelal hebben gevormd. Clusters in de fase van botsing worden *botsende clusters* genoemd. Studies schatten dat deze grote structuren zich hebben gevormd toen het heelal slechts 3-4 miljard jaar oud was.

Cluster botsingen zijn de meest energieke gebeurtenissen sinds de oerknal. Tijdens deze botsingen komt een deel van de energie vrij in turbulentie en schokgolven. Deze hebben een grote invloed op het ICM, resulterende in een verstoorde morfologie. Bovendien zijn botsende clusters in staat om de elektronen die tussen sterrenstelsels zwerven te versnellen tot bijna de lichtsnelheid en om de magnetische velden van clusters te versterken. De interactie van versnelde deeltjes met magnetische velden produceert grootschalige diffuse radio-emissie, die niet geassocieerd is met de emissie van een zwarte gat in het centrum van een sterrenstelsel. Deze structuren van diffuse radiostraling worden *radio halo's* of *radio relikwieën* genoemd (Fig. 6.13).
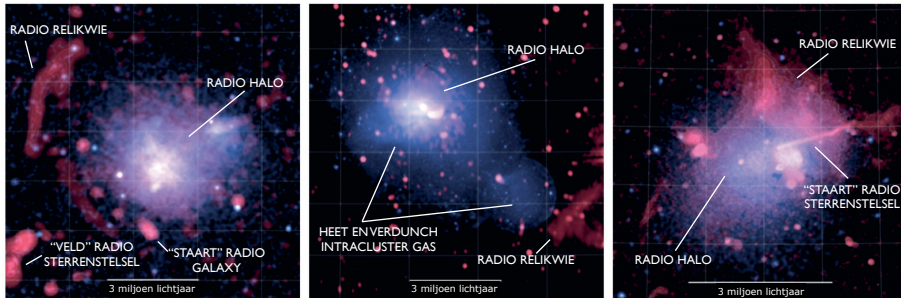
Figuur 6.13: Drie voorbeelden van lokale clusters van sterrenstelsels waargenomen op radio (rood) en röntgen (blauw) golflengtes. Van links naar rechts: Abell 2744, Coma en Abell 2256. De radio-emissie traceert versnelde deeltjes en magnetische velden, terwijl de röntgenemissie het hete en verdunde intraclustergas. Afbeeldingen gemaakt en aangepast van van Weeren et al. (2019).

- Radio halo's zijn min of meer ronde bronnen die zich in het midden van de cluster bevinden. Ze volgen over het algemeen de morfologie van het ICM van röntgenstraling.

- Radio relikwieën zijn langwerpige structuren die zich aan de randen van een cluster bevinden. Recente gecombineerde radio- en röntgen waarnemingen hebben aangetoond dat ze zich op de positie van röntgenschokken bevinden. Radio waarnemingen met hoge resolutie hebben aangetoond dat relikwieën een filamentaire structuur hebben.

Ondanks de vooruitgang van kennis van de afgelopen decennia is het nog onduidelijk wat de oorsprong is van de diffuse radiostraling in clusters. Er wordt aangenomen dat radio-relikwieën worden geproduceerd als gevolg van een schok die propageert naar de rand van het cluster. Het idee is dat de schokgolf magnetische velden ordent en versterkt, terwijl deeltjes worden versneld in de schok. De precieze aard van het fysische versnellingsmechanisme is nog onduidelijk. Een van de uitdagingen is dat cluster schokken niet heel sterk zijn ($\mathcal{M} \lesssim 3$), en dan zouden de deeltjes niet efficiënt versneld moeten kunnen worden. Daarom is de aanwezigheid van reeds bestaand relativistisch plasma, zoals dat in de lobben van radiostelsels, vereist. In sommige clusters is een duidelijk morfologisch verband gevonden tussen radiostelsels en radio relikwieën, wat het laatste scenario ondersteunt. Ten slotte, als gevolg van de compressie van het magnetische veld, zijn radio relikwieën ook gepolariseerd. Aangenomen wordt dat radio halo's worden geproduceerd als gevolg van de turbulentie die wordt gegenereerd door de botsende clusters. Recente studies hebben een duidelijk verband gevonden tussen de dynamische toestand van clusters en de ken-

merken van radio halo's. Vooral in de meest massieve (en dus energetische) systemen blijken zich de meest heldere radiohalo's te bevinden.

Diffuse radiostraling in clusters is overtuigend bewijs voor de aanwezigheid van magnetische velden op μGauss niveau. Deze waarde wordt verkregen voor objecten in de buurt, waarbij de verandering van de gepolariseerde emissie van achtergrondbronnen wordt geanalyseerd (d.m.v. Faraday rotatiemetingen). Het is nog een open vraag hoe magnetische velden dergelijke niveaus bereiken, en waar de magnetische velden vandaan komen. Er zijn twee hoofdscenario's geïdentificeerd: men gaat ervan uit dat magnetische velden worden gegenereerd tijdens de eerste fasen van de geschiedenis van het heelal, vóór de vorming van de eerste sterren en sterrenstelsels (d.w.z. *oorspronkelijke oorsprong*); de andere veronderstelt dat magnetische velden worden uitgestoten door sterrenstelsels, winden en/of jets (d.w.z. *astrofysische oorsprong*). Voor beide scenario's moeten de initiële magnetische velden worden versterkt gedurende de tijd om de niveaus te bereiken die we meten in het huidige universum. Algemeen wordt aangenomen dat turbulentie als gevolg van botsingen van clusters een grote rol speelt, hoewel het exacte proces dat de versterking veroorzaakt nog steeds niet goed wordt begrepen.

Dit proefschrift heeft als doel de versnellingsmechanismen te onderzoeken die worden aangedreven door botsing-geïnduceerde schokgolven en turbulentie, en de evolutie van de diffuse radio-emissie (en dus magneetvelden in clusters) in de kosmologische tijd. Dit onderzoek is mogelijk dankzij hooggevoelige en hoge resolutie radio- en röntgenwaarnemingen. In het bijzonder zijn in dit proefschrift radiowaarnemingen met de Karl-Jansky VLA, LOFAR en verbeterde uGMRT gecombineerd met röntgenobservaties van Chandra, XMM-Newton en Suzaku. In **Hoofdstuk 2** en **Hoofdstuk 5** zijn de spectrale en polarisatie-eigenschappen van het radiorelikwie in CIZA J2242.8+5301 bestudeerd. Dankzij diepe VLA-waarnemingen met hoge resolutie werd ontdekt dat de bron uit verschillende filamenten bestaat. Het is nog onduidelijk of dit komt door de complexe vorm van het schokoppervlak en/of door inhomogeniteiten van magnetische velden. De eigenschappen van de schok in ZwCl 0008.8+5215 zijn weergegeven in **Hoofdstuk 3**. Hier werden met behulp van diepe Chandra en Suzaku waarnemingen variaties in de schoksterkte over de lengte van de schok onderzocht om de morfologische eigenschappen van de diffuse radiostraling te verklaren. De evolutie van de magnetische velden op cluster schaal wordt gepresenteerd in **Hoofdstuk 4**, waarin een groep van verre ($z \geq 0.6$) clusters van sterrenstelsels wordt bestudeerd die zijn waargenomen met LOFAR. De radio sterkte is vergelijkbaar met die gemeten in nabijgelegen systemen een resulteert in verrassend hoge magnetische velden ($\sim$ few μGauss). De spectrale eigenschappen van deze verre radio halo's worden onderzocht in **Hoofdstuk 6** met behulp van nieuwe uGMRT-waarnemingen. Deze informatie is cruciaal om het huidige model van vorming van de diffuse radiostraling te testen.

SUMMARY

Galaxy clusters are the largest objects in the Universe held together by gravity. They can reach a size of a few millions of light years ($\gtrsim$ 1 Megaparsec) and masses of hundreds of trillion times the mass of the Sun ($\gtrsim 10^{14}$ M$_\odot$). Galaxy clusters consist of thousands of galaxies, which only represent a small percentage of the total mass of these objects. The largest fraction of the visible light is emitted by particles (electrons and protons) filling the space in-between galaxies, the so-called the *intracluster medium* (ICM). The ICM is visible at X-ray wavelengths (Fig. 6.14). According to the current models, galaxy clusters grow via collisions with other clusters or galaxy groups. Galaxy clusters in the phase of collision are called *merging clusters*. Multi-wavelength studies have set an approximate time for the formation of these large structures when the Universe was only 3–4 billion years old.

Cluster mergers are the most energetic events since the Big Bang. During these events, part of the energy is released in turbulence and shock waves. These affect the ICM, which is therefore observed to have a disturbed morphology. Moreover, cluster mergers are able to accelerate the electrons roaming between galaxies to velocities close to the speed of light, and to amplify cluster magnetic fields. The interaction of accelerated particles with cluster-scale magnetic fields produces large-scale diffuse radio emission, which is not associated with the emission from black holes at the centre of galaxies (i.e. radio galaxies). These diffuse radio sources are called *radio halos* or *radio relics* (Fig. 6.14).

- Radio halos are roundish, roughly smooth sources located in the cluster centre. They generally follow the morphology of the intra-
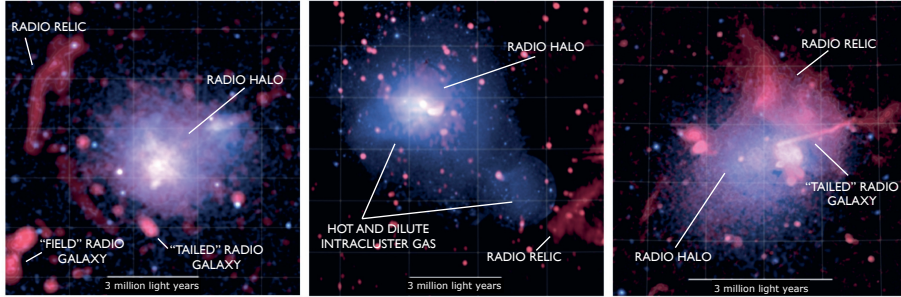
Figure 6.14: Three examples of local clusters of galaxies observed at radio (red) and X-ray (blue) wavelengths. From left to right: Abell 2744, Coma and Abell 2256. The radio emission traces accelerated particles and magnetic fields, while the X-ray emission traces the hot and dilute intracluster gas. Images taken and adapted from van Weeren et al. (2019).

cluster medium from the X-rays.

- Radio relics are elongated structures located in the cluster outskirts. Recent observations have found that they are located at the position of X-ray shocks. Radio observations at high resolutions have revealed that relics have a filamentary structure.

Despite the progress in our understanding during the last decades, it is still unclear what the origin of the diffuse radio emission in clusters is. Radio relics are thought to be produced as a consequence of the shock propagation towards the cluster outskirts. The basic idea is that the shock wave aligns and amplifies magnetic fields, while particles become ultra-relativistic by scattering back and forth across the shock. The detailed physical understanding of the acceleration mechanisms is unclear. One of the challenges is that cluster shocks have mild strengths ($\mathcal{M} \lesssim 3$), and hence should not be able to efficiently accelerate the particles associated with the ICM. Therefore, the presence of pre-existing relativistic plasma, like that in the lobes of radio galaxies, is required. In some clusters, a clear morphological link between radio galaxies and radio relics has been found, supporting the latter scenario. Finally, as a consequence of the magnetic field alignment and compression, radio relics are also polarised structures. Radio halos are thought to be produced as a consequence of the turbulence generated by the cluster mergers. Recent studies have found a clear relation between the cluster dynamical state and the characteristics of radio halos. In particular, the most massive (and therefore energetic) systems have been found to host the most luminous radio halos.

Diffuse radio emission in the cluster volume is compelling evidence of the presence of μGauss-level magnetic fields. This value is obtained in

nearby objects, analysing the change of the polarised emission from background sources (i.e. Faraday Rotation Measurements). It is still an open question where the magnetic fields come from. Two main scenarios have been identified: one assumes that magnetic fields are generated during the first phases of the Universe's history, before the formation of the first stars and galaxies (i.e. *primordial origin*); the other one assumes that magnetic fields are ejected from galaxies, winds and/or jets (i.e. *astrophysical origin*). For both scenarios, the initial magnetic fields need to be amplified over cosmic time to reach the levels we measure in the present-day Universe. It is widely believed that turbulence due to cluster mergers plays a major role, although the exact amplification process is still not well understood.

This Thesis aims to investigate the acceleration mechanisms driven by merger-induced shock waves and turbulence, and the evolution of the diffuse radio emission (and therefore cluster magnetic fields) over cosmic time. This was possible thanks to high-sensitivity and high-resolution radio and X-ray observations. Particularly, throughout this Thesis, radio observations with the Karl-Jansky VLA, LOFAR and upgraded GMRT have been combined with X-ray Chandra, XMM-Newton and Suzaku observations. In **Chapter 2** and **Chapter 5** the spectral and polarisation properties of the radio relic in CIZA J2242.8+5301 have been studied. Thanks to deep high-resolution VLA observations, it was discovered that the source consists of several filaments. It remains unclear whether this is due to the complex shape of the shock surface and/or magnetic field inhomogeneities. The properties of the shock in ZwCl 0008.8+5215 have been presented in **Chapter 3**. Using deep Chandra and Suzaku observations, variations in the shock strength along the length of the shock were investigated to explain the morphological properties of the diffuse radio emission. The evolution of the cluster-scale magnetic fields is presented in **Chapter 4**, studying a sample of distant ($z \geq 0.6$) galaxy clusters observed with LOFAR. The similar radio luminosity to that measured in nearby systems, in the same cluster mass range, results in surprisingly high magnetic fields ($\sim$ few μGauss). The spectral properties of these distant radio halos are investigated in **Chapter 6**, using new uGMRT observations. This information is crucial to test the current model for formation of the diffuse radio emission.

RIEPILOGO

Gli ammassi di galassie sono gli oggetti più grandi dell'Universo tenuti insieme dalla gravità. Possono raggiungere dimensioni di alcuni milioni di anni luce ($\geq$ 1 Megaparsec) e masse centinaia di trilioni di volte quelle del Sole ($\geq 10^{14}$ M$_\odot$). Gli ammassi di galassie sono formati da migliaia di galassie, che rappresentano solo una piccola percentuale della massa complessiva di questi oggetti. La frazione più grande di luce visibile è data da particelle (elettroni e protoni) che riempiono lo spazio tra le galassie, il cosiddetto *mezzo intracluster* (ICM). L'ICM è osservabile a lunghezze d'onda X (Fig. 6.15). Secondo i modelli attuali, gli ammassi di galassie crescono via collisioni con altri ammassi o gruppi di galassie. Ammassi di galassie in fase di collisione prendono il nome di *merger*. Studi a diverse lungheze d'onda hanno stabilito che la formazione di queste grandi strutture sia avvenuta approssivamente quando l'Universo aveva appena 3-4 miliardi di anni.

Gli scontri tra ammassi sono gli eventi più energetici a partire dal Big Bang. Durante questi eventi, parte dell'energia è rilasciata in turbolenza e onde d'urto. Questi eventi disturbano l'ICM, il quale presenta quindi morfologie distorte. Inoltre, gli scontri di ammassi accelerano gli elettroni che vagano tra le galassie a velocità prossime a quelle della luce, e amplificano i campi magnetici. L'interazione di particelle accelerate e campi magnetici nell'intero volume degli ammassi produce emissione radio diffusa su larga scale, che non è associata con l'emissione proveniente dai buchi neri nel centro delle galassie (i.e. radio galassie). Queste sorgenti di emssione radio diffusa prendono il nome di *aloni radio* o *relitti radio* (Fig. 6.15).

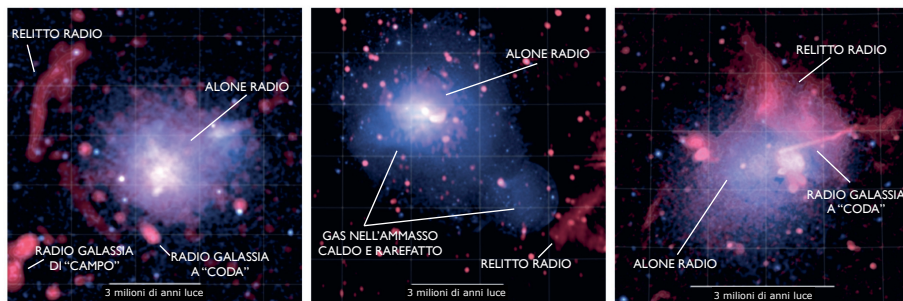- Gli aloni radio sono oggetti più o meno sferici e regolari, che si trovano

231

Figura 6.15: Tre esempi di ammassi di galassie locali osservati a lunghezze d'onda radio (rosso) e X (blu). Da sinistra a destra: Abell 2744, Coma and Abell 2256. L'emissione radio mostra particelle accelerate e campi magnetici, mentre l'emissione X mostra il gas caldo e tenue nell'ammasso. Immagini prese e adattate da van Weeren et al. (2019).

al centro degli ammassi. Di solito seguono la morfologia del mezzo intracluster osservato a lunghezze d'onda X.

- I relitti radio sono strutture allungate che si trovano nelle zone periferiche degli ammassi. Osservazioni recenti hanno mostrato che questi si trovano in corrispondenza di onde d'urto visibili in banda X. Osservazioni radio ad alta risoluzione hanno inoltre rivelato che i relitti hanno una struttura filamentare.

Nonostante i progressi degli ultimi decenni, non è ancora chiara quale sia l'origine dell'emssione radio diffusa negli ammassi. Si pensa che i relitti radio siano prodotti come conseguenza della propagazione di onde d'urto verso le parti periferiche degli ammassi. L'idea di base è che l'onda d'urto allinea e amplifica i campi magnetici, mentre le particelle diventano ultra-relativistiche muovendosi avanti e indietro l'onda d'urto. Uno dei problemi è che le onde d'urto negli ammassi sono relativamente deboli ($\mathcal{M} \leq 3$) e quindi non riuscirebbero ad accellerare le particelle associate all'ICM in modo efficiente. Quindi, è necessaria la presenza di plasma già precedentemente relativistico, come quello nei lobi delle radio galassie. In alcuni casi, è stata osservata una chiara connessione morfologica tra radio galassie e relitti, supportando quest'ultimo scenario. Infine, come conseguenza dell'allineamento e della compressione dei campi magnetici, i relitti radio sono anche polarizzati. Si pensa che gli aloni radio siano prodotti come conseguenza della turbolenza generata dallo scontro di ammassi. Studi recenti hanno trovato infatti una chiara connessione tra lo stato dinamico dell'ammasso e le proprietà degli aloni radio. In particolare, si è osservato che i sistemi più massicci (e quindi più energetici) ospitano gli aloni radio più luminosi.

La presenza di emissione radio diffusa nel volume degli ammassi è un'indicazione importante della presenza di campi magnetici dell'ordine del μGauss. Questo valore è ottenuto in oggetti vicini, analizzando il cambiamento dell'emissione polarizzata da sorgenti che si trovano dietro l'ammasso (i.e. Misura di Faraday). Una domanda aperta, comunque, riguarda l'origine dei campi magnetici. Sono stati identificati due scenari principali: uno assume che i campi magnetici siano generati durante le prime fasi della storia dell'Universo, prima della formazione delle prime stelle e galassie (*origine primordiale*); l'altro assume che i campi magnetici siano emessi dalle galassie, ed espulsi tramite venti o getti (*origine astrofisica*). In entrambi gli scenari, il campo magnetico iniziale deve essere amplificato durante il tempo cosmologico per raggiungere i livelli che sono misurati nell'Universo attuale. È ampiamente condivisa l'idea che la turbolenza dovuta agli scontri di amamssi giochi un ruolo principale, sebbene il processo esatto di amplificazione non sia ancora ben compreso.

Lo scopo di questa Tesi è quello di investigare i meccanismi di accelerazione guidati dalle onde d'urto e dalla turbolenza dovuta allo scontro, e l'evoluzione dell'emissione radio diffusa (e quindi i campi magnetici negli ammassi) durante il tempo cosmico. Questo è stato possibile grazie ad osservazioni estremamente sensibili e ad alta risoluzione in banda radio e X. In particolare, durante il lavoro di Tesi, osservazioni radio con il Karl-Jansky VLA, LOFAR e l'upgraded GMRT sono state combinate con osservazioni X con Chandra, XMM-Newton e Suzaku. Nel **Capitolo 2** e **Capitolo 5** sono state studiate le proprietà spettrali e di polarizzazione del relitto radio nell'ammasso CIZA J2242.8+5301. Grazie ad osservazioni profonde e ad alta risoluzione con il VLA, è stato scoperto che il relitto è composto da diversi filamenti. È ancora non chiaro se questo sia dovuto da una complessa superficie dell'onda d'urto e/o da inomogeneità dei campi magnetici. Le proprietà dell'onda d'urto nell'ammasso ZwCl 0008.8+5215 sono presentate nel **Capitolo 3**. Usando osservazioni profonde con Chandra e Suzaku sono state investigate variazioni nella forza dell'onda d'urto per spiegare le proprietà morfologiche dell'emissione radio diffusa. L'evoluzione dei campi magnetici su scale degli ammassi è presentata nel **Capitolo 4**, studiando un campione di ammassi distanti ($z \geq 0.6$) osservati con LOFAR. Le luminosità radio simili a quelle misurate in sistemi locali, nello stesso intervallo di masse, corrisponde a campi magnetici sorprendemente alti ($\sim$ alcuni μGauss). Le proprietà dello spettro di questi aloni radio distanti sono studiate nel **Capitolo 6**, usando nuove osservazioni con l'uGMRT. Queste informazioni sono cruciali per testare i modelli attuali di formazione dell'emissione radio diffusa.

<div style="border: 1px solid black; text-align: center; padding: 1em;">

LIST OF PUBLICATIONS

</div>

First author

1. **Di Gennaro**, van Weeren, Cassano, Brunetti, Brüggen, Hoeft, Osinga, Botteon, Cuciti, de Gasperin, Röttgering, Tasse. *A LOFAR-uGMRT spectral index study of distant radio halos*, to be submitted, A&A.

2. **Di Gennaro**, van Weeren, Rudnick, Hoeft, Brüggen, Ryu, Röttgering, Forman, Stroe, Shimwell, Kraft, Jones, Hoang. *Downstream depolarization in the Sausage relic: a 1–4 GHz Very Large Array study*, 2021, ApJ, 911, 3.

3. **Di Gennaro**, van Weeren, Brunetti, Cassano, Brüggen, Hoeft, Shimwell, Röttgering, Bonafede, Botteon, Cuciti, Dallacasa, de Gasperin, Domínguez-Fernández, Ensslin, Gastaldello, Mandal, Rossetti, Simionescu. *Fast magnetic field amplification in distant galaxy clusters*, 2021, Nat. Astron., 5, 268.

4. **Di Gennaro**, van Weeren, Andrade-Santos, Akamatsu, Randall, Forman, Kraft, Brunetti, Dawson, Golovich, Jones. *Evidence for a merger induced shock wave in ZwCl 0008.8+5215 with Chandra and Suzaku*, 2019, ApJ, 873, 64

5. **Di Gennaro**, Venturi, Dallacasa, Giacintucci, Merluzzi, Busarello, Mercurio, Bardelli, Gastaldello, Grado, Haines, Limatola, Rossetti. *Cosmic dance in the Shapley Concentration Core. I. A study of the radio emission of the BCGs and tailed radio galaxies*, 2018, A&A, 620, 25

6. **Di Gennaro**, van Weeren, Hoeft, Kang, Ryu, Rudnick, Forman, Röttgering, Brǧgen, Dawson, Golovich, Hoang, Intema, Jones, Kraft, Shimwell, Stroe. *Deep Very Large Array observations of the merging cluster CIZA J2242.8+5301: continuum and spectral imaging*, 2018, ApJ, 865, 24

Contributed author

1. Hoang, Zhang, Stuardi, Shimwell, Bonafede, Brüggen, Brunetti, Botteon, Cassano, de Gasperin, **Di Gennaro**, Intema, Rajpurohit, Röttgering, Simionescu, van Weeren, *A 3.5 Mpc-long radio relic in the galaxy cluster ClG 0217+70*, A&A, in press.

2. Botteon, Cassano, van Weeren, Shimwell, Bonafede, Brǧgen, Brunetti, Cuciti, Dallacasa, de Gasperin, **Di Gennaro**, Gastaldello, Hoang, Rossetti, Röttgering, *Discovery of a radio halo (and relic) in a $M_{500} < 2 \times 10^{14}$ M$_\odot$ cluster*, ApJL, in press.

3. van Weeren, Shimwell, Botteon, Brunetti, Brüggen, Boxelaar, Cassano, **Di Gennaro**, Andrade-Santos, Bonnassieux, Bonafede, Cuciti, Dallacasa, de Gasperin, Gastaldello, Hardcastle, Hoeft, Kraft, Mandal, Rossetti, Röttgering, Tasse, Wilber, *LOFAR observations of galaxy clusters in HETDEX - Extraction and self-calibration of individual LOFAR targets*, A&A, in press.

4. Bruno, Rajpurohit, Brunetti, Gastaldello, Botteon, Ignesti, Bonafede, Dallacasa, Cassano, van Weeren, Cuciti, **Di Gennaro**, Shimwell, Brüggen. *The LOFAR and JVLA view of the distant steep spectrum radio halo in MACS J1149.5+2223*, A&A, in press.

5. Osinga, van Weeren, Boxelaar, Brunetti, Botteon, Brüggen, Shimwell, Bonafede, Best, Bonato, Cassano, Gastaldello, **Di Gennaro**, Hardcastle, Mandal, Rossetti, Röttgering, Sabater. *Diffuse Radio Emission from Galaxy Clusters in the LOFAR Two-metre Sky Survey Deep Fields*, 2021, A&A, 648A, 11

6. Rajpurohit, Brunetti, Bonafede, van Weeren, Botteon, Vazza, Hoeft, Riseley, Bonnassieux, Brienza, Forman, Röttgering, Rajpurohit, Locatelli, Shimwell, Cassano, **Di Gennaro**, Brüggen, Wittor, Drabent, Ignesti. *Physical insights from the spectrum of the radio halo in MACS J0717.5+3745*, 2021, A&A, 646, A135

7. Urdampilleta, Simionescu, Kaastra, Zhang, **Di Gennaro**, Mernier, de Plaa, Brunetti. *X-ray study of Abell 3365 with XMM-Newton*, 2021, A&A, 646, A95

8. Rajpurohit, Wittor, van Weeren, Vazza, Hoeft, Rudnick, Locatelli, Eilek, Bonafede, Bonnassieux, Forman, Riseley, Brienza, Brunetti, Brüggen, Loi, Rajpurohit, Röttgering, Botteon, Clarke, Drabent, Domínguez-Fernández, **Di Gennaro**, Gastaldello. *Understanding the radio relic emission in the galaxy cluster MACS J0717.5+3745: spectral and curvature analysis*, 2021, A&A, 646, A56

9. Bonafede, Brunetti, Vazza, Simionescu, Giovannini, Bonnassieux, Shimwell, Brüggen, van Weeren, Botteon, Brienza, Cassano, Drabent, Feretti, de Gasperin, Gastaldello, **Di Gennaro**, Rossetti, Röttgering, Stuardi, Venturi. *The Coma cluster at LOFAR frequencies I: insights into particle acceleration mechanisms in the bridge region*, 2020, ApJ, 907, 32

10. Ignesti, Shimwell, Brunetti, Gitti, Intema, van Weeren, Hardcastle, Clarke, Botteon, **Di Gennaro**, Brüggen, Browne, Mandal, Röttgering, Cuciti, de Gasperin, Cassano, Scaife. *The great Kite in the sky: a LOFAR observation of the radio source in Abell 2626*, 2020, A&A, 643, A172

11. Botteon, van Weeren, Brunetti, de Gasperin, Intema, Osinga, **Di Gennaro**, Shimwell, Bonafede, Brüggen, Cassano, Cuciti, Dallacasa, Gastaldello, Mandal, Rossetti, Röttgering. *A giant radio bridge connecting two clusters in Abell 1758*, 2020, MNRAS, 499, 11

12. Botteon, Brunetti, van Weeren, Shimwell, Pizzo, Cassano, Iacobelli, Gastaldello, Bîrzan, Bonafede, Brüggen, Cuciti, Dallacasa, de Gasperin, **Di Gennaro**, Drabent, Hardcastle, Hoeft, Mandal, Röttgering, Simionescu. *The beautiful mess in Abell 2255*, 2020, ApJ 897, 93.

13. Mandal, Intema, van Weeren, Shimwell, Botteon, Brunetti, de Gasperin, Brüggen, **Di Gennaro**, Kraft, Röttgering, Hardcastle, Tasse. *Revived Fossil Plasma Sources in Galaxy Clusters*, 2020, A&A, 634, 4

14. Andrade-Santos, van Weeren, **Di Gennaro**, Wittman, Ryu, Vir Lal, Placco, Fogarty, Jee, Stroe, Sobral, Forman, Jones, Kraft, Murray, Brüggen, Kang, Santucci, Golovich, Dawson. *Chandra observations of the spectacular A3411-12 merger event*, 2019, ApJ, 887, 31

15. Cassano, Botteon, **Di Gennaro**, Brunetti, Sereno, Shimwell, van Weeren, Brüggen, Gastaldello, Izzo, Bîrzan, Bonafede, Cuciti, de Gasperin, Röttgering, Hardcastle, Mechev, Tasse. *LOFAR Discovery of a Radio Halo in the High-redshift Galaxy Cluster PSZ2 G099.86+58.45*, 2019, ApJ, 881, 18

16. Brüggen, Rafferty, Bonafede, van Weeren, Shimwell, Intema, Röttge-
    ring, Brunetti, **Di Gennaro**, Savini, Wilber, O'Sullivan, Ensslin, de
    Gasperin, Hoeft. *Discovery of large-scale diffuse radio emission in
    low-mass galaxy cluster Abell 1931*, 2018, MNRAS, 477, 3461

17. Venturi, Bardelli, Dallacasa, **Di Gennaro** Gastaldello, Giacintucci,
    Rossetti. *Extended Radio Emission in the Perhipheral Regions of the
    Shapley Concentration Core*, 2017, Galax, 5, 16

CURRICULUM VITAE

I was born on 16 July 1992 in Mugnano di Napoli, nearby Naples, in Italy. Since I was young I was fascinated by the starry sky, despite the large amount of light pollution in the metropolitan area of Naples. However, I never dreamt about being a scientist. I enjoyed writing, short stories and football articles, and for a period I thought to become a journalist. I started to get engaged with maths thanks to a book, *The Number Devil: A Mathematical Adventure*, which explained mathematical problems through tricks and games.

During the last year of my high school with scientific subjects, I realised that I wanted to study pure science, and to pursue a path of studies in Astronomy. I therefore moved to Bologna, one of the two cities in Italy with a Bachelor program in Astronomy, where I enrolled at the ALMA Mater Studiorum University of Bologna. I received my Bachelor degree on 18 July 2013, and the Master degree in Astrophysics and Cosmology on 18 March 2016. During these years, I gained interests in radio astronomy and the physics of the largest structures in the Universe. I started my research experience by studying the properties of the radio galaxy population in several galaxy clusters located in a supercluster, the Shapley Concentration, using GMRT observations, under the supervision of Prof. Dr. Daniele Dallacasa and Dr. Tiziana Venturi. This work led to a publication, and it was presented with a poster at the "Galaxy Environment and Evolution 4" and "Active Galactic Nuclei 12: a Multi-Messenger perspective" conferences. After my graduation, I was selected to participate at the Leiden/ESA Astrophysics Program for Summer Students (LEAPS), where I worked on low-frequencies (P-band, 230–470 MHz) VLA observations of M87 under the supervision of Dr. Francesco de Gasperin and Dr. Huib

Intema.

I started my PhD in October 2016, where I studied the physics of particle acceleration and magnetic field amplification in merging galaxy clusters, under the supervision of Prof. Dr. Huub Röttgering and Dr. Reinout van Weeren. I spent the first two years of my PhD working at the Center for Astrophysics | Harvard & Smithsonian in Cambridge (MA), USA, as a Pre-Doctoral Fellow. There, I had the chance to work with the major experts in cluster X-ray analysis, such as Dr. William Foreman and Dr. Christine Jones. At the same time, I improved my skills in radio analysis. During these two years, I mostly worked with *Chandra* and VLA data, and I realised the importance of combining among the farthermost wavelengths in the electromagnetic spectrum to get new insights in cluster astrophysics. At the end of the two years, I was invited to present my work at the internal High Energy Seminar. I moved to Leiden in October 2018, where I started to work also with LOFAR data. My work on diffuse radio emission in clusters at high redshift, published in *Nature Astronomy*, was shared with the non-astronomical community through several press releases, and got a great impact in online scientific blogs and magazines. For this project, I was also interviewed by the Italian podcast *Co.scienza*. Since 2019, I have been participating with the outreach website "She speaks science" (http://www.shespeaksscience.com) to translate science-related stories and experiences from female scientists from English to Italian. The aim of this outreach association is to increase the science engagement by inspiring young people into STEM, and to make STEM inclusive by promoting women and minority scientists. During 2019, I also co-supervised the project of a Master student at Leiden Observatory, whose results has become part of a peer-reviewed publication. During the four years as PhD candidate at Leiden Observatory, I have led several successful observing proposals, and I have started collaborations with researchers outside my working group, both in the LOFAR and in international collaborations. I shared the results of my work at several conferences and workshops, in Italy, Germany, USA, India, Netherlands, and Vietnam. I have also been invited to present my work at the next European Astronomical Society (EAS) meeting, occurring in June-July 2021.

Starting from September 2021, I will be a von Humboldt Fellow at the Hamburg Observatory, Germany, and a member of the Quantum Universe – Cluster of Excellence. I will continue my work on the physics of particle acceleration and magnetic field amplification in the largest structures in the Universe.

passed by Garden Street, thank you for the wonderful time and chats in the coffee lounge. Felipe, thanks for being such a patient (non-)supervisor. Everything I know about X-ray is because of you (I'm sorry, you must take the blame!). And thank you for all the BBQs and Caipirinhas, you set a bar that will be hard to reach. Alessandro, Lorenzo, Raffaele, Gerrit, thank you for including me in your special group. I somehow miss the Fridays with terrible (mostly) shark-related movies, and graphs on pizza consumption (tho, I'm still upset by the poor choice of the colour palette). Susanna, Federica, Micaela, you have been such amazing friends. The trips, dinners, concerts, will be always in my heart. Vincenzo, thank you for showing me that playing guitar is always a good idea, even in a moving car or in front of the city hall of Palermo, Maine.

To my wonderful American parents, Bill and Shelley. Words will be never enough to express how grateful I am to both of you for welcoming me in your house, and to consider me as your daughter #4. Having a home and a family during my time on the other side of the ocean was incredible important to me. I will always miss you, and the Sunday family dinners. Steve, Maria, thank you for everything you have done for me. Zena (and Alex), you have been such an amazing flatmate. I am so glad we have met, and that somehow we are still in touch.

I would like to thank all the members of the LOFAR group/collaboration: Alessandro, Alex, Alexander, Andrea, Annalisa, Anniek, Aurora, Chiara, Christian, Cristina, Daniele, Dennis, Duy, Erik, Fabio, Fra, Franco, Frits, George, Gianfranco, Ian, Joe, Joseph, Josh, Julius, Kamlesh, Kim, Lydia, Marisa, Marcus, Matthias, Mariachiara, Marisa, Martijn, Paola, Rafäel, Roland, Rossella, Sarah, Tim, Virginia, Wendy, Xuechen, Yuhan, and those I might have missed. Science discussions and conferences would have been so boring without you all. Gianfranco, Daniele, Fabio, thank you for mixing science discussion and football teasing. Rossella, thank you for being such a caring scientist and person. Marcus, working with you was fun from the first moment, and I am very glad we will continue to interact even more closely. Virginia, thanks for the continuous encouragement, and to have introduced Bill and Shelley to me. Tiziana, Simona, a great part my love for cluster radio astronomy comes from you. Your appreciation in these years was such a honour for me, and I will always consider myself a member of the Shapley Lovers group.

A huge thank to all my (current and previous) STRW fellows for the great time we had during the borrels, lunches, coffee breaks, BBQs and all the social activities: Aayush, Alessandro, Andrea, Alex, Andrej, Anna, Anniek (thank you so much for the Nederlandse samenvatting), Christos, Dario, Dilovan, Eleonora, Emanuele, Erik, Francisca, Fraser (my fakemean buddy who always provided me food at the borrels), Frits, Gaby, Hiddo (my least favourite Dutch person :P), Igone, Josh, Jit, Kim, Kirsty (I will never be thankful enough for introducing me to the basketball team), Lammim (thank you so much for taking care of my plants when I was

not around!), Mantas, Maria Cristina, Marta, Martijn, Martijn, Matteo, Matus, Omar, Pooneh, Rafäel, Roland, Santiago, Stijn, Tommaso, Valeriya. Igone, Joe, MJ, Matteo, thanks for being such nice officemates. Jit, I am so glad you are one of the first person I ever met in Leiden, and that we could walk together through the tough path that is called PhD. I learned a lot from you. Ale, we shared the office during our Master project in Bologna and I am so happy we could repeat the experience in Leiden for few months. Discussing and sharing bad-quality news was such a nice distraction during the infinite LOFAR and VLA processing. Christos (and Andrea), Ele, Jit, MariCri, Tom, Vince, even before I officially moved in Leiden you have been so welcoming, and such great friends. Thank you all for the dinners, laughs, chats and tough words. Dilovan, it's incredible how quickly we clicked, I couldn't have found a better person to have fun with. Thank you for all the time spent together, the walks, the biking to the tulip fields and to the beach. Drinking wine, and all the conversations that came with that, with you and Omar is one of the funniest memories I will carry with me.

I strongly believe that (watching and playing) sport makes you forget about all the issues you may have. To "my" Inter, a huge metaphor of life: going through (several) failures and disappointments before reaching (few) moments of joy and satisfaction: thank you for constantly forging my strength, for being crazy and never boring. I am extremely thankful to everyone at the LUSV for the games, training, pub crawling and borrels we had. To all the girls in the Ladies 3 and 1 teams: Ana, Annalise, Arthur, Carmen, Debbie, Emily, Faye, Floor, Ib, Jorike, Kim, Kirsty, Louise, Lotti, Marjan, Myrenka, Ratima, Rosanne, Sabine, Salma, Satu, Sifra, Yaël, Wypkie. Playing basketball and hanging out with you was so fun. To my (almost entirely) Dutch family, Aydin, Debbie, Giac, Jessie, Leon, Luuk, Marco, Marlon, Sandy. Thank you for keeping me mentally sane during the lockdown, and reminding me that age is just a number (unless you are older than 27, then apparently all the troubles start). I have so many gezellinge *memories of you*. Jess, having you around made me extremely lucky, and proves that opposites attract. Thank you for your emotional support, the continuous encouragement, the silly moments and serious conversations, and the late drinking nights: everything was incredibly important to me. I am extremely happy to be your Gabber.

Nella lista di persone che meritano menzioni speciali non possono mancare quelle che mi hanno accompagnato dai primi giorni in cui ho deciso di iniziare il percorso in Astrofisica: Ali, Circos, Euge, Franci, Sara, dirvi grazie è quanto di più banale, ma estremamente vero, ci possa essere. Per tutte le conversazioni stupide per alleggerire i momenti difficili, per il supporto costante che mi date, per le verità scomode (e talvolta moralizzatrici) e per i confronti scientifici… grazie, grazie, grazie. Avervi nella mia vita è un bellissimo privilegio, e so di poter contare su di voi in qualunque angolo di mondo ci possiamo trovare (anche se Bologna resterà sempre il nostro

punto di riferimento). Bob, Luca e Peppe, grazie anche a voi per essere parte di questa famiglia. Raffi, grazie perchè mantenere un'amicizia per quindici anni, dieci dei quali a distanza, non è semplice, ma è sempre bello sapere che comunque ci proviamo.

Alla mia famiglia, nessuno escluso: essere fisicamente lontana da voi è sempre la cosa più difficile. Adina, cocca mia: grazie per la tantissima forza che mi trasmetti quando ci parliamo. Ai miei genitori, che ogni giorno spero di rendere orgogliosi: grazie per essermi sempre vicino, e per avermi insegnato a non accontentarmi mai. Vinz, grazie per avermi sopportata in casa, che fosse Milano o Mumbai. Irene, grazie per aver reso il (primo) periodo delle application meno stressante solo con la tua presenza, e perdonami se ho adorato vedere la tua faccia della tristezza. Infine, ma non per ultimo, un grazie speciale a Giulia, la persona cui questa tesi è dedicata. Se dovessi mai diventare la metà di quello che sei, potrei solo ritenermi fortunata.

Aan iedereen: dank je wel[1].

---

[1]Thanks Jess for double checking this, as my Dutch skills stop at: *Ik heb een glas wijn nodig.*

Dicette o pappice vicino a' noce, ramm' o tiemp' ca te spertose.

The warm said to the nut, give me time and I'll break you.